

Understanding Microwave Treatment of Ores

Dafydd Aled Jones

**Thesis submitted to The University of Nottingham for the Degree of
Doctor of Philosophy**

November 2004

Abstract

Microwave energy has previously been shown to have a major influence on the comminution behaviour of minerals and ores. Significant reductions in strength have been observed for microwave-treated ores. Other workers have reported increases in liberation after treatment. However, the majority of the work has been carried out at energy inputs too high for economic implementation. Whilst it was thought that the weakening and enhanced liberation was due to differential expansion of the heated constituent phases resulting in increased predominance of inter-granular fracture, the exact mechanisms have been poorly understood. Due to difficulties in measuring events inside a microwave cavity and inside the material being irradiated, it was suggested that numerical modelling could be used to simulate a simplified system in order to determine the underlying mechanisms. The model was used to examine the development of stresses as heat was applied to certain mineral phases. No heat was applied directly to the matrix component of the simulated ore. Given sufficient energy input, the stresses would exceed the strength of the material. It was found that the shear stresses in particular were likely to be highest at the edges of the grain boundaries of 2-D circular heated particles inside an unheated (microwave-transparent) matrix. This explained the increased occurrence of intergranular fracture which has led to observations of enhanced liberation. It was also discovered that weakening is facilitated at very high microwave power densities, due to the increased magnitude of expansion and subsequent forces generated. The overall energy balance can be made favourable by using microwave exposure times of less than 0.1 seconds. Shorter exposure times result in less time for conduction to occur from the heated phase into the unheated phase, and temperature gradients are maximised leading to elevated shear stresses and increased likelihood of fracture.

Acknowledgements

I wish to express sincere gratitude to Dr. Sam Kingman of the School of Chemical, Environmental and Mining Engineering at The University of Nottingham for his supervision and guidance during the study, and for offering me the opportunity to undertake the project. I would also like to thank Dr. David Whittles, Dr. Keith Jackson for their technical expertise. I also wish to convey my appreciation to Rio Tinto Technology Development, and the EPSRC, for funding my research. Finally, I wish to thank my girlfriend, Kate, for her support throughout.

List of Contents

Abstract	i
Acknowledgements	ii
List of Figures	x
List of Tables	xvii
List of Symbols	xx
Chapter 1 - Statement of Objectives	1
Chapter 2 - Theoretical Aspects of Microwave Heating	
2.1. Introduction	3
2.2. Electromagnetic Spectrum	4
2.3. Microwave Heating Mechanisms	5
2.3.1. Conduction Mechanism – Dipolar Polarisation	5
2.3.2. Dipolar Polarisation	6
2.3.3. Interfacial Polarisation	7
2.4. Dielectric Properties	8
2.4.1. Introduction	8
2.4.2. Relative Permittivity	8
2.4.3. Dielectric Constant and Loss Angle	9
2.4.4. Variation of Dielectric Properties with Temperature and Frequency	9
2.5. Calculation of Penetration Depth	12
2.6. Power Absorption	12
2.7. Temperature Rise Calculation	13
2.8. Thermal Stresses	14
2.9. Microwave Engineering	15
2.9.1. Introduction	15
2.9.2. Industrial Microwave Heating	15
2.9.3. Microwave Generator Types	16
2.9.3.1 Magnetrons	17
2.9.3.2 Klystrons	19
2.9.4. Transmission	20

2.9.5. Microwave Applicator Types	20
2.9.5.1 Multimode Cavities	20
2.9.5.2 Single Mode Resonant Cavities	21
2.9.6. Reflected Power Dissipation	22
2.9.7. Active Tuning	22
2.10. Conclusions	23

Chapter 3 - Applications of Microwave Radiation for Minerals Processing

3.1. Introduction	24
3.2. Thermally Assisted Liberation	26
3.3. Dielectric Properties of Minerals	28
3.4. Previous Research on Microwave Processing of Minerals	32
3.4.1. Heating Studies	32
3.4.2. Penetration Depth Measurement	34
3.5. Applications of Microwave Radiation in Extractive Metallurgy	35
3.6. Microwave Reduction of Metal Oxides	36
3.7. Hydrometallurgical Applications	38
3.8. Applications of Microwave Radiation in Gold Extraction	38
3.9. Applications of Microwave Radiation in the Processing of Coal	39
3.10. Effects on the Magnetic Susceptibility of Minerals	41
3.11. Application of Microwave Treatment for Improved Comminution	42
3.11.1. Introduction	42
3.11.2. Improved Grindability	42
3.11.3. Reduction in the Point Load Index	44
3.11.3.1 Introduction	44
3.11.3.2 Theory and Background	44
3.11.3.3 Methodology and Previous Results	46
3.11.4. Drop Weight Tests	49
3.11.5. Determination of the Uniaxial Compressive Strength	52
3.11.6. Liberation	58
3.11.7. QEM*SEM	59
3.12. Theoretical Studies	59
3.13. Conclusions	61

Chapter 4 - Methods for Predicting Stresses and Strains in Rock Mechanics

4.1	Introduction	62
4.2	Nature of Rock Mechanics	64
4.3	Computer based numerical modelling methods	67
4.3.1	Introduction	67
4.3.2	Geomechanical Modelling	68
4.4	Numerical Modelling Methodologies	70
4.4.1	Introduction	70
4.4.2	Continuum Methods	70
4.4.2.1	Finite Element Method	70
4.4.2.2	Finite Difference Method	72
4.4.2.3	Boundary Element Method	76
4.4.3	Discontinuum Methods	77
4.4.3.1	Distinct Element Method	77
4.4.3.2	Particle Flow Code	78
4.5	Numerical Modelling Methodologies	79
4.5.1	Ultimate Design Tool	79
4.5.2	Method of Last Resort	79
4.5.3	Aid to Judgement	80
4.5.4	Calibrated Model	80
4.6	Fast Lagrangian Analysis of Continua (<i>FLAC</i>)	82

Chapter 5 - Numerical Methods

5.1	Introduction	84
5.2	Numerical Modelling of Thermally Generated Stresses and Strains	85
5.2.1	Introduction	85
5.2.2	Simulating Fractures in Continuum Modelling	86
5.2.3	The Finite Difference Grid Specification	87
5.2.4	Discretisation	88
5.2.5	<i>FLAC</i> Constitutive Models	89
5.2.5.1	Null Model	89
5.2.5.2	Elastic Isotropic Model	89
5.2.5.3	Plasticity Models	90
5.2.5.3.1	Mohr-Coulomb Model	90

5.2.5.3.2	Strain-softening model	91
5.2.6	Simulation of Microwave Heating and Thermally Induced Stresses and Strains	91
5.2.6.1	Introduction	91
5.2.6.2	Modelling of Microwave heating	92
5.2.6.3	Modelling of Transient Heat Conduction	93
5.2.6.4	Thermally Generated Stresses and Strains	98
5.2.7	Mechanical Modelling	99
5.2.7.1	Mechanical Constitutive Modelling	99
5.2.7.2	Strain Softening	100
5.2.8	Modelling Input Parameters	101
5.2.8.1	Introduction	101
5.2.8.2	Density	102
5.2.8.3	Strength Parameters	102
5.2.8.4	Bulk Modulus	102
5.2.8.5	Shear Modulus	103
5.2.8.6	Mohr-Coulomb Strength Criterion Determination	103
5.2.8.6.1	Cohesion	104
5.2.8.6.2	Tensile Strength	104
5.2.8.6.3	Friction Angle	104
5.2.8.6.4	Poisson's Ratio	104
5.2.9	Thermal-Mechanical Coupling	105
5.2.9.1	Introduction	105
5.2.9.2	Determination of Characteristic Length	105
5.2.9.3	Coupling the Thermal-Mechanical Models	106
5.2.9.4	Mechanical Timestep Calculation	107
5.2.9.5	Thermal Timestep Calculation	108
5.2.10	Thermodynamic Properties	109
5.2.10.1	Introduction	109
5.2.10.2	Specific Heat Capacity	110
5.2.10.3	Thermal Volumetric Expansion Coefficient	112
5.2.10.4	Thermal Conductivity	114
5.2.11	Implementation of Thermal Behaviour in <i>FLAC</i>	116
5.2.11.1	Introduction	116

5.2.11.2	Specific Heat Capacity	116
5.2.11.3	Thermal Conductivity	119
5.2.11.4	Thermal Expansion	121
5.2.12	Construction of the Ore Model in <i>FLAC</i>	123
5.2.12.1	Introduction	123
5.2.12.2	Grid Specification	123
5.2.12.3	Random Distribution of Heated Particles	123
5.2.12.4	Power Density Specification	125
5.2.12.5	Initial Temperature of Sample	127
5.2.12.6	Implementation of Heating Simulation	127
5.3	Practical Use of the <i>FLAC</i> Software	130
5.3.1	Introduction	130
5.3.2	Miscellaneous Model Output Plot Types	131
5.3.3	Vector Output Plots	138
5.3.4	Contour Output Plots	142
5.3.5	Parameter History Plots	146
5.3.6	Profile Output Plots	148
5.3.7	Simulations of the Uniaxial Compressive Strength Tests	150
5.3.7.1	Introduction	150
5.3.7.2	Methodology	150
5.3.7.3	Crack Propagation during UCS Test	151
5.3.7.4	Discussion	161
5.4	Conclusions	162

Chapter 6 - Results and Discussion

6.1	Introduction	163
6.2	Initial Demonstration of Fracturing in Simple 2-Phase Model	165
6.2.1	Introduction	165
6.2.2	Methodology	165
6.2.3	Results and Discussion	167
6.2.4	Validation	171
6.2.5	Implications for Mineral Processing	172
6.3	Parameter Variation with Position and Time	175
6.3.1	Introduction	175

6.3.2	Methodology	175
6.3.3	Results	178
6.3.4	Discussion	191
6.4	Closer Examination of Stress Regime	192
6.4.1	Introduction	192
6.4.2	Methodology	192
6.4.3	Results	193
6.4.4	Discussion	196
6.5	Further Parameter Variation with Position inside the Particle	197
6.5.1	Introduction	197
6.5.2	Methodology	197
6.5.3	Results	198
6.5.4	Discussion	206
6.6	Influence of Grain Size on Development of Stresses and Strains	207
6.6.1	Introduction	207
6.6.2	Methodology	207
6.6.3	Results	208
6.6.4	Discussion	215
6.7	Quantification of Damage in the Sample	217
6.7.1	Introduction	217
6.7.2	Methodology	217
6.7.3	Results	221
6.7.4	Discussion	229
6.8	Effects of Power Density and Exposure Time on Damage Parameter	230
6.8.1	Introduction	230
6.8.2	Methodology	230
6.8.3	Results	230
6.8.4	Discussion	232
6.9	Investigating Effects of Decreased Time for Conduction	233
6.9.1	Introduction	233
6.9.2	Methodology	233
6.9.3	Results	234
6.9.4	Discussion	242
6.10	Investigation of Increased Magnitude of Particle Boundary Acceleration	243

6.10.1	Introduction	243
6.10.2	Methodology	243
6.10.3	Results and Discussion	244
6.11	Effect of Varying Exposure Time on Damage Incurred	245
6.11.1	Introduction	245
6.11.2	Methodology	245
6.11.3	Results	246
6.11.4	Discussion	247
6.12	Comparison of Damage Parameter with UCS results	248
6.12.1	Introduction	248
6.12.2	Methodology	248
6.12.3	Results	249
6.12.4	Discussion	252
6.13	Correlation between UCS and Damage Parameters	253
6.13.1	Introduction	253
6.13.2	Methodology	253
6.13.3	Results	254
6.13.4	Discussion	262
6.14	Influence of Microwave Energy Input on Strength Reduction	264
6.14.1	Introduction	264
6.14.2	Methodology	264
6.14.3	Results of Low Power Longer Exposure Simulations	265
6.14.4	High Power Short Exposure Simulations	268
6.14.5	Constant Energy Results	269
6.14.6	Discussion	271
6.15	Effects of Varying Texture on Strength	272
6.15.1	Introduction	272
6.15.2	Methodology	272
6.15.3	Results and Discussion	273
6.16	Conclusions	276
 Chapter 7 – Conclusion and Further Work		
	Conclusion	278
	Future Work	283

List of Figures

Chapter Two

- Figure 2.1 Electromagnetic Spectrum
- Figure 2.2 Representation of electron cloud moving in perfect phase with incident radiation for perfect conductor
- Figure 2.3 Dipolar polarisation schematic
- Figure 2.4 Relationship between the dielectric loss factor and ability to absorb microwave power for some common materials
- Figure 2.5 Schematic diagram of a magnetron shown in cross-section
- Figure 2.6 Sectional view of a typical microwave

Chapter Three

- Figure 3.1 The dependence of dielectric constant of sulphide minerals with temperature measured at 615MHz
- Figure 3.2 The dependence of loss factor of sulphide minerals with temperature measured at the frequency of 615 MHz.
- Figure 3.3 The dependence of dielectric constant of sulphide minerals with temperature measured at 2.216GHz
- Figure 3.4 The dependence of loss factor of sulphide minerals with temperature measured at the frequency of 2.216 GHz.
- Figure 3.5 The dependence of dielectric constant of quartz with temperature measured at different packing densities
- Figure 3.6 The dependence of loss factor of quartz with temperature measured at different packing densities
- Figure 3.7 Principle of operation of point load apparatus

- Figure 3.8 Point load index test results
- Figure 3.9 Stress-strain profile for a tough, brittle material
- Figure 3.10 Stress-strain profile for a softer material
- Figure 3.11 Schematic showing liberated valuable mineral and gangue, and the locked portions.

Chapter Four

- Figure 4.1 Fontainebleau sandstone
- Figure 4.2 Micrograph of shear bands obtained with binocular magnifying glass.
- Figure 4.3 a) continuous and (b) discontinuous behaviour of uniaxially loaded specimen
- Figure 4.4 Basic explicit calculation cycle, finite difference method
- Figure 4.5 Holling's conceptual classification of modelling problems

Chapter Five

- Figure 5.1 Discretisation schematic for *FLAC*
- Figure 5.2 Variation of specific heat capacity of calcite and pyrite with temperature and linear fit portions
- Figure 5.3 *FISH* function used to specify specific heat capacity over prescribed ranges
- Figure 5.4 Variation of thermal conductivity with temperature
- Figure 5.5 *FISH* function used to describe thermal conductivity over expected temperature range
- Figure 5.6 Variation of thermal expansion with temperature for calcite and pyrite

Figure 5.7	<i>FISH</i> function used to describe thermal expansion of constituent phases.
Figure 5.8	<i>FISH</i> function to describe random heater distribution and its material properties
Figure 5.9	<i>FISH</i> function describing power density application to heated zones
Figure 5.10	<i>FISH</i> closing statements for ‘trop’ function
Figure 5.11	Default plot in <i>FLAC</i> , showing regions, marked grid points, applied boundary conditions.
Figure 5.12	Detail of Figure 5.11
Figure 5.13	Plot showing model type
Figure 5.14	Marked regions – detailing geometry of calcite and pyrite regions
Figure 5.15	Plot showing material groups
Figure 5.16	Plasticity plot showing tensile cracks, past yield regions and current shear zones
Figure 5.17	State plot showing tensile cracks forming radially outwards, past yield regions and current shear zones
Figure 5.18	Plot showing displacements in the model
Figure 5.19	Detail of pyrite boundary, and zero vectors in centre.
Figure 5.20	Velocity vectors
Figure 5.21	Detail of ‘crack’ above right from centre of Figure 5.21
Figure 5.22	Temperature contours in the sample.
Figure 5.23	Contours of horizontal stress,
Figure 5.24	Contours of vertical stress
Figure 5.25	Contours of shear stress
Figure 5.26	History function plot of variation of temperature with time

- Figure 5.27 Illustration showing method of drawing profile line
- Figure 5.28 Temperature profile line from centre of heated particle across grain boundary and into transparent phase
- Figure 5.29 Initial crack development during UCS test after 25000 loading steps
- Figure 5.30 Corresponding stress-strain plot for loading step 25000
- Figure 5.31 Further development of crack after 25100 loading steps
- Figure 5.32 Further development of crack after 25200 loading steps
- Figure 5.33 Further development of crack after 25300 loading steps
- Figure 5.34 Corresponding stress-strain plot for loading step 25300
- Figure 5.35 Shear strain bands after 26000 steps
- Figure 5.36 Shear strain bands after 40000 steps
- Figure 5.37 Corresponding stress-strain plot for loading step 40000

Chapter Six

- Figure 6.1 Plot showing extent of circular heated particle (deep red) within circular transparent matrix (reddish-pink)
- Figure 6.2 10 μ s – state after first step – no plasticity or fractures yet
- Figure 6.3 250 μ s – first sign of plasticity around grain boundary, tensile regime around edges
- Figure 6.4 300 μ s – shear plasticity has spread around the heated particle's grain boundary very quickly.
- Figure 6.5 600 μ s - shear cracks forming radially outward from grain boundary, first sign of tensile cracks also appearing as shear is exacerbated.
- Figure 6.6 1000 μ s – extensive tensile cracks, also forming from boundary inwards

Figure 6.7	SEM photograph of chalcopyrite particle in transparent matrix exposed to high power short exposure time microwave radiation
Figure 6.8	Extensive fractures in all-pyrite sample
Figure 6.9	Fewer fractures in all-calcite sample due to lower stiffness
Figure 6.10	Close-up of history locations - boundary lies between 80,61 and 80,60.
Figure 6.11	Variation of temperature with timestep for different positions in the model
Figure 6.12	Plot showing volumetric strain increment profiles for various positions in the sample
Figure 6.13	Volumetric strain rate histories
Figure 6.14	Shear strain increment histories at various positions.
Figure 6.15	Plot showing variation of shear stress with timestep
Figure 6.16	First appearance of plasticity after 1600 steps (0.16ms).
Figure 6.17	Displacement in vertical direction
Figure 6.18	State plot detailing fractures outside heated particle boundary
Figure 6.19	Stress difference contours, minimum 25MPa
Figure 6.20	Stress difference contours, minimum 20MPa
Figure 6.21	Stress difference contours, minimum 15MPa
Figure 6.22	Temperature profile plot along diagonal from centre
Figure 6.23	Volumetric strain increment profile plot
Figure 6.24	Shear strain increment profile plot
Figure 6.25	Stress difference profile plot
Figure 6.26	Shear stress profile plot
Figure 6.27	Principal stress profile

- Figure 6.28 Compressive stress in the vertical direction
- Figure 6.29 Compressive stress in the horizontal
- Figure 6.30 Line plot for peak temperature in the sample for varying power density and heated particle size, for 10ms exposure time
- Figure 6.31 Detail of *FISH* function devised for obtaining damage parameter.
- Figure 6.32 Distribution of heated particles in 5mm circular transparent particle
- Figure 6.33 Distribution of heated particles in 100mm circular transparent particle
- Figure 6.34 Plot showing residual tensile strength in the 5mm sample
- Figure 6.35 Plot showing residual tensile strength in the 100mm sample
- Figure 6.36 Close-up of Figure 6.35
- Figure 6.37 Heater distribution
- Figure 6.38 Key to tensile strength contours.
- Figure 6.39 Cohesion contours in the 5mm sample, showing greatest cohesion reduction in vicinity of heated particle centres.
- Figure 6.40 Plot of Cd, Td versus diameter
- Figure 6.41 Temperature history plots for $1 \times 10^{15} \text{ W/m}^3$ for 1 μs .
- Figure 6.42 Temperature history plots for $1 \times 10^{14} \text{ W/m}^3$ for 10 μs .
- Figure 6.43 Temperature history plots for $1 \times 10^{13} \text{ W/m}^3$ for 100 μs .
- Figure 6.44 Temperature history plots for $1 \times 10^{12} \text{ W/m}^3$ for 1ms.
- Figure 6.45 Temperature history plots for $5 \times 10^{11} \text{ W/m}^3$ for 2ms.
- Figure 6.46 Plot showing variation of Td and Cd with timestep for $1 \times 10^9 \text{ (W/m}^3\text{)}$ and $1 \times 10^{15} \text{ (W/m}^3\text{)}$ for 1 μs
- Figure 6.47 Stress vs strain plot for untreated 40mm diameter sample with 1% heated particles
- Figure 6.48 UCS test on the $1 \times 10^9 \text{ W/m}^3$ sample for 1s

- Figure 6.49 Stress vs strain plot of the UCS test on the $1 \times 10^{15} \text{ W/m}^3$ sample for $1\mu\text{s}$.
- Figure 6.50 Comparison of percentage reduction in UCS, and total number of strain softened zones.
- Figure 6.51 Temperature contours for the low power long exposure after 10s heating at $1 \times 10^9 \text{ W/m}^3$
- Figure 6.52 State plot for the low power long exposure after 10s heating at $1 \times 10^9 \text{ W/m}^3$
- Figure 6.53 Temperature contours after $10\mu\text{s}$ high power short exposure heating at $1 \times 10^{15} \text{ W/m}^3$.
- Figure 6.54 State plot for the high power short exposure case
- Figure 6.55 Variation of UCS with low power long exposure
- Figure 6.56 Variation of UCS with high power short exposure
- Figure 6.57 Summary of reduction in UCS with constant energy inputs
- Figure 6.58 Plot detailing strength reduction with varying composition

List of Tables

Chapter Two

- Table 2.1 Dielectric constant for selected materials
- Table 2.2 Dielectric loss factor for selected materials

Chapter Three

- Table 3.1 Effect of power level on heating rate
- Table 3.2 Depth of penetration in selected minerals
- Table 3.3 Change in field strength of minerals after irradiation
- Table 3.4 Matrix for point load tests
- Table 3.5 $I_s(50)$ as a function of microwave exposure time for material -53 +45 mm showing statistical measures
- Table 3.6 Nominal energy input particle size combinations for JKMRC drop weight energy input levels.
- Table 3.7 Breakage parameters for treated and non-treated ore

Chapter Four

- Table 4.1 Comparison of explicit and implicit solution schemes

Chapter Five

- Table 5.1 Summary of parameter values for thermal diffusivity calculation
- Table 5.2 Specific heat capacity of minerals at various temperatures, and coefficients of heat capacity
- Table 5.3 Variation in volumetric expansion with temperature
- Table 5.4 Variation of thermal conductivity of minerals with temperature

Table 5.5	Summary of correlations between UCS and other breakage parameters
-----------	---

Chapter Six

Table 6.1	Peak stresses and strains for 1ms at $1 \times 10^8 \text{ W/m}^3$
Table 6.2	Peak stresses and strains for 1 ms at $1 \times 10^9 \text{ W/m}^3$
Table 6.3	Peak stresses and strains for 1 ms at $5 \times 10^9 \text{ W/m}^3$
Table 6.4	Peak stresses and strains for 1 ms at $1 \times 10^{10} \text{ W/m}^3$
Table 6.5	Peak stresses and strains for 1 ms at $5 \times 10^{10} \text{ W/m}^3$
Table 6.6	Peak stresses and strains for 1 ms at $1 \times 10^{11} \text{ W/m}^3$
Table 6.7	Damage parameter results with variation in size of sample.
Table 6.8	Number of zones with tensile strength reduction
Table 6.9	Number of zones with cohesion reduction
Table 6.10	Theoretical particle boundary velocities and accelerations
Table 6.11	UCS values for various model configurations
Table 6.12	Calculation of reduction in cohesion damage for the high power short exposure case
Table 6.13	Calculation of reduction in tensile strength damage for high power short exposure case
Table 6.14	Equivalent UCS reduction for high power short exposure case
Table 6.15	Calculation of reduction in tensile strength damage for low power long exposure case
Table 6.16	Calculation of reduction in cohesion damage for low power long exposure case
Table 6.17	Equivalent UCS reduction for high power short exposure case

Table 6.18	Low power longer exposure uniaxial compressive strength test matrix of results (MPa)
Table 6.19	High power short exposure uniaxial compressive strength matrix of results (MPa)
Table 6.20	Results from the variation of percentage of heaters with constant energy input

List of Symbols

c	Speed of light (299 792 458 m/s)
λ	Wavelength (m)
f	Frequency (Hz)
ε^*	Complex permittivity
ε'	Permittivity or dielectric constant
ε''	Dielectric loss factor
ε'_r	Relative dielectric constant
ε'_{eff}	Effective relative loss factor
ε_0	Permittivity of free space (8.85×10^{-12} F/m)
σ	Electrical conductivity of the material (S/m)
θ	Phase angle (radians)
j	Square root of -1
D	Penetration depth (m)
$P.d.$	Power density (W/m^3)
E	Root mean square Electric Field Strength (V/m)
dT	Temperature change ($^{\circ}\text{K}$)
dt	Time increment (s)
C	Specific heat capacity (J/g.K)
ρ	Density (kg.m^{-3})
l_1, l_2	Distances from the junction to the short-circuit pistons in a single mode cavity
$I_s(50)$	Point load index
t_{10}	Amount passing 10% the original mean size

$t_2, t_4, t_{25}, t_{50}, t_{75}$ Equivalent amounts passing 2%, 4%, 25%, 50% and 75% of original size

A, b Breakage parameters

E_{cs} Specific comminution energy (kW.h/t)

S_n Total distance to be graded

r Aspect ratio

a_1 Length of zone 1

n Number of zones

σ_{xx} Compressive stress in horizontal direction (MPa)

σ_{yy} Compressive stress in vertical direction (MPa)

σ_{zz} Compressive stress in out-of-plane direction (MPa)

σ_{xy} Shear stress (MPa)

K Bulk Modulus (GPa)

G Shear Modulus (GPa)

E Young's Modulus (GPa)

ν Poisson's ratio

q_i Heat-flux vector in (W/m³)

q_v Volumetric heat-source intensity (W/m³)

ζT Heat stored per unit volume in (J/m³)

M_T Material constant

β_v Material constant

T Temperature (°C)

C_v Specific heat capacity at constant volume (J/kg.K)

C_p Specific heat capacity at constant pressure (J/kg.K)

\underline{q}	Heat flux vector (J/s.m)
k	Thermal conductivity tensor (W/m.°C)
$\underline{T_{diff}}$	Temperature difference vector (°C)
Q	Rate of change of thermal energy (J/s)
s	Surface of the zone (m)
v	Volume of the zone (m)
ds	Surface increment (m)
dv	Volume increment (m)
\underline{n}	Unit normal vector to the surface (m)
$k_{(i,j)}$	Thermal conductivity of zone (i, j) (W/m.°C)
l	Length of the sides of the zones (m)
$T_{(i,j)}$	Temperature of zone (i, j) (°C)
$\Delta\beta$	Change in stored energy (J)
Δt	Time increment (s)
$\Delta T_{(i,j)}$	Temperature change in zone (i, j) (°K)
$m_{(i,j)}$	Mass of zone (i, j) (kg)
$C_{(i,j)}$	Specific heat of zone (i, j) (J/kg.K)
$T_{(i,j)}(n)$	Temperature of zone (i, j) at time increment n
$Pd(i, j)$	Power density of zone (i, j)
n	Time increment number
ht	Heating time (s)
$\varepsilon_{(i,j)}$	Strain in zone (i, j)
$\alpha_{(i,j)}$	Thermal expansion coefficient (1/°K) of zone (i, j)

$T_{n(i,j)}$	Final temperature of zone (i, j) ($^{\circ}\text{C}$)
$T_{1(i,j)}$	Initial temperature of zone (i, j) ($^{\circ}\text{C}$)
$\sigma_{(i,j)}$	Isotropic thermal induced stress in zone (i, j) assuming perfect restraint (Pa)
$E_{(i,j)}$	Young's Modulus of zone (i, j) (GPa)
$\nu_{(i,j)}$	Poisson's Ratio of zone (i, j)
τ	Shear stress (N/m^2)
σ_n	Normal stress (N/m^2)
ϕ	Friction angle
C	Cohesion (N/m^2)
L_c	Characteristic length (m)
t_c	Characteristic time (s)
δV	Volumetric expansion of the solid (m^3)
α_v	Coefficient of volumetric expansion (K^{-1})
V_0	Original volume (m^3)
V_n	New volume (m^3)
V_c	Percentage change in volume
V_0	Original volume (m^3)
Q	Heat conducted (W)
A	Surface area (m^2)
θ_1	Original temperature ($^{\circ}\text{C}$)
θ_2	Final temperature ($^{\circ}\text{C}$)
l	Length (m)
P	Failure load (Pa)

D	Distance between tips of point load tester (m)
I_s	Strength index
K_{IC}	Mode 1 fracture toughness

Chapter 1

Statement of Objectives

Due to environmental and economic drivers there is great scope for improvement in size reduction process efficiency within the global mining industry. Comminution is one of the most energy-intensive and least efficient processes within the process flowsheet (Schwechten and Milburn, 1990). It is estimated that approximately 3% of the total World electricity energy generated is consumed in comminution. Current methods of size reduction are inherently inefficient; it is reported that grinding is less than 1% efficient based on the energy required to produce new surfaces (Rhodes, 1998). Consequently even a marginal improvement in the operational efficiency can lead to a substantial energy saving and reduced environmental impact.

One increasingly attractive method of improving efficiencies within comminution may be the use of high electric field strength microwave radiation. An increasing body of work has been completed over the last twenty years investigating the effects of exposing minerals to microwave radiation. Work using high power microwave equipment has yielded significant reductions in strength and improvements in liberation and subsequent recovery (Kingman et al, 2004). Until recently, the many reported advantages of exposing minerals to microwaves have only been achieved at energy inputs too high to be considered potentially economic. However, the work carried out by Kingman and his co-workers has shown that by maximising microwave power density (volumetric heating rate) and by reducing exposure times, reduced comminution energy and increased recovery of valuable mineral phases can be achieved for energy inputs of less than 1kW.h/t. This is the first laboratory scale study where this technology has been shown to be economically attractive.

It is foreseen that the application of high electric field strength microwave radiation will have major implications for the minerals processing industry. Potential improvements include:

- o Increase in throughput for existing plant,
- o Reduced wear and tear for a given tonnage through existing plant,
- o Reduced comminution energy requirement for new plant,
- o Increase in liberation size for existing processes and subsequent increase in recovery
- o Reduction in plant capital costs.

Microwaves are thought to facilitate improvements in efficiencies by inducing disorder at grain boundaries as a result of differential heating and subsequent expansion. It is suspected that high thermal stresses are generated, and that these stresses can exceed the strength of the material. Enhanced liberation is thought to be possible as a consequence of increased occurrence of inter-granular micro-cracking. However, due to the difficulty in measuring events inside the material being irradiated, the exact mechanism is difficult to quantify experimentally, and therefore these mechanisms are yet to be fully understood and proven. The nature of the interactions between electromagnetic, thermal and mechanical properties of the ore results in an extremely complex system. This work attempts to better understand these underlying mechanisms by linking for the first time, interactions between microwave heating, mineralogy and texture using numerical modelling and simulation.

Chapter 2

Theoretical Aspects of Microwave Heating

2.1. Introduction

This chapter details the mechanisms by which materials heat within a microwave field, the factors which typically govern the rate of heating, and the means by which microwave radiation is applied to materials.

2.2. Electromagnetic Spectrum

Microwaves form part of a continuous electromagnetic spectrum that extends from low frequency alternating currents to cosmic rays. Microwave radiation lies between infrared and radio waves in this spectrum, and is non-ionising. Wavelengths typically range from 1mm to 1m. Their properties are governed by equation 2.1 (Parker, 1993)

$$c = \lambda \cdot f \quad \text{(Equation 2.1)}$$

where: c is the speed of light (299 792 458 m/s)

λ is the wavelength (m)

f is the frequency (Hz)

Figure 2.1 shows the part of the electromagnetic spectrum which is concerned with microwave radiation. Microwave heating applications usually make use of the 0.915 (0.896 in the UK) and 2.45GHz frequencies in order to minimise interference with communication band microwaves. Frequencies allocated to electroheat are often designated ISM - ‘industrial, scientific and medical’ frequencies. The frequencies chosen for microwave heating are the result of historical evolution and a complexity of international committees which constantly review the use of the electromagnetic spectrum (Meredith, 1998).

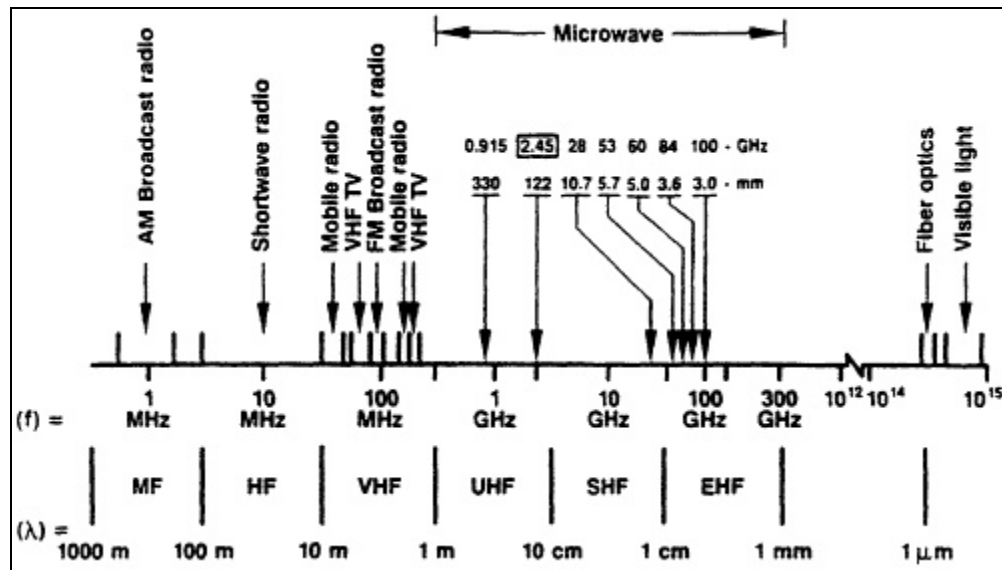


Figure 2.1: Electromagnetic Spectrum (after Sutton, 1993)

2.3. Microwave Heating Mechanisms

Microwaves are said to affect materials in three ways in that they conduct, insulate or absorb the radiation. (Church, 1993) Microwave energy is said to selectively heat materials as differences in material composition give rise to differences in dielectric properties. This in turn leads to certain materials having the ability to heat quicker than others. This is one advantage that dielectric heating has over conventional heating methods in that no energy needs to be wasted in heating the sample throughout. The material is heated insitu and is not reliant on heat transfer through the material. Conventional heating depends on the generation of temperature gradients between the outside of the body to be heated and the centre. Heat is transferred through the medium by conduction. This may result in uneven temperature distributions inside the material, and may take some time to achieve uniformity. Microwaves allow for the generation of extremely high temperatures over very short time intervals as long as that particular phase is sufficiently absorbent. High temperatures can be achieved without having to bulk-heat the material.

Heating may result from one of four main mechanisms. These are the conduction mechanism, ionic or dipolar polarisation, and interfacial or Maxwell-Wagner polarisation.

2.3.1. Conduction Mechanism

Where the irradiated sample is an electrical conductor, the charge carriers (electrons, ions, etc) are moved through the material under the influence of the electric field, E , resulting in a polarisation, P . These induced currents will cause heating in the sample due to electrical resistance. For a very good conductor, complete polarisation may be achieved in approximately 10^{-18} seconds, indicating that under the influence of a 2.45GHz microwave field, the conducting electrons move precisely in phase with the field (Whittaker, 1997). This is shown schematically in Figure 2.2.

If the sample is too conductive, such as a metal, most of the microwave energy does not penetrate the surface of the material, but is reflected. However, the colossal surface voltages which may still be induced are responsible for the arcing that is observed from metals under microwave radiation

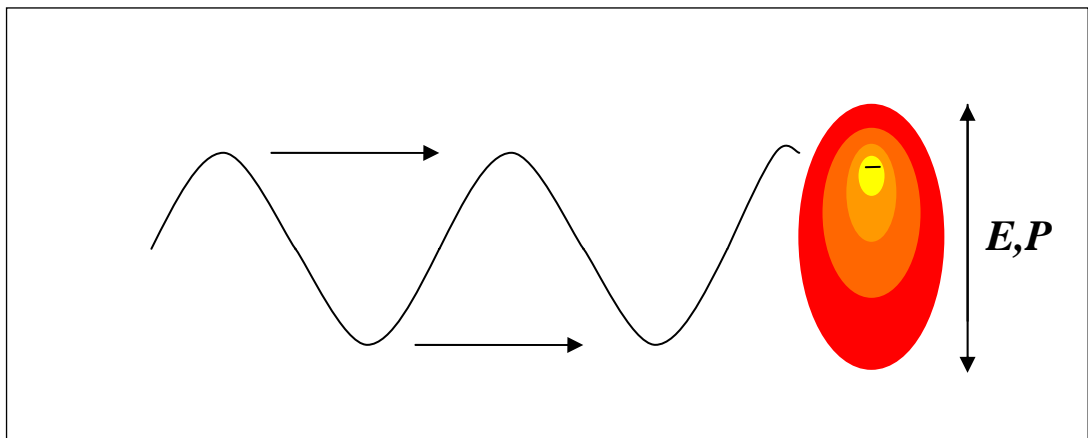


Figure 2.2: Representation of electric field moving in perfect phase with incident radiation for perfect conductor. (after Whittaker, 1997)

2.3.2. Dipolar Polarisation

Induced dipoles arise from the displacement of electrons around nuclei (electronic polarisation) or from the relative displacement of atomic nuclei as a result of the unequal distribution of charge in molecule formation (atomic polarisation). In the presence of microwave radiation these induced dipoles will cause heating in the sample due to any electrical resistance.

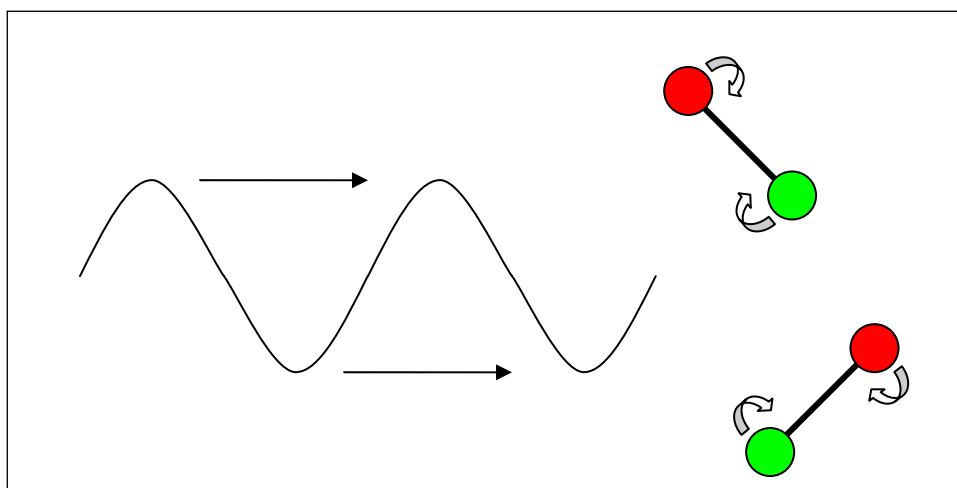


Figure 2.3: Dipolar polarisation schematic

Polar liquids, such as water, methanol or ethanol contain permanent dipoles due to the asymmetric distribution of charge around the molecules. These tend to align under the influence of electric field giving rise to orientation polarisation (Whittaker, 1997 and Meredith & Metaxas, 1983). Under very high electric field strength radiation the molecules will attempt to follow the field but intermolecular inertia prevents significant motion before the field has reversed and no net motion occurs. If the frequency of the oscillation is very low, then the molecules will be polarised uniformly. In the intermediate case, the frequency of the field will be such that molecules will simply lag the field polarity. It is this motion that gives rise to frictional losses and subsequent increase in temperature.

2.3.3. Interfacial Polarisation

This mechanism is caused by polarisation arising from charge build up between components in heterogeneous systems. It occurs in systems comprised of conducting inclusions in a second non-conducting material (Meredith & Metaxas, 1983). An example would be a dispersion of metal particles in sulphur. Sulphur is transparent to microwave radiation and metals conduct, yet this combination is readily heated. The actual mechanism is a combination of conduction and dipolar effects, and so is very difficult to treat in a simple manner.

For a (non-superconducting) metal, there will always be a very thin surface layer in which some of the incident microwaves are attenuated, and in which induced currents will give rise to heating. For a bulk metal this heating effect is so small as to be irrelevant, but in powders this surface layer makes up a large proportion of the material. However, the polarisation induced in the metal is also subject to the properties of the surrounding medium - in simple terms, it induces a 'drag' on the polarisation of the metallic inclusions - making it less effective than it might otherwise be. Under these circumstances, the polarisation of the metallic particles does not take place instantaneously, but lags behind the induced field, as for the polar molecule in the dipolar polarisation mechanism. Hence, the frequency dependence of the sample's heating properties is similar to that of the dipolar polarisation mechanism, despite being due to a conduction mechanism.

2.4. Dielectric Properties

2.4.1. Introduction

The ability of materials to absorb microwave energy is dependent on their dielectric properties. Cavity design requires detailed knowledge of the material's response to microwave radiation. This response is governed by the material's complex permittivity, ε^* :

$$\varepsilon^* = \varepsilon' - j\varepsilon'' = \varepsilon_0 \left(\varepsilon'_r - j\varepsilon''_{eff} \right) \quad (2.2)$$

where: ε^* = the complex permittivity

ε' = permittivity or dielectric constant

ε'' = dielectric loss factor

ε'_r = relative dielectric constant

ε''_{eff} = effective relative loss factor

ε_0 = permittivity of free space (8.85×10^{-12} F/m)

2.4.2. Relative Permittivity

The permittivity of free space can be defined in terms of the mechanical force exerted between two charged particles spaced apart in vacuo. If the space is filled with dielectric material the force is increased by a factor, namely the relative permittivity for that material (ε'_r). Relative permittivity is a dimensionless number which for a lossless homogeneous material is equivalent in all three rectangular coordinate directions. It is related to the refractive index for optical materials, and analogously with optics the lines of electric field entering the surface of the dielectric material are refracted (i.e. direction changed as well as magnitude), and also partially reflected. Other important related effects are the change in propagation velocity of a plane wave entering the material, and the change in characteristic impedance (Meredith, 1998).

2.4.3. Dielectric Constant and Loss Angle

For completeness, the total loss in a material is made up of the dielectric loss (from polarisation) and the conductive (ohmic) loss, as follows.

$$\varepsilon_t'' = \varepsilon'' + \frac{\sigma}{\omega \varepsilon_0} \quad (2.3)$$

where σ = electrical conductivity of the material

The Phase angle is defined as the angular difference in phase between the sinusoidal alternating potential difference applied to a dielectric and the component of the resulting alternating current having the same period as the potential difference. The angle is often symbolized by the Greek letter θ (theta); the cosine of which is the power factor. The loss factor can thus be shown to be:

$$\varepsilon'' = \varepsilon' \cdot \tan \theta \quad (2.4)$$

Some authors use a complex permittivity when dealing with the theoretical aspects of dielectric heating (Von Hippel, 1954):

$$\varepsilon'' = \varepsilon' - j\varepsilon'' \quad (2.5)$$

where $j = \sqrt{-1}$

2.4.4. Variation of Dielectric Properties with Temperature and Frequency

The main factors that affect dielectric properties of materials are composition, temperature and frequency. Moisture content is also often stated as being a contributing factor, as water has a high dielectric constant. Bulk density also affects behaviour as skin losses are more predominant in finely ground powders, where the surface area to mass ratio is higher.

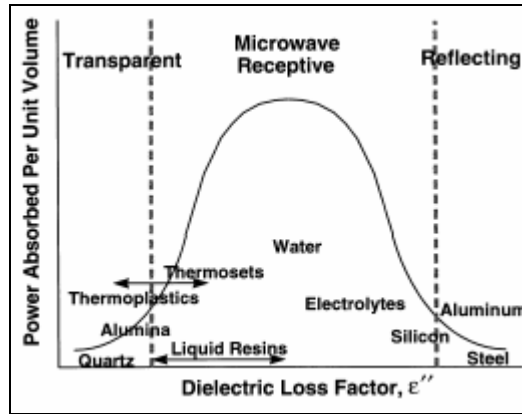


Figure 2.4: Relationship between the dielectric loss factor and ability to absorb microwave power for some common materials (after Thostenson and Chou, 1999)

Examples of dielectric properties of selected materials are shown in Tables 1 and 2.

	Temperature (°C)	ϵ'		
		30MHz	1GHz	2.5GHz
Water, ice	-12	3.8	3	3.2
Snow	-20	1.2	1.2	1.2
Distilled Water	25	78	77	77
Distilled Water	85	58	56	56
Ethyl Alcohol	25	23	12	7
Alumina Ceramic	25	8.9	8.9	8.9
Fused Quartz	25	3.78	3.78	3.78
Bakelite	24	4.6	3.8	3.7

Table 2.1: Dielectric constant for selected materials (after Meredith, 1998)

The nature of temperature dependence is a function of the dielectric relaxation processes operating under the particular conditions existing and the applied frequency. Dielectric relaxation is the time taken for dipoles to return to random orientation when the electric field is removed (Nelson and Kraszewski, 1990). As temperature increases, the relaxation time decreases and the dielectric constant will increase (Bottcher and Bordewijk, 1978). Distribution functions have been shown to be useful in expressing the temperature dependence of dielectric properties, but the frequency and temperature dependence of the dielectric properties of most materials is complex and can be best determined by measurement at the frequencies and conditions of interest.

	Temperature	ϵ''		
Material	(°C)	30MHz	1GHz	2.5GHz
Water, ice	-12	0.7	0.004	0.003
Snow	-20	0.01	0.001	0.0001
Distilled Water	25	0.4	5.2	13
Distilled Water	85	0.3	1	3
Ethyl Alcohol	25	3	3	6.5
Alumina Ceramic	25	0.0013	0.008	0.009
Fused Quartz	25	<0.001	<0.001	<0.001
Bakelite	24	0.34	0.26	0.23

Table 2.2: Dielectric loss factor for selected materials (after Meredith, 1998)

2.5. Calculation of Penetration Depth

It is essential to have knowledge of penetration depth for the application of microwaves in industrial processes. The amplitude of the wave diminishes as the wave propagates into the material due to power absorption. The field intensity and the associated power flux density fall exponentially with distance from the surface. The penetration depth, D is defined as the depth into the material at which the power flux has fallen to $1/e = (0.368)$ of its surface value and is given by:

$$D_p = \frac{\lambda_0}{2\pi\sqrt{(2\varepsilon')}} \frac{1}{\sqrt{\left[\left\{ 1 + \left(\frac{\varepsilon''}{\varepsilon'} \right)^2 \right\}^{0.5} - 1 \right]}} \quad (2.6)$$

where: λ_0 = wavelength of incident radiation. (Metaxas and Meredith, 1993)

2.6. Power Absorption

The rate at which heat is absorbed in the material can be expressed as power density.

Power density is given by the following equation:

$$P.d = 2\pi \cdot f \cdot E^2 \cdot \varepsilon_0 \cdot \varepsilon'' \quad (2.7)$$

where: $P.d.$ = power density (W/m^3)

f = frequency (Hz)

E = root mean square Electric Field Strength (V/m)

ε_0 = permittivity of Free Space (F/m)

ε'' = dielectric Loss Factor

Power density increases with the square of the electric field strength. A doubling of the electric field strength will quadruple the power density. If a 5kW generator is capable of $1 \times 10^8 \text{ W/m}^3$ then a 10kW generator will be capable of $4 \times 10^8 \text{ W/m}^3$. Therefore by maximising the generator power it is possible to generate extremely high power densities.

2.7. Temperature Rise Calculation

The temperature rise of a material during heating can be expressed by the following equation:

$$\frac{dT}{dt} = \frac{P.d.}{C \cdot \rho} \quad (2.8)$$

where: dT = temperature change ($^{\circ}\text{K}$)

dt = time increment (s)

$P.d.$ = power density (W/m)

C = specific heat capacity (J/kg.K)

ρ = density (kg/m)

By substitution of (2.7) we can write:

$$\frac{dT}{dt} = \frac{2\pi \cdot \varepsilon'' \cdot f \cdot E^2}{C \cdot \rho} \quad (2.9)$$

The temperature rise is therefore very difficult to determine accurately as it depends on the dielectric properties, which often vary with temperature. The electric field strength can also fluctuate as the frequency is of the order of a billion cycles per second. It is therefore convenient to use an average power density value.

2.8. Thermal Stresses

Meredith (1998) stated that thermal limitations may arise from non-uniform heating, and that “impressed temperature gradients may result in mechanical stress gradients in the workload and possible fracture”. This is true in more conventional microwave applications such as ceramics or superconductor manufacture, whereas for the proposed microwave pre-treatment of ores it is exactly the mechanism that is being exploited.

2.9. Microwave Engineering

2.9.1. Introduction

There is little evidence of research into microwave research before the Second World War commenced. However, with the advent of war, rapid growth occurred in the development of microwave systems for telecommunications and radar for military programs (Metaxas and Meredith, (1983), Kingman et al., (1999)). Microwave radiation was first developed for heating purposes in 1951 when a large floor standing model was produced by the Raytheon Company of North America (Osepchuck, 1984). Ovens for domestic purposes became available in the early 1960's, and a competitive market soon developed. The first industrial microwave heating applications included rubber extrusion, plastic manufacture, and the treatment of foundry core ceramics. The oil crisis of the mid-1970's led to an increase in energy costs and since then alternative energy sources have been the subject of increased research. Microwave heating is seen as an alternative to traditional methods because of potential increases in efficiency, in that no energy is wasted bulk heating the sample.

2.9.2. Industrial Microwave Heating

Microwaves systems usually consist of a power supply, a generator, an applicator and waveguide. There are many possible configurations depending on the requirements of the application.

2.9.3. Microwave Generator Types

Most industrial heating systems demand power in excess of 10kW, often extending into the range 100kW to 1MW (Meredith, 1998). In addition, a number of criteria need to be satisfied:

- (i) A high conversion efficiency from incoming power to useable microwave power output, especially important as power rating rises;
- (ii) Operation within the prescribed frequency band at all times;
- (iii) A low capital cost per kilowatt of output power; this is important because the generator often represents more than half the cost of the installation;
Robustness in surviving incidents typical of industrial operation: electrical power surges and transients, arcing in the applicator and feed system, incorrect adjustment of operating conditions, vibration etc;
- (iv) Simple to operate, with the absolute minimum of user adjustable controls;
- (v) Simple to maintain, fault find and remedy;
- (vi) Low running cost, not only in electrical power consumed but also in replacement of consumables, notably the microwave power tube itself.
This implies a long magnetron life; and
- (vii) Comprehensive, accurate documentation to enable installation, service and operating teams to understand the equipment fully within their designated roles. (after Meredith, 1998)

As of 1997, the magnetron was overwhelmingly superior in satisfying needs compared with the klystron or with solid-state power sources. Although progress is being made in solid-state power supplies, they are short of the power-output requirement and are very expensive, and will not be considered further (Meredith, 1998).

2.9.3.1 Magnetrons

The magnetron was developed as a result of radar research in the Second World War. They are found in all kitchen-type ovens, and are cheaply mass-produced for low power output units. Typical power capability ranges from 1kW to 1MW. They have high conversion efficiencies. The principal components of a high-power industrial, continuous wave magnetron are:

- o A cylindrical heated cathode emitting electrons;
- o A circular anode concentric with and surrounding the cathode, having an array of radial slots forming resonators tuned to the desired operating frequency;
- o A high strength magnetic field aligned axially to the anode-cathode assembly. This may be provided by a permanent magnet in small magnetrons, or an electromagnet for higher power magnetrons;
- o A high-value DC EHT voltage (usually in the range 2-20kV) applied between anode and cathode, with the anode earthed for convenience, and the cathode at negative potential;
- o The whole enclosed in a vacuum envelope and sealed with a high vacuum of about 10^{-6} mm Hg;
- o A probe antenna or slot, coupled to the resonator and sealed by an output window of microwave transparent material; and
- o A construction that provides for easy rebuilding after end-of-life failure or accidental damage. (Meredith, 1998)

The magnetron is the major player in a class of tubes termed "crossed field," so named because the basic interaction depends upon electron motion in electric and magnetic fields that are perpendicular to one another and thus "crossed." In its most familiar embodiment, shown schematically in figure 2.5, a cylindrical electron emitter, or cathode, is surrounded by a cylindrical structure, or anode, at high potential and capable of supporting microwave fields. Magnets are arranged to supply a magnetic field parallel to the axis and hence perpendicular to the anode cathode electric field.

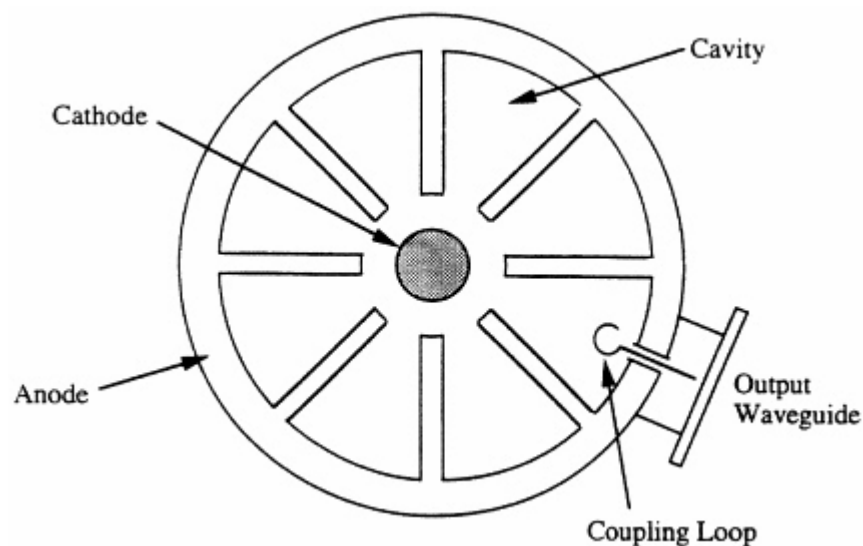


Figure 2.5: Schematic diagram of a magnetron shown in cross-section.

The interaction of electrons travelling in this crossed field and microwave fields supplied by the anode causes a net energy transfer from the applied DC voltage to the microwave field. The interaction occurs continuously as the electrons traverse the cathode anode region. The magnetron is the most efficient of the microwave tubes,

with efficiencies of 90 % having been achieved and with 70-80 % efficiencies common. A more detailed schematic is shown in Figure 2.6.

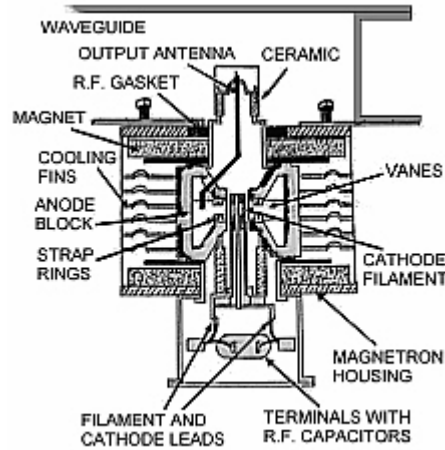


Figure 2.6: Sectional view of a typical microwave
(courtesy of Michael S. Wagner)

2.9.3.2 Klystrons

Klystrons can generate adequate power and are widely used in radar, communications, television and scientific research. Klystrons are sometimes considered when driving resonant applicators, where their frequency stability is important. Traditionally, klystrons have been capable of higher powers than magnetrons at the common heating frequency of 2.45GHz, with a 50kW unit having been available for over 20 years (Meredith, 1998). This sometimes necessitates their use.

2.9.4. Transmission

The energy is transmitted from the generator to the applicator by means of hollow rectangular metal pipes, usually of 2:1 aspect ratio. They are coated with high-conductivity metals such as brass or aluminium as to minimise attenuation losses. They are usually classed as either TE (transverse electric, or H) mode or TM (transverse magnetic or E) mode. When in TE mode, the electric field vector is normal to the direction of propagation. Conversely, when in TM mode, the magnetic field vector is normal to the direction of propagation. (Meredith, 1998)

2.9.5. Microwave Applicator Types

Once transmission is achieved the radiation must be conveyed as efficiently as possible to maximise energy dissipation in the load. The main types are detailed in the following section.

2.9.5.1 Multimode Cavities

Multimode cavities are the most common applicator types, and are found in over 50% of industrial applications and all kitchen microwave ovens (Fletcher, 1995). They are mechanically simple to construct and are also very versatile in terms of being able to heat a wide range of different sized loads and also wildly varying electrical properties. The energy is conveyed to the cavity from the waveguide and subsequent reflections result in a relatively even distribution of energy.

Meredith and Metaxas (1983), stated that in principle, the multimode oven supports a large number of resonant high-order waveguide-type modes simultaneously, which add vectorially in space and time to give a resultant field pattern.

It is easier to achieve uniformity of heating when a large number of modes are present, and this is important in manufacturing and heating applications. Many multi-mode cavities incorporate turntables so that the load is rotated through the cavity – taking it through minima and maxima in order to minimise localised heating. However, they are not best suited to applications where high temperatures are required, as the energy is dissipated throughout a relatively large volume. Therefore some low-loss materials do not heat sufficiently in multimode cavities.

2.9.5.2 Single-Mode Resonant Cavities

In a microwave cavity, theoretical analysis can be performed to describe the response of the incident radiation. Given the geometry of the applicator, it is often possible to solve the Maxwell equations analytically or numerically with the appropriate boundary conditions. The design of single mode cavities is based on the solution of the Maxwell equations to support one resonant mode. Consequently, the size of single mode applicators is of the order of approximately one wavelength, and to maintain the resonant mode, these cavities require a microwave source that has little variation in the frequency output (Thostenson and Chou, 1999). In general, single mode cavities have one well defined ‘hot spot’ where microwave field strength is maximised. These cavities are therefore capable of extremely high heating rates in excess of 100°C/s. They have been used for plasma generation, and their use has historically been limited as they are difficult to control. The dielectric properties of the material vary with temperature, and results in the drifting of the resonant frequency of the cavity during operation, making steady matching difficult. Within such a cavity only one mode of propagation is permitted and hence the field pattern is defined in space, and the target load can be positioned accordingly. The energy is

propagated through the cavity and reflects against a short circuit tuner. With careful tuning the incident and reflected waves achieve superposition here, and power density is maximised.

2.9.6. Reflected Power Dissipation

It is usually necessary to have a terminating load to absorb residual power that is not absorbed by the material to be heated. This is very important as to minimise potential damage to system components. Water is usually used due to its abundance and high loss factor. Reflected power can then be calculated using calorimetry. Knowledge of the reflected power along with forward power is valuable for impedance matching. (Metaxas and Meredith, 1983)

2.9.7. Active Tuning

The advent of microprocessor control systems has enabled the advancement of the technology so that power densities can be maximised inside the cavity. Changing conditions inside the cavity due to spatial, temperature, chemical or phase changes alter the impedance. A magic-T junction can be used to maximise the forward power into the cavity to facilitate impedance matching. Two moveable pistons reflect the total radiation back towards the four-port junction but the radiation will now be phase-shifted by $4\pi l_1$ and $4\pi l_2$ respectively, where l_1 and l_2 are the adjustable distances from the junction to the short-circuit pistons. (Metaxas and Meredith, 1983)

2.10. Conclusions

The nature of microwaves and the main microwave heating mechanisms have been detailed. The specifics of microwave generation, transmission and application have been presented. High power microwave treatment is now possible with the aid of relatively simple techniques. This fact facilitates the current laboratory research into the effects of microwave on minerals and necessitates the current study.

Chapter 3

Applications of Microwave Radiation for Minerals Processing

3.1. Introduction

Economic growth is dependent on a number of factors, one of which is the availability of natural resources for raw materials for manufacturing, and energy generation. Everything that is used today is either mined or grown. This highlights the scale and importance of the mining industry. The size of current mining and mineral processing operations and the energy intensive nature of the size reduction process necessitate a large energy burden. High production costs and unwanted generation of greenhouse gases ensue. There is therefore considerable scope for large increases in efficiencies, with even marginal savings resulting in significant benefits. Improving mineral processing techniques can yield dramatic reductions in energy consumption and can also conserve primary sources of raw materials. It is estimated that up to 1 million tonnes of copper mined each year are lost to tailings (Wills, 1997). If the ore can be ground in a way such that less copper metal reports to the undersize fraction then these losses can be minimised.

Comminution is the unit operation responsible for the liberation of valuable minerals from gangue so that concentration can occur. Liberation in comminution processes is achieved by grinding ores to sizes finer than the grain size, which may be as fine as 10µm. Size reduction at these low sizes is even more energy intensive, as particles have proportionally fewer flaws. The energy efficiency of conventional grinding is about 1%, where most of the energy is wasted as heat generated in the material and equipment (Walkiewicz, 1991).

Comminution is usually accomplished by applying external forces to the particle. It accounts for the largest proportion of any mineral processing plant's capital and operating costs. Cohen (1983) estimated that 30-50% of total plant energy consumption at most sites and up to 70% for hard rock types is consumed by comminution. Napier-Munn et al (1996) stated that improvements can be of two types:

- o Fundamental changes in existing technology or the introduction of novel technology
- o Incremental improvement in the technology, i.e. its application and operating practice.

The former requires investment in non-conventional processes whereas the latter relies on gradual optimisation of plant circuit and equipment design. Efforts have long been made towards fundamental changes in technology, with both conventional and non-conventional processes being considered in order to increase efficiency and reduce mineral recovery costs.

It is preferable that liberation occurs with the complete release of the crystals of targeted minerals by the intergrannular breakage of ore fragments. The aim is to produce single-mineral particles with minimal distortion of their original boundaries by undesirable transgranular fragmenting. Current liberation is achieved with a substantial degree of transgranular breakage (Andres et al., 2001).

3.2. Thermally Assisted Liberation

The use of heat to assist in mineral liberation is typically referred to as “thermally assisted liberation” or TAL. The constituents of ore typically have very different thermal and mechanical properties. Thermal pre-treatment has long been identified as a potential method of improving comminution and liberation characteristics of ores by exploiting (often large) differences in the magnitude of the thermal expansion coefficient of various phases in the lattice. The premise is that if uniform heating is applied to the sample, then differing rates of expansion will result in areas that are subjected to elevated stresses. It is also possible that non-uniform heating will result in differing rates of expansion. The use of heat to assist liberation has been studied throughout the 20th century (Yates 1919, Pocock et al., 1998). Traditionally, thermal assisted liberation has been attempted using conventional heating methods such as furnaces. However the majority of studies have concluded that the treatment will not be viable, as excessive energy is required to yield sufficient improvements in grindability. There are suggestions that fluidised beds should be used to improve the heat transfer into the sample. Fitzgibbon & Veasey (1990) concluded that if cheaper and more efficient methods of heating can be employed the process may become more profitable. They also stated that economic viability was only possible if improvements to the product were such that the cost of bulk heating was justified.

Many studies have been carried out on quartz - a common gangue mineral. Early work involved heating 1” cubic samples of quartz, and then quenching in cold water. After treatment it was found that the cubes could be crushed between finger and thumb, and passed through a 500µm screen, (Holman, 1926). Calculations of grindability yielded improvements of up to 50%. Bond work index and reductions in strength have also

been made. It was found that when quartz is heated above 573°C, the associated α - β inversion, as well as the anisotropic expansion of quartz crystals results in significant reductions in the work index. The inversion produces a volume increase of 0.86% (Dana, 1952). Rapid quenching from the inversion temperature freezes the structure leading to micro-fracturing due to internal forces. Drost and Mahan (1973), Kanellopoulos and Ball (1975), and Hariharan and Venkatchalam (1977) have observed embrittlement after heating and quenching from temperatures above the α - β inversion temperature of quartz and quartzite.

Most materials expand when heat is applied. Previous studies show that thermal expansion of low porosity, crystalline rocks depends not only on temperature, but also confining pressure. Wong and Brace (1979) reported that the coefficient of thermal expansion for granite increases with temperature and decreases with confining pressure. Decreases in the mean coefficient of thermal expansion for Westerly granite of as much as 40% were observed as the confining pressure was increased from 7.6 to 55.2MPa on specimens heated to 300°C (Wong and Brace, 1979).

Heating, even to moderate temperatures, produces damage in the form of micro-cracks in granites (Veasey and Fitzgibbon, 1990). The formation of micro-cracks in granite specimens during thermal cycling is due to the differential thermal expansion of quartz and feldspars along grain boundaries as well as the α - β phase transition at 573°C.

3.3. Dielectric Properties of Minerals

Cumbane (2003) completed a detailed study of the variation of dielectric properties of five powdered sulphide minerals with frequency and temperature. The measurement system comprised of a circular cylindrical TM_{0n0} cavity, and was based on a perturbation technique. The powders were examined at frequencies of 625MHz, 1410MHz and 2210MHz, and the complex permittivity measured from ambient to 650°C. The dielectric properties of galena (PbS) and sphalerite (ZnS) exhibited little variation with temperature, whilst pyrite (FeS), chalcocite (Cu_2S) and chalcopyrite ($CuFeS_2$) showed significant variation. It was concluded that these changes were related to composition and phase transformations. The detailed results obtained by Cumbane (2003) show the behaviour of the dielectric properties at three different frequencies and over a range of temperatures. They are detailed in this section.

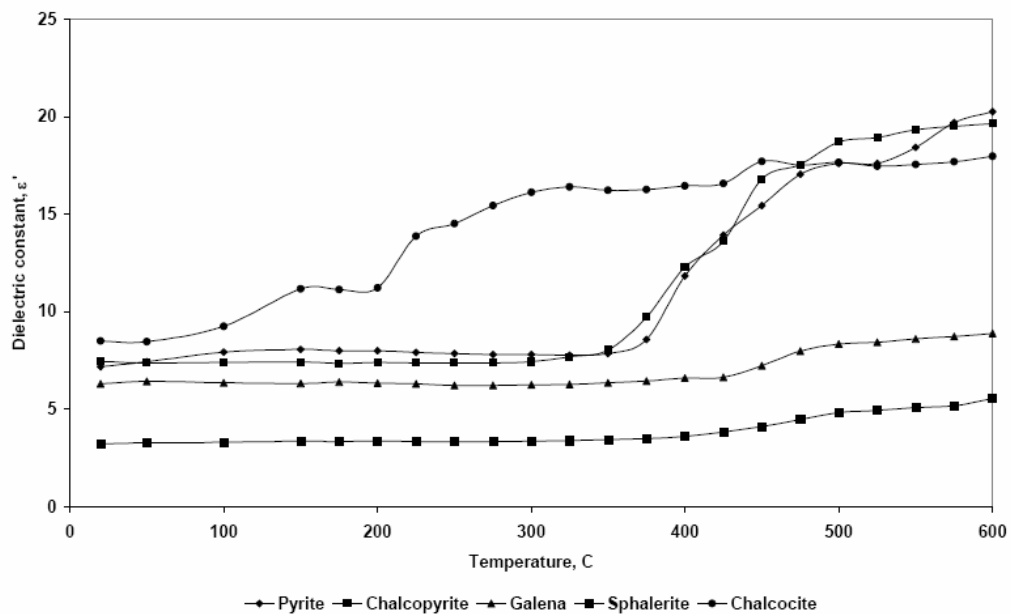


Figure 3.1: The dependence of dielectric constant of sulphide minerals with temperature measured at 615MHz

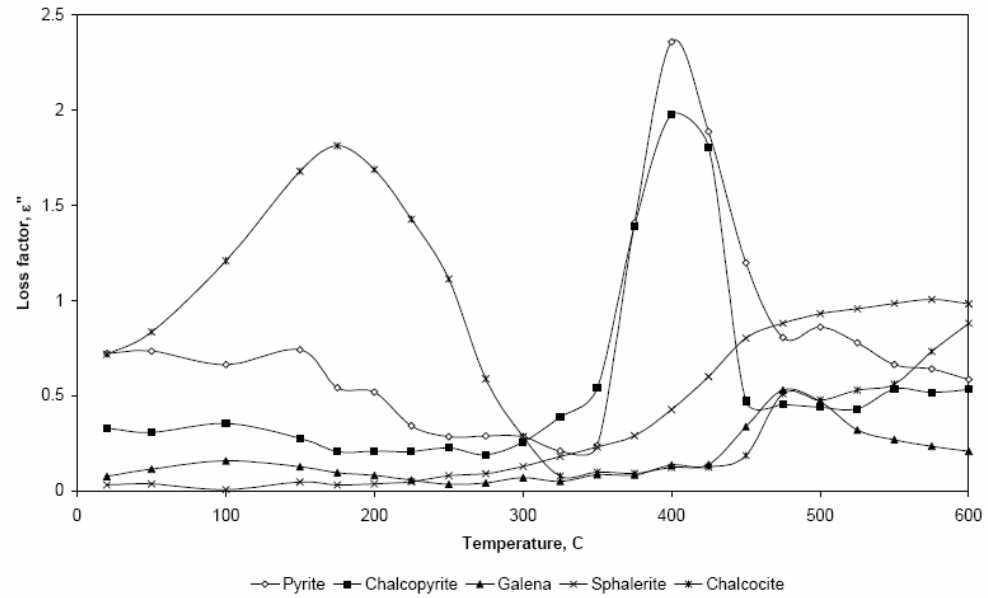


Figure 3.2: The dependence of loss factor of sulphide minerals with temperature measured at the frequency of 615 MHz.

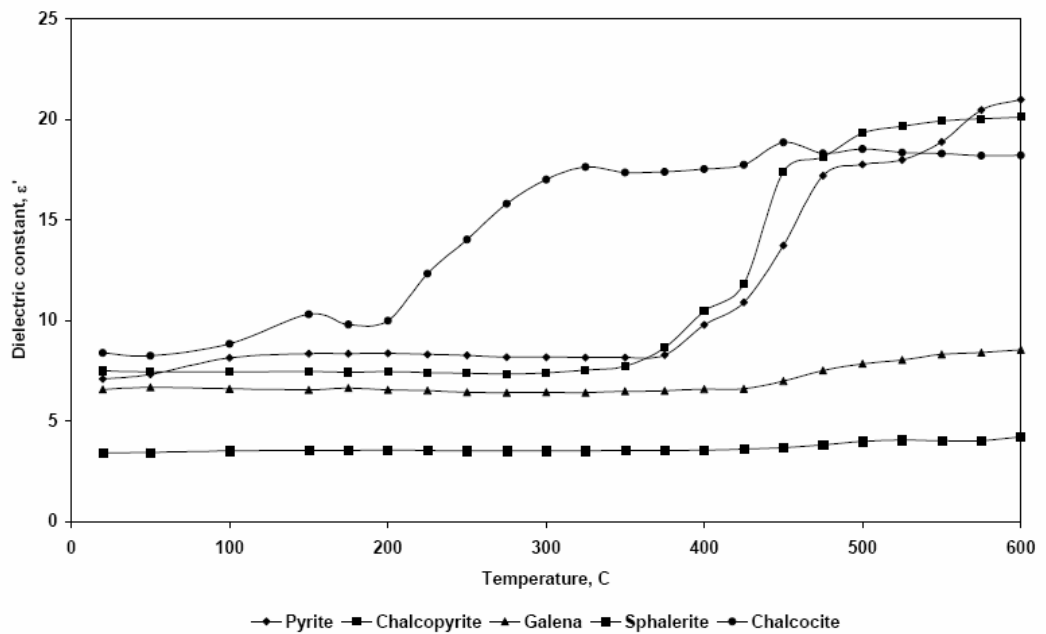


Figure 3.3: The dependence of dielectric constant of sulphide minerals with temperature measured at 2.216GHz

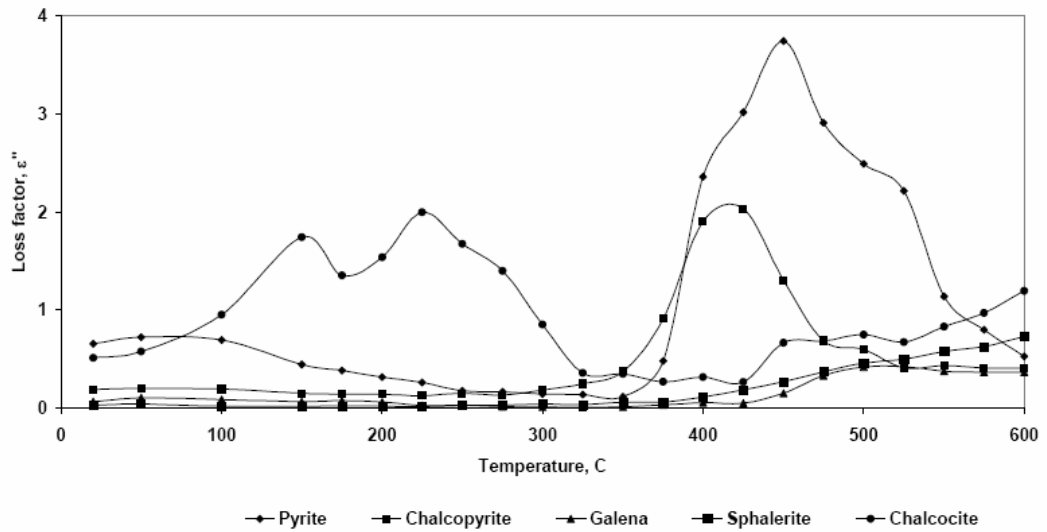


Figure 3.4: The dependence of loss factor of sulphide minerals with temperature measured at the frequency of 2.216 GHz.

It can be seen that the dielectric properties vary considerably with temperature, with absorbance typically increasing at higher temperatures. In contrast, the dielectric constant and loss factor for quartz, a typical gangue mineral, are far lower than for any of the sulphide minerals shown, and also show very little variation with temperature. These are presented in Figures 3.5 and 3.6. Quartz is effectively pure silica, and most gangue minerals predominantly consist of silicates.

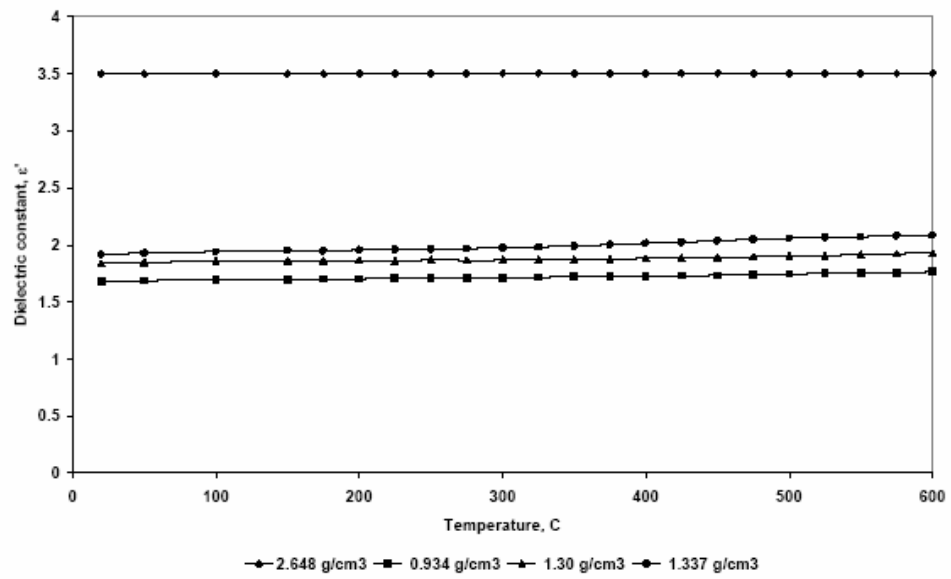


Figure 3.5: The dependence of dielectric constant of quartz with temperature measured at different packing densities

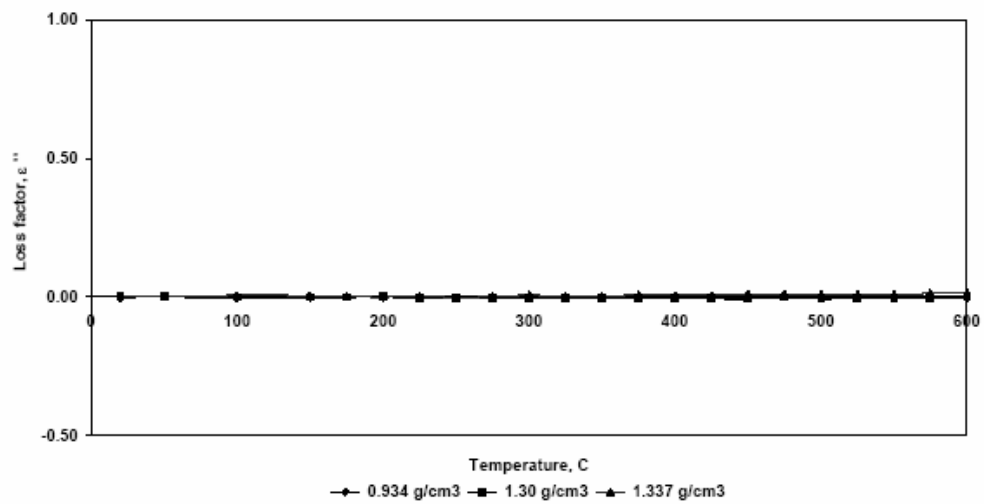


Figure 3.6: The dependence of loss factor of quartz with temperature measured at different packing densities (after Cumbane, 2002).

3.4. Previous Research on Microwave Processing of Minerals

3.4.1. Heating Studies

There has been considerable research in the microwave treatment of minerals over the last twenty years or so. The first known instance of microwave research with minerals was in 1978 by Zavitsanos and this resulted in a patent application for the desulphurisation of coal. Jacobs et al (1982) confirmed this by showing that pyrite may be oxidised to pyrrhotite, which can then be removed magnetically. Chen et al (1984) exposed 40 minerals to relatively low power microwave radiation to ascertain their behaviour. It was concluded that microwave effects were compositionally dependent. Minerals, such as silicates, carbonates and some oxides, were transparent to microwave energy. Other metal oxides and most sulphides were readily heated. It is possible to conclude that many valuable ore minerals respond favourably to microwave radiation whereas often gangue minerals do not. Studies at the USBM (Walkiewicz, 1988) exposed a variety of iron ores to microwave radiation in a 1kW and 3kW applicator. Temperature measurements were made using a metal-sheathed thermocouple. Scanning Electron Microscopy on the samples verified fracturing along grain boundaries. Standard Bond Grindability tests yielded a work index reduction of up to 24%. It was recognised that microwave-assisted grinding could lead to increased throughput, less recycled ore, less wear and maintenance and improved liberation. It was also suggested that the economics of the process could be improved if higher power microwaves of the order of 6-12 kW were used to increase the heating rate. However, most of the early work on minerals has involved the use of microwaves of only modest power. McGill et al, (1988) investigated the effect of power density on the heating rates of minerals using power levels of between 500W and 2000W at 2.45GHz. Samples were irradiated for 7 minutes where possible; arcing and melting

caused some tests to be terminated early. It was seen that iron oxides could be heated readily whilst silica remained largely unheated. The results are as follows.

Mineral	500W		1000W		1500W		2000W	
	Temp°C	Time	Temp°C	Time	Temp°C	Time	Temp°C	Time
Fe ₂ O ₃	60	7	87	7	101	7	130	7
Fe ₃ O ₄	1118	7	1144	3.5	1123	2	905	1
PbS	984	0.5	992	0.4	----	----	----	----
SiO ₂	33	7	44	7	55	7	73	7
TiO ₂	67	7	109	7	150	7	228	7

Table 3.1: Effect of power level on heating rate (McGill et al. 1988)

Harrison (1998) investigated heating characteristics of 25 mineral samples in a 650W, 2.45GHz microwave oven, and classified them into three groups:

Group I: High heating rate (common valuable ore minerals)

- o Minimum temperature 175°C after 180s treatment
- o Metalliferous ore minerals e.g. pyrite, galena, magnetite, pyrrhotite, bornite, chalcopyrite

Group II: Medium heating rate (some common valuable ore minerals)

- o Temperature varies 69-110°C after 180s treatment
- o Ore minerals e.g. ilmenite, hematite, cassiterite, bauxite

Group III: Low heating rate (silicates, carbonates and other typical gangue minerals)

- o Maximum temperature 50°C after 180s treatment
- o Mainly gangue with some ore minerals e.g. quartz, feldspar, calcite, mica, barites, sphalerite, rutile.

The microwave cavity used was relatively low power; therefore higher heating rates could be expected with higher power microwaves, especially with the more microwave-absorbent species. Dielectric property measurement of these mineral species explains why these mineral species have differing heating rates, and aids identification of highly absorbent species that are likely to yield the highest temperature increases. The highly absorbent species are thought to facilitate greater weakening of the ore rock.

3.4.2. Penetration Depth Measurement

Harrison (1998) completed a number of tests at the National Physics Laboratory on the penetration depth for a range of minerals for microwave radiation at 2.45GHz. It was noted that the depth of penetration in the silicates such as quartz, mica and feldspar, which often form gangue minerals in metalliferous mining, was much larger than in the metalliferous species such as ilmenite and pyrites. The results are presented in Table 3.2.

Mineral	Depth of Penetration at 2.45GHz (m)
Quartz	5.86
Haematite	0.21
Ilmenite	0.31
Chalcopyrite	0.33
Pyrite	0.11
Magnetite	0.06
Galena	0.84

Table 3.2: Depth of penetration in selected minerals (after Harrison, 1998)

3.5. Applications of Microwave Radiation in Extractive Metallurgy

As many minerals, most notably metal oxides and sulphides, have been shown to absorb microwave radiation readily, research has been carried out on its potential use for extractive metallurgy, using hydrogen gas as a reactant (Ford and Pei, 1967).

In 1985, researchers observed the formation of a black mass whilst attempting to dry a mixture of brown coal and chalcopyrite. This black mass was found to be completely soluble in a dilute ammonia solution. Metallic copper had been found by reduction, and similar results were obtained with mixtures of carbon and hematite. Since this instance, many pyrometallurgical applications have been proposed, ranging from the production of iron-nickel alloys from a low grade sulphide ore to the reduction of tungsten ores at temperatures of up to 3000°C.

Warner et al. (1989) identified numerous significant benefits of microwave treatment over conventional pyrometallurgical methods:

1. Many minerals exhibit rapid heating characteristics in microwave fields, and poor heaters can be heated by the addition of fine particulate active carbon sources such as charcoal
2. Microwave absorbent minerals or mixtures can be heated to very high temperatures quickly.
3. For most minerals and forms of carbon, as temperature increases, coupling also improves, thus energy utilisation is more efficient.
4. Metals reflect radiation so once formed they do not overheat.
5. Microwaves are capable of bulk heating a sample, negating the need for conduction from outer surfaces.
6. Microwave radiation stimulates endothermic reactions through direct supply of heat energy.
7. Owing to atomic or molecular vibrations, smelting or other high temperature reactions take place at significantly lower temperatures than by conventional means.
8. A high degree of control and automation should be possible with microwave technology as power application is easily controlled.
9. At temperatures less than 1000°C refractories do not couple with microwave energy, and heat can be applied where required.

3.6. Microwave Reduction of Metal Oxides

The reduction of metal oxides with carbon is an extremely important metallurgical process worldwide. Large tonnages of iron, tin, lead and zinc are produced in this way.

For the reduction of iron oxide the following applies:



The iron oxide for this reaction is often formed into pellets. It has been found that in carbothermic reduction, gasification of carbon is the controlling step in the reaction, even if active carbon is used (Seaton). The major disadvantage of this is that conventional heating methods are unable to supply the heat of the interior of the pellet fast enough to cover the heat consumed by the gasification reaction, this results in the centre of the iron ore pellets having cooler centres.

Various researchers have studied this obvious application for microwave energy (Ford, 1967; Warner et al., 1989; Standish, 1990), and have concluded that:

1. Volumetric heating was apparent throughout all pellets tested, i.e. the problem with ‘cold centres’ was alleviated.
2. Small masses could be heated much faster than conventional methods, larger masses even more so.
3. Some phase changes occurred on reduction, possible enhancing heating rates.
4. A possible lowering of activation energy.
5. Significant increase in reduction rates.

It was also suggested that on making reasonable assumptions of capital and operating costs, the cost of the microwave approach maybe up to 50% lower than any conventional process (Standish, 1990).

3.7. Hydrometallurgical Applications

Various attempts have been made to investigate the influence of microwave radiation on ‘typical’ leaching reactions (Florek et al, 1996) & (Baláž et al., 1995). All investigations concluded that microwave application resulted in strictly thermal effects and therefore did not provide any specific activation.

3.8. Applications of Microwave Radiation in Gold Extraction

The application of microwave radiation for the extraction and processing of gold and its ores has been suggested as an area of research, and several advantages have been reported. The suggested application was as a pre-treatment step before more traditional processing techniques such as cyanidation and also during the extraction or recovery stages of the metal.

The effects of microwave radiation on the various stages of conventional processing methods were reviewed by Woodcock et al. (1989). During the treatment of gravity concentrates, it was suggested that microwaves could have application in cracking locked iron/manganese oxides from gold particles, thus increasing the recovery of gold to the concentrate. The roasting and subsequent cyanidation of gold ores has been investigated in some detail by Haque (1986). A typical refractory arsenopyrite gold concentrate was microwave-roasted in air to 550°C. More than 80% of volatiles in the form of arsenic and sulphur were emitted and most of the iron present was oxidised to

hematite. Cyanidation of the resultant calcine extracted 98% of the gold present. However, no indication was given to results obtained for conventional methods. Other useful applications of microwave radiation in the processing of gold include the treatment of carbon from the carbon in pulp (CIP) process (Woodcock et al., 1989). It was thought that microwaves may have applications in the following areas of the circuit:

1. Heating of gold desorbing solution.
2. Heating if electrowinning solution.
3. Heating of carbon to remove organics, and thus reactivate it.

Conclusions were made that microwaves have a part to play in the treatment of carbon and other modes of gold recovery, but considerably more work was required in the field before microwaves could possibly be included in modern flowsheets.

An American organisation has extended theories for the application of microwave energy within the gold processing industry (Mining Magazine 1998). This was achieved by applying for Canadian patents concerning the fluidised bed roasting (by microwaves) of arsenopyrite gold concentrates. Early laboratory test work on an arsenopyrite concentrate suggested that almost complete oxidation of the mineral was possible allowing the use of conventional cyanide recovery technology. Little further technical details were elucidated by the authors.

3.9. Applications of Microwave Radiation in the Processing of Coal

Microwave pre-treatment of coal has up until now been the most significant application of microwave radiation within the mining industry. Research activities have examined

possible drying, pyrolysis, desulphurisation, grinding applications as well as the dielectric property measurement required for fundamental understanding.

Marland et al. (2001) found that coal was transparent to microwave radiation, whilst the inherent moisture and sulphide contaminants are good absorbers. Microwave treatment has been found to enhance uniform drying of coal due to preferential heating of water, with efficiencies of up to 97% reported for various types and sizes (Chatterjee et al., 1991; Lanigan, 1989 and Marland et al., 2001). Microwave treatment was also reported to enhance coal desulphurisation, an important technique for the mitigation of atmospheric pollution. Magnetic separation was facilitated after microwave treatment due to the oxidation of pyrite to pyrrhotite. High intensity magnetic separation was utilised by Zavitsanos (1981), Kelland (1988), and Viswanathan (1990). Preferential dissolution of sulphur by molten caustics was demonstrated by Zavitsanos (1979) and Rowson et al. (1990). The molten caustics' excellent microwave absorbance resulted in high temperatures local to the sulphur in the coal, and this lead to a greater occurrence of a water-soluble form of sulphur which was then easily removed by washing. Rowson et al. (1990) demonstrated 70% removal from high sulphur coals by irradiating at 2.45GHz and 500W for up to 1 minute in the presence of 300g/l caustic solution, and subsequent low gradient magnetic separation.

Improvements in coal grindability have also been facilitated by microwave radiation, as demonstrated by Lyttle et al., (1992), Herbst, (1981), Viswanathan, (1990) Harrison and Rowson (1996), and Marland et al., (2001). Reductions in grinding energy of as much as 20-30% were reported.

3.10. Effects on the Magnetic Susceptibility of Minerals

Few quantitative studies exist on the effects of conventional heat treatment on the magnetic properties of minerals. One comprehensive study of Wolframite by Blackburn (1983) revealed that slight increases in magnetic susceptibility could be observed after exposure to heat. It was also found that intergrowths of commonly associated minerals had a significant influence on magnetic properties, particularly under reducing conditions.

The effects of microwave radiation on the magnetic susceptibility of minerals have been investigated for minerals containing Fe^{2+} , Fe^{3+} , Cu^{2+} ions (Harrison, 1995). Minerals were exposed to microwaves at 2.45GHz at powers ranging from 650 to 4500W. The results are detailed as follows.

	650W	1500W	3000W	4500W
Mineral	% change in field strength	% change in field strength	% change in field strength	% change in field strength
Bornite	-82	-95	-94	----
Chalcopyrite	+103	+85	+49	----
Hematite	+5	+14	+31	----
Ilmenite	+5	----	+35	+13
Magnetite	-21	-7	----	-23

Table 3.3: Change in field strength of minerals after irradiation (after Harrison, 1995)

No explanation was given by the authors for the changes in field strength. However, it is thought that the changes are most likely due to change in chemical species of the mineral such as the change from hematite to magnetite at 350°C. The author suggested

that any changes in the susceptibility could have significant process benefits downstream, as it could enhance the ease with which the mineral constituents were to be separated. Other studies by Florek et al. (1996, 1997) investigated the possible benefits of downstream magnetic separation, and it was concluded that enhanced separation was possible when certain sulphide species were oxidised to more susceptible forms, such as the oxidation of pyrite to pyrrhotite.

3.11. Application of Microwave Treatment for Improved Comminution

3.11.1. Introduction

An increasing body of work is examining the effects that microwaves have on the strength of rocks for facilitated comminution. As reviewed previously, comminution in the mining and minerals industry is an extremely energy intensive process with very low efficiencies. Therefore improvements to the process can yield significant benefits. Many specific measures of the ease by which the constituent phases of an ore mineral are separable are detailed here, as well as breakage characterisation and the effects that microwaves have on these measures are detailed.

3.11.2. Improved Grindability

Work using a 15kW generator feeding into a single-mode microwave cavity on a copper carbonatite ore has yielded significant increases in grindability (Kingman et al, 2003). Samples were exposed for between 0.1 and 1 seconds. This was the first study of its kind to use such high power densities for such low exposure times, and it is the first such study to show power levels and exposure times that facilitate economic viability.

To understand the grindability behaviour of the material, 2 x 500 g samples of 5 size fractions from 19mm to 3.35mm were arranged. One sample from each size fraction was left untreated and the other was exposed to microwave energy in the single mode cavity for 0.2 s at 15 kW. The samples were then ground for increasing lengths of time (1–5 min) in a ball mill with a standard Bond mill charge at a speed at 70 rpm - the mass left in the original fraction after a specific time being determined by sieving. The data were evaluated using a standard population balance method (Austin et al., 1984; Wang and Forrsberg, 2000). The breakage function was evaluated by plotting the natural logarithm of mass remaining in a specific size fraction as a function of cumulative grinding time. It was seen that the difference in specific rate of breakage decreases with particle size. The largest particle size fraction (-19 + 16 mm) was most influenced with over 70% difference between the untreated and treated samples. For the smallest size fraction (-4.75 + 3.35 mm), the percentage change was 11%, which is still significant for such small sizes. The reason for the reduction in efficiency with particle size was deemed to be related to the mineralogy or texture of the samples. The major microwave absorbing phase within the material was magnetite. The magnetite occurred in large aggregates sometimes greater than 10 mm in size. It is thought that in order for differential expansion as a result of microwave heating to occur the heated phase must be entirely surrounded by transparent material. As the particle size decreases, the amount of magnetite, which is not totally surrounded by microwave transparent gangue, will increase and thus the percentage change in specific rate of breakage will drop. It is likely therefore that greater changes in specific rate of breakage could be achieved in ores which have a finer texture. It can also be seen that the specific rate of breakage in the larger size fractions is low. This is expected for laboratory mills and has previously been noted (King, 2001).

3.11.3. Reduction in the Point Load Index

3.11.3.1 Introduction

This section details the theory behind, and mode of operation of, the point load index test. This test has been used to compare the breakage characteristics of microwave-treated and untreated ores.

3.11.3.2 Theory and Background

Aspects of the point load test as used in determining rock strength, have been discussed by a number of authors, including Goodier (1933), Hondros (1959) and Protodyakonov (1960). The main themes of the discussions can be divided into two groups; test on irregularly shaped specimens and cube tests carried out on rock cores. The work carried out by Protodyakonov was later recommended by the International Bureau of Rock Mechanics in 1961 as a suggested method for testing irregular lumps of rock (Broch, 1971). It was recommended that specimens with a ratio of the longest to the smallest diameter of about 1:1.5 should be used. In addition it was recommended that the specimen should be tested parallel to its longest axis and perpendicular to the plane of the laminations. Despite criticisms by Hobbs (1963), the test procedure was successfully used by Diernat and Duffaut (1966) in classifying rock. They reported that scatter is more prevalent with irregular specimens than when testing regular specimens. Duffaut (1968), and Duffaut and Maury (1970) further investigated the Protodyakonov test in depth. Duffaut showed that the results depend on weight, size and shape effects, and specimen orientation. Duffaut and Maury (1970) studied thirteen plane models, and concluded that the failure load is highly dependent on the specimen orientation and recommended that testing across their large length should be avoided.

When conducting a point load test on a regular specimen such as a core, the failure load, P , is applied by the tips of the tester, and is recorded. The distance between the tips where the sample is failing, D , is also recorded. The result of the point load index test is expressed as a strength index (I_s) and is defined as:

$$I_s = \frac{P}{D^2} \quad (\text{Equation 3.3})$$

Statistical relevance is a matter of great importance when attempting to gain meaningful data from rock samples due to their natural variability. Many authors recommend that there should be at least 10 test pieces within a 96% confidence interval of the mean strength. It is also recommended that a size of specimen should be between 25 and 50mm diameter (Broch, 1972) and 50mm should be adopted as standard (ISRM commission, 1979).

Therefore when conducting point load tests on irregular samples with varying diameter, the results need to be presented for the equivalent index value at 50mm diameter, and this is the $I_{s(50)}$ index. Several empirical equations have been developed to convert the test data to $I_{s(50)}$ and then to an approximation of compressive strength (Hoek and Brown, 1980).

$$I_{s50} = \frac{\left(\frac{\text{depth}}{50}\right)^{0.45} \times \text{force}}{\frac{4 \times \text{width} \times \text{depth}}{\pi}} \quad (\text{Equation 3.4})$$

For other values of D , a size correction is necessary and the following approximate relation between σ_c , I_s and the equivalent core diameter, D , measured in millimetres:

$$\sigma_c = (14 + 0.175D) \cdot I_s \quad (\text{Equation 3.5})$$

3.11.3.3 Methodology and Previous Results

In practice the test is very simple; a particle is measured and placed between a pair of specially shaped, hardened-steel tips. Force is then applied between the tips and the maximum force sustained by the particle is recorded. A schematic of the test is shown in Figure 3.7.

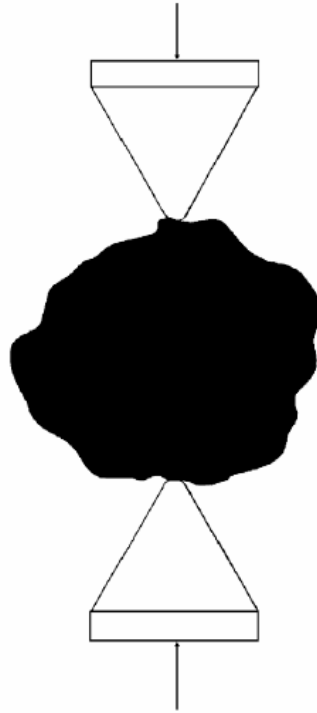


Figure 3.7: Principle of operation of point load apparatus

Kingman et al. (2004) subjected samples of ore were subjected to point load tests both as untreated material and after each type of microwave treatment, and the matrix of tests is shown in Table 3.4. For each test, 10 pieces of ore were treated and the $I_s(50)$ value for each sample calculated. The value reported is the median of the 10 tests, also given for completeness is the mean standard deviation and range.

Particle Size (mm)	Applied power level (kW)	Exposure time (s)
-53 +45	Untreated	N/A
-53 +45	5	0.1, 0.5, 1
-53 +45	10	0.1, 0.5, 1
-53 +45	15	0.1, 0.5, 1
-37 +31	Untreated	N/A
-37 +31	5	0.1, 0.5, 1
-37 +31	10	0.1, 0.5, 1
-37 +31	15	0.1, 0.5, 1

Table 3.4: Matrix for point load tests (after Kingman et al, 2004)

The change in $I_s(50)$ as a function of microwave exposure time for material in the size range -53 +45mm is presented in Figure 3.8. It can clearly be seen that microwave treatment has a significant effect on the strength of the ore, with exposures as short as 0.1s giving reductions in $I_s(50)$ of approximately 40%. Table 3.5 shows the full data set for the experiment. It can be seen that the results for microwave treated material show a larger standard deviation than the untreated. Examinations of the upper and lower limits reveals why this is the case. Indeed, for most of the microwave treated material, the strength of at least one (or often more) particles was close to zero. Naturally, this gives rise to the large standard deviation for treated samples because the untreated samples all had reasonable strength.

Treatment	Time	$I_s(50) \times 10^{-6}$ MPa				
	(s)	Mean	Standard Deviation	Median	Upper Limit	Lower Limit
Untreated	-	3.32	0.88	3.28	4.67	1.95
15 kW	0.1	2.06	1.73	2.06	5.47	0.53
15 kW	0.5	0.93	1.02	0.62	3.18	0.06
15 kW	1	1.29	1.06	0.88	3.26	0.06
10 kW	0.1	1.82	1.3	1.28	3.83	0.16
10 kW	0.5	1.86	1.74	0.83	4.89	0.06
10 kW	1	1.98	1.48	1.59	4.36	0.07
5 kW	0.1	1.82	1.3	3.16	4.64	1.36
5 kW	0.5	2.34	1.07	2.89	3.44	0.06
5 kW	1	2.29	1.07	2.19	4.13	0.74

Table 3.5: $I_s(50)$ as a function of microwave exposure time for material -53 +45 mm showing statistical measures

Kingman et al. (1999) also showed that reduction in ore strength to be related to microwave power level. This is also shown here with significant reductions in strength showed for 10 and 15kW but not for 5kW. It is apparent that a critical power density exists above which the damage is significant. For this ore within the cavity used, this is shown to be at least 10kW. After the initial drop in strength, little benefit is gained by increased exposure time. This was suggested in the paper by Whittles et al. (2003).

The point load index results for the -53 +45mm size fraction in Figure 3.8 below show that in general, higher power densities and shorter exposure times are more efficient, although there is a degree of variability in the result where the reduction from the 10kW treatment results in a greater reduction in strength than the 15kW treatment after 0.1s.

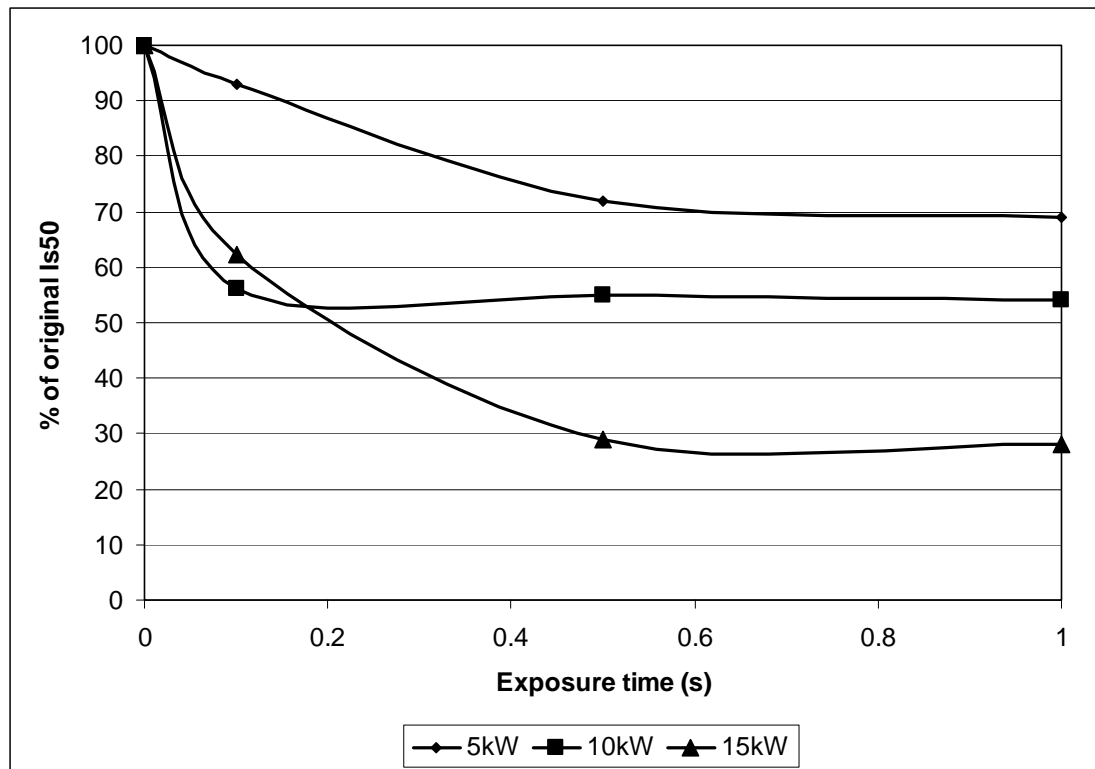


Figure 3.8: Point load index test results, (Kingman et al., 2003)

3.11.4. Drop Weight Tests

Point load index tests are useful for comparative purposes but are difficult to interpret in terms of changes in process efficiency. A standard test has been developed by the Julius Kruttschnitt Mineral Research Centre (JKMRC) University of Queensland, Australia (Napier-Munn et al., 1996). It characterises ore in terms of “impact breakage parameters”.

In the drop weight test, a known mass falls through a given height onto a single particle providing an event that allows characterisation of the ore under impact breakage. Although the test is physically simple, it is supported by detailed data analysis. This lends statistical reliability to the data, but as a consequence each test is relatively time-consuming. For each test, 15 samples are tested in 5 size fractions at 3 energy input

levels. Details of the recommended size fractions, number of particles and energy levels are given in Table 3.6. After each test is completed, the resulting fragments are collected and sieved to obtain a product size distribution. This is then used to determine the breakage functions for the material.

Particle Size Range (mm)	Number of Particles	Energy 1 (kW.h.t ⁻¹)	Energy 2 (kW.h.t ⁻¹)	Energy 3 (kW.h.t ⁻¹)
63 x 53	10	0.2	0.125	0.05
45 x 37.5	15	0.5	0.125	0.05
31.5 x 26.5	30	1.25	0.5	0.125
22.4 x 19	30	1.25	0.5	0.125
16 x 13.2	30	1.25	0.5	0.125

Table 3.6: Nominal energy input particle size combinations for JKMRC drop weight energy input levels.

The analytical procedure is based on the assumption that product size distributions are a function of input energy or specific comminution energy (Ecs, kWh/t). To model the breakage process, the JKMRC developed a method for relating energy to geometric size reduction. The basic principle of the method is as follows. If a single particle is broken, the size distribution of the daughter particles may be considered as a $\sqrt{2}$ series and a cumulative size distribution curve is obtained. The graph is then replotted after dividing the x-axis by the original particle size. A series of marker points are then used to describe the size distribution. These are defined as a percentage passing t , a fraction of the original particle size. Thus t_2 is the percentage passing half the original size, etc. The value of t_{10} , i.e. the amount passing 10% the original mean size, is used as a characteristic of size reduction and may be considered a fineness index. To make use of this technique, the marker points t_2 , t_4 , t_{25} , t_{50} and t_{75} are stored in matrix form against

t_{10} . This information is then used to calculate the values of A and b , which are defined as the ore impact breakage parameters. A and b are related to E_{cs} by the following equation 3.6:

$$t_{10} = A(1 - e^{(-b.E_{cs})}) \quad (\text{Equation 3.6})$$

The drop weight test provides effective characterisation of an ore for crushing. It should be remembered that chipping and abrasion occur in tumbling mills and that additional tests would be required to obtain a comprehensive assessment of the benefits of microwave treatment. The impact parameter $A \times b$ has been correlated, although not well using equation 3.7 (Napier-Munn et al., 1996):

$$A \times b = -3.5WI + 117 \quad (\text{Equation 3.7})$$

To enable comparison, Kingman and his co-workers carried out drop weight tests both on untreated and material treated at 15kW for 0.2s. From the results, breakage parameters and specific comminution energy were calculated. The energy levels used in the investigation were half those recommended by the standard method, as the standard energies resulted in no difference between treated and untreated characteristics despite significant visible fractures in the treated material. It was thought that if lower impact energies were used then the difference between the treated and untreated behaviour would be enhanced. The following table details the breakage parameters obtained for the treated and untreated fractions. A higher value of b indicates a much softer ore. It is an indicator of the amenability of the ore to size reduction by impact.

Treatment	A	b	$A \times b$
15kW 0.2s	52.5	2.35	123.4
Untreated	54.3	1.61	87.4

Table 3.7: Breakage parameters for treated and non-treated ore

3.11.5. Determination of the Uniaxial Compressive Strength

The following section details the experimental determination of the Uniaxial Compressive Strength (UCS) and in particular the relationship between the UCS and Point Load Index. When a material is loaded, the stress is said to increase with the strain. This is to say that as the load increases the displacement or deformation in the sample also increases. If this relationship is linear then the material is said to be behaving elastically, and the strain is often recoverable. However, materials very rarely behave in a perfectly elastic way, and some of this extension is lost. When the material does behave elastically, the ratio of stress to strain is known as the stiffness, or modulus of elasticity. Also known as the Young's modulus, the values range from <10 GPa for marble and weak sedimentary rocks, to >70 GPa for certain quartzite and igneous rocks (Bass, 1995).

Great care is required when interpreting results from UCS tests. The results depend on the nature and composition of the rock and the conditions experienced by the test specimens. For similar mineralogy, the UCS will decrease with increased porosity, increasing degree of weathering and micro-fissuring. Suggested techniques for determining the UCS and deformability of rocks are given by the International Society of Rock Mechanics Commission on Standardization of Laboratory Field Tests (ISRM commission, 1979). The UCS test is the most widely used test performed on rock (Brady & Brown, 1993).

Figure 3.9 shows the stress-strain behaviour of the loading of an elastic material until brittle failure. Here the UCS is reached and no further plastic behaviour is observed. The sample effectively fractures catastrophically.

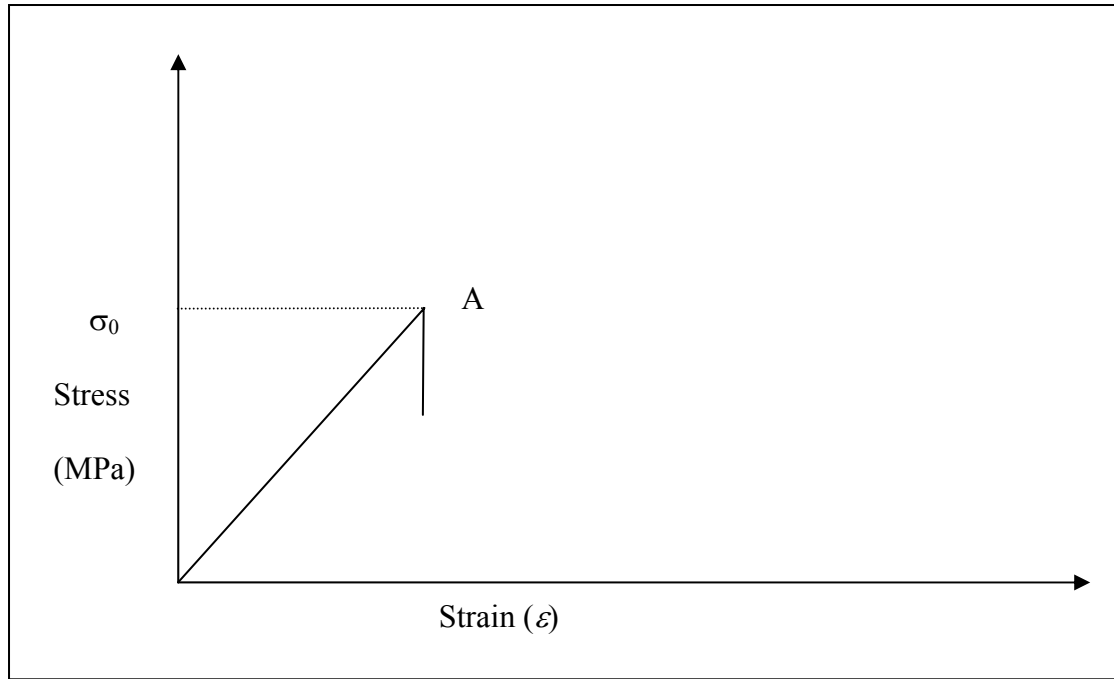


Figure 3.9: Stress-strain profile for a tough, brittle material

Figure 3.10 below shows a typical example of a stress-strain plot for the uniaxial compression of a cylindrical rock sample (after Jaeger and Cook, 1979). The stress-strain relationship is linear until point A is reached. Until this point, the material can be considered to be behaving elastically. At this point, the material is said to yield, and the corresponding stress value is said to be the yield stress (σ_0). From this point onwards the material is no longer behaving elastically, but behaviour is said to be plastic, or ductile. The material will continue to deform plastically as the stress increases until point B is reached. At this point, the stress has reached its maximum, and the corresponding stress, C_0 is the Uniaxial Compressive Strength. As the strain increases, no further increase in load is experienced by the sample, and it deforms according to the displacement of the loading medium, usually in shear. The point C denotes the residual strength of the material.

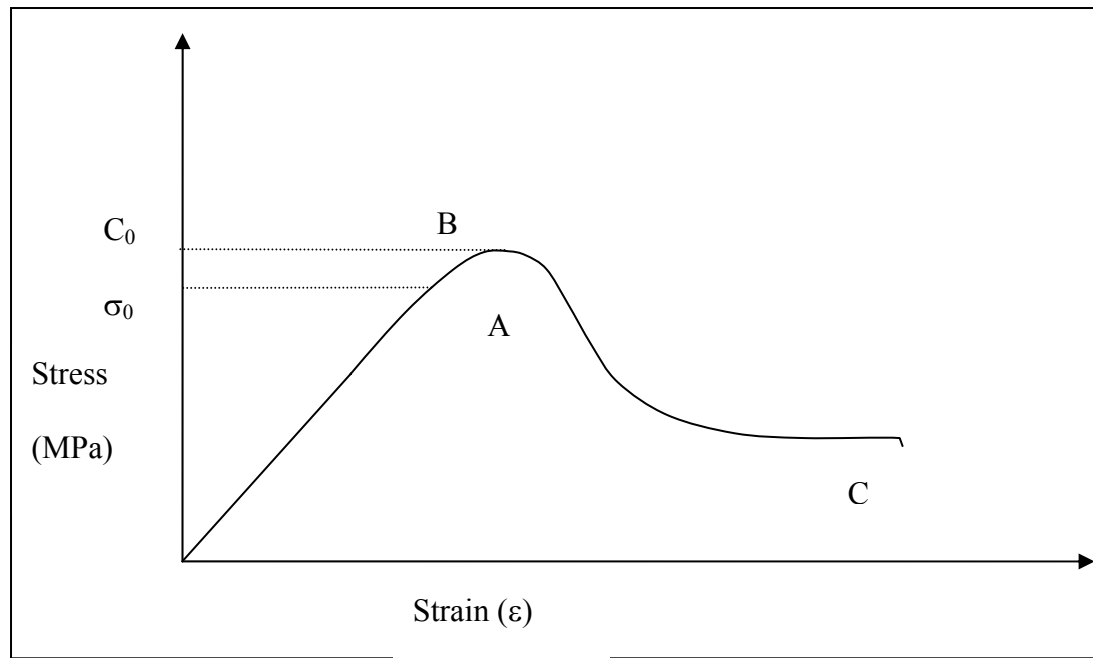


Figure 3.10: Stress-strain profile for a softer material

In reality for the UCS test, a cylindrical core of rock is prepared from drill cores to specific dimensions, usually of aspect ratio of 2:1. The diameter of the samples is usually of the order of 40mm, with actual dimensions dependent on where the test is being carried out and availability of equipment. The sample is ground so that the two top surfaces are parallel. This sample is then loaded between two ground hardened steel platens under displacement control.

Kahraman (2001) reviewed the various correlations of UCS to point load strength detailed by various authors. It is stated by the ISRM that on average, the compressive strength is 20-25 times $I_{s(50)}$. However, it is also reported that in tests on many different rock types the range varied between 15 and 50, especially for anisotropic rocks. So, errors of up to 100% should be expected if an arbitrary ratio value is chosen to predict compressive strength from point load tests.

Reference	Equation
D’Andrea et al.	$q_u = 15.3I_{s50} + 16.3$
Broch & Franklin	$q_u = 24I_{s50}$
Bienawski	$q_u = 23I_{s50}$
Hassani et al.	$q_u = 29I_{s50}$
Read et al.	
(1) Sedimentary Rocks	$q_u = 16I_{s50}$
(2) Basalts	$q_u = 20I_{s50}$
Forster	$q_u = 14.5I_{s50}$
Gunsallus and Kulhawy	$q_u = 16.5I_{s50} + 51.0$
ISRM	$q_u = 20.....25I_{s50}$
Chargill and Shakoor	$q_u = 23I_{s50} + 13$
Chou and Wong	$q_u = 12.5I_{s50}$
Grasso et al.	$q_u = 9.30I_{s50} + 20.04$
(After Kahraman, 2001)	

Bearman (1999) showed that the point load index is intimately related to Mode 1 fracture toughness:

$$K_{IC} = 0.209I_{s50} \quad \text{(Equation 3.8)}$$

Mode 1 fracture toughness has also been shown to have highly significant correlation with the breakage parameters A and b (Bearman et al. 1997). It was shown that

$$b = 2.2465 \times K_{IC}^{-1.6986} \quad \text{(Equation 3.9)}$$

$$Ab = 126.96 \times K_{IC}^{-1.8463} \quad \text{(Equation 3.10)}$$

From the information given, it is possible to tabulate the indexes for a given UCS value. It is then possible to determine the increase in t_{10} as the UCS is reduced. This then enables us to determine the potential energy saving gained from the use of microwaves, for a given specific comminution energy. The calculations whose results are shown in Table 3.8 used an Ecs of 3 kWh/t. As Ecs is increased, the t_{10} curve tends towards a limiting value governed by the equation for the breakage parameter A .

However, UCS tests have not been carried out on microwave-treated cores, as often the treatment results in a sample that is longer intact. It is then not possible to subject the broken core for UCS testing. Yet as it is possible to correlate the point load index with the UCS and vice versa, it was thought that detailed investigation was necessary.

UCS (MPa)	I_{s50}	K_{IC}	$A \times b$	b	A	$-b \times ECS$	t_{10}
240	10.00	2.09	32.55	0.64	50.68	-0.64	24.02
230	9.58	2.00	35.21	0.69	51.00	-0.69	25.43
220	9.17	1.92	38.23	0.74	51.34	-0.74	26.96
210	8.75	1.83	41.65	0.81	51.69	-0.81	28.60
200	8.33	1.74	45.58	0.88	52.07	-0.88	30.37
190	7.92	1.65	50.11	0.96	52.46	-0.96	32.28
180	7.50	1.57	55.37	1.05	52.88	-1.05	34.32
170	7.08	1.48	61.53	1.15	53.33	-1.15	36.51
160	6.67	1.39	68.82	1.28	53.81	-1.28	38.83
150	6.25	1.31	77.53	1.43	54.33	-1.43	41.29
144	6.00	1.25	83.59	1.53	54.66	-1.53	42.82
140	5.83	1.22	88.06	1.60	54.88	-1.60	43.85
130	5.42	1.13	100.97	1.82	55.49	-1.82	46.49
120	5.00	1.05	117.05	2.08	56.15	-2.08	49.17
110	4.58	0.96	137.45	2.42	56.87	-2.42	51.80
100	4.17	0.87	163.89	2.84	57.68	-2.84	54.32
90	3.75	0.78	199.09	3.40	58.59	-3.40	56.63
80	3.33	0.70	247.45	4.15	59.61	-4.15	58.67
70	2.92	0.61	316.64	5.21	60.80	-5.21	60.47
60	2.50	0.52	420.89	6.77	62.20	-6.77	62.13
50	2.08	0.44	589.33	9.22	63.90	-9.22	63.89
40	1.67	0.35	889.78	13.47	66.04	-13.47	66.04
30	1.25	0.26	1513.41	21.96	68.91	-21.96	68.91
20	0.83	0.17	3199.43	43.73	73.16	-43.73	73.16
10	0.42	0.09	11504.42	141.95	81.05	-141.95	81.05

Table 3.8: Summary of correlations between UCS and other breakage parameters

From Table 3.8, it can be seen that if the strength is reduced from 144MPa to 90MPa for example, then the t_{10} is increased from 54.1% to 58.6%. As previously stated, even marginal increases in efficiency can result in dramatic reduction in energy consumption.

3.11.6. Liberation

Liberation is the term used to describe the degree of separation of a particular phase in the mineral from another. For example, in a typical copper ore, the copper is present as a sulphide mineral. In order to minimise the tonnage of ore to be processed in the smelter it is essential that the copper sulphide phase introduced to the smelter be as pure as possible, and separated out from the uneconomic phase, or gangue mineral. When a particle is predominantly copper sulphide, then it is liberated from the gangue mineral. The gangue mineral can also be liberated in the same respect. Refer to Figure 3.11.

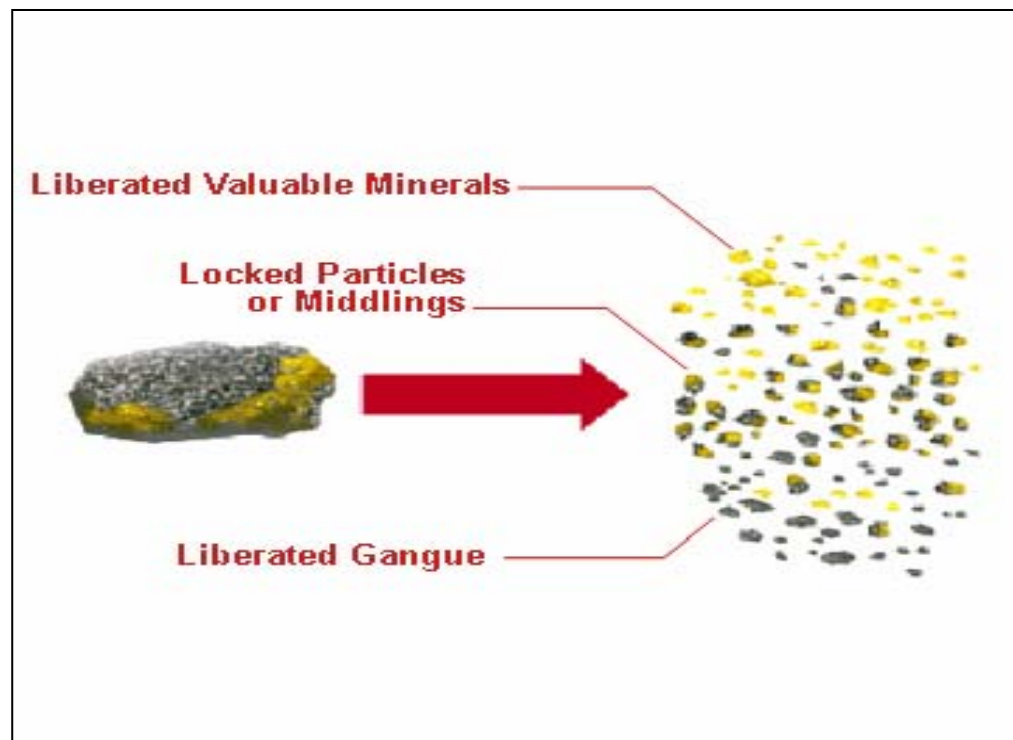


Figure 3.11: Schematic showing liberated valuable mineral and gangue, and the locked portions.

3.11.7. QEM*SEM

This SEM-based QEMScan is a fast chemical data collection system that uses a combination of backscattered electron (BSE) images and EDS analysis to create an image of a sample based on chemical composition. These images can then be

processed off-line to provide information on modal abundance, grain size, mode of occurrence, liberation characteristics and how much of a particular mineral phase is recoverable. The information can be used to develop processing routes and improve plant operations. In the study by Kingman et al., the percentage amount of liberated copper sulphides in the coarsest size fraction for the treated material was over double that for the untreated material. This could effectively increase the liberation size for a particular process. Consequently, grinding energy consumption is reduced, and less ore would be over-ground and potentially lost to slimes.

3.12. Theoretical Studies

Salsman et al. (1996) suggested that the generation of high stresses were dependent on heating rates. It was suggested that short pulses of high-energy microwaves were the best means of delivering such heating rates. The paper examined the feasibility of short-pulsed microwave treatment of ores using finite-element numerical modelling of a single pyrite particle in a calcite matrix to predict the thermo-mechanical response. Salsman suspected that given sufficient heating rates, the stresses generated would exceed the strength of the material. The simulations yielded promising results in terms of the magnitude of stresses developed when realistic power densities were applied in very short bursts. It was stated that these stresses were due to large thermal gradients across grain boundaries. However it was discovered that Salsman et al. used bulk and shear moduli that were 10 times higher than the values found in the paper by Simmons and Birch (1963). No reference to the source of these values was given. A higher stiffness modulus will result in higher stresses being generated per unit strain. Therefore Salsman et al. results may have proven to be optimistic in terms of the magnitude of the stresses, yet it is still possible that these stresses will exceed the

strength of the material. Geller (1975) modelled the stresses induced in rock samples when heat was applied by considering the simplified case of convective heat transfer at the surface of perfectly elastic and isotropic spheres. The assumption of sphericity was justified since, of the basic shapes, spheres are most resistant to thermal shock and therefore if conditions were severe enough to cause failure in spheres then other shapes will also fail.

Whittles et al. (2002) used finite difference numerical modelling to elucidate the influence of electric field strength on the microwave treatment of a simulated ore. The 2-D 15 x 30 mm simulated sample consisted of 10%, 1mm² microwave-absorbing pyrite particles, in a calcite matrix - a low-absorption mineral. A volumetric heating rate was applied to the pyrite grains, and the subsequent thermal conduction and expansion modelled. No heat was applied to the calcite. The elevated stress resulting from the expansion was sufficient to exceed the strength of the material, and this damage was quantified using a simulation of a uniaxial compressive strength test. The UCS was then used to derive a number of parameters useful for the minerals processing engineer such as *A* and *b*. These were then used to calculate the specific comminution energy for each treatment regime. The study concluded that higher power densities for lower exposure times were more effective at weakening. The work suggested that higher stresses are possible in the high power density case as there is less time for conduction between the responsive and transparent phases. Unfortunately the bulk and shear moduli used in this study were the same as those used by Salsman et al. Numerical modelling is discussed in detail in the following chapter.

3.13. Conclusions

It is clear that there is scope for research into the microwave treatment of ores. There are numerous studies where downstream benefits to process have been illustrated in the laboratory. There have been many studies of the heating rate experienced by numerous ore species, and it is possible to conclude that many valuable ore minerals heat very rapidly, whilst the silicates and carbonates that make up the majority of gangue minerals are found to be relatively transparent to microwave radiation. This results in more energy being available to heat the absorbent species disseminated in a matrix, and maximising the heating rate of absorbent species. Kingman and his co-workers have shown that at higher energy inputs and shorter exposure times, the thermal gradients are maximised, and consequently the energy balance becomes more favourable. Salsman et al. (1996) showed that higher heating rates are likely to generate higher stresses, and that these stresses were likely to exceed the strength of the material. Whittles et al. (2003) showed the potential process benefits using a numerical simulation technique. Although these studies are detailed and show interesting possibilities, there is more scope to determine certain aspects of the work. It is deemed necessary to further investigate the effect of size on the potential weakening of the ore in order to explain the results in Section 3.11.2. As it is not yet possible to test the full range of potential power densities, more detailed studies of the effect of power density and exposure time is required, as the behaviour is unlikely to be linear. It is also evident that no work has been carried out on the effect of the variation of the mechanical and thermal properties of the mineral species involved. It is also desirable to investigate the effect of the mechanical properties on the optimum weakening. Ultimately, there is scope for the investigation of the mechanisms by which increased liberation is possible.

Chapter 4

Methods for Predicting Stresses and Strains in Rock Mechanics

4.1 Introduction

It was necessary to investigate the methods by which it was possible to determine the stress/strain response of a granular, heterogeneous rock material experiencing partial rapid heating from microwaves. As it is impossible to observe the behaviour occurring inside these materials that were being irradiated in a microwave cavity, it was desirable to devise a way where the direction and magnitude of the stresses are determined. Previous studies (Salsman et al., 1996, & Whittles et al., 2002) have shown that numerical modelling is a valid method for investigating these mechanisms. With a realistic model it is possible to investigate a wide range of conditions that are either not always possible to replicate in the laboratory, or would be prohibitively time-consuming.

Also, it has often been the case that irradiated samples can not be tested for reductions in strength (one of the main indicators of the effects of microwave radiation), as the cracks generated result in a particle which was smaller than the original untreated sample. Therefore this particle must be discarded from the test, and the positive effects of the size reduction are not included in the final result.

The aim was to build a numerical model that would explain the observed phenomenon of weakening and increased liberation when certain phases are heated rapidly. Therefore this chapter will detail the main numerical modelling methodologies, and explain the choices that were made for the most suitable software for the investigation.

The chapter also details some of the background behind the various numerical modelling techniques and methodologies that are currently in use in geomechanics to elucidate on the physical mechanisms of thermal expansion and rock fracture involved in microwave treatment.

Computer modelling in geomechanics is characterised by the complexity of the properties of the materials which, being natural also have a degree of uncertainty. To simulate the thermal-mechanical behaviour of complex materials, a large range of parameters are required. Unfortunately, many of these are also difficult to measure, and so often approximate values obtained from a variety of published sources and databases are frequently used.

Thus due to the assumptions in the input parameters the computer modelling was used to investigate the suspected mechanisms, rather than provide real values that can be validated against laboratory observations.

The realistic representation of a brittle, granular, heterogeneous material is a difficult task. Certain methodologies have been well documented and validated, however the computer modelling of the discontinuous rock fracture has not yet been fully resolved. Precise data on the mechanical, thermal and electrical properties of the minerals being modelled was not available. Therefore significant assumptions are necessary. However, these assumptions will be valid as long as the values used are within a realistic range of observed values. This chapter will discuss these methods in detail.

4.2 Nature of Rock Mechanics

Numerical modelling of geomechanical processes requires consideration of the characteristic length scale of the problem. Rock consists of crystals, grains, cementitious materials, voids, pores and cracks (Jaeger & Cook, 1979). The orientation, distribution and size of the grains, pores and grain boundaries define the fabric of the rock. Superimposed on the fabric are larger scale discontinuities, such as joints, faults, and bedding planes. The arrangement of such discontinuities is termed the rock structure. Although in rock engineering design the rock structure is a major consideration, with in most cases the rock fabric being considered as homogeneous. When considering the microwave treatment of pre-crushed rock it is the fabric of the ore material that is of significance. Thus with modelling of the response of rock material to microwave radiation we are concerned with the distribution, shape, size, orientation of the mineral grains and associated voids and grain boundaries and also their thermal and mechanical properties.

At the microscopic scale (of the order of grain size, say, from 1 μ m to 1mm), rock is a heterogeneous material whose brittle fracture is a complicated progressive process caused by isolated microstructural changes, known as dissipative processes. These processes are particularly difficult to predict and model in the compressive field (Fang & Harrison, 2002).

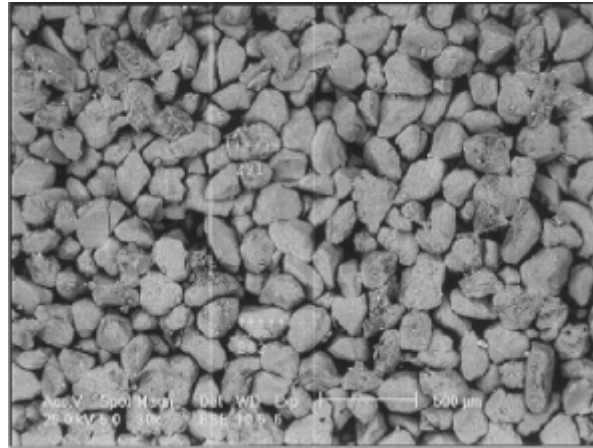


Figure 4.1: Fontainebleau sandstone (El Bied et al, 2002)

Above is a microphotograph of Fontainebleau sandstone (Figure 4.1). The grains in this case are of the order of $250\mu\text{m}$, although the shape, size, orientation and separation of the grains can vary considerably, and this will have an effect on the local strength of the rock. This results in variations in local stress and strain conditions when the rock is loaded. As compressive loading increases, local defects act as stress concentrators leading to microcracking and slippage occurring at various sites within the rock. These microstructural changes further influence the local stress-strain distribution and a subsequent increase in loading results in the coalescence of those cracked sites that are aligned in favourable directions with respect to the applied stress state, leading eventually to the formation of macroscopic fractures (Peng, 1976). During compression tests when confining pressure is low, rock often fails by splitting parallel to the major principal stress. With moderate confining pressure, failure is characterized by diagonal shear faults as illustrated by the next micrograph (Figure 4.2). If the confining pressure is sufficient then sliding between grains and crack surfaces becomes the dominant regime.

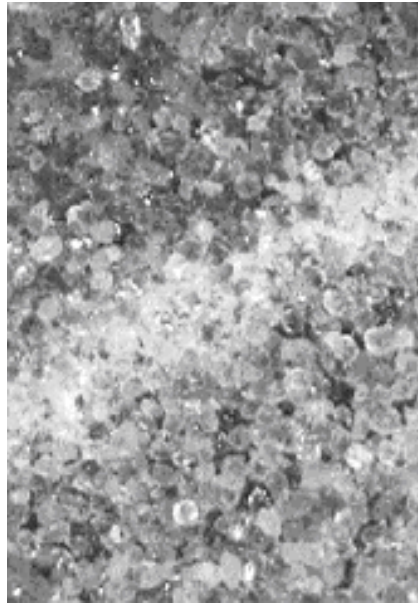


Figure 4.2: Photograph of shear bands obtained with binocular magnifying glass.

Characteristic white colour on the shear band where grains have been degraded locally (after El Bied et al, 2002)

Significant advances have been made in the fundamental understanding of the micromechanics of compressive failure in rock. It is now recognized that the macroscopic fracture process in a brittle rock actually involves a multiplicity of microcracks and its essential nature lies not only in the initiation and propagation of individual cracks but also in the interaction and coalescence of the crack population (Wu et al., 1999). In a seminal study, Hallbauer, Wagner and Cook (1973) conducted optical microscope observations to elucidate the spatial evolution of cracking and development of shear localisation in a compact quartzite. Subsequent studies using scanning electron microscopy (SEM) have provided additional details on the geometric attributes and anisotropy of stress-induced cracking (Tapponier & Brace, 1976 and Kranz, 1979) and the instability mechanisms associated with crack coalescence.

As previously stated, it can be extremely difficult to predict the behaviour of granular heterogeneous materials, due to the variation in the grain size and shape, porosity, permeability, and composition at particular points in the sample as well as in different samples. It is often the case that simplifications and assumptions are required in order to achieve a meaningful representation of the system. It is an important consideration in the numerical modelling to derive a set of assumptions that allows the modelling to be undertaken using the available data, whilst the assumptions are not to result in a meaningless model result.

4.3 Computer based numerical modelling methods

4.3.1 Introduction

There are a wide variety of modelling techniques for the determination of the physical response of rocks, such as thermal conduction and expansion, and mechanically derived stresses and strains of rock materials to a set of applied loads. These techniques vary from numerical techniques and limit equilibrium methods, to the use of physical models (Roberts, 1994). Numerical techniques can vary from relatively simple closed form solutions to complex computer modelling applications. Major advances have been possible in recent years as personal computers become have powerful enough to be able to complete simulations of complex natural systems such as rock material. This section will focus on the use of computer based numerical modelling methods of mechanical and thermal analyses.

4.3.2 Nature of Geomechanical Modelling

Early numerical modelling was limited in that only linear elastic materials could be modelled, and no representation of fracture or unrecoverable plastic strain was possible. However now it recently became possible to represent this behaviour using failure criterion and plasticity models. This has allowed for the prediction of stresses, displacements and failure zones around structures in rock masses that exhibit complex non-linear constitutive behaviour. Numerical modelling methods may be divided into continuum methods, where the rock is treated as a continuous media that deforms, or discontinuum methods, where the rock may break and separate. Several different continuum numerical solution methods have been adopted for use within modelling of rock mechanics but most methods have utilised the same approach of solving the partial differentiation equations that describe the system using an approximate technique by dividing the area into smaller physical and mathematical components which are usually called elements (Hoek et al., 1991). In continuum methods such as distinct element methods, grid formation is not necessarily a requirement. Each element is a single body where the material properties are constant. The physical properties such as stress and displacement within or on the boundaries of a body are governed by a set of mathematical equations. The physical quantities of the element interact with adjacent or all other elements in order to bring the overall modelling system into a state of equilibrium.

Jing and Hudson (2002) presented a review of the techniques, advances, problems and likely future development directions in numerical modelling for rock mechanics and rock engineering. They suggested that as a result of numerical modelling experience over the past decades, it has become clear that the most important step in numerical

modelling is, perhaps counter-intuitively, not operating the computer code, but the earlier ‘conceptualization’ of the problem in terms of the dominant processes, properties, parameters and perturbations, and their mathematical presentations. This is true for scales varying from regional modelling of rock masses with dimensions of the order of often several kilometres, to modelling the propagation of individual cracks of a length scale of fractions of a millimetre. The associated modelling steps of addressing the uncertainties and estimating their significance via sensitivity analyses is similarly important. Moreover, success in numerical modelling for rock mechanics and rock engineering can depend almost entirely on the quality of the characterization of the problem geometry, the physical behaviour of the individual features and their interactions.

Today’s numerical modelling capability can handle very large scale and complex equation systems, but the quantitative representation of the physics of inhomogeneous and complex rocks remains unresolved, although much progress has been made in this direction (Jing and Hudson, 2002). The usefulness of modelling for the engineer is in the predictive capability of the modelling. This predictive capability can only be achieved if the key features of the rock reality have indeed been captured in the model. Furthermore, the engineer needs some reassurance that this is indeed the case. It is therefore often required to audit rock mechanics modelling and rock engineering design to ensure that the modelling is adequate in terms of the modelling or engineering design objective (Jing and Hudson, 2002). Increased confidence in the quality of the model is gained by validating the model against actual observation and measurement.

4.4 Numerical Modelling Methodologies

4.4.1 Introduction

The main fundamental types of numerical modelling methods that are most commonly used in rock mechanics are detailed in the following section. These have typically been used for large scale excavations such as mine and tunnel excavations and slope stability calculations, and the use of numerical modelling for smaller scale applications is relatively novel. Examples include:

- o Continuum: Finite Element Method, Finite Difference, Boundary Element
- o Discontinuum: Distinct Element Method

The deformation of a body due to imposed loads can be regarded as being either continuous or discontinuous. The deformation illustrated in Figure 4.3 (a) is continuous, whereas that shown in figure (b) involves discontinuous behaviour.

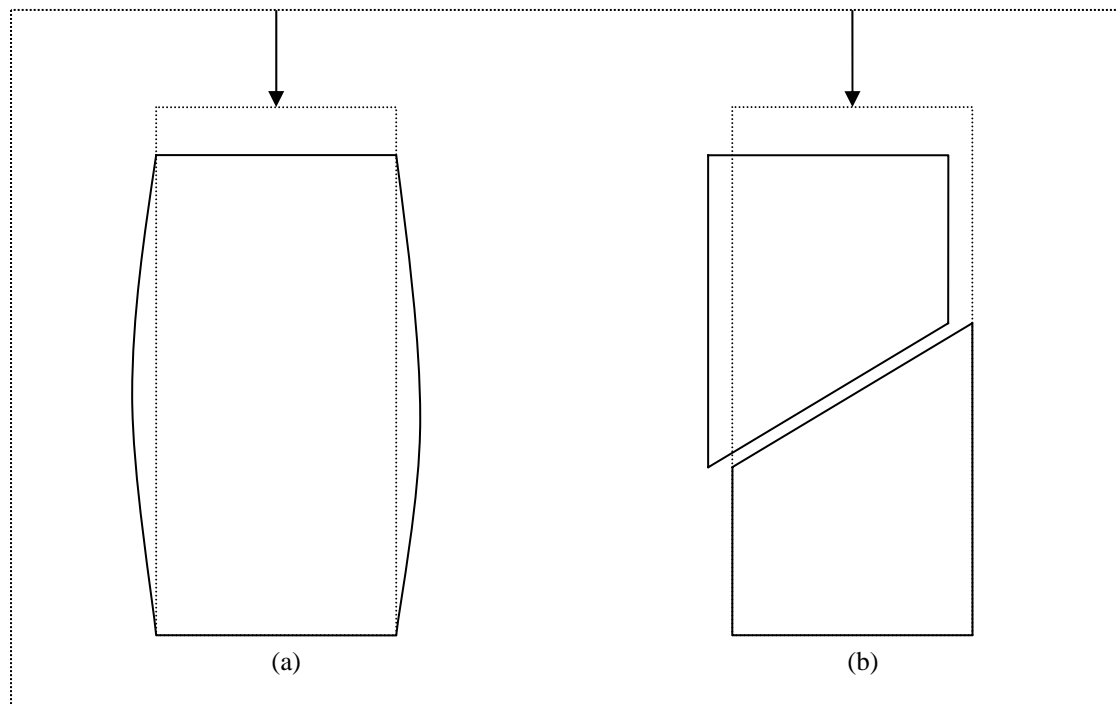


Figure 4.3: (a) continuous and (b) discontinuous behaviour of uniaxially loaded specimen (after Hoek et al., 1991)

4.4.2 Continuum Methods

4.4.2.1 Finite Element Method

In the finite element method, the entire modelled rock material is divided into elements. The elements are connected at nodal points, with the elements and nodal points constituting the finite element mesh. During the solution process the loads and displacements at the nodal points are determined from the load and displacement conditions within the finite area enclosed by the nodal points i.e. within the elements. A central requirement for the finite element method is that the field quantities (stress, displacements) vary throughout in accordance with the governing equations. The solution is obtained by adjusting the parameters used in the equations to minimise error terms on local or global energy (Hoek et al 1991).

In the Finite Element method it is usual to form a series of simultaneous equations to represent the behaviour of the elements concerned. These equations can then be arranged into matrices and vectors, and then solved using matrix algebra. The element matrices are often combined into a large global stiffness matrix. This is a matrix or implicit solution technique which is the most efficient technique for solving problems with comparatively simple constitutive behaviour. For more complex behaviour multiple steps and matrix reformulation are required, which consequently lower the efficiency of the solution.

In this method the field variables vary continuously throughout the elements defined by a function known as a shape function. The finite element model is suitable for modelling heterogeneous or non-linear materials as the material behaviour in each element is individually calculated. Prior to solving the model, boundary conditions are

usually required to be applied to the models outer edges. The model mesh needs to be extended beyond the zone of influence of the excavation and the boundary conditions applied therefore represent the in-situ far field conditions. Although finite element methods analyse the rock mass as a continuum, discontinuities can be explicitly represented. However for a heavily discontinuous rock mass it is more efficient to use the distinct element method. Material non-linearity is accounted for by modifying the material stiffness properties within the global stiffness matrix in an iterative manner. The matrix itself is solved for each iteration, and this can be time consuming for materials with complex non-linear behaviour, as many iterations of the matrix calculation may be required to bring the model into equilibrium (Coetzee et al 1993).

4.4.2.2 Finite Difference Method

When explicit or dynamic relaxation techniques experience a disturbance it is assumed to only affect the cells in the immediate vicinity. With each computational step the effects of the disturbance propagate throughout the model until equilibrium is established. Thus each step is analogous to a discrete period of time. This method requires the damping of numerical oscillations and is relatively slow for simple problems. However the formulation or solution of large matrices is not required, and is therefore the most efficient means of solving for materials with complex constitutive relationships. With finite difference methods, field variables such as stress, displacement, and velocity are defined at nodal positions only, and not within zones.

The finite difference model is constructed in the same manner as a finite element model. The mesh and the manner of prescribing boundary conditions and material properties are similar. However, for solving the problem the finite difference method uses an explicit solution technique. Implicit and explicit methods are contrasted in Table 4.1. This technique involves the direct replacement of every derivative in the set of governing equations with an algebraic expression written in terms of the field variables (e.g. stress and displacement) at discrete points in space (Coetzee et al 1993). In this manner the large matrices which are a feature of the finite element method are not formed. The finite difference solution is analogous to a time stepping process with each calculation wave representing one timestep. The general calculation sequence used in the commercially available *FLAC* finite difference code is shown as Figure 4.4.

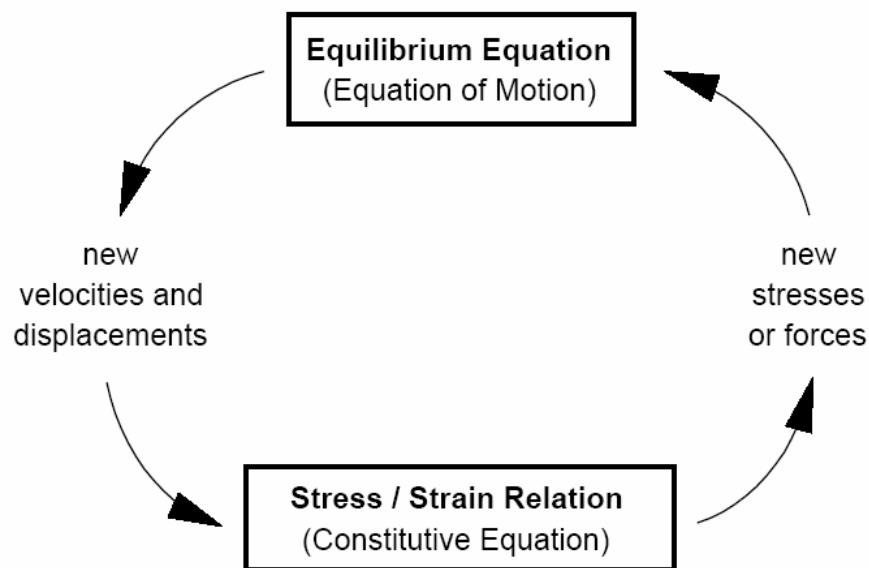


Figure 4.4: Basic explicit calculation cycle, finite difference method (after Coetzee et al 1993)

In the calculation sequence, equations of motion are first invoked to derive velocities and displacements from stresses and forces. Strain rates are derived from the velocities and new stresses from the strain rates. During one calculation sequence the values are fixed and not affected by the values calculated for adjacent localities. For instance the velocities associated with the locality are not affected by stresses calculated for adjacent points. It is therefore necessary to represent each calculation loop as a very small time step. However after each cycle interaction occurs between adjacent points and after several cycles disturbances can propagate across several elements as they would in a natural system. No iteration process is required to compute stress from strains and this method is the best method to use for modelling non-linear, large strain systems.

Explicit	Implicit
Time step must be smaller than a critical value for stability	Timestep can be arbitrarily large, with unconditionally stable schemes
Small amount of computational effort per timestep	Large amount of computational effort per timestep
No significant numerical damping introduced for dynamic solution	Numerical damping dependent on timestep present with unconditionally stable schemes
No iterations necessary to follow nonlinear constitutive law	Iterative procedure necessary to follow nonlinear constitutive law
Provided that the timestep criterion is always satisfied, nonlinear laws are always followed in a valid way	Always necessary to demonstrate the above mentioned procedure is: (a) stable, and (b) follows the physically correct path (for path sensitive problems)
Matrices are never formed. Memory requirements are always at a minimum. No bandwidth restrictions	Stiffness matrices must be stored. Ways must be found to overcome associated problems such as bandwidth. Memory requirements tend to be large
Since matrices are never formed, large displacements and strains are accommodated without additional computing effort	Additional computing effort needed to follow large displacements and strain

Table 4.1: Comparison of explicit and implicit solution schemes (*FLAC* Manual, Itasca)

4.4.2.3 Boundary Element Method

Only the boundaries of the model geometry are divided into elements (discretized) in this method. The rock mass is represented within the model as a mathematically infinite continuum. The method utilises a fundamental solution for determining the stress and displacement at any point in the medium. The solution is used as a basis for determining the relationship between conditions on the surface of the boundary elements (such as an excavation in geomechanical applications) and the conditions of all points within the remaining medium (Hoek et al., 1991). Within the model each boundary element can have an effect on all the other boundary elements. To calculate the interaction effects a system of linear equations is assembled into a matrix, termed the coefficient matrix, which represents the influence of one element on another. As each element can influence every other element, the coefficient matrix is said to be fully populated. This means that the solution time increases exponentially with respect to the number of elements. As the state at any point in the medium is determined solely by the conditions on the discretized boundaries it is not necessary to approximate the far field stresses. However, boundary element models have limited capability in modelling heterogeneous and non-linear materials. (Whittles, 1999)

4.4.3 Discontinuum Methods

4.4.3.1 Distinct Element Method

In this method the rock mass is considered as discontinuous, consisting of discrete interacting particles, free to move except during contact with neighbouring objects (Dorfmann et al, 1997). Particles can undergo large displacements and large rotations and are typically used to model failure of weakly cemented discrete systems under high loads. The particles are usually considered as rigid bodies with the rock mass deforming by interactions at the block contacts with the surrounding blocks (Hoek et al, 1991). The distinct element method models this by constructing data structures that represent the blocky nature of the system being analysed. The blocky rock mass behaves in a highly non-linear manner and hence explicit solution techniques such as used in the finite difference method are usually favoured for distinct element methods (Hoek et al, 1991). This allows the constitutive modelling of joint behaviour with little increase in computational effort, and results in the computing time being only linearly dependent on the number of elements used. However, one common disadvantage is that results can be sensitive to assumed values of material properties, especially the properties of the discontinuity. A commonly used commercial distinct element is *UDEC* and *UDEC3D* (Itasca, 1995).

4.4.3.2 Particle Flow Code

Particle flow codes are programs for modelling the movement and interaction of assemblies of arbitrarily-sized circular (2D) or spherical (3D) particles. Particles are rigid but may deform locally at contact points using a soft contact approach, in which finite normal and shear stiffness are taken to represent measurable contact stiffness.

The particles may represent individual grains in a granular material or they may be bonded together to represent solid material, in which case, fracturing occurs via progressive bond breakage. Solution by the distinct element method allows dynamic stress waves to propagate through the particle assembly, which may exhibit slip or separation, with unlimited displacement, under the action of applied loading. Bonded assemblies exhibit complex macroscopic behaviours such as strain softening, dilation, and fracture that arise from extensive microcracking.

Particle flow codes have recently been used to model the micromechanical processes of rock fragmentation and crack propagation without the explicit use of complex constitutive equations for rock behaviour (Cundall, 2000),

4.5 Numerical Modelling Methodologies

Unlike in other branches of engineering, rock engineering problems tend to be characterised by a lack of information relating to the structure and properties of the material being modelled (Starfield and Cundall, 1988).

Whilst not wholly applicable in this instance due to the novel application of geotechnical software for smaller scale effects, Whyatt and Julien (1988) described four styles of implementing numerical models within rock engineering design which are as follows:

4.5.1 Ultimate Design Tool

In this style, numerical modelling is used as a precise prediction technique. For numerical models to be used in such a way the properties of the system being modelled should be fully defined. Using numerical modelling as an ultimate design tool has been successful in the mechanical and aerospace engineering industry but has limited applicability in rock engineering due to the lack of data and the variability of rock as an engineering material. This usually prevents the engineer from obtaining precise solutions.

4.5.2 Method of Last Resort

This style is used when the numerical model is used to establish some basis for design when empirical methods are not available or not known to the design engineer.

4.5.3 Aid to Judgement

Numerical models are used in studies to identify the most threatening (as regards geotechnics applications) failure mechanisms and/or to assess the relative merits of alternative designs. This includes parametric studies to assess the sensitivity of the model to changes in parameter values. This style is suitable for data limited situations typical of rock engineering problems.

4.5.4 Calibrated Model

In this style models are adjusted or ‘fudged’ to fit measurements taken from existing applications. The calibrated model analysis requires a detailed numerical model often based on extensive laboratory and insitu tests that are combined with observations of field displacement and stress redistribution. The laboratory results are adjusted until the model behaviour is similar to the field measurements. This readjustment is a reflection of the fact that rock behaviour often deviates significantly from that predicted from laboratory tests. This style has been used for the numerical modelling of coal mine excavations within UK coal mines (Garratt, 1997) where often a calibrated model is developed for a region and is utilised as a basis for parametric studies undertaken as an aid to judging support requirements within that region.

Starfield and Cundall (1988) suggested that a distinctive modelling methodology that is both purposeful and effective should be developed for rock mechanics modelling. Using a classification proposed by Holling for the use of modelling ecological problems they stated that modelling problems can be divided into four groups dependant on the level of data and understanding of the project.

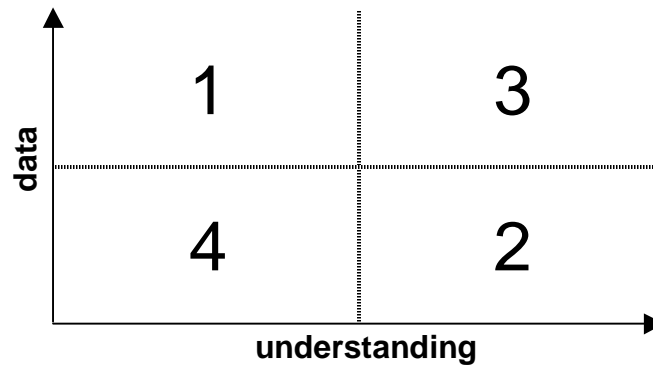


Figure 4.5: Holling's Conceptual Classification of Modelling problems

(after Starfield and Cundall 1988)

Modelling problems that lie within region 1 in Figure 4.5 have good data but little understanding and this is where statistics is the most approximate modelling tool. In region 3, modelling problems are characterised by good data and good understanding of the problem. For models situations falling in this zone, models can be constructed, validated and used with conviction.

Modelling problems that lie within regions 2 and 4 are characterised by limited data, due either to the data not being available or easily obtained. Starfield and Cundall (1988) stated that rock mechanics problems fall into the data limited categories and that there is not enough information about a rock mass to model it unambiguously. They state that one should attempt not to try to incorporate complex detail within a rock mechanics model but the designer should use the simplest model that will allow the important mechanism to occur. They consider that the validation of a data limited model may be impossible. Therefore instead of attempting to use the model as a fully predictive tool the models should be used to discover the potential mechanism of failure and deformation within the rock mass.

It is fair to say that this investigation is of the type described by region 4. The data is limited, and our understanding of the mechanisms is poor. It is not therefore possible to use the proposed model as an ultimate design tool to predict crack propagation and the exact degree of weakening. The simplest model must be constructed to examine the simple mechanism of one rapidly heating phase impinging on another cooler phase thereby generating high stresses and subsequent weakening.

4.6 Fast Lagrangian Analysis of Continua (FLAC)

FLAC is a 2-dimensional explicit, finite difference program that performs a Lagrangian analysis (Itasca, 1995). *FLAC* Version 4.0 has been used extensively within the University of Nottingham's School of Chemical, Environmental and Mining Engineering for the computer modelling of mining environments. The code has also been used successfully to simulate small scale heterogeneous rock samples exposed to microwave radiation (Whittles et al, 2003). In many respects this study is a continuation of the work detailed in that paper. *FLAC* has also been extensively used to model brittle failure of heterogeneous materials. Currently a full list of publications relating to applications of *FLAC* in rock mechanics and geotechnical problems is available at the Itasca Codes website. (<http://www.itascacg.com/site.html>)

FLAC models the material as a continuum. This may appear to exclude the micro-cracking and micro-sliding that characterises compressive loading and fracture in rock. These microstructural changes influence the local stress-strain distribution, and a subsequent increase in loading results in the coalescence of those cracked sites that are aligned in favourable directions with respect to the applied stress state, leading to the formation of macroscopic fractures (Fang & Harrison, 2002). However, *FLAC*

simulates brittle modes of fracture by degrading strength properties of an element according to the level of strain experienced in that element. This strain-softening is explored in more detail in sections 5.2.5.3.2. and 5.2.7.2.

The advantage for using *FLAC* is that it allows for the coupling thermal and mechanical behaviour. This will allow for the generation of stresses from the expansion caused by elevated temperatures in the sample. What is also useful is that as it allows for time-stepping, the development of stresses can be monitored as heating progresses. This is ideal for determining the influence of exposure time on the microwave treatment of ores.

Chapter 5

Numerical Methods

5.1 Introduction

This chapter details the numerical modelling methodologies for determination of the fundamental underlying mechanisms that govern microwave-assisted breakage.

Section 5.2 of this chapter details the implementation of a numerical model to quantify the thermal damage that a theoretical mineral system undergoes when exposed to high electric field strength microwave radiation. This involves the formulation of the thermal and mechanical coupling in the *FLAC* software which allows for the generation of stresses arising from thermal changes in the model. The section also details the specification of the thermal and mechanical properties of the materials used for the simulations.

Section 5.3 of this chapter details the practical use of the numerical modelling programme for the purpose of understanding the microwave heating of ores. This involves the use of various plotting techniques which help the understanding of the system in terms of the variation of stress, strain and temperature.

5.2 Numerical Modelling of Thermally Generated Stresses and Strains

5.2.1 Introduction

FLAC has been chosen as the most suitable commercially available code for the purpose of understanding microwave heating of ores due to its ability to simulate fractures in rock arising from thermal stresses, and easy management of the sample heat input. The chapter outlines the methodology used by *FLAC* to simulate thermal and mechanical behaviour, and the specification of the constitutive thermal and mechanical modes that are required in these models to accurately describe thermal and mechanical behaviour. The chapter also details the specification of the geometry of the system and how it was best chosen to yield an effective tool for the study.

It is often the case that real world behaviour could be expressed in the model to an acceptable degree of realism. Although it is potentially possible to generate highly realistic and complex models using high resolution meshing, in order to do so would render simulation times prohibitively long, and memory requirements excessive. A judgment must be made to compromise between what is possible on a personal computer, what is necessary to relate to the real world and what is necessary to investigate the underlying mechanisms. It is usual that approximate values are made to specify a particular property as long as this value is within a range of acceptable or realistic behaviour.

The model is constructed using a series of commands that are written in *FLAC*'s own programming language, *FISH* (which is simply an abbreviation of *FLACish*) using a normal text editor and saved as a *FLAC* data file. The sequence of commands within the data file corresponds closely with the physical sequence they represent. As *FLAC*

solves the problem using an explicit time marching scheme, the model problem may be constructed on a time related basis, for instance with incremental stages of loading or the time related application of heat.

5.2.2 Simulating Fractures in Continuum Modelling

It is of fundamental importance in geophysics and geotechnics to understand the interaction between phenomena at the micro-scale level, such as the deformation and microstructure evolution and rock properties at the macroscopic scale such as porosity, permeability and strength. It is impossible to represent porosity and permeability realistically in most numerical modelling packages. However, shear band formation is one of the main fracture mechanisms in rocks, and it is possible to represent this behaviour by other means. Shear band formation is generally seen as a result of strain localisation in inelastic solids. In brittle rocks it corresponds to the coalescence of clusters of damage to form a failure surface.

In geotechnical engineering, propagation of localised shear deformation zones of finite thickness is controlled by the softening behaviour of the material inside the band (El Bied et al., 2002). Shear bands often appear naturally when a rock is loaded beyond its ultimate strength. They appear as zones of localised intense damage, and are often misinterpreted as being weaker than the surrounding rock. However, what is often the case is that it is the geometry of the system and the loading conditions which result in increased likelihood of fracture that give rise to these zones of localised damage.

5.2.3 The Finite Difference Grid Specification

The first stage in the construction of a 2-dimensional *FLAC* model is the discretisation of the problem by the construction of finite difference grid. The grid or mesh is organized in a row and column fashion. The size of the grid is specified by the number of zones, i , required in the horizontal (x) direction and the number of zones, j , required in the vertical (y) direction. Each zone is identified by a pair of i,j coordinates. The vertices of the zones meet at grid points which are called nodes. Also each node is also identified by a pair of i,j coordinates. The grid is sized and distorted to model the physical situation by mapping the i,j node coordinates to xy space which represents the dimensions of the real environment. This mapping process allows the *FLAC* grid to be distorted and graded. Finer grids lead to more accurate results as they provide a better representation of high stress and temperature gradients. However as the grid is made finer the number of zones also increases. This dramatically increases the computational time and computer memory requirements. Grading the grid allows a finer grid to be constructed near an area of interest such as an excavation or particular phase, and an increasingly coarse grid with distance from the object of interest. This has the benefit of a finer grid but with a reduced number of zones. A useful equation that can be used to determine the aspect ratio i.e. the ratio between the dimensions of each successive zone is given as Equation 5.1. To retain accuracy the aspect ratios should be kept reasonably close to unity (Itasca 1995).

$$S_n = a_1 \frac{(1 - r^n)}{(1 - r)} \quad (5.1)$$

where S_n = total distance to be graded, r = aspect ratio

a_1 = length of zone 1 n = number of zones

5.2.4 Discretisation

The solid body is divided by the user into a finite difference mesh composed of quadrilateral elements. Internally, *FLAC* subdivides each element into two overlaid sets of constant-strain triangular elements as shown in Figure 5.1.

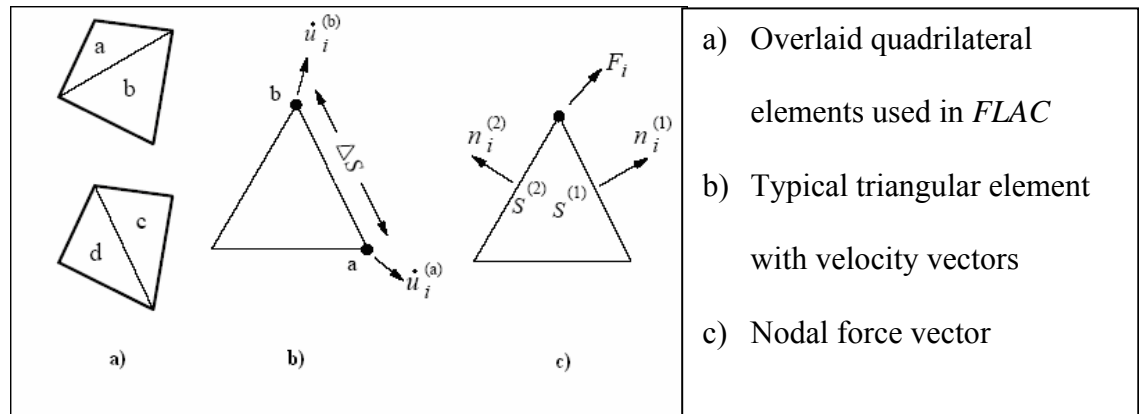


Figure 5.1: Discretisation schematic for *FLAC*

The four triangular sub-elements are termed *a*, *b*, *c* and *d*. The deviatoric stress components of each triangle are maintained independently, requiring sixteen stress components to be stored for each quadrilateral ($4 \times \sigma_{xx}, \sigma_{yy}, \sigma_{zz}, \sigma_{xy}$). The force vector exerted on each node is taken to be the mean of the two force vectors exerted by the two overlaid quadrilaterals. In this way, the response of the composite element is symmetric, for symmetric loading. If one pair of triangles becomes badly distorted (e.g. if one of the triangles becomes much smaller than the area of its companion) then the corresponding quadrilateral is not used; only nodal forces from the other (more-reasonably-shaped) quadrilateral are used. If both overlaid sets of triangles are badly distorted, *FLAC* reports an error message (after Itasca Codes, 1996).

5.2.5 *FLAC* Constitutive Models

Nine standard constitutive models are provided in *FLAC* version 4.0 (Itasca 1995) and these can be arranged into null, elastic and plastic model groups (Itasca 1995). Constitutive models and material properties can be assigned individually to every zone within a *FLAC* model.

5.2.5.1 Null Model

A null material model is used to represent material that is removed or excavated. This region will have no material properties defined, and is treated as free space.

5.2.5.2 Elastic Isotropic Model

This is the simplest *FLAC* constitutive model and represents the material as a linear elastic isotropic medium with infinite strength. This model is valid for homogeneous, isotropic, continuous material that exhibit linear stress strain behaviour with no hysteresis on unloading. To characterise the elastic material *FLAC* requires as input parameters the Bulk (K) and Shear (G) moduli of the material. These moduli are calculated from the Young's modulus (E) and Poisson Ratio (ν) using Equations 5.2 and 5.3.

$$K = \frac{E}{3(1 - 2\nu)} \quad (5.2)$$

$$G = \frac{E}{2(1 + \nu)} \quad (5.3)$$

FLAC can also model the material as an elastic, transversely isotropic medium.

5.2.5.3 Plasticity Models

All *FLAC*'s plasticity models involve the potential to model linear-elastic deformations and permanent, path dependant plastic deformations. Stress strain relations within the plasticity models are as a consequence non-linear. The different plastic models within *FLAC* are characterised by their yield function, hardening or softening functions and flow rule. The yield functions define the stress conditions at which plastic flow takes place. *FLAC*'s plastic models are based on plane strain conditions. The plasticity models can also produce localisation. Localisation is the development of families of discontinuities such as shear bands in material that starts as a continuum (Itasca 1995). Further details on the formation of these shear bands were discussed in section 4.2.

5.2.5.3.1 Mohr-Coulomb Model

This is the conventional model used to represent shear failure in soils and rocks. The yield function for this model corresponds to a Mohr Coulomb Failure Criterion (shear yield function) with a tension cut-off (tensile yield function). The input parameters required by *FLAC* to determine the yield function are the Mohr-Coulomb parameters of material internal friction and cohesion and the tensile strength of the material. At yield *FLAC* calculates the plastic flow within the medium. The flow rule within *FLAC* assumes that the total strain increment may be divided into elastic and plastic parts with only the elastic part contributing to an incremental change in stress which is calculated by means of an elastic law. The Mohr-Coulomb model models the material as an elastic perfectly plastic medium.

5.2.5.3.2 Strain-softening model

This constitutive model is based on the *FLAC* Mohr-Coulomb model as described earlier. However this method takes into account the possibility that the cohesion, friction, dilation and tensile strength may harden or soften after the onset of plastic yield. Within the Mohr-coulomb model these properties are assumed to remain constant. Within the strain-softening model the user can define the cohesion, friction, dilation properties as a piecewise linear softening law dependant on the shear strain increment. The tensile strength can also be prescribed in terms of another hardening parameter measure termed the plastic tensile strain. In order to get the model to behave realistically, strain softening behaviour was specified for all phases involved. This procedure is explained in more detail in section 5.2.7.2.

5.2.6 Simulation of Microwave Heating and Thermally Induced Stresses and Strains

5.2.6.1 Introduction

To simulate the microwave heating, thermally induced damage and its effects on crushing strength, the modelling was undertaken in the 4 main stages given below and more fully described later:

1. Microwave heating of the responsive mineral phase
2. Transient heat conduction during heating process between minerals
3. Development of peak temperatures, and thermal damage due to induced stresses
4. Simulation of a rock strength test on the microwave treated sample to determine strength changes on treatment

5.2.6.2 Modelling of Microwave heating

The amount of thermal energy deposited into a material due to microwave heating (power absorption density) is dependent on the internal electric field strength within the mineral, frequency of the applied microwave radiation, and the dielectric constant and loss factor of the material. If the electric field strength is known the power absorption density per unit volume of the mineral can be approximated from Equation 5.4.

$$Pd = 2\pi f \varepsilon_0 \varepsilon_r'' E_0^2 \quad (5.4)$$

where:

Pd is the power density (W/m^3)

f is the frequency of the microwave radiation (Hz)

ε_0 is the permittivity of free space ($8.854 \times 10^{-12} \text{ F/m}$)

ε_r'' is the dielectric loss factor of the mineral

E_0 is the magnitude of the electric field of microwave energy inside the material (V/m).

Due to natural rock having differing dielectric properties, the electric field and hence the power density within the grains is difficult to estimate and impossible to determine by direct measurement. To address these issues in this modelling work the power density has been approximated to application of heat energy per unit volume. It is appreciated that this is a simplistic approach, and that naturally occurring variability will arise within the material due to differences in packing density, composition, and effects such as thermal runaway and penetration. It is therefore necessary to assume that the heated phase (pyrite) is evenly heated by the incoming microwave radiation. When the penetration depth of the material in question is considered as in section 3.4.2 then the validity of such an assumption can be verified.

5.2.6.3 Modelling of Transient Heat Conduction

FLAC also allows simulation of transient heat conduction in materials and the development of thermally induced displacements and stresses. It features the following options:

1. There are three material models for the thermal behaviour of the material – isotropic conduction, anisotropic conduction and a temperature dependent conductivity model
2. Different zones may have different models and properties.
3. Any of the mechanical models may be used with any of the thermal models.
4. Several different thermal boundary conditions may be prescribed.
5. Heat sources may be inserted into the material either as line sources or as volume sources. These sources may be made to decay exponentially with time.
6. Both explicit and implicit solution algorithms are available.
7. The thermal option provides for one-way coupling to the mechanical stress and pore pressure calculations through the thermal expansion coefficients.
8. Temperatures can be accessed via *FISH*, allowing users to define temperature dependent properties.

In *FLAC* the differential expression of the energy balance has the form:-

$$-q_{i,i} + q_v = \frac{\partial \zeta T}{\partial t} \quad (\text{Equation 5.5})$$

where q_i is the heat-flux vector in (W/m³), q_v is the volumetric heat-source intensity in (W/m³) and this is said to equate to the power density within the material, and ζT is the heat stored per unit volume in (J/m³).

In general, temperature changes may be caused by changes in energy storage and volumetric strain, %, and the thermal constitutive law relating those parameters may be expressed as:

$$\frac{\partial T}{\partial t} = M_T \left(\frac{\partial \zeta T}{\partial t} - \beta_v \frac{\partial \varepsilon}{\partial t} \right) \quad (\text{Equation 5.6})$$

where M_T and β_v are material constants, and T is temperature.

FLAC considers a particular case of this law for which $\beta_v = 0$ and $M_T = \frac{1}{\rho C_v}$.

ρ is the mass density of the medium in (kg/m³), and C_v is the specific heat at constant volume in (J/kg °C). The hypothesis here is that strain changes play a negligible role in influencing the temperature - a valid assumption for quasi-static mechanical problems involving solids. Accordingly, we may write:

$$\frac{\partial \zeta T}{\partial t} = \rho C_v \frac{\partial T}{\partial t} \quad (\text{Equation 5.7})$$

Substitution of Equation 5.5 in Equation 5.7 yields the energy-balance equation

$$-q_{i,i} + q_v = \rho C_v \frac{\partial T}{\partial t} \quad (\text{Equation 5.8})$$

Note that for nearly all solids and liquids, the specific heats at constant pressure and at constant volume are essentially equal; consequently, C_v and C_p can be used interchangeably.

The basic concept in the thermal conduction modelling was that a thermal energy flux might occur between a zone and its four immediately adjacent zones. The direction, i.e. into or out of the zone, and the magnitude of the thermal energy flux was dependent on the temperature gradient that existed between the zones and the conductivity of the zone.

The basic law which was used to determine the thermal energy flow between the zones was Fourier's law, which is given as Equation 5.9.

$$\underline{q} = k\underline{T}_{diff} \quad (\text{Equation 5.9})$$

Where \underline{q} is the heat flux vector in J/s.m

k is the thermal conductivity tensor in W/m.°C

\underline{T}_{diff} is the temperature difference vector (°C)

The rate of change of thermal energy within a zone, Q , can be determined by multiplying the volume of the zone by the change in the amount of heat flux entering the zone as in Equation 5.10. For the finite difference modelling it was easier to apply a divergence theorem, which related the volume integral of the divergence of the heat flux to the flux entering that volume (Equation 5.11).

$$Q = \int_v \text{div}(\underline{q}) dv \quad (\text{Equation 5.10})$$

$$\text{And} \quad \int_v \text{div}(\underline{q}) dv = \int_s \underline{q} \cdot \underline{ds} \quad (\underline{ds} = ds \underline{n}) \quad (\text{Equation 5.11})$$

Where Q = rate of change of thermal energy (J/s)

s = surface of the zone (m)

v = volume of the zone (m)

ds = surface increment (m)

dv = volume increment (m)

\underline{n} = unit normal vector to the surface (m)

Expressing this in an explicit finite difference form for a square zone i,j , side length l gives Equation 5.12:

$$Q_{(i,j)} = k_{(i,j)}l[(T_{(i,j)} - T_{(i,j-1)}) + (T_{(i,j)} - T_{(i,j+1)}) + (T_{(i,j)} - T_{(i+1,j)}) + (T_{(i,j)} - T_{(i-1,j)})]$$

(Equation 5.12)

where $k_{(i,j)}$ is the thermal conductivity of zone (i, j)

l is the length of the sides of the zones

$T_{(i,j)}$ is the temperature of zone (i, j)

Thus the change in stored energy per time increment, Δt , is given by Equation 5.13:

$$\Delta\beta = \Delta t Q$$

(Equation 5.13)

where $\Delta\beta$ is the change in stored energy (J)

Again expressing this in an explicit finite difference form for a square zone i,j , side length l (Equation 5.14).

$$\Delta\beta_{(i,j)} = \Delta t k_{(i,j)} l \left[(T_{(i,j)} - T_{(i,j-1)}) + (T_{(i,j)} - T_{(i,j+1)}) + (T_{(i,j)} - T_{(i+1,j)}) + (T_{(i,j)} - T_{(i-1,j)}) \right] \quad (\text{Equation 5.14})$$

where Δt is the time increment in seconds

The relationship between thermal energy in joules and temperature in °K for a given time increment, Δt , is given by Equation 5.15:

$$\Delta T_{(i,j)} = \frac{\Delta\beta_{(i,j)}}{m_{(i,j)} C_{(i,j)}} \quad (\text{Equation 5.15})$$

where $\Delta T_{(i,j)}$ = temperature change in zone i,j (°K)

$m_{(i,j)}$ = mass of zone i,j (kg)

$C_{(i,j)}$ = specific heat of zone i,j (J/kg.K)

Thus at the end of each time increment the new temperatures of each zone due to thermal conduction and microwave heating are determined using Equation 5.16.

$$\Delta T_{(i,j)}(1) = 283K \quad T_{(i,j)}(n+1) = T_{(i,j)}(n) + \Delta T_{(i,j)} + Pd_{(i,j)} / C_{(i,j)} \Delta t \quad (\text{Equation 5.16})$$

where $T_{(i,j)}(n)$ is the temperature of zone (i,j) at time increment n

$Pd(i,j)$ is the power density of zone (i,j)

The microwave heating and thermal conduction for a specified heating time, ht , was simulated by iterating Equations 5.13, 5.14, 5.15 and 5.16 until Equation 5.17 was satisfied.

$$ht = n\Delta t \quad (\text{Equation 5.17})$$

where: n is the time increment number

Δt is the time increment in seconds

ht is the heating time in seconds

The time increment, Δt , is restricted to ensure numerical stability. This stable time increment also has a physical meaning being the characteristic time needed for the thermal diffusion front to propagate through a zone.

5.2.6.4 Thermally Generated Stresses and Strains

At the end of the heating interval, the thermally induced volumetric strains within a zone, assuming perfect restraint by the surrounding zones and isotropic expansion, is given by Equation 5.18.

$$\varepsilon_{(i,j)} = -\alpha_{(i,j)} (T_{n(i,j)} - T_{1(i,j)}) \quad (\text{Equation 5.18})$$

where $\varepsilon_{(i,j)}$ is the strain in zone i,j

$\alpha_{(i,j)}$ is the thermal expansion coefficient ($1/^{\circ}\text{K}$) of zone i,j

$T_{n(i,j)}$ is the final temperature of zone i,j

$T_{1(i,j)}$ is the initial temperature of zone i,j

5.2.7 Mechanical Modelling

5.2.7.1 Mechanical Constitutive Modelling

The mechanical behaviour of the simulated ore was described using a constitutive model of the material. It is the constitutive model that simulates the material response such as elastic and plastic strains and the development of shear planes and strain softening to the thermally generated strain and the stress within the material. Many different constitutive models have been developed to characterise the mechanical behaviour of different rock types. In general, rocks behave as a brittle material that deform elastically until a critical stress condition is met, thereupon progressive microscopic damage of the material leads to plastic deformation and an observable strain softening. As stated, initially below a limiting stress condition the material can be modelled as a linearly elastic medium. In the elastic state the calculated thermally induced stress within a zone can be determined using Hoek's law for isotropic elastic behaviour (Duncan, 1981).

$$\sigma_{(i,j)} = \frac{\varepsilon_{(i,j)} E_{(i,j)}}{(1 - 2\nu_{(i,j)})} \quad (\text{Equation 5.19})$$

Where $\sigma_{(i,j)}$ isotropic thermally induced stress in zone i,j assuming perfect restraintment

$E_{(i,j)}$ = Young's Modulus of zone i,j

$\nu_{(i,j)}$ = Poisson's Ratio of zone i,j , (0.25 assigned for each phase)

Deformation ceases to be purely elastic after a critical stress condition is obtained. This critical stress condition is known as the yield point and can be determined by a failure criterion expressed in terms of the stress invariants (principal stress magnitudes) or a criterion expressed in terms of the resolved normal and shear stresses and tensile stress acting on or across a potential plane of failure.

The most popular criterion for rock materials and the one adopted for this exercise was the Mohr-Coulomb criterion, which relates the shear strength of the material using the material parameters friction and cohesion to the shear stress (Equation 5.20). The sample may also fail in tension once the tensile strength of the sample has been obtained. To detect whether tensile failure may occur a tensile cut off is incorporated into the yield criterion.

$$\tau = \sigma_n \tan \phi + C \quad (\text{Equation 5.20})$$

Where τ = shear stress (N/m²)

σ_n = normal stress (N/m²)

ϕ = friction angle

C = cohesion (N/m²)

5.2.7.2 Strain Softening

At yield the material was simulated as behaving plastically due to the assumption that the brittle nature of the minerals generated progressive damage of the material leading to a reduction in strength until a fully developed fracture plane developed. This process is known as strain softening, as the reduction in strength is a function of the accumulated plastic strain. The tensile strength was deemed to fall to 0.1MPa after 0.1% strain and cohesion was specified to fall to 2.5MPa after 1%. Although *FLAC* simulated the material as a continuum, the localisation of the strain into distinctive bands during strain softening allowed the continuum model to simulate the progressive fracture development of the material. In *FLAC*, shear hardening and softening are simulated by making Mohr-Coulomb properties (cohesion and friction, along with dilation) functions of plastic strain. These functions are included in the strain-softening

models. Softening parameters must be calibrated for each specific analysis and zone size, with values that are generally back-calculated from results of laboratory triaxial tests. This is usually an iterative process. Due to the lack of specificity in the model used in this study, it was deemed impossible to conduct this back-calculation, as no known material has similar properties to the one which is being modelled. This may seem like an evasive tactic, in that a model has been chosen to represent the simplest possible case in order to represent the simplest mechanisms, which does not lend itself to validation. However, concessions like these are necessary whilst modelling data-limited and understanding-limited problems as shown in chapter 4.

5.2.8 Modelling Input Parameters

5.2.8.1 Introduction

This section details the parameters required in the thermal and mechanical constitutive models. Careful consideration of the input parameters was considered of high importance as the validity of the model is dependant on these values. Thermal and mechanical data is often limited for minerals, and it was often necessary to approximate or simplify the behaviour of the materials involved in order to get a useable model. In some cases, further research of the literature on a particular parameter was deemed unnecessary as it would not help in the investigation of the actual mechanisms at work, and actual experimental determination of parameters would prove be excessively time-consuming. Principally, data used by Whittles et al. (2002) was refined, with greater representation of the change in behaviour with temperature. The transparent phase was represented by calcite and the heated phase was represented by pyrite.

5.2.8.2 Density

The calcite density used for the transparent phase was 2712 kg/m^3 (Hearmon, 1979). Therefore any change in volume that occurs will still mean that the density remains below 3000 kg/m^3 . The pyrite density used for the heated phase was 5000 kg/m^3 .

5.2.8.3 Strength Parameters

As the principal objective of the study was to predict the degree of damage and reduction in strength due to microwave heating, accurate representation of these parameters is one of the most important areas for the entire study, especially for the later loading simulations. They are of lesser importance for the heating simulation as the most important thing to note here is the magnitude of the stresses. If the material was even ten times stronger than specified then the magnitude of the stresses would still be similar (except of course for the redistribution of stresses after the strength of that material at that particular point is exceeded). However if a representation of the degree of weakening the sample is undergoing is to be incorporated then the strength behaviour must be represented realistically.

5.2.8.4 Bulk Modulus

The value for bulk modulus for calcite and pyrite were taken from Bass (1995). Elasticity constants for many minerals and glasses were contained in this paper. The bulk modulus (K) was listed as 142.7 GPa for pyrite and 73.3 GPa for calcite. From this it is evident that pyrite can be said to be twice as strong as calcite. Bulk modulus is related to Young's modulus, E , and Poisson's ratio, ν , by Equation 5.2.

5.2.8.5 Shear Modulus

Again the values tabulated by Bass (1995) were used to characterise the shear modulus of the materials involved. The shear modulus (G) was listed as 125.7 GPa for pyrite and 32.0 GPa for calcite. Shear modulus is related to Young's modulus, E , and Poisson's ratio, ν , by Equation 5.3. It is also possible to express E and ν in terms of the bulk and shear moduli.

$$E = \frac{9KG}{3K + G} \quad (\text{Equation 5.21})$$

$$E = \frac{3K - 2G}{2(3K + G)} \quad (\text{Equation 5.22})$$

5.2.8.6 Mohr-Coulomb Strength Criterion Determination

The in-situ strength parameters required within the constitutive models of the rock were determined using an in-house Visual Basic software application. The programme was used to determine the friction and cohesion strength parameters of the rock strata over the range of confining stresses expected to have developed within the model. The failure criterion used within the programme was the Hoek-Brown criterion (Hoek and Brown 1997) with an m value assumed for a crystalline limestone, and a UCS value of 144 MPa which is typical of strong limestone (Hoek and Brown, 1980). The input data required to determine the strength parameters using this criterion include the range of confining stress of between 0 and 15MPa for the friction and cohesion to be averaged over, and an estimate of the unconfined compressive strength.

5.2.8.6.1 Cohesion

Cohesion relates to the internal resistance of individual particles to separate from one another. This was determined as 25 MPa for both materials from the application. This is slightly higher than to be expected for a typical ore of this type in order to give a worst case scenario.

5.2.8.6.2 Tensile Strength

The tensile strength is the maximum stress in uniaxial tension testing which a material will withstand prior to fracture. This was specified as 15 MPa for both materials. This is typical for most hard rock types.

5.2.8.6.3 Friction Angle

The friction angle was calculated to be 54° from the Visual Basic application based on the input parameters.

5.2.8.6.4 Poisson's Ratio

The value of Poisson's ratio was assumed to be 0.25 for both mineral phases (Ji et al., 2002). These values have been determined to be characteristic of hard rock types. In addition, *FLAC* modelling has been found not to be particularly sensitive to changes in Poisson's ratio (Mohammad, 1998).

5.2.9 Thermal-Mechanical Coupling

5.2.9.1 Introduction

This section details how the thermal changes result in the generation of stresses within the model. There follows a certain set of requirements that should be fulfilled before an analysis should be performed.

5.2.9.2 Determination of Characteristic Length

To calculate the stable step used for the numerical solution of thermal conduction, the following dimensionless numbers are useful in the characterisation of transient heat conduction. The stable timestep itself physically represents the time taken for heat to conduct across a single zone.

Characteristic length:

$$L_c = \frac{\text{volume of solid}}{\text{surface area exchanging heat}} \quad (\text{Equation 5.23})$$

In order to calculate this value it must be remembered that the model is in 2-dimensions, and unit depth. If zones are of the order of 1mm;

$$\text{Volume of solid} = (1 \times 10^{-3})^2 = 1 \times 10^{-6} \text{ m}^2$$

$$\text{Surface area conducting heat} = 4 \times 10^{-3} \text{ m}$$

$$L_c = 2.5 \times 10^{-4} \text{ m}$$

$$\text{Thermal Diffusivity: } \kappa = \frac{k}{\rho C_v} \quad (\text{Equation 5.24})$$

Where k is the thermal conductivity

ρ is the density

C_v is the specific heat at constant

Parameter	Pyrite	Calcite
Thermal Conductivity (W/mK)	38	4
Specific Heat Capacity (J/kg.K)	Approximately 500	Approximately 1000
Thermal Expansion Coefficient ($^{\circ}\text{C}^{-1}$)	4×10^{-5}	2×10^{-5}
Density (kg/m^3)	5000	2712

Table 5.1: Summary of parameter values for thermal diffusivity calculation

$$\kappa = \frac{38}{5000 \times 500} = 1.52 \times 10^{-5} \text{ m}^2 \cdot \text{s}^{-1}$$

Characteristic time: $t_c = \frac{L_c^2}{\kappa}$ (Equation 5.25)

$$t_c = \frac{(2.5 \times 10^{-4})^2}{1.52 \times 10^{-5}} = 4.111 \times 10^{-3} \text{ s}$$

5.2.9.3 Coupling the Thermal-Mechanical Models

The thermal solving can be combined with mechanical calculation to perform a thermal-mechanical analysis with *FLAC*. All of the features of the thermal calculation, including transient and steady-state heat transfer and thermal solution by either the explicit or implicit algorithm, were available in a thermal-mechanical calculation. The thermal-mechanical coupling is provided by the influence of temperature change on the volumetric change of a zone (see equation 5.18 – thermally generated strains).

In the *FLAC* modelling software, thermal-mechanical analysis may be performed with any of the built-in mechanical models for plane-strain analysis. Plane-stress analysis can only be performed with the elastic isotropic model and the strain-hardening/softening model. Note that the thermal model is made null automatically for zones that are made null mechanically. However there are cases in which mechanically null zones are required to conduct heat (e.g. if the thermal boundary has to be much further away than the mechanical boundary). In this case, the thermal model can be specified after the mechanically null model has been specified, thus reactivating zones thermally. Although the zones are active, they will not be shown when printing or plotting unless they are given a mechanical model temporarily.

5.2.9.4 Mechanical Timestep Calculation

There are two issues that must be taken into consideration when performing a thermal-mechanical analysis. The first one is concerned with the different time scales associated with the thermal and mechanical processes. Because timesteps correspond to the time needed for information to propagate from one node to the next, their formulation can be used to compare time scales. Typically, the timesteps associated with the mechanical process is of the form:

$$\Delta t_{mech} = \sqrt{\frac{\rho}{K + \frac{4}{3}G}} L_c \quad (\text{Equation 5.26})$$

where K = bulk modulus;

G = shear modulus;

ρ = density; and

L_c = characteristic length

Δt_{mech} represents time taken for stress disturbance to propagate across a single zone.

5.2.9.5 Thermal Timestep Calculation

The ratio of thermal-to-mechanical timestep may be expressed by:

$$\frac{\Delta t_{ther}}{\Delta t_{mech}} = \sqrt{\frac{K + \frac{4}{3}G}{\rho}} \frac{L_c}{\kappa} \quad (\text{Equation 5.27})$$

where κ = is the thermal diffusivity. For non-metals, this property is of the order of $10^{-6} \text{m}^2/\text{s}$, at most. For rock, ρ is of the order of 10^3kg/m^3 , while $K + (4/3)G$ is approximately 10^{10}N/m^2 . Using these orders of magnitude in equation 5.27 it may be observed that the ratio of thermal-to-mechanical time scales is in the order of $10^5 L_c$. This ratio remains very large, even if L_c is in the order of 1mm. In practice, mechanical effects can be assumed to occur instantaneously when compared to diffusion effects; this is also the approach adopted in *FLAC*, where no time is associated with any of the mechanical steps taken in association with the thermal steps. In this study, the ratio of mechanical to thermal steps was kept at the default setting of 10 steps.

The second issue concerns the thermal-mechanical coupling in *FLAC*. This coupling occurs only in one direction; temperature changes cause thermal strains which influence the stresses to occur, while the thermal calculation is unaffected by the mechanical changes taking place. In most modelling situations, the initial mechanical conditions correspond to a state of equilibrium that must first be achieved before the coupled analysis is started. If the medium is elastic and the thermal-mechanical response must be investigated, for instance, at a certain thermal time, a thermal-only calculation may be performed until the desired time. The thermal calculation may then be turned off, and the mechanical system on. Following this, the system may be cycled to mechanical equilibrium before the response is analysed.

For non-linear mechanical models (i.e. where plasticity is involved), the thermal changes must be communicated to the mechanical module at closer time intervals in order to respect path-dependency of the system. Typically, at small, dimensionless thermal time, a certain number of mechanical steps must be taken for each thermal step to allow the system to adjust according to the different time scales involved. At large dimensionless thermal time, if the system approaches thermal equilibrium, several thermal timesteps may be taken without significantly disturbing the mechanical state of the medium. A corresponding numerical simulation may be controlled manually by alternating between thermal-only and mechanical-only. Such a tedious task may be avoided by using the ‘STEP’ or ‘SOLVE’ command while both mechanical and thermal modules are on. By default, one mechanical step will be taken for each thermal step. Here thermal steps are assumed to be so small that one mechanical step is enough to re-equilibrate the system mechanically after each thermal step is taken.

5.2.10 Thermodynamic Properties

5.2.10.1 Introduction

In order to describe the thermo-mechanical response of a system, the specific heat capacity, thermal conductivity and thermal expansion must all be determined. As with most mineral properties, data is sparse. Thermodynamic data is readily available for other engineering materials such as metals and alloys, concrete, glass, ceramics, plastics and composites. The variation in composition with most minerals results in difficulties in obtaining reliable data. There is also the issue of the influence of sample size on the observed parameters. It is often difficult to obtain mineral samples of sufficient purity for testing.

5.2.10.2 Specific Heat Capacity

Knowledge of the specific heat capacity enables the determination of heating rates after application of heat. Different materials will heat at different rates if the same amount of thermal energy is applied. The specific heat capacity of a material is defined as the energy required to raise the temperature of a unit mass of material (usually 1g or 1kg) by one degree Kelvin. It is described by the following relationship.

$$Q = mC_p\Delta T \quad (\text{Equation 5.28})$$

where Q = Energy (J)

m = Mass (kg)

C_p = Specific Heat Capacity (J/kg.K)

ΔT = Temperature change

Rearranging yields:

$$C_p = \frac{Q}{m\Delta T} \quad (\text{Equation 5.29})$$

The specific heat capacity varies with temperature for most solids. Some data for common minerals are detailed overleaf in Table 5.1. This variation can also be described by the following relationship:

$$C_p = a + bT + cT^{-2} \quad (\text{Equation 5.30})$$

where a, b and c are constants.

	Specific Heat Capacity at 298K	Specific Heat Capacity at 500K	Specific Heat Capacity at 1000K	Coeff. of Heat Capacity	Coeff. of Heat Capacity	Coeff. of Heat Capacity
Mineral	C_p (J/kg.K)	C_p (J/kg.K)	C_p (J/kg.K)	a (J/kg.K)	b (J/kg.K ⁻²)	c (J.K/kg)
Calcite	818.7	1051.00	1238.50	1045.16	0.219	-26x10 ⁶
Rutile	688.75	850.75	933.75	916.82	0.038	-21x10 ⁶
Sphalerite	467.63	514.85	557.01	507.69	0.054	-5x10 ⁶
Quartz	740.50	991.17	1167.17	682.83	0.743	-14x10 ⁶
Feldspar	567.23	951.73	1175.83	1857.21	0.418	-45x10 ⁶
Fluorspar	860.90	925.51	1248.33	529.38	0.711	11x10 ⁶
Barytes	436.65	546.39	591.80	606.94	0	-15x10 ⁶
Wolframite	377.46	454.52	527.33	437.04	0.098	-8x10 ⁶
Dolomite	843.32	1015.54	-	843.62	0.436	-12x10 ⁶
Corrundum	772.84	1057.16	1217.16	1151.83	0.102	-36x10 ⁶
Gypsum	579.36	695.23	982.27	408.18	0.574	0
Bauxite	338.21	338.21	-	387.28	0	0
Cassiterite	348.34	450.93	539.34	440.17	0.110	-11x10 ⁶
Hematite	654.81	820.31	641.25	614.23	0.486	-9x10 ⁶
Ilmenite	654.61	774.41	874.01	767.15	0.120	-13x10 ⁶
Chalcopyrite	516.52	597.01	1068.70	-134.38	1.203	0
Pyrite	517.08	600.42	683.83	574.60	0.117	-8x10 ⁶
Pyrrhotite	572.61	827.27	693.18	580.05	0.113	0
Chalcocite	477.00	604.19	529.00	529.01	0	0
Magnetite	654.22	829.91	865.65	394.64	0.871	0
Bornite	487.30	740.42	659.94	413.08	0.291	-1x10 ⁶
Galena	208.95	215.23	234.94	195.54	0.039	0

Table 5.2: Specific Heat Capacity of minerals at various temperatures, and coefficients of heat capacity. Taken from Thermochemical Properties of Inorganic Compounds (Knacke, Kubachewski and Hesselmann, 1991)

5.2.10.3 Thermal Volumetric Expansion Coefficient

The volumetric expansion of a solid is given by:

$$\delta V = \alpha_v V_0 (\theta_2 - \theta_1) \quad (\text{Equation 5.31})$$

where δV = volumetric expansion of the solid (m^3)

α_v = coefficient of volumetric expansion (K^{-1})

V_0 = original volume (m^3)

θ_1 = original temperature ($^{\circ}\text{C}$)

θ_2 = final temperature ($^{\circ}\text{C}$)

It is possible to then define the coefficient of volumetric expansion as:

$$\alpha_v = \frac{\delta V}{V_0 (\theta_2 - \theta_1)} \quad (\text{Equation 5.32})$$

The data given in Clark et al (1996) is in the form of % change in volume. In order to calculate the change in volume, the new volume must first be found.

$$V_n = \left(\frac{V_c}{100} \times V_0 \right) + V_0 \quad (\text{Equation 5.33})$$

where V_n = new volume (m^3)

V_c = % change in volume

V_0 = original volume (m^3)

The change in volume can then be found by subtracting the original volume from the new volume. This can then be substituted into Equation 5.31 to determine the thermal expansion coefficient. Table 5.2 contains data for a range of minerals.

	α_v (K ⁻¹)	α_v (K ⁻¹)	α_v (K ⁻¹)	α_v (K ⁻¹)	α_v (K ⁻¹)	α_v (K ⁻¹)
Mineral	373K	473K	673K	873K	1073K	1273K
Calcite	13.1x10 ⁻⁶	15.8x10 ⁻⁶	20.1x10 ⁻⁶	24.0x10 ⁻⁶	-	-
Rutile	22.7x10 ⁻⁶	24.1x10 ⁻⁶	25.4x10 ⁻⁶	25.8x10 ⁻⁶	26.4x10 ⁻⁶	13.1x10 ⁻⁶
Sphalerite	19.5x10 ⁻⁶	24.4x10 ⁻⁶	23.6x10 ⁻⁶	24.8x10 ⁻⁶	25.5x10 ⁻⁶	13.1x10 ⁻⁶
Quartz	45.0x10 ⁻⁶	43.3x10 ⁻⁶	49.7x10 ⁻⁶	77.9x10 ⁻⁶	56.6x10 ⁻⁶	13.1x10 ⁻⁶
Feldspar	6.1x10 ⁻⁶	8.6x10 ⁻⁶	15.3x10 ⁻⁶	20.4x10 ⁻⁶	24.4x10 ⁻⁶	13.1x10 ⁻⁶
Fluorspar	58.7x10 ⁻⁶	62.2x10 ⁻⁶	-	-	-	-
Barytes	54.2x10 ⁻⁶	56.8x10 ⁻⁶	62.6x10 ⁻⁶	-	13.1x10 ⁻⁶	-
Corrundum	17.8x10 ⁻⁶	19.6x10 ⁻⁶	22.5x10 ⁻⁶	24.1x10 ⁻⁶	24.9x10 ⁻⁶	13.1x10 ⁻⁶
Hematite	25.2x10 ⁻⁶	26.9x10 ⁻⁶	30.9x10 ⁻⁶	-	-	-
Chalcopyrite	52.5x10 ⁻⁶	-	-	-	-	-
Pyrite	27.3x10 ⁻⁶	29.3x10 ⁻⁶	33.9x10 ⁻⁶	-	-	-
Pyrrhotite	66.2x10 ⁻⁶	-	-	-	-	-
Magnetite	26.5x10 ⁻⁶	28.5x10 ⁻⁶	34.9x10 ⁻⁶	39.3x10 ⁻⁶	41.5x10 ⁻⁶	43.4x10 ⁻⁶
Galena	61.2x10 ⁻⁶	61.0x10 ⁻⁶	63.2x10 ⁻⁶	66.8x10 ⁻⁶	-	-

Table 5.3: Variation in volumetric expansion with temperature (Clark et al, 1966)

Fei (1995) used a polynomial expression to fit experimental data for the thermal expansion coefficient over a specific range:

$$\alpha(T) = a_0 + a_1T + a_2T^{-2} \quad (\text{Equation 5.34})$$

where a_0 , a_1 and a_2 (≤ 0) are constants determined by fitting the experimental data.

This approach yields slightly different results to the values by Clark et al. but are sufficiently similar for the purposes of this study. However, specific, accurate behaviour is deemed unnecessary, as it would not only increase model complexity beyond what is possible on a personal computer, but only the simplest model that will allow the important mechanism to be quantified should be designed.

5.2.10.4 Thermal Conductivity

The general equation for heat flow through a slab of material is given by:

$$\frac{Q}{t} = \frac{kA(\theta_2 - \theta_1)}{l} \quad (\text{Equation 5.35})$$

where Q = heat conducted (W)

t = time (s)

A = surface area of slab (m^2)

θ_1 = original temperature ($^{\circ}\text{C}$)

θ_2 = final temperature ($^{\circ}\text{C}$)

l = length of slab (m)

k = thermal conductivity (W/mK)

Rearranging the equation the thermal conductivity, k , is defined as:

$$k = \frac{Ql}{At(\theta_2 - \theta_1)} \quad (\text{Equation 5.36})$$

Thermal conductivity is a constant and is temperature dependent, the S.I. unit is W/mK.

Data for the thermal conductivity of various minerals is contained in Table 5.3.

		Thermal Conductivity (W/m.K)	Thermal Conductivity (W/m.K)	Thermal Conductivity (W/m.K)	Thermal Conductivity (W/m.K)
Mineral		273K	373K	500K	1000K
Calcite	(i)	3.00	-	-	-
	(ii)	4.02	3.01	2.55	-
Rutile	(i)	6.36	-	-	-
	(ii)	12.55			
Sphalerite		26.61	-	-	-
Quartz	(i)	1.07	-	1.39	1.69
	(ii)	11.42	7.94	6.32	-
Feldspar	(i)	2.44	-	-	-
	(ii)	4.18			
Fluorspar	(i)	10.40	-	-	-
	(ii)	10.29	7.99		
Barytes		1.84	1.50	-	-
Gypsum	(i)	0.51	-	-	-
	(ii)	1.29			
Hematite		10.46	-	-	-
Pyrite		37.90	-	-	-
Magnetite		5.27	-	-	-

Table 5.4: Variation of thermal conductivity of minerals with temperature

(i) – Thermal Conductivity of Non-Metallic Solids –

Y.S. Touloukian et al 1970

(ii) - Handbook of Physical Constants, S.P. Clark et al, 1966

Note the discrepancies between the values obtained by the various researchers, especially for quartz. This illustrates why modelling of this kind is likely to be data-limited, and that occasionally only values within a realistic range of values can be selected for incorporation into the model.

5.2.11 Implementation of Thermal Behaviour in *FLAC*

5.2.11.1 Introduction

The *FLAC* graphical user interface, GUI allows for the specification of single values for specific heat capacity, thermal conductivity and thermal expansion. However it was thought that as these values change with temperature then the behaviour should be incorporated into the model. This is possible by writing simple *FLAC* functions to express the behaviour for that particular phase. The methodology behind incorporating specific heat capacity, thermal conductivity and thermal expansion behaviour for the heated and unheated phases is described in the following section.

5.2.11.2 Specific Heat Capacity

The specific heat capacity behaviour is governed by an equation of the form shown in Equation 5.30. However, if this equation is expressed in *FLAC* to describe the transparent phase behaviour then the model run becomes prohibitively lengthy. This would involve solving the polynomial for each zone and each step in the run. It was therefore deemed necessary to simplify this behaviour, and for this purpose, two linear portions were fitted to the polynomial curve to lessen the computational load.

Figure 5.2 shows the variation of specific heat capacity with temperature for both pyrite and calcite. It can be said that calcite requires roughly double the energy to raise its temperature to the same degree as pyrite. The two linear portions are applied to the data so that the R^2 values are maximised. It is possible to improve the fit at lower temperatures by adding an extra linear portion but this approximation is deemed sufficient.

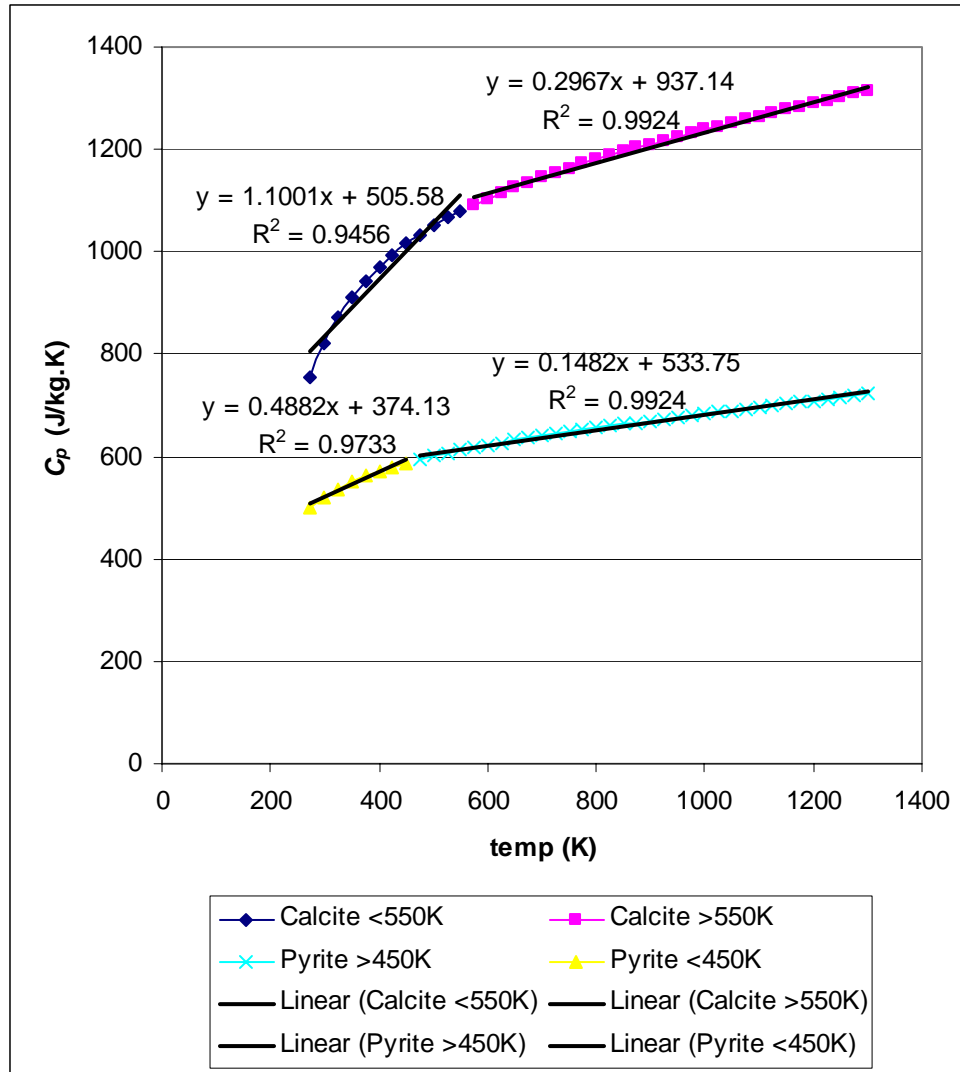


Figure 5.2: Variation of specific heat capacity of calcite and pyrite with temperature and linear fit portions.

A *FISH* function is then derived to describe the behaviour above and below 550K for pyrite and 450K for calcite. This function is shown in Figure 5.3.

```

; for transparent phase, upper portion  (- code beginning with ';' is ignored by the
                                          compiler)

if density(i,j)<3000 and                    (- specifies transparent phase zones)
if (temp(i,j)+273)>550 then                  (- FLAC expresses temperature in °C)
spec_heat(i,j)=(0.2967*(temp(i,j)+273)) + 937.14      (- values from curve fit)
end_if                                          (- closes condition)
end_if

; for transparent phase, lower portion of the curve:


if density(i,j)<3000 and                    (- specifies transparent phase zones)
if (temp(i,j)+273)<550 then                  (- ensures lower curve portion is used)
spec_heat(i,j)= (1.1001*(temp(i,j)+273)) + 505.58 (-equation for lower curve fit)
end_if
end_if

; for heated phase, lower portion

if density(i,j)>4000 and
if (temp(i,j)+273)<450 then
spec_heat(i,j)=(0.4882*(temp(i,j)+273))+374.13
end_if
end_if

; for pyrite, upper portion                    (- process is repeated for heated phase)
if density(i,j)>4000 and
if (temp(i,j)+273)>450 then
spec_heat(i,j)=(0.1482*(temp(i,j)+273))+533.75
end_if

```


Figure 5.3: *FISH* function used to specify specific heat capacity over prescribed ranges

5.2.11.3 Thermal Conductivity

There is very limited data on thermal conductivity and again the values reported by Touloukian (1981) are used. Only 3 values are available for both calcite and pyrite, so again an approximation is used to describe behaviour beyond what is given in the literature. As the highest temperature data was for 500K (227°C). It was decided to extrapolate the data to 0.1W/m.K after 500°C for both calcite and pyrite. This would result in each phase losing heat more slowly at elevated temperatures than would be expected in reality. However, the intention is that elevated temperatures are not examined in too much depth as this would involve the incorporation of complex phase changes or the alteration of surface chemistry. Also, as it is the conductivity of the calcite that surrounds the pyrite that governs the rate of heat lost from the pyrite, and the calcite thermal conductivity is far lower and more constant than pyrite's thermal conductivity, it is said that this effect is negligible.

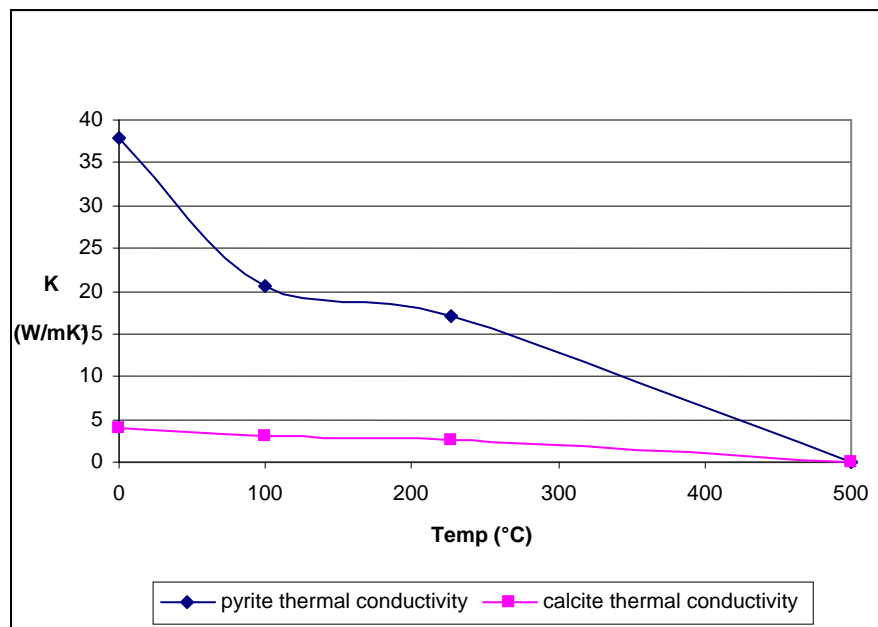


Figure 5.4: Variation of thermal conductivity with temperature

Figure 5.5 details the *FISH* function used to describe the thermal conductivity of the specific phases. The procedure is very similar to that described in Figure 5.3.

```

; for transparent phase, linear approximation to curve

if density(i,j)<3000 then                (- specifies calcite zone density)
conductivity(i,j)=((temp(i,j)+273)*(-0.0053)) + 4.02
end_if

if temp(i,j)>485 then                    (- upper limit for data)
conductivity(i,j)=0.1                    (- sets lower limit for conductivity value)
end_if

; for pyrite, linear approximation to curve

if density(i,j)>4000 then
conductivity(i,j)=((temp(i,j)+273)*(-0.07545)) + 37.9
end_if

; upper limit for data

if temp(i,j)>485 then
conductivity(i,j)=0.1
end_if

```

Figure 5.5: *FISH* function used to describe thermal conductivity over expected temperature range

5.2.11.4 Thermal Expansion

Again the data is limited for values of thermal expansion coefficients. Fei (1995) fitted a polynomial function to the available experimental data, and then a linear approximation has been fitted over the narrow range of values to be investigated. As no value was reported for a_2 for pyrite, the curve is reduced to a linear relationship. Figure 5.6 shows that pyrite has a higher expansion coefficient than calcite, and this could result in a greater level of stress in the presence of pyrite as it generates greater expansion per unit of energy absorbed.

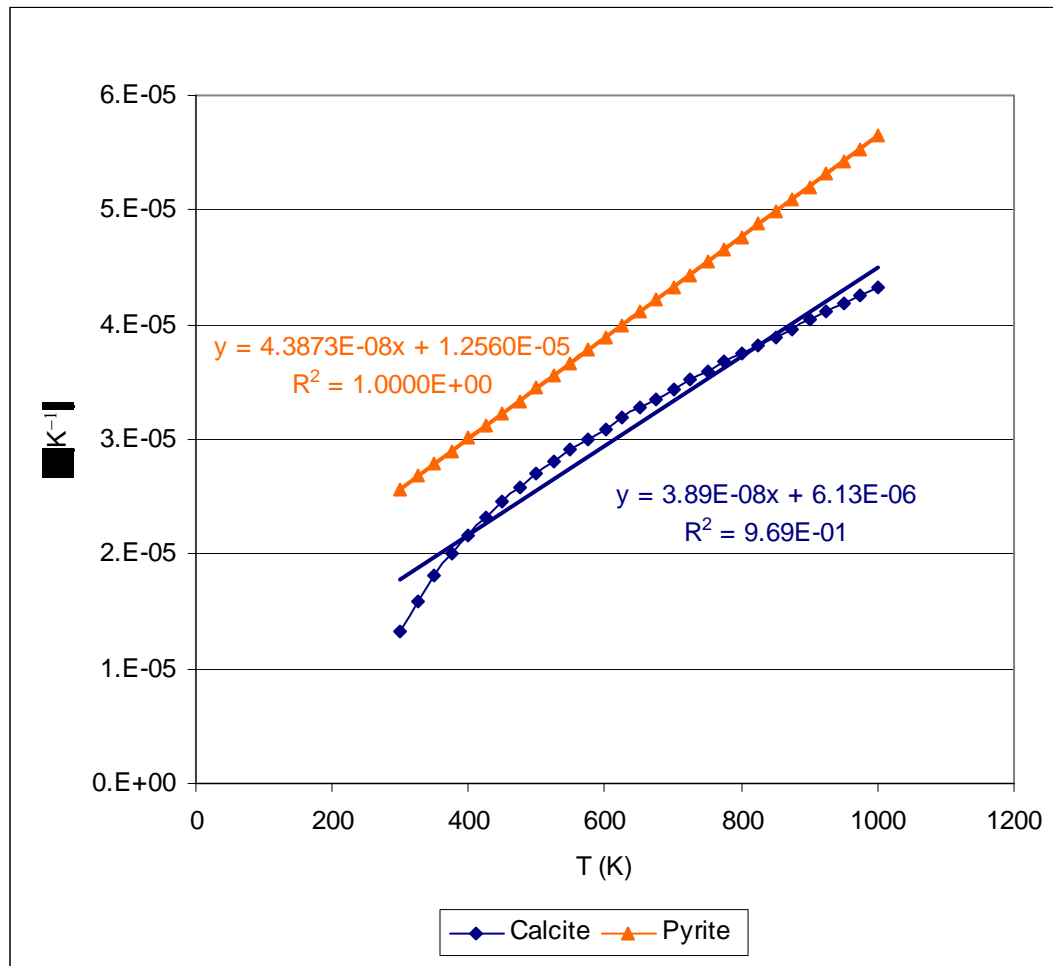


Figure 5.6: Variation of thermal expansion with temperature for calcite and pyrite

The *FISH* function used to describe the variation of thermal expansion with temperature is shown in Figure 5.7. Note the use of exponentials, (e) to describe the power to which ten is raised to. This is how the software reads the code.

```
; for calcite
if density(i,j)<3000 then
thexp(i,j)=((3.89e-8)*(temp(i,j)+273))+(6.13e-6)
end_if

; for pyrite
if density(i,j)>4000 then
thexp(i,j)=((4.3873e-8)*(temp(i,j)+273))+(1.256e-6)
end_if
```

Figure 5.7: *FISH* function used to describe thermal expansion of constituent phases.

5.2.12 Construction of the Ore Model in *FLAC*

5.2.12.1 Introduction

This section details some of the other steps that are required in order to build the model within *FLAC*. This involves the specification of the geometry of the system, the application of distribution of heaters within the model, and the application of heat to these heated phases.

5.2.12.2 Grid Specification

One of the first steps to be undertaken is to specify the grid in terms of the number of zones, and the actual area to be covered. *FLAC* is very efficient in that it can accommodate grids containing many hundreds of thousands of zones, on any scale from millimetres to kilometres. The computation time is governed by the fineness of the grid. The simulation will not run if excessively fine grids are used due to the memory requirements increasing with the square of the sample diameter. Increased fineness of grid leads to greater detail, and a reduction in distortion of stress and temperature fields. Initial models were made to simulate single ‘spherical’ (in effect, circular) particles in a square calcite matrix.

5.2.12.3 Random Distribution of Heated Particles

This was used to give the model a sense of variability analogous to a ‘real’ ore texture. Again a *FISH* function as shown in Figure 5.8 is devised so that pyrite ‘crystals’ (which shall be referred to as heated grains or particles) are disseminated throughout the calcite. The function is derived by asking the software to return 2 random numbers between 0 and 1. These 2 numbers are then multiplied by the number of i and j zones respectively to yield a Cartesian coordinate pair. The function is then run again for a

specified number of ‘loops’, until the required percentage of pyrite is applied to the system. For example: if the sample is 74 zones wide and 148 zones tall, then the total number of zones is 10952. If the sample is to contain 1% pyrite then we need:

$$0.01 \times 10952 = 110 \text{ zones}$$

The function then loops for the specified number of zones to be filled, and specifies the material properties for those zones.

```
* randomly generates pyrite distribution

def RandomPyr                                (- names the function)

loop m (1,110)                                (- loops for specified number of heated particles)
coox = (urand*74)                             (- defines a random number between 1 and 74)
cooy = (urand*148)+28                         (- as above but compensates for bottom platen)

command

group 'User: pyrite' I=37 J=102                (- specifies region as pyrite)
prop density=5000.0 bulk= 1.427e11 shear=1.257e11 group 'User: pyrite'
prop coh=25e6 fric=54.0 dil=0.0 ten=15e6 group 'User: pyrite'
group 'User: pyrite' I= coox J= cooy
prop density=5000.0 bulk= 1.427e11 shear=1.257e11 group 'User: pyrite'
prop coh=25e6 fric=54.0 dil=0.0 ten=15e6 group 'User: pyrite'

end_command

end_loop

end

RandomPyr                                (- executes random pyrite distribution function)
```

Figure 5.8: *FISH* function to describe random heater distribution and its material properties

A limitation of this approach is that no variability can be assigned to the size and shape of the pyrite grains. Also the shape of the pyrite grains is represented as perfect squares. This approach was used as it is relatively simple to apply to many models, and is computationally efficient for a grid of this size. Finer grids are possible for simple heating applications but the loading simulation to determine strength is too computationally intensive to accommodate these finer grids. One possible alternative approach is to again randomly distribute pyrite in the calcite matrix, but instead of occupying a single zone, a coordinate centre and a randomly selected radius could be specified for a range of pyrite grain sizes. This has not yet been implemented as was foreseen that no further insights would be obtained into the basic mechanisms.

5.2.12.4 Power Density Specification

Power density was defined in chapter 2 and expressed by Equation 2.7. The power density values applied to the heated particles to simulate microwave heating ranged from 1×10^7 to 1×10^{15} W/m³. Exact determination of the power density values in a real situation is impossible, as the maxima occur inside the absorbent material or near its edges. As the dielectric properties of each phase reported in the literature varies from author to author, and electric field strength depends on many transient variables, it was decided for the main body of the study to use the same power density throughout the heated material. This simplification will allow the effects of the following to be ignored:

- o The frequency of the radiation results in a rapidly fluctuating power density that at 2.45GHz completes a cycle every $1/2.45 \times 10^9 = 0.4$ nanoseconds. Therefore the power density reaches a maximum value at each cycle. This is usually ignored and

a time-averaged value is used due to the length of the cycle being so small compared to the residence time.

- o In a real cavity, the power density will vary throughout the sample due to distance from the point where the radiation is incident and differences arising from compositional differences along the line of incidence towards the interior of the sample. It is possible to determine this penetration depth using the relationship described in section 2.5. Here the grain sizes are too small to significantly affect penetration depth.
- o Compositional differences within each phase would affect the dielectric properties of a particular point in the sample, however there are orders of magnitude difference between the heated and unheated phases' dielectric properties in this case.
- o The geometry of a single mode applicator such as a TM_{010} cavity results in power densities being higher at the point of incidence into the sample. Therefore the positioning of the sample in the cavity would result in a power density differential between the 'front' of the sample and the 'back'. However this is of minor importance here.

In order to achieve temperature dependence, detailed knowledge of the internal electric field strength would be required. However, this property is also dependent on the dielectric properties of the material. If the electric field strength data were available, a table of values would be drawn up to detail the variation of both the dielectric constant and loss factor. A *FLAC* function would then be derived to yield the power density for a particular zone. It is intended that in future, these thermo-mechanical models be intimately coupled with outputs from electromagnetic simulations of microwave

cavities to provide much more accurate representation of real situations. At present, it is possible to generate a power density distribution for a grid of randomly distributed pyrite as follows.

5.2.12.5 Initial Temperature of Sample

The initial temperature of the sample was set to be 10°C in order to represent the temperature in the laboratory, and for ease of use with the code. No attempts were made at verification of the temperature of the actual rock samples in the laboratory.

5.2.12.6 Implementation of Heating Simulation

Once the geometry has been specified, and the distribution of heated particles completed, the model then specifies the power density to be applied to the model. Again a simple *FLAC* function was derived to describe the behaviour and this is shown in Figure 5.9.


```

* applies interior heating source

def source                                (- defines name to be applied to FISH function)

loop i (1,74)                             (- examines i zones from left to right)

loop j (28,175)                           (- examines j zones from bottom to top of sample)

if density(i,j) = 5000.0 then              (- e.g. for pyrite)

command

interior source 1e15 i=i j=j              (- applies power density of  $1 \times 10^{15} \text{ W/m}^3$ )

end_command

end_if

end_loop                                  (- ends loop for i zones)

end_loop                                  (- ends loop for j zones)

end

source                                    (- runs the 'source' FISH function)

; thermal portion

initial temperature 10.0 i 1 75 j 28 175  (- sets sample temperature to 10°C)

model th_isotropic i 1 75 j 28 175        (- applies isotropic conditions throughout)

mod null i=27                             (- reiterates interface conditions)

mod null j=176                             (- reiterates interface conditions)

def trop                                  (- defines name to be applied to FISH function)

```

Figure 5.9: *FISH* function describing power density application to heated zones

The *FLAC* function ‘trop’ is then a summation of all the composite *FLAC* functions to describe the specific heat capacity, thermal expansion, and thermal conductivity. Once the *trop* function has been compiled there remains a few conditions that require finalising and these are shown in Figure 5.10.

end_loop	<i>(- ends loop for i zones)</i>
end_loop	<i>(- ends loop for i zones)</i>
command	
step 1000	<i>(- sets model to run for 1000 steps)</i>
end_command	
end	
set thdt=0.0000000010	<i>(- sets thermal timestep as 1 nanosecond to set total heating time to 1ms)</i>
trop	<i>(- compiles and executes ‘trop’ FISH function)</i>

Figure 5.10: *FISH* closing statements for ‘trop’ function

5.3 Practical Use of the *FLAC* Software

5.3.1 Introduction

This section details the practical use of the *FLAC* software, and illustrates how it is possible to obtain detailed information on the variation of the stresses and strains from the various graphical outputs. These output types are detailed in this section.

Once the model has completed a simulation, the task of interpreting the data is carried out by calling the various graphical outputs that are possible. The Graphical User Interface (GUI) can immediately show contour, index, and where applicable, vector plots of the following parameters: temperature, shear strain increment, compressive stress, displacement, velocity and plasticity. These are the main output plot types used in this study. There are variations on some of the stress output plots and these are explained in detail in this section.

5.3.2 Miscellaneous Model Output Plot Types

Figure 5.11 shows a model of a 2mm diameter calcite particle with a 500 μ m diameter pyrite particle within. Each zone is 12.5 μ m across. This is the default screen for the software. This screen is showing marked grid points, and indicated an 'x' where a node marks a particular region. Note the edges of the sample. The plot is also showing the applied boundary conditions in yellow, and these indicate the application of heat to the pyrite heated phase in this instance.

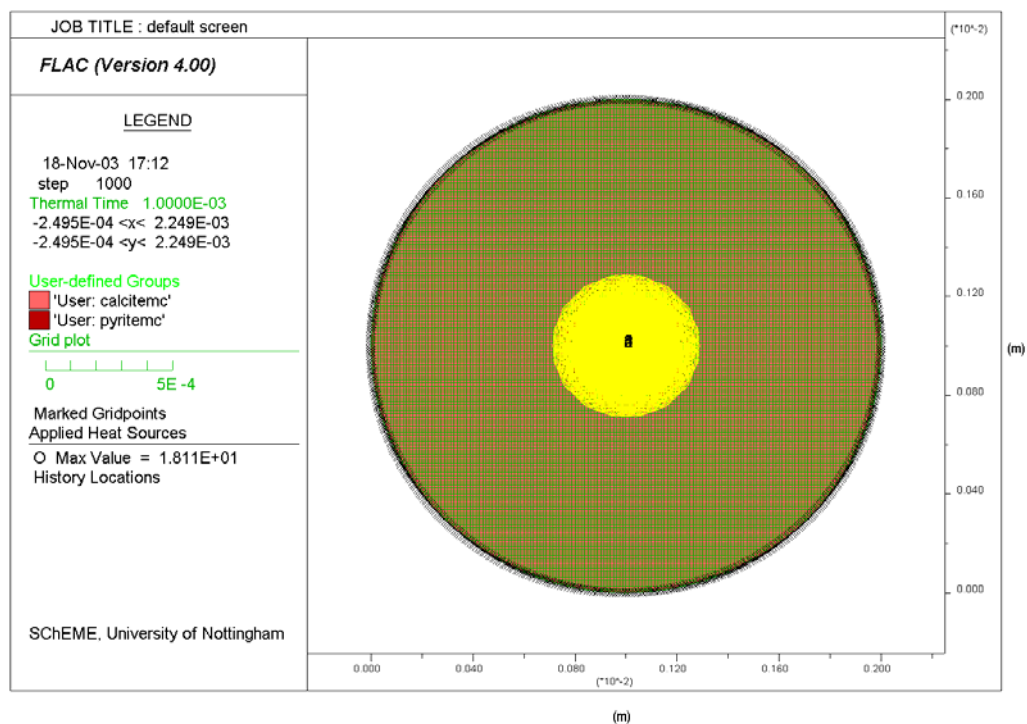


Figure 5.11: Default plot in *FLAC*, showing regions, marked grid points, applied boundary conditions.

In Figure 5.12 below the software has effectively zoomed in to show the boundary between heated pyrite in darker red and transparent calcite in pink. The applied boundary conditions to each pyrite zone (yellow circles) are also shown. Note the automatic grid deformation where required at the edges of the circular heated particle.

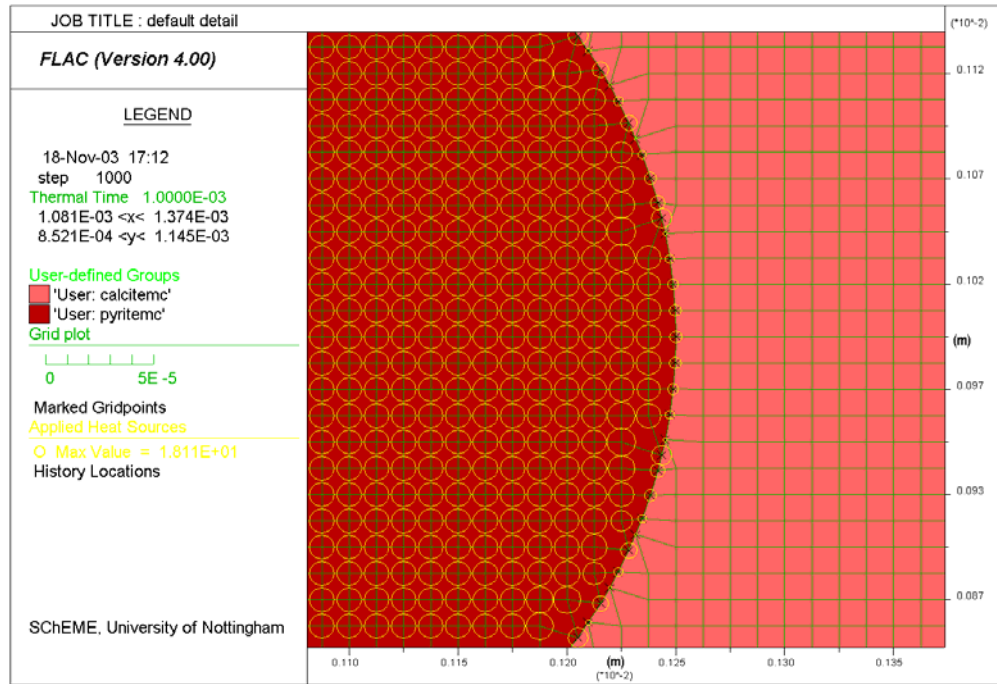


Figure 5.12: Detail of previous figure showing heated phase in dark red and transparent phase in pink, with yellow circles denoting the applied heat

Figure 5.13 shows the type of model used for the simulation, whether it be elastic, Mohr-Coulomb or strain softening. In the early stages of the study, perfectly elastic models were used. Complexity was then increased to incorporate a Mohr-Coulomb regime. Finally a strain-softening model was used to represent a measure of weakening into the sample. For the loading simulation, which is discussed in detail later, the steel platens were specified as elastic. Steel is much stronger and less stiff than rock so this assumption was thought valid. In this case the entire model is in shear softening mode, as denoted by ‘ss’ in the left side of the screen. Other model types would be denoted by a different colour.

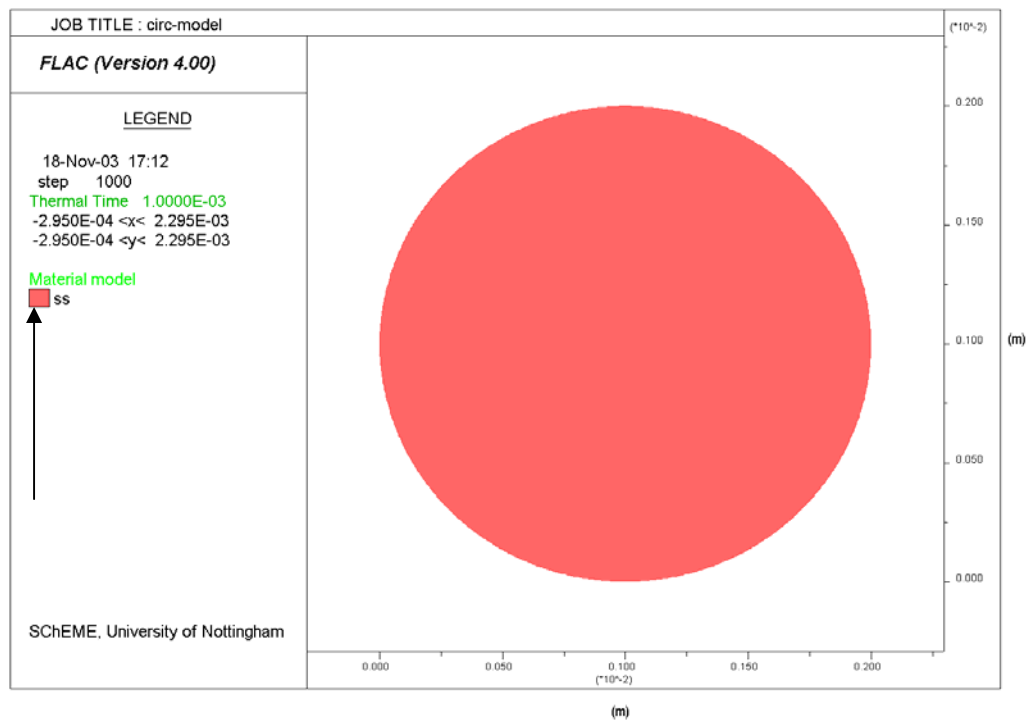


Figure 5.13: Plot showing model type, denoted by ‘ss’ on left side of plot.

Figure 5.14 shows the boundaries of any region in the model, such as circular pyrite grains or any boundaries of particular phases within the sample. Any regions that have been specified geometrically will have a separate colour applied to the area in this type of plot.

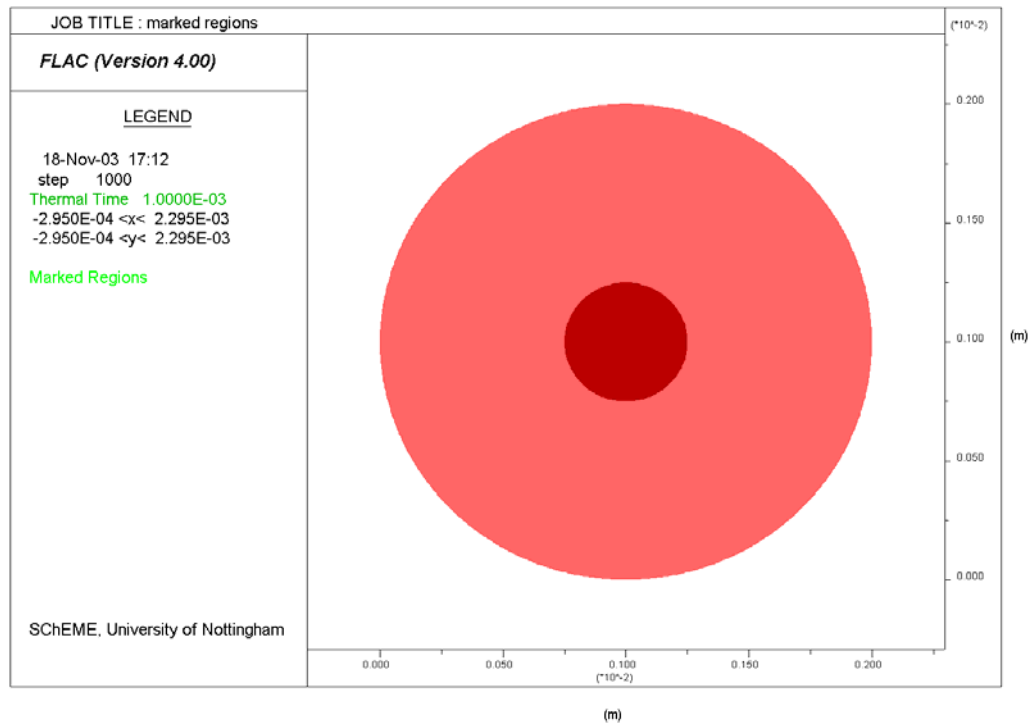


Figure 5.14: Marked regions – detailing geometry of calcite and pyrite regions

Figure 5.15 shows the constituent phases in the sample in various colours. Pyrite and calcite are shown as two different colours. Again, any other materials introduced into the model will have a separate colour.

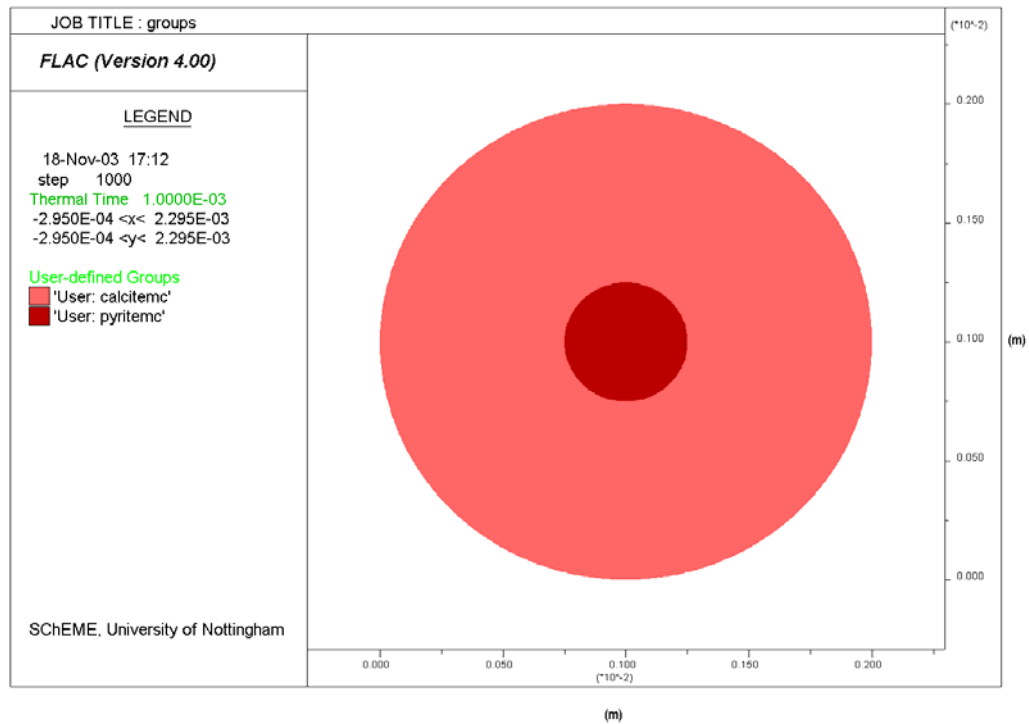


Figure 5.15: Plot showing material groups. The plot is identical to the previous figure due to marked regions matching the groups' geometry in this case.

Figure 5.16 shows the plasticity indicators, which show the state of the material at that particular point in terms of whether it has exceeded its strength criterion to denote fracture. The categories are as follows and are denoted by small crosses, asterisks or circles.

- o Elastic, not reached yield (no indicator – blank space)
- o At yield in shear or vol. (red/pink asterisk - *)
- o Elastic, at yield in past (large green X)
- o At yield in tension (small purple circle – o)

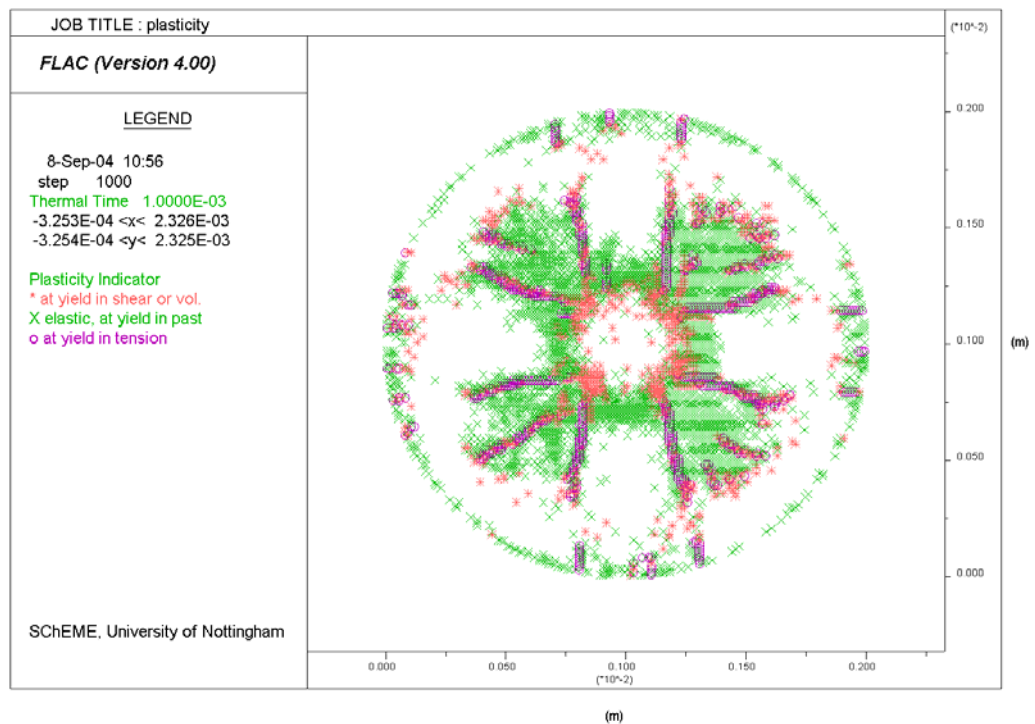


Figure 5.16: Plasticity plot showing tensile cracks, past yield regions and current shear zones

The state function shown in Figure 5.17 fulfils essentially the same purpose as the plasticity indicators but the state of the material is shown in colour. The available states are as follows:-

- o Elastic (salmon pink)
- o At yield in shear or vol. (dark red)
- o Elastic, at yield in past (purple)
- o At yield in tension (yellow)

The yellow lines are interpreted as tensile cracks. The level of strain in these regions has resulted in the tensile strength of the material being reduced. This particular sample has been exposed to $1 \times 10^{11} \text{ W/m}^3$ for 1 ms. For this particular section, the power density and exposure time applied result in high damage so that the damage incurred can be seen clearly.

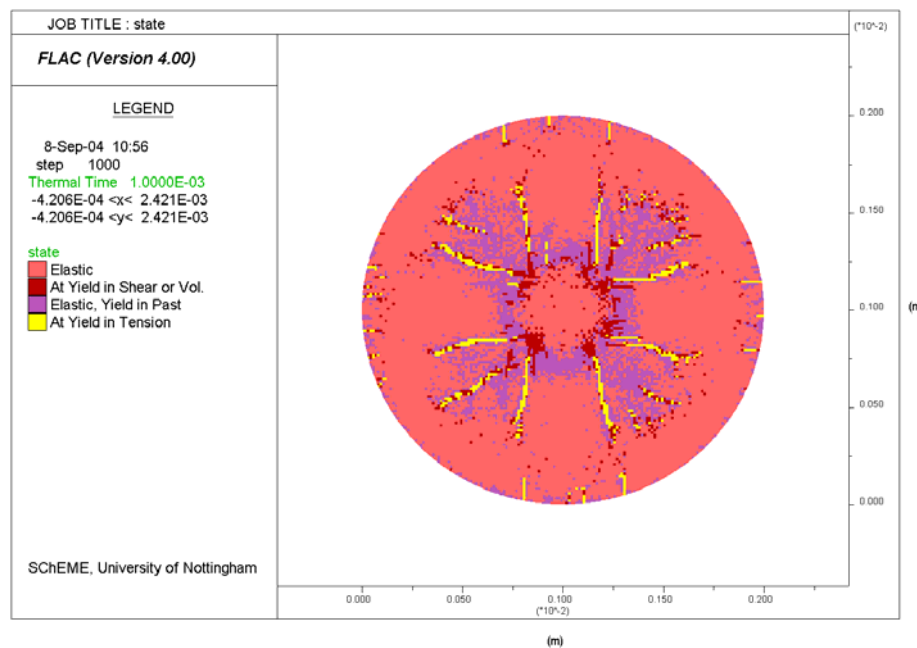


Figure 5.17: State plot showing tensile cracks forming radially outwards, past yield regions and current shear zones

5.3.3 Vector Output Plots

Vector plots show any parameter that has both magnitude and direction. Hence the following plots showing displacements and velocities. As the central heated particle is expanding, the directions of the vectors in this case are pointing towards the nearest edge of the circle. It is difficult to observe Figure 5.18 in this case that the vectors of highest magnitude are outside the heated particle boundary. The maximum vector magnitude is $0.37\mu\text{m}$ in this case.

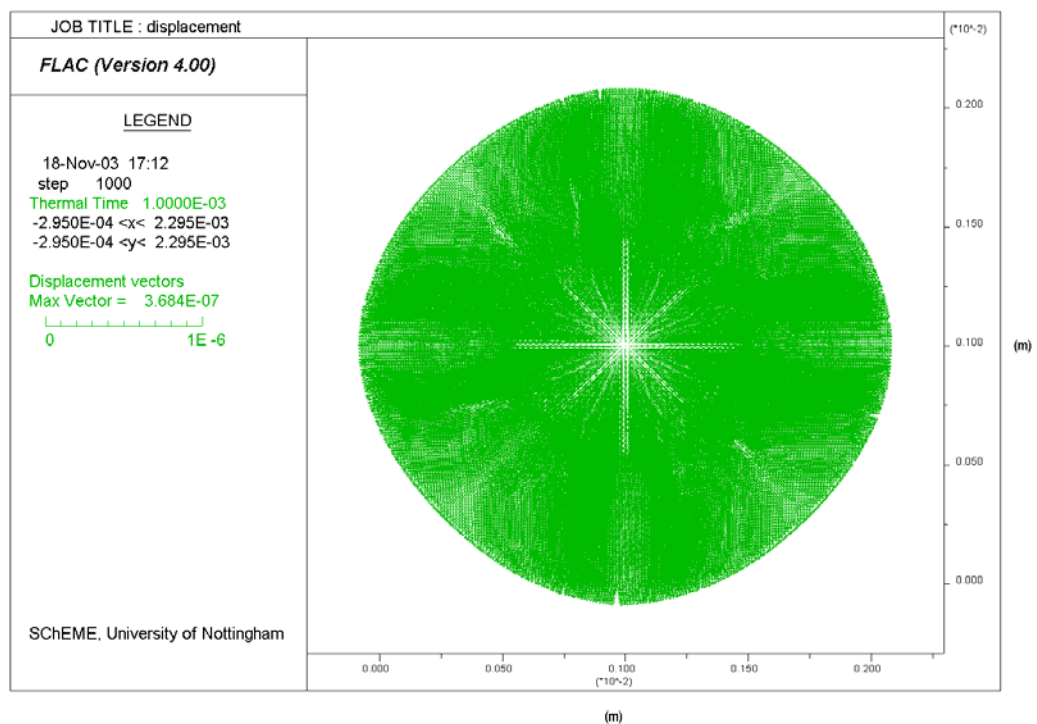


Figure 5.18: Plot showing displacements in the model.

The software was used to zoom in on the previous figure to yield Figure 5.19. Note the zero magnitude vector at the central zone where there is effectively empty space. The expansion vector magnitude appears to be cumulative with the portions of the heated particle experiencing gradually greater displacement as the heated particle boundary is approached.

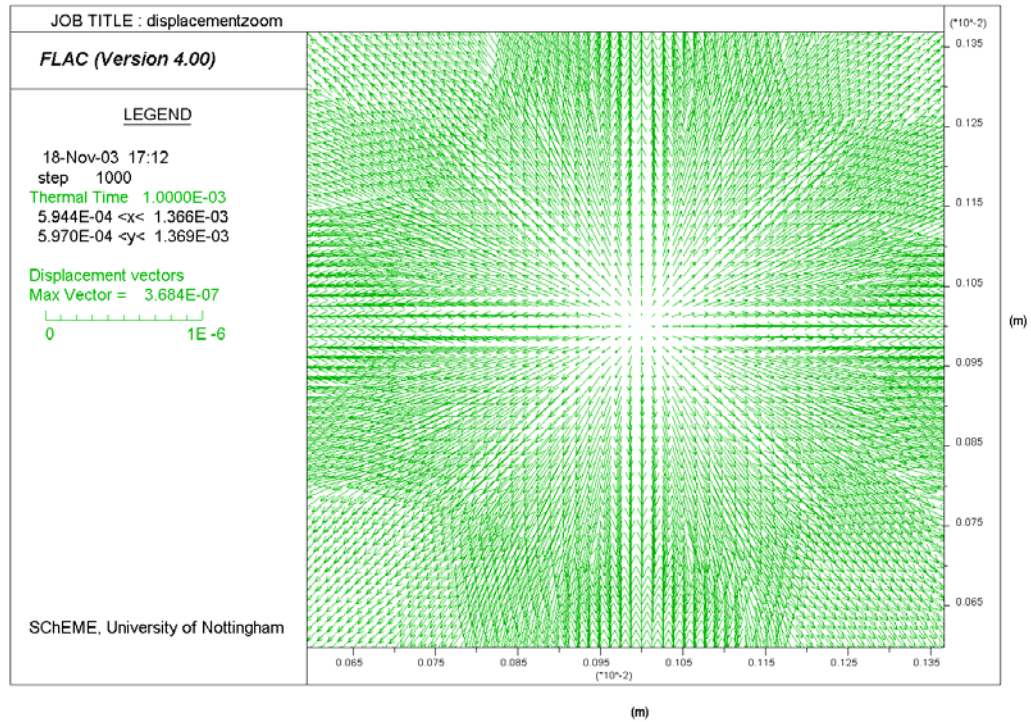


Figure 5.19: Detail of pyrite boundary, and zero vectors in centre.

Figure 5.20 shows the velocity of all points within the medium. Again most of the vectors are directed towards the nearest edge of the transparent particle. Note the distortion around ‘tensile cracks’, which correspond well to Figure 5.17.

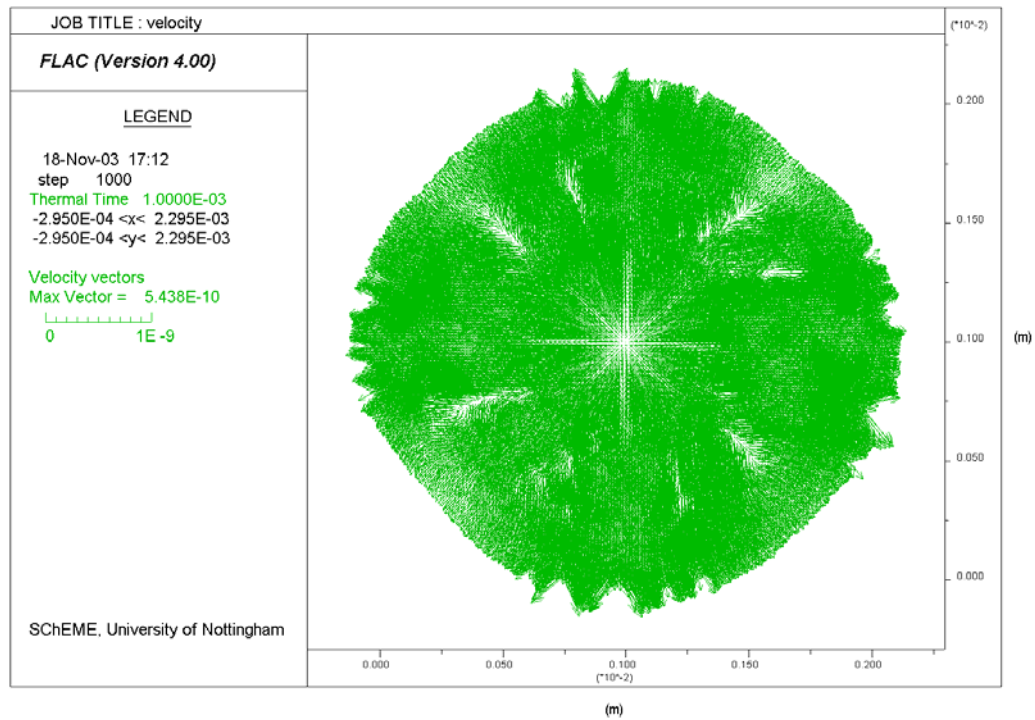


Figure 5.20: Velocity vectors showing distortion around areas where shear has occurred.

The following plot contains evidence of the tensile nature of fracture as well as shear.

There is a difference in stress regimes on either side of crack.

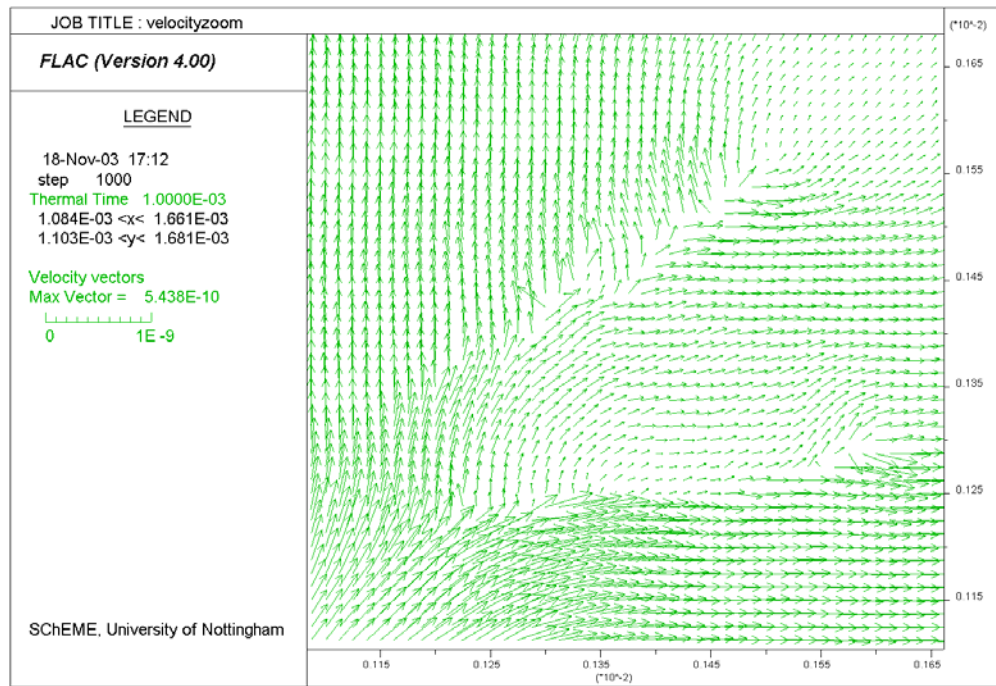


Figure 5.21: Detail of ‘crack’ above right from centre of Figure 5.20

5.3.4 Contour Output Plots

The following plots show the various contour plots that are possible, in order to show the variation of temperature and stress with position. Figure 5.22 shows the temperature distribution in the sample, with the highest temperature of 45°C to be found in the centre of the heated phase. The temperature then falls rapidly outside the grain boundary and then tails off gradually towards the edge of the sample.

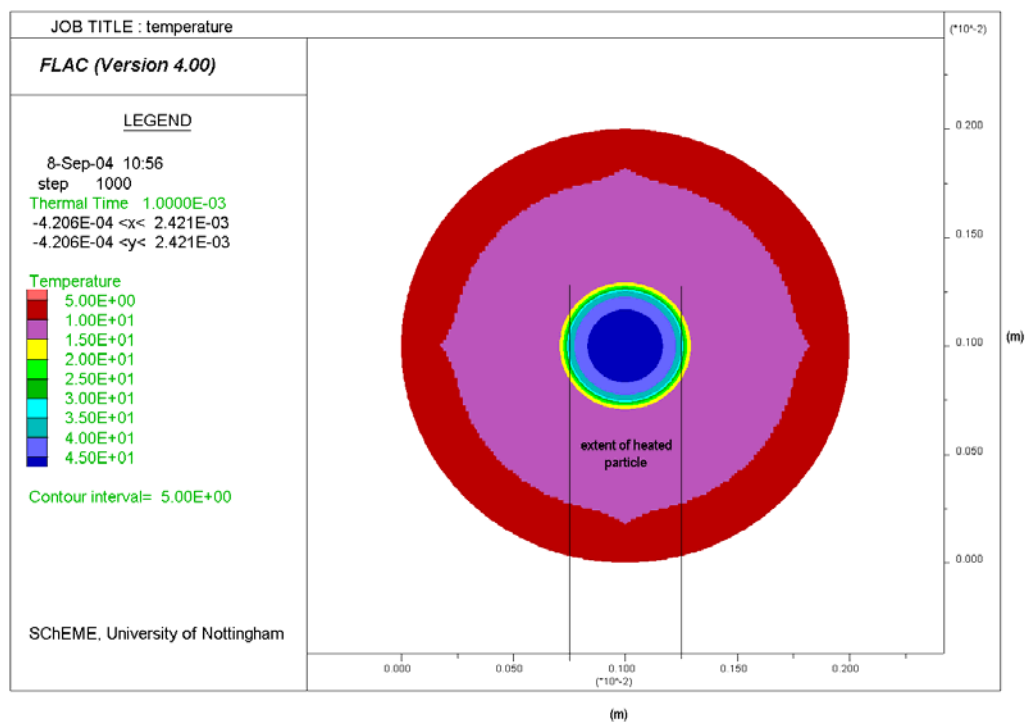


Figure 5.22: Temperature contours in the sample.

In Figure 5.23 the compressive stress in the horizontal direction is shown, and the stresses are highest in the centre of the heated particle, with a maximum here of 125MPa. This corresponds with Figure 5.22. The energy input into the sample has caused high plasticity and as a result there is a large degree of irregularity in the stress field as regions fail and their stresses redistributed.

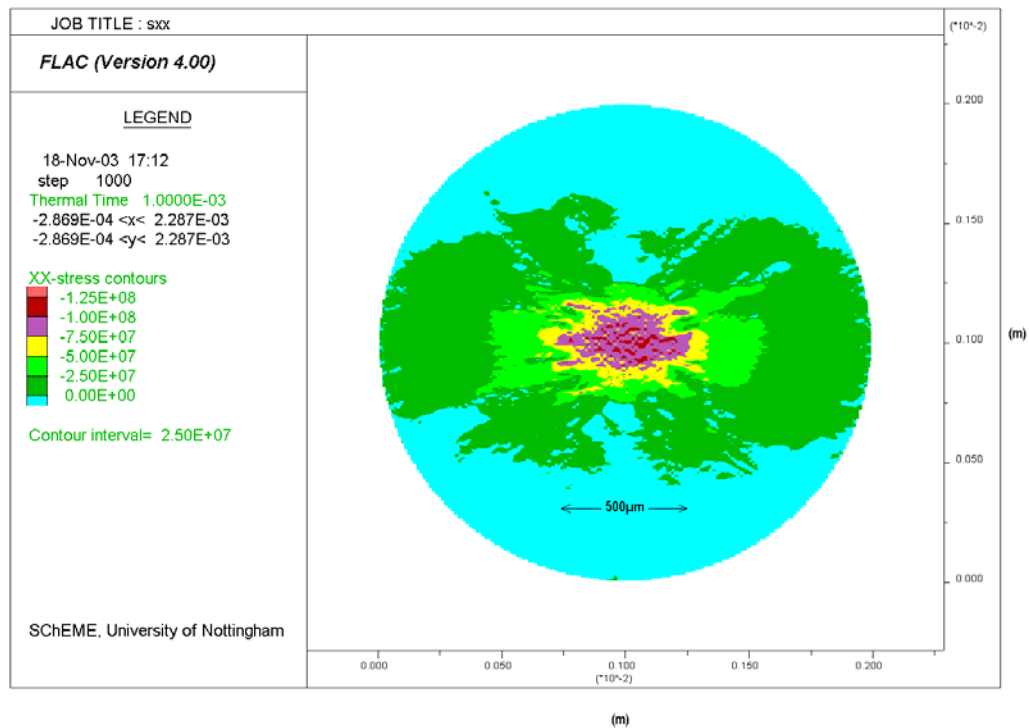


Figure 5.23: Contours of horizontal stress,

Figure 5.24 shows the distribution of compressive stresses in the vertical direction. Due to circular symmetry it is very similar to the previous Figure 5.23. Again note distortion of stress field due to high plasticity. The highest compressive stress is to be found in the pyrite particle.

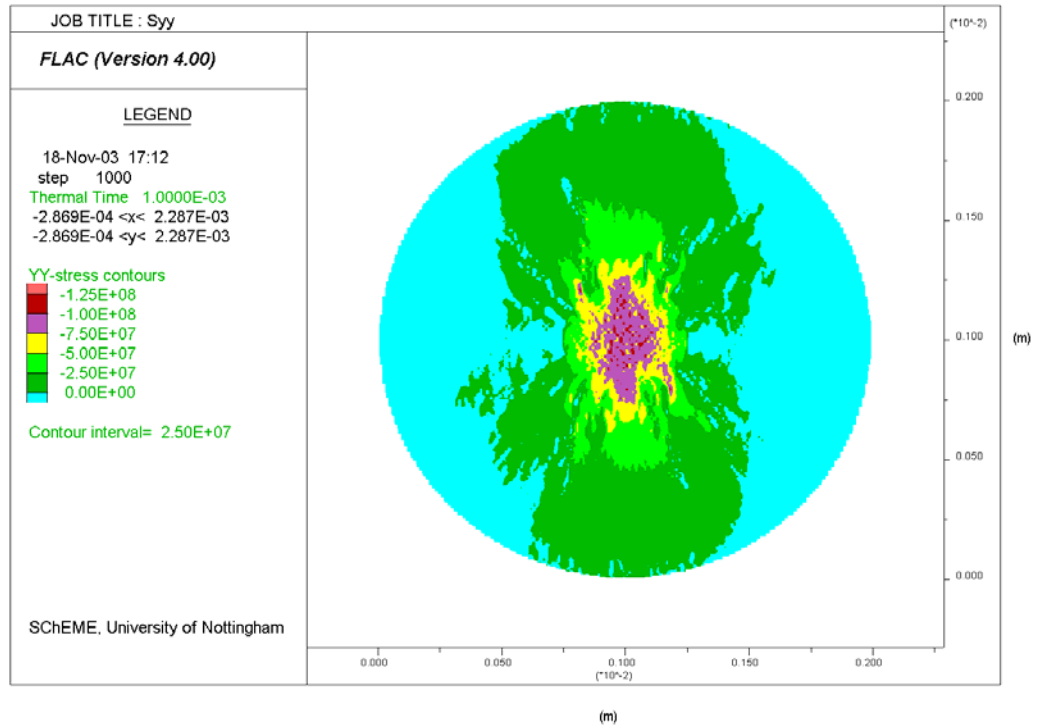


Figure 5.24: Contours of compressive stress in the vertical direction.

Figure 5.25 displays the shear stress contours in the sample. Note the symmetry of this plot indicating the directions in which positive and negative stresses are acting. Positive stresses are acting along the top-right-to-bottom-left direction. The highest shear stresses are to be found outside the pyrite boundary, slightly inside the pyrite. Here the stress convention results in the highest shear stresses occurring at 45° to the vertical due to the directional convention. Conversely, the highest negative shear stresses will be occurring along the diagonal from the top-left-to-bottom-right direction. However, this is not the best plotting tool for illustrating the high shear stresses across the heated particle boundary as the contours do not give sufficient detail of variation with position or indeed time. The next section details the methods by which parameters are studied as they vary over time.

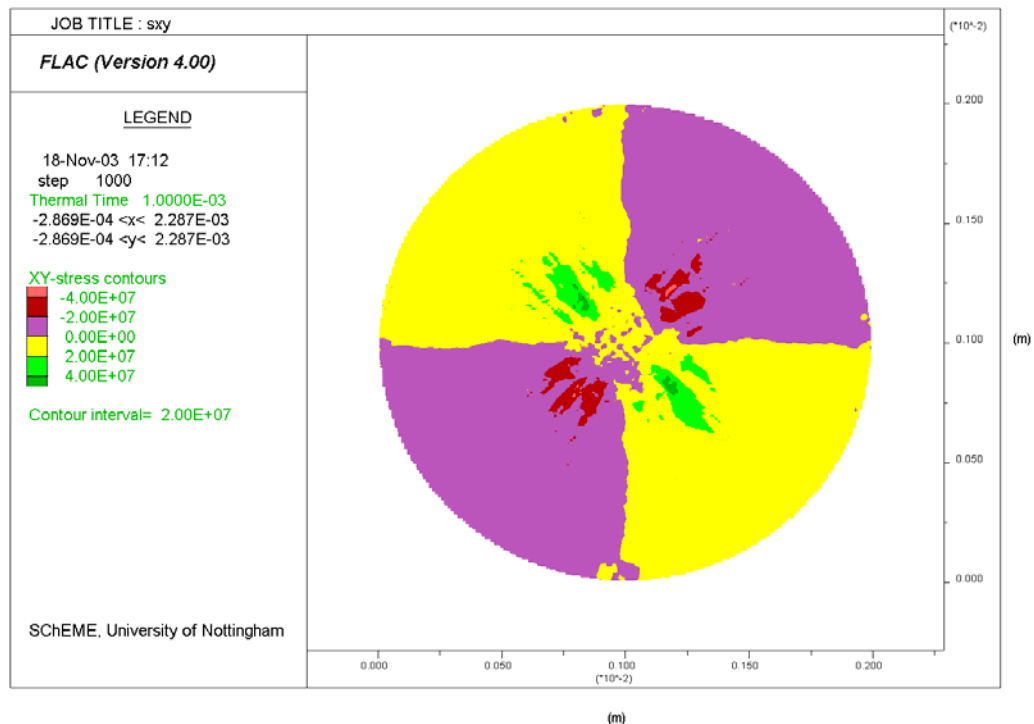


Figure 5.25: Contours of shear stress.

5.3.5 Parameter History Plots

Occasionally the variation of a particular parameter as the simulation progresses is required for examination, and the “History” function performs this task. Essentially a history location can be assigned to any area within the model, and any parameter can be assigned to that location. For example, the history of temperature could be recorded as it receives more thermal energy from the applied source, and observe how behaviour changes with time due to conduction effects as in Figure 5.26. Again a variety of parameters can be applied to the history lines to observe the change in behaviour with time. It is useful to determine when particular events such as specific strength criterion being exceeded as heating progresses.

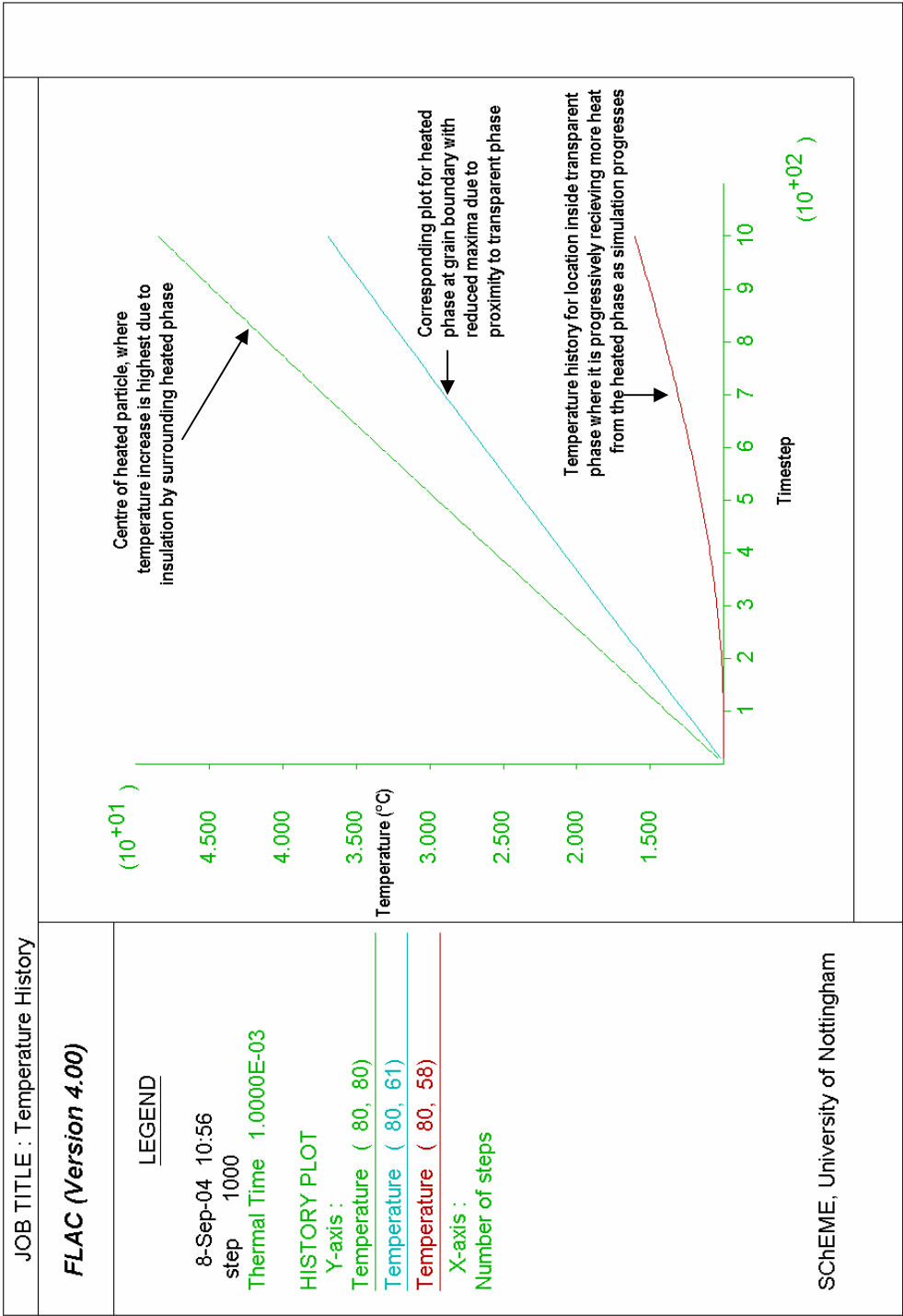


Figure 5.26: History function plot of variation of temperature with time

5.3.6 Profile Output Plots

These output plot types are ideal for showing detailed variation of various parameters with position. A line is drawn over the range that is required for examination. Such a line might be drawn from the centre of the heated particle as shown below and into the transparent phase in order to examine how the temperature varies with position.

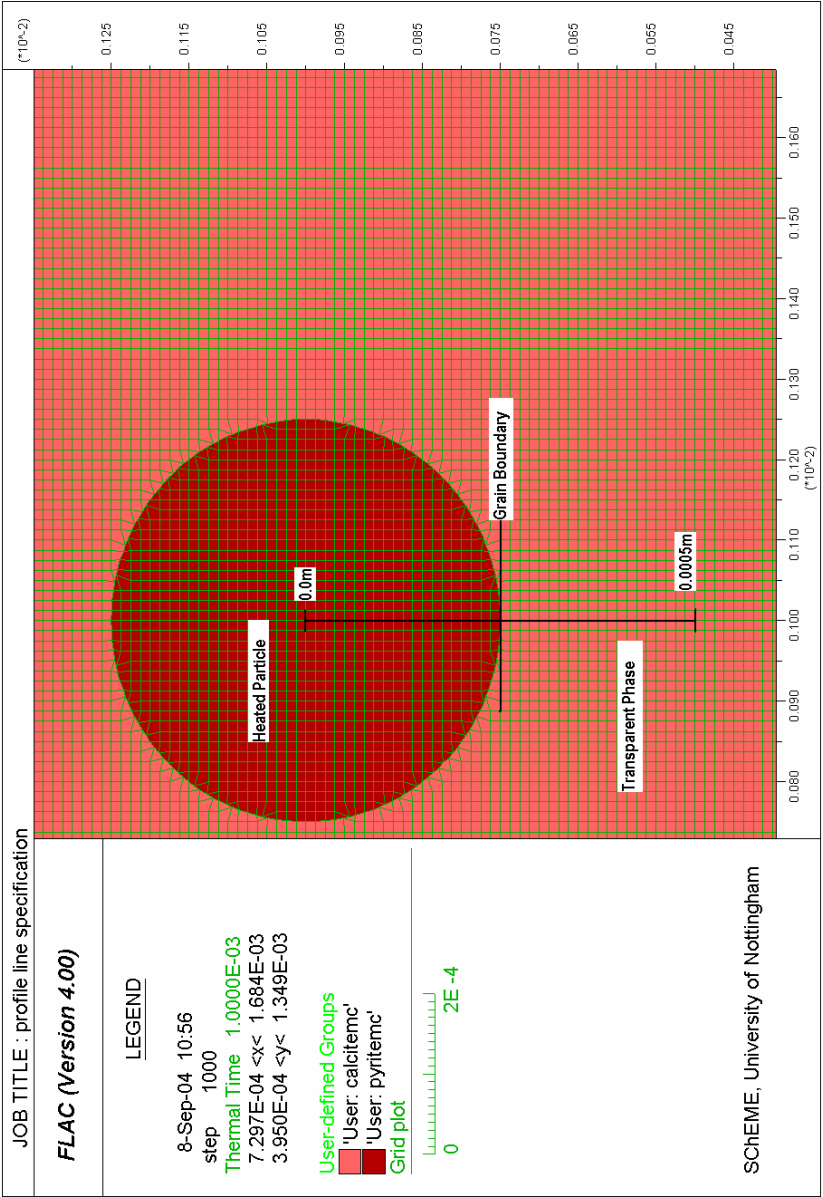


Figure 5.27: Illustration showing method of drawing profile line

Parameters such as temperature, stress, strain, displacements and velocities can be applied to the profile line. Precise placement of the profile line will allow for identification of underlying mechanisms. In Figure 5.28 below, the temperature profile is plotted. The vertical axis shows the temperature scale, and the maximum temperature here is around 48°C. This occurs at 0m along the profile line. Note *FLAC*'s use of multipliers for each scale, 10^{-5} in this case. The total profile line length is therefore $50 \times 10^{-5} = 0.0005\text{m}$. The temperature falls gradually inside the heated particle as the profile line approaches the grain boundary which lies at 0.00025m. At the grain boundary the temperature drops off rapidly due to the change in thermal conductivity. The rate of temperature change then drops off as the driving force of temperature difference lessens as the profile line moves away from the heated phase.

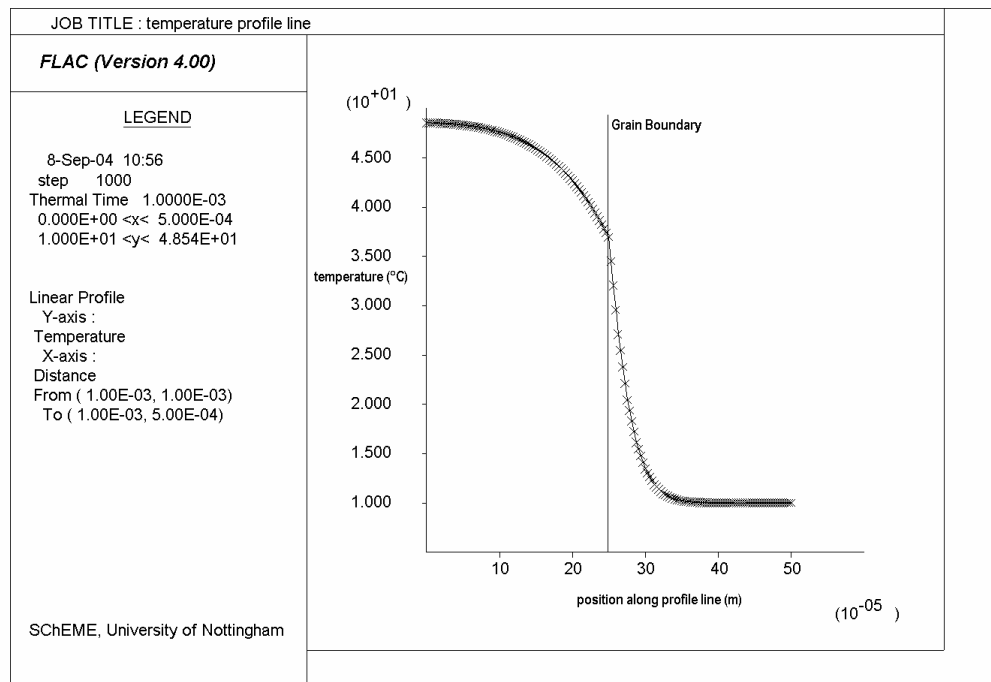


Figure 5.28: Temperature profile line from centre of heated particle across grain boundary and into transparent phase.

5.3.7 Simulations of the Uniaxial Compressive Strength Tests

5.3.7.1 Introduction

A test was required to quantify the damage incurred by the material after thermal simulation. A test was required which related to quantification of breakage in rock in reality. The uniaxial compressive strength (UCS) test was chosen as it is comparatively simple to construct a model, and the UCS relates to the breakage parameters A and b and can be correlated with the Point Load results detailed in section 3.11.3.

5.3.7.2 Methodology

The technique was based on that used by Whittles et al. (2003). Finer grids were used to improve the resolution, and the appearance of the plots. Finer grids tend to yield more realistic crack propagation as the zone size tends towards a realistic grain size and the contouring of the parameters tends to be more efficient and accurate. The simulation was undertaken as a plane strain analysis with the material being considered as continuous in the out of plane direction. A cylindrical sample of aspect ratio 2:1 is usually used for the test but for the simulation this is approximated to a rectangular sample. Loading involved applying a constant velocity to the grid points positioned at the top and base of the model domain whilst the left and right boundaries were unstrained. This is analogous to a displacement-controlled uniaxial compressive strength test. To monitor the load–deformation relationship within the samples during testing, history files were generated from the average stress conditions at the top and bottom boundaries. The models were run until approximately 0.2% axial strain of the sample whereupon the models predicted failure strength and some strain softening details of the samples was obtained.

5.3.7.3 Crack Propagation during UCS Test

This section details an example of the growing degree of shear strain that occurs when the UCS sample is loaded. This particular UCS simulation example was conducted on a 40mm diameter sample, containing 1% pyrite. The sample in this case was exposed to $1 \times 10^{15} \text{ W/m}^3$ for $1\mu\text{s}$.

The initial plot begins at step 25000. The thermal simulation (i.e. the $1 \mu\text{s}$ of heating) requires 1000 steps in this case. The threshold for the shear strain increment which is to be plotted has been set as 1×10^{-2} . This ensures that a continuous contour interval is used from this first plot in Figure 5.29 to the end of the simulation in Figure 5.36. If this contour interval were to be left alone as the default, it would appear that cracks would appear and then disappear as the contour interval adjusted to encompass the ever-increasing range of shear strain increment as the loading simulation proceeded. Therefore Figure 5.29 shows the first area where shear strain exceeds 0.01 (1%). As is to be expected with a UCS test the first cracks appear in the centre of the sample as this is where the confinement generated by the steel platens is least effective at maintaining the sample's integrity. The corresponding stress-strain plot for this point in the simulation is shown in Figure 5.30. As the simulation progresses the area of increased strain appears to lengthen along a plane that runs from the top right to bottom left corners of the sample. This is the easiest means by which the sample can fail. Eventually more and more areas along this inclined plane soften as the vertical displacement increases. The corresponding stress-strain curves for loading steps 253000 and 40000 are shown in Figures 5.34 and 5.37 respectively.

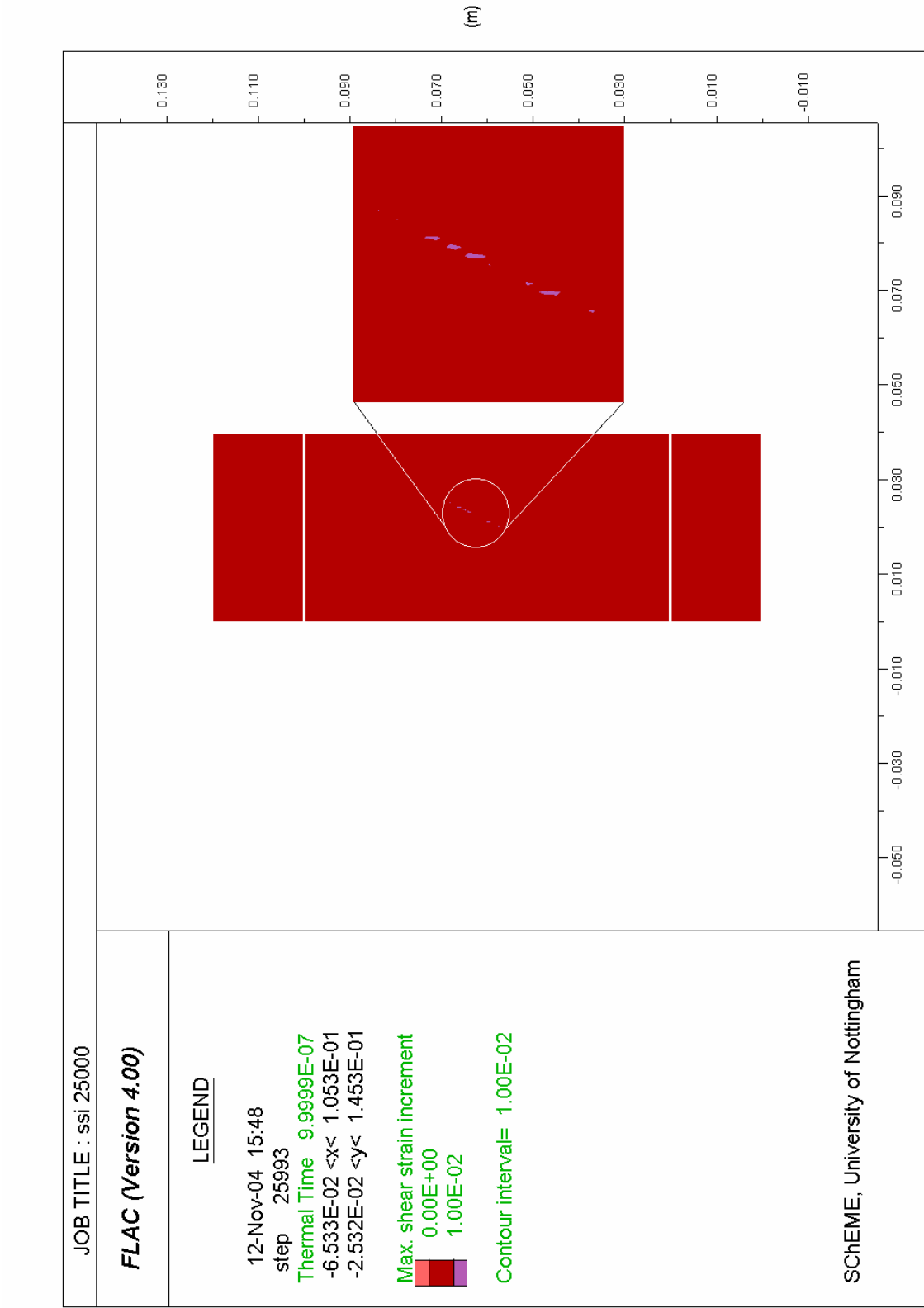


Figure 5.29: Initial crack development during UCS test after 25000 loading steps

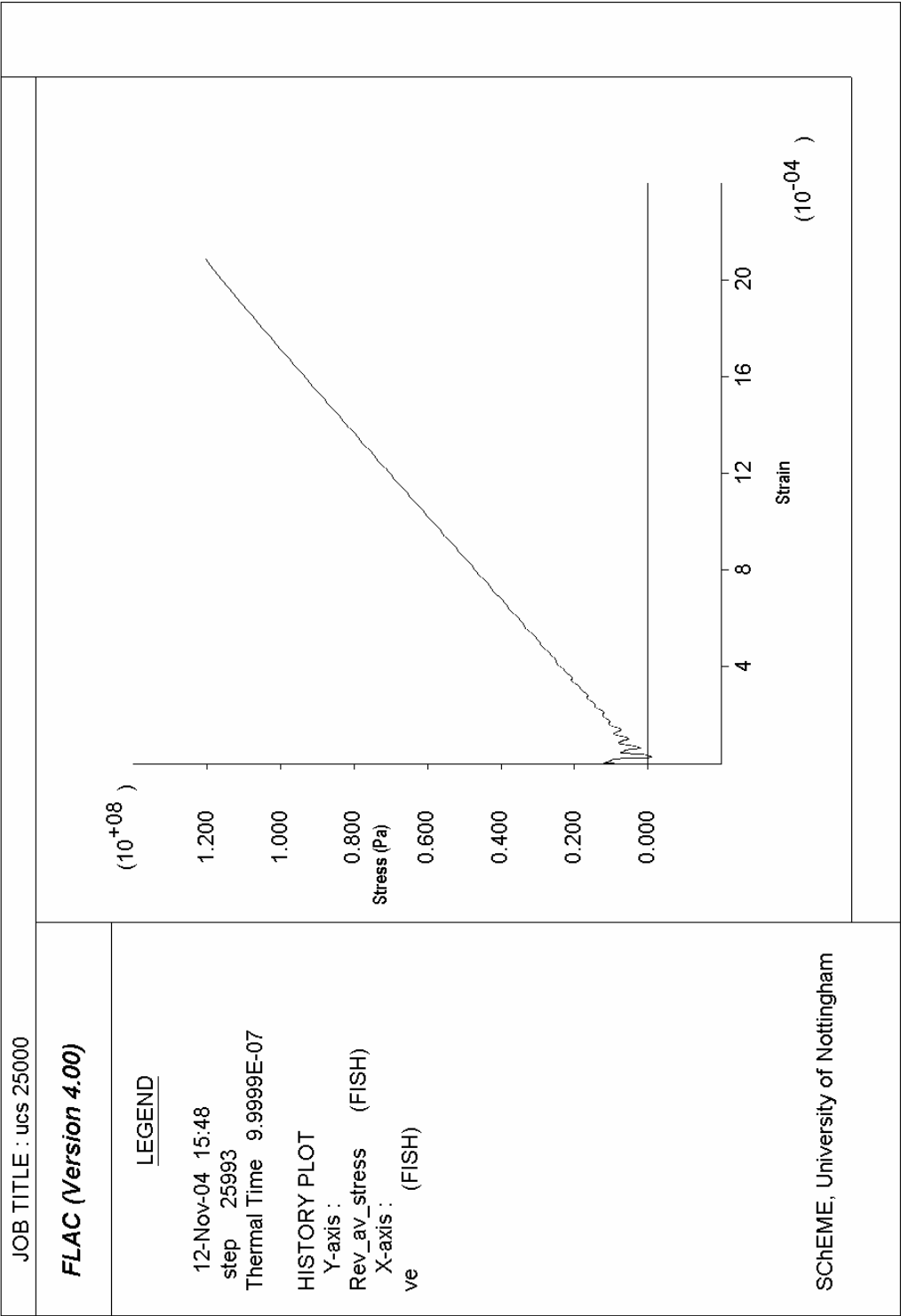


Figure 5.30: Corresponding Stress-Strain plot for loading step 25000

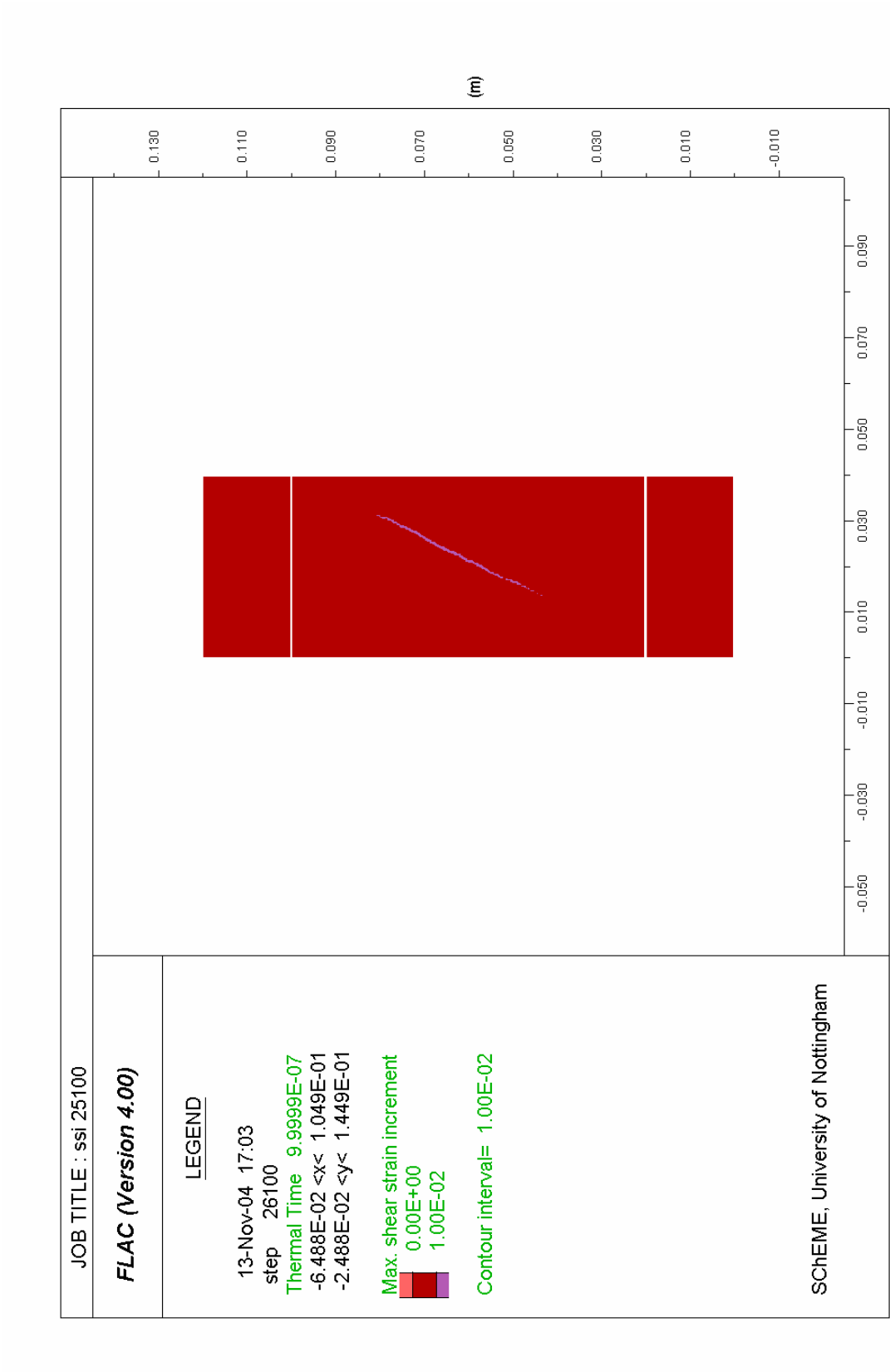


Figure 5.31: Further development of crack after 25100 loading steps

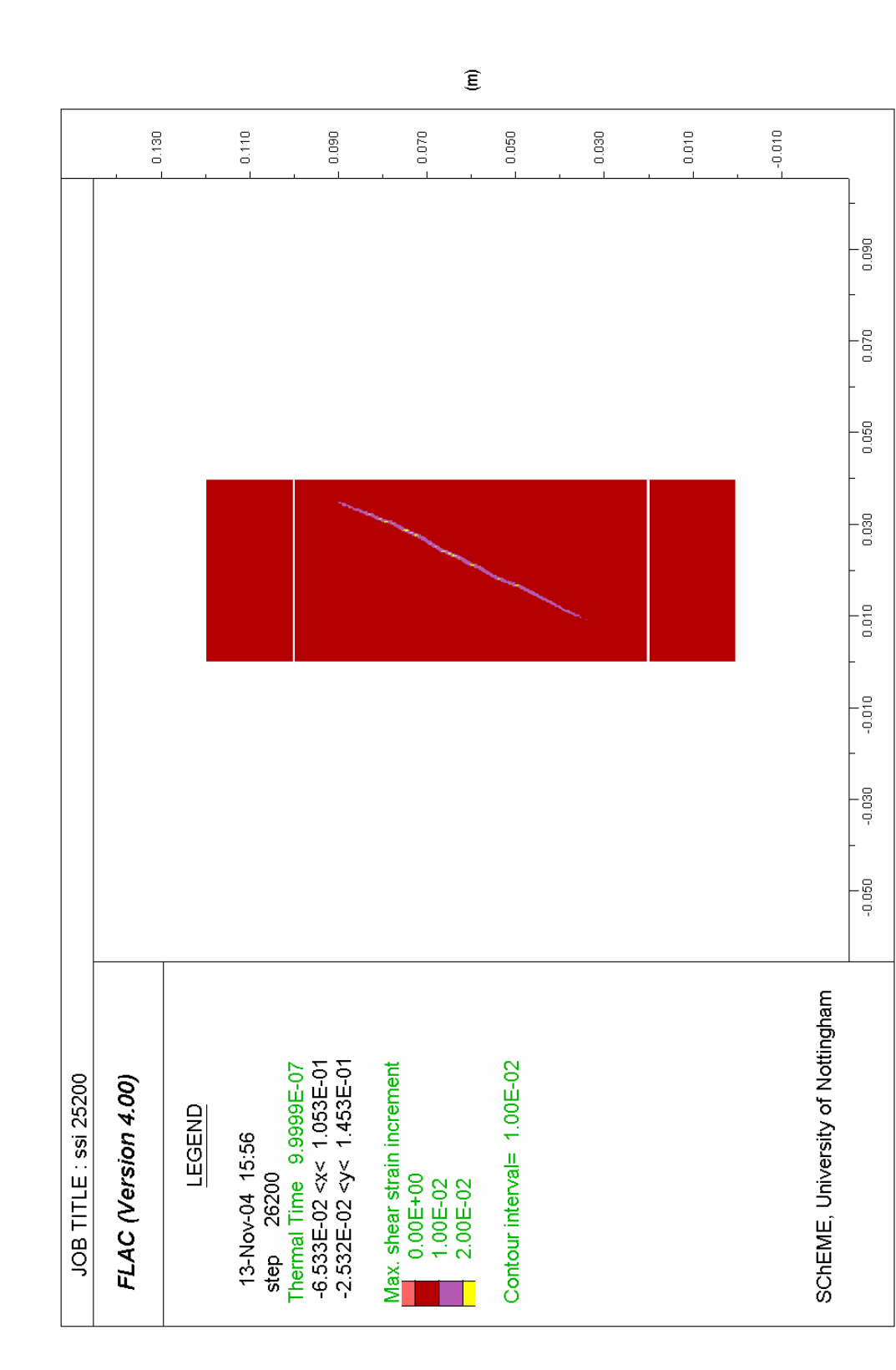


Figure 5.32: Further development of crack after 25200 loading steps

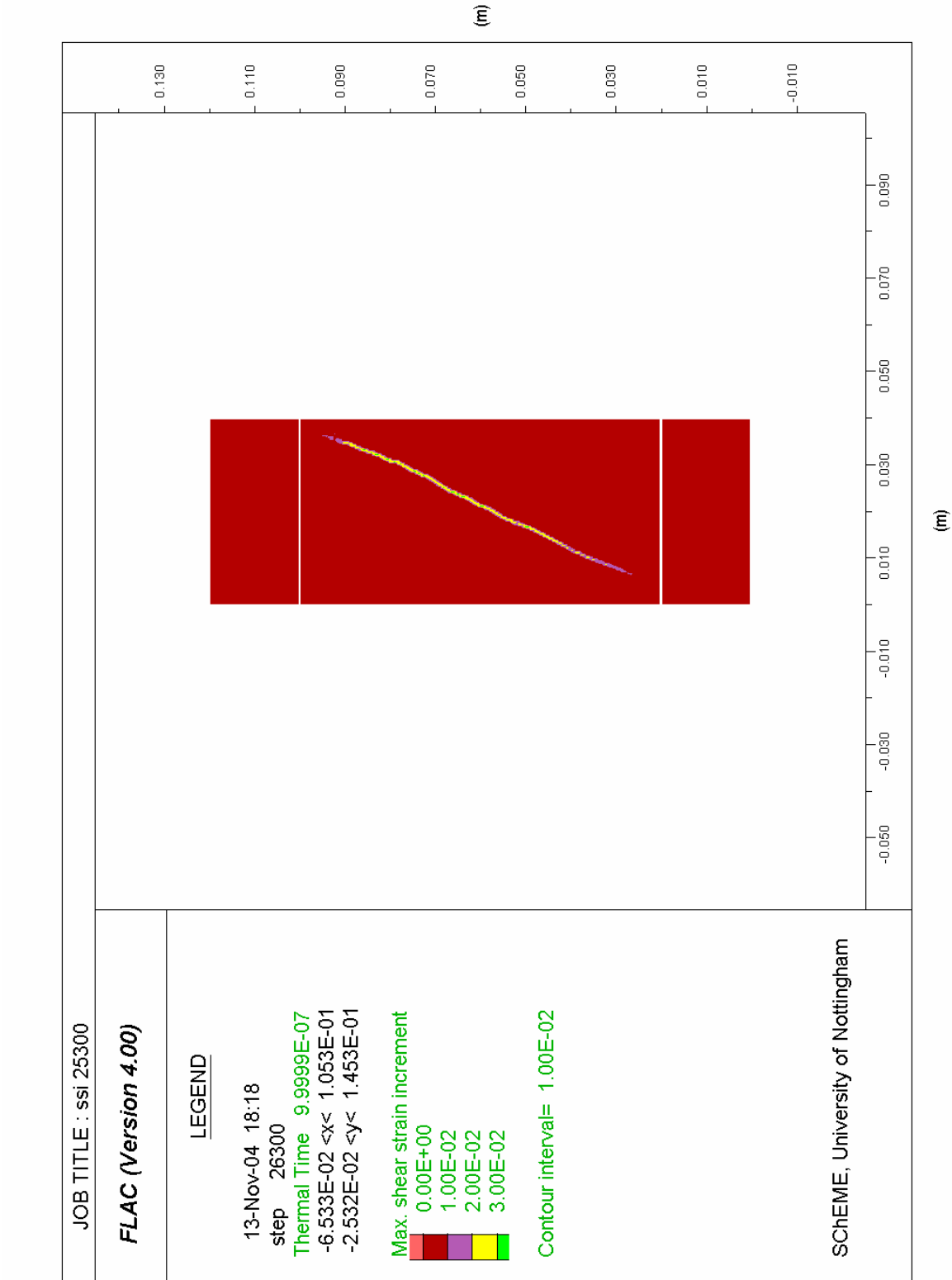


Figure 5.33: Further development of crack after 25300 loading steps

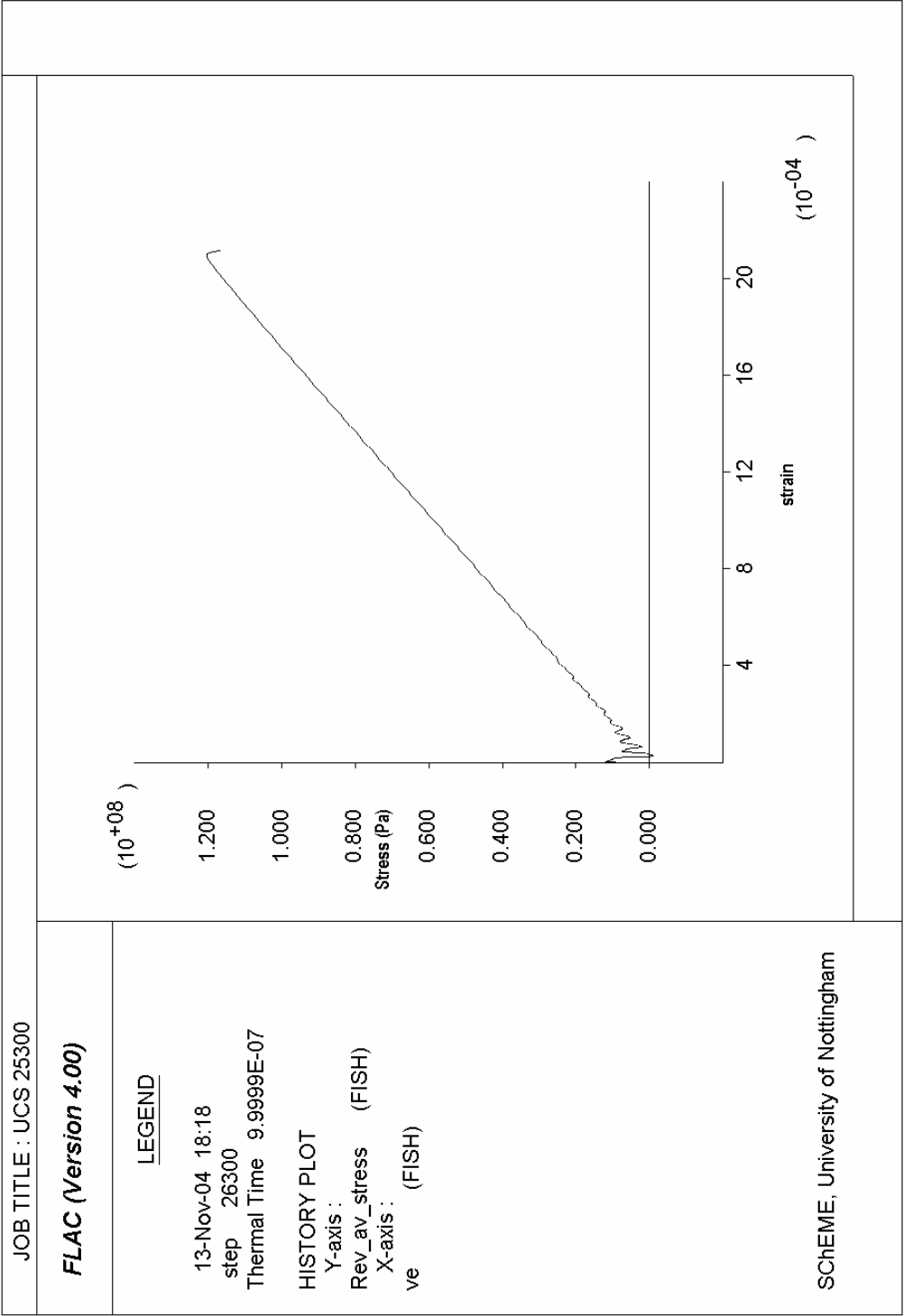
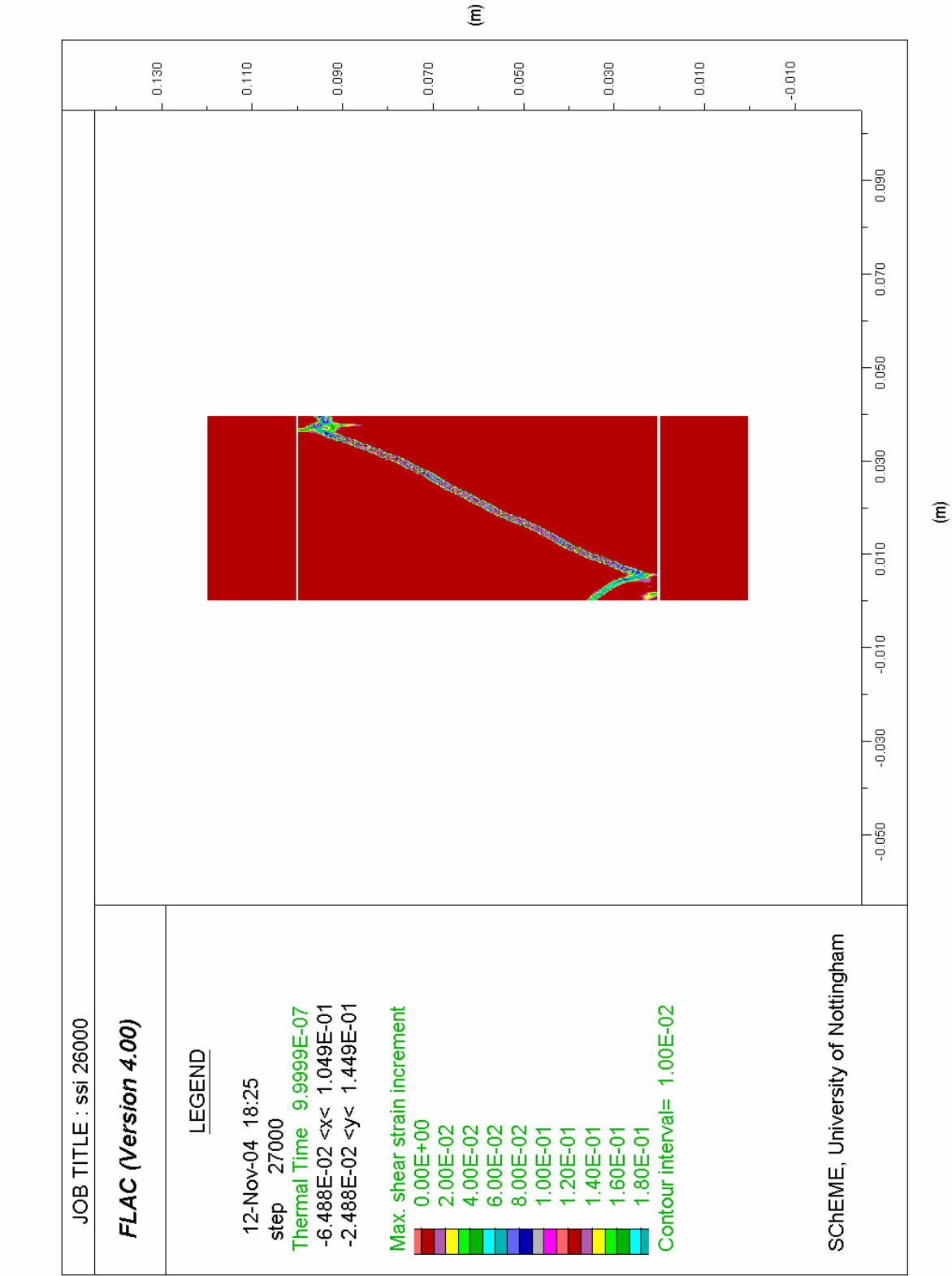
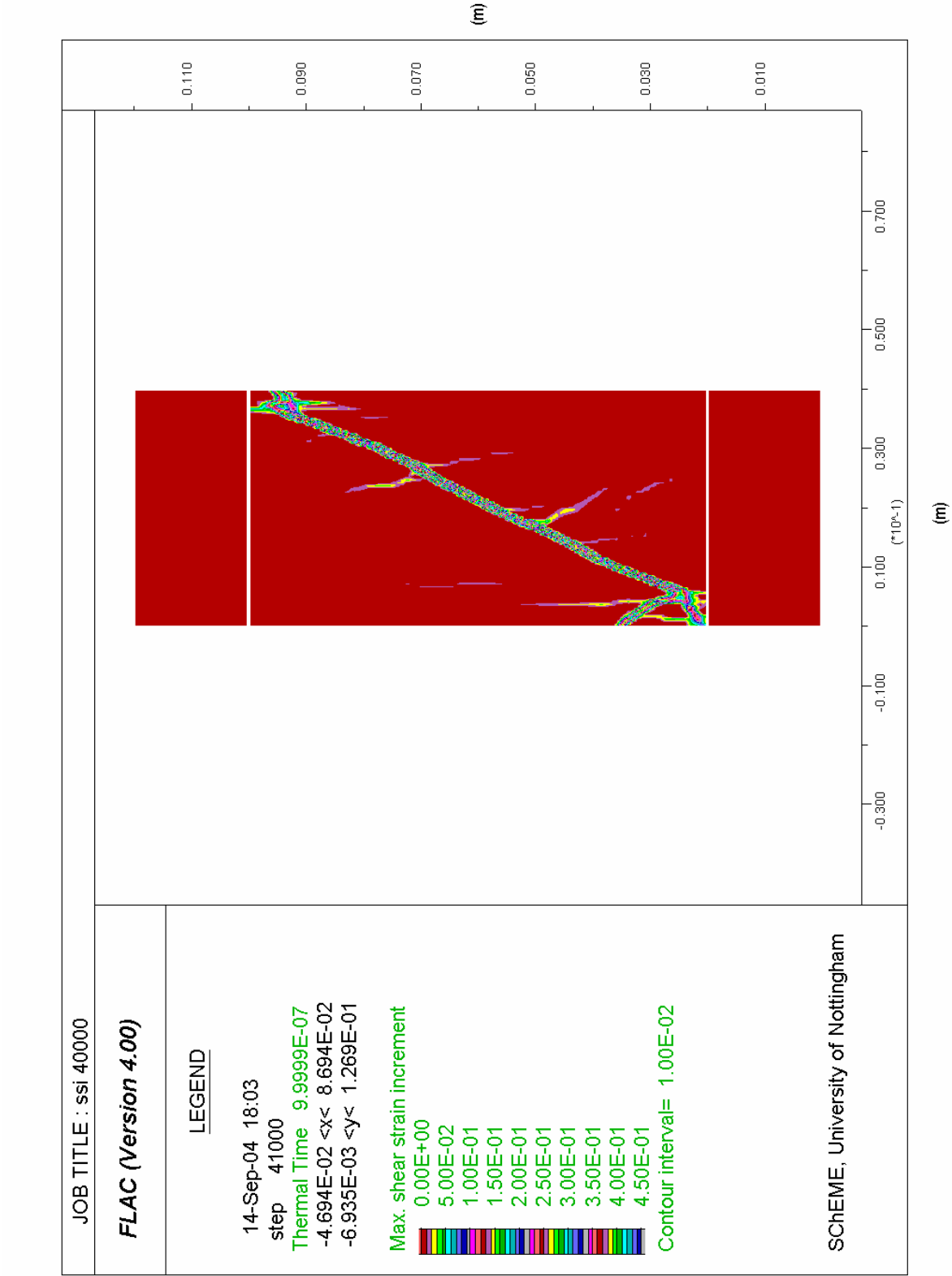


Figure 5.34: Corresponding stress-strain plot for loading step 25300





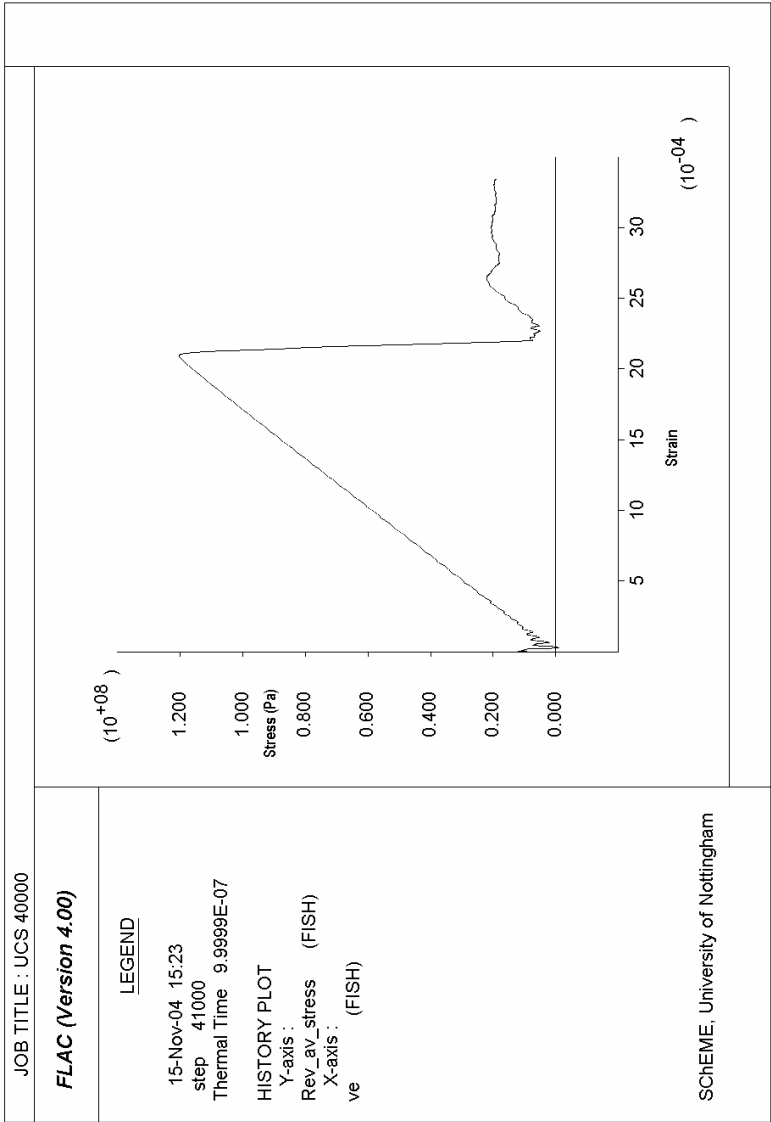


Figure 5.37: Corresponding Stress-Strain plot for loading step 40000

Here the full loading simulation stress-strain history is presented and the post failure behaviour is shown. The material has failed quickly over the course of a few hundred steps. The material has then reached a plateau of residual strength which fluctuates slightly as further cracks open and coalesces.

5.3.7.4 Discussion

The development of a shear plane has been shown and the corresponding stress-strain plots have illustrated how the material fails under uniaxial compressive loading. The development of the shear plane begins as the material reaches its uniaxial compressive strength, or ultimate stress, and develops rapidly in the context of the entire loading procedure. The propagation of the shear plane matches the theoretical case presented in Section 3.11.

5.4 Conclusions

The Fast Lagrangian Analysis of Continua (*FLAC*) method was utilised for the determination of the degree of weakening to be expected when minerals are exposed to microwave radiation. The explicit finite difference method has been shown to be suitable for this application. Advances in processing power have resulted in the capability to express complex non-linear constitutive behaviour. The strain softening model can be implemented into *FLAC* using its internal *FISH* functions. This method has been shown to be effective at simulating brittle failure in rock. However, it is difficult to represent exact behaviour due to difficulties in obtaining exact values for the strain softening properties from real situations and it is therefore suitable to choose values that are within a realistic range of behaviour. Adopting a continuum modelling approach to model a discontinuum process will not capture all the subtleties of brittle failure. However, in practice, what is of paramount importance to this study is that the stresses are of sufficient magnitude to result in localised strength reduction. The proposed modelling approach is capable of filling this need reliably. *FLAC* was also chosen because of its thermo-mechanical coupling module – this allows the simulation of transient heat conduction in materials and the development of thermally induced displacement and stress. This is ideal for this particular application.

The practical use of the software for the determination of the stress regime that arises when certain phases are subjected to rapid heating has been detailed in section 5.3. The various plotting methods have been listed and detailed. The implementation of the thermal behaviour found in the literature has been detailed. The method used for comparing the strengths of thermally damaged cores has also been shown to follow the experimental characteristics.

Chapter 6

Results and Discussion

6.1 Introduction

This chapter details the simulations undertaken and the results obtained. The aims were to vary parameters such as exposure time and power density to study the effects on the stresses generated and the degree of weakening induced, in order to explain some of the phenomenon observed and results obtained previously in the laboratory.

Initially only simple geometries were examined, usually with a single circular heated particle. This was to enable determination of the likely stress magnitude and the locations within the material where these stresses occurred. The effects of varying the size of heated particles were also investigated in order to explain the observed decrease in weakening efficiency that occurs when treating small particle sizes in the laboratory. The effects of the rate at which energy was delivered into the sample were then studied in detail, with both the exposure time and the power density varied in order to yield different total energy inputs, as well as quantifying the individual effects of exposure time and power density. The plotting methods discussed in sections 5.3 were used to yield information about how various parameters varied with position, time and energy input.

More complex geometries were also incorporated into the models in order to improve the realism of the represented ore texture. Random distributions of heaters were applied to a transparent matrix, yielding a simplified mineral texture. It was then possible to vary the proportions of heated particles in the sample and quantify the effects of doing so.

The effects of rapid heating on this bulk sample in terms of the likely strength reduction required quantification. This was carried out using a so-called ‘damage parameter’, and with a simulated uniaxial compressive strength (UCS) test. The practical and numerical implementation of this test was discussed in Chapter 3 and 5 respectively, and later in this chapter the results are presented and discussed and conclusions drawn.

6.2 Initial Demonstration of Fracturing in Simple 2-Phase Model

6.2.1 Introduction

This section details an introductory investigation into the effects of rapid heating of a binary mineral system. This model was run to demonstrate the development of simulated fractures within the sample with time. The objective was to demonstrate that rapid heating of certain phases was likely to yield high stresses and induce fracturing in the sample.

6.2.2 Methodology

The model was specified as a 500 μ m circular microwave-absorbent heated phase contained within a 2mm microwave-transparent circular matrix. This is the simplest geometry that could be tested in order to negate any stress concentration effects induced by the corners of the sample. The sample was subjected to heating at 1×10^{11} W/m³ for 1 millisecond (ms), in order to ensure that the material begins to fracture, and that the model is able to show these fractures clearly. The thermal model was run for 1000 steps with the thermal timestep set at 1 μ s so that 1000 steps yielded 1ms. The model was paused at various stages throughout the heating in order to show the fractures as they progress.

Figure 6.1 illustrates the geometry of the system, and for subsequent plots in this section the deep red circle that indicates the presence of heated particles will be removed. This is a limitation of the software in that it is not possible to display fractures whilst also displaying the distribution of each phase.

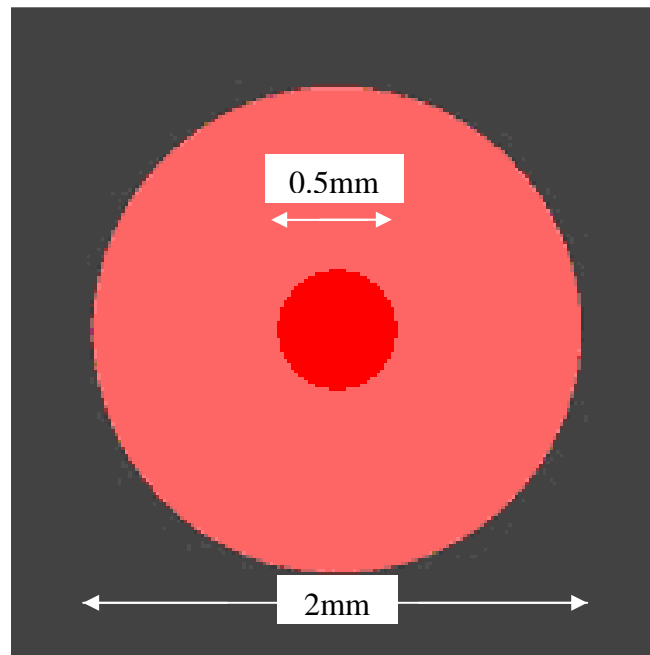


Figure 6.1: Plot showing extent of circular heated particle (deep red) within circular transparent matrix (reddish-pink)

6.2.3 Results and Discussion

The following series of plots shows the fractures that develop as the sample is heated for a total of 1ms. Figure 6.2 shows the model state after the first calculation step and shows that no fractures have developed as yet. The model remains intact and therefore remains in the original pink colour. It is assumed that at this point insufficient heat has been applied to generate the significant thermal expansion which is thought to result in high stresses and therefore fractures.

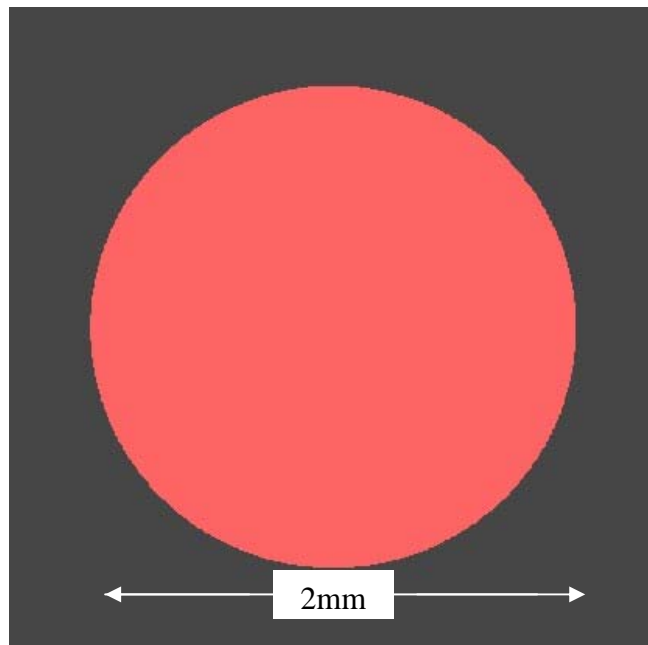


Figure 6.2: 10 μ s – state after 1st step – no plasticity or fractures yet

As described in section 5.3, the yellow colours correspond to tensile fractures, deep red colours now correspond to shear fractures, and the purple colour corresponds to regions where the material has previously been at yield but has subsequently receded due to redistribution of stresses. Figure 6.3 shows the first signs of plasticity in the sample after 250 μ s. It can be seen that there is a significant area of tensile fracturing in the upper-left side of the transparent particle. It is assumed that this is due to the internal heated particle's expansion resulting in the outer perimeter of the transparent particle being stretched. It can also be seen that there are a few zones showing plasticity in the vicinity of the heated particle grain boundary.

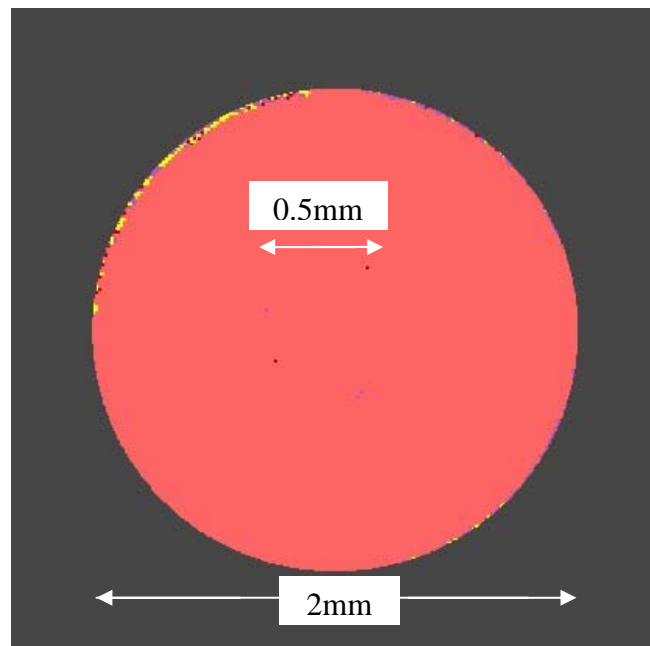


Figure 6.3: 250 μ s – first sign of plasticity around grain boundary, tensile regime around edges

Figure 6.4 shows that the plasticity has now spread around the grain boundary completely after 300 μ s. Figure 6.1 showed the extent of the pyrite particle in the calcite matrix, and here it can be seen that in only 50 μ s, the first signs of plasticity have appeared and then spread completely around the grain boundary. This is indicative of rock in that catastrophic failure often occurs in a matter of microseconds. It is extremely interesting to note the pattern of plasticity here, in that it followed around the grain boundary in a very narrow band.

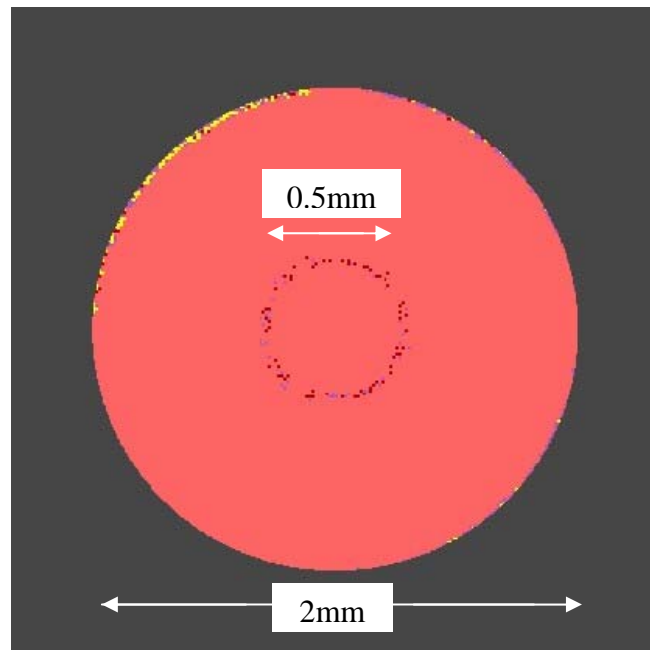


Figure 6.4: 300 μ s – shear plasticity has spread around the heated particle's grain boundary very quickly.

Figure 6.5 shows the model state after $600\mu\text{s}$. Shear cracks are beginning to propagate radially outwards from the heated particle. The regions in purple are areas where the material is at yield, or has been in the past due to redistribution of stresses. There is also the first sign of tensile cracks occurring around the grain boundary. Again it is interesting to note how localised the plasticity is around the grain boundary. Also note the lack of plasticity inside the heated particle.

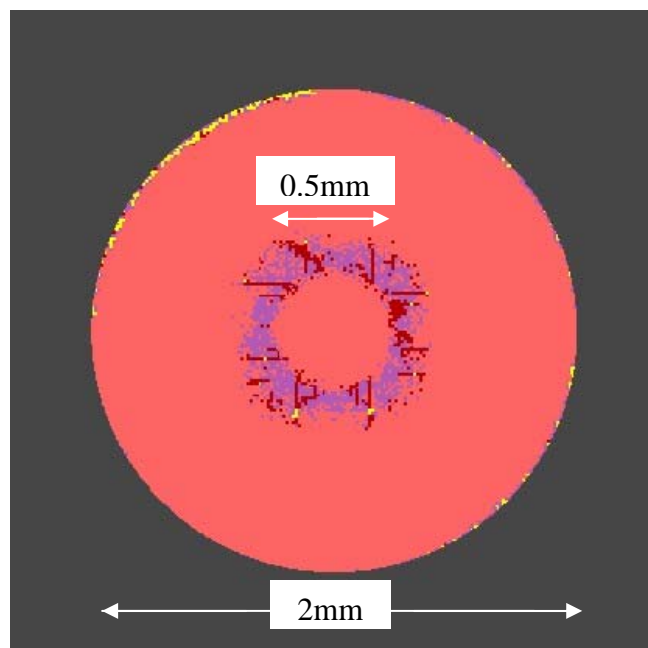


Figure 6.5: $600\mu\text{s}$ - shear cracks forming radially outward from grain boundary, first sign of tensile cracks also appearing as shear is exacerbated.

Figure 6.6 shows the model state after the end of the simulation at 1ms. The plot shows extensive shear and tensile cracks – radiating inwards from the transparent particle boundary and radially outwards from the heated particle boundary. There is still comparatively little damage inside the heated particle.

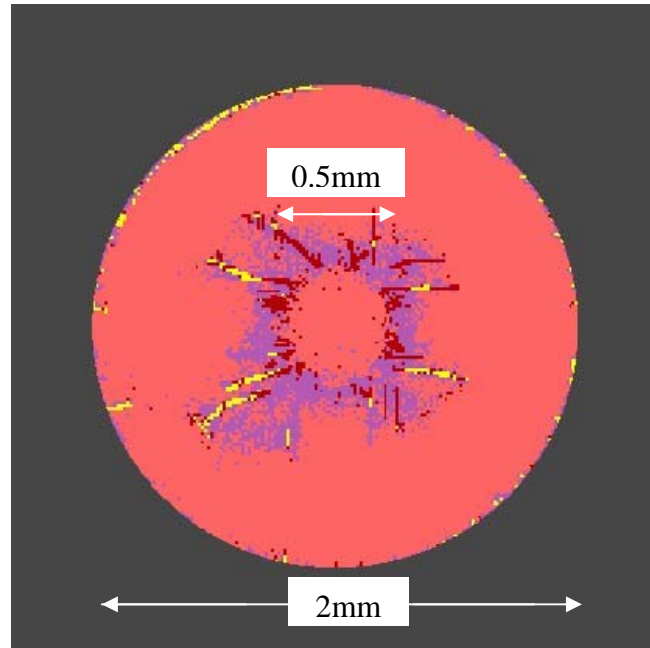


Figure 6.6: 1000 μ s – extensive tensile cracks, also forming from boundary inwards

6.2.4 Validation

After completion of this experiment it was noticed that the pattern of fractures closely matched the following captured image from a Scanning Electron Microscope (SEM) shown in Figure 6.7. This was a chalcopyrite particle of around 100 μ m diameter surrounded by a transparent phase matrix which had been exposed to microwave radiation pulses of 3MW and very short exposure time of 1 μ s repeated at 50Hz for a total of 10 seconds. Pulsed microwave treatment was discussed in section 5.1. It can be seen clearly that there are fractures surrounding the chalcopyrite particle, with additional fractures appearing to radiate outwards from the central particle. The

chalcopyrite particle has remained intact. It was thought that this SEM image provided good agreement with the pattern of fractures shown in the modelling, particularly in Figure 6.6.

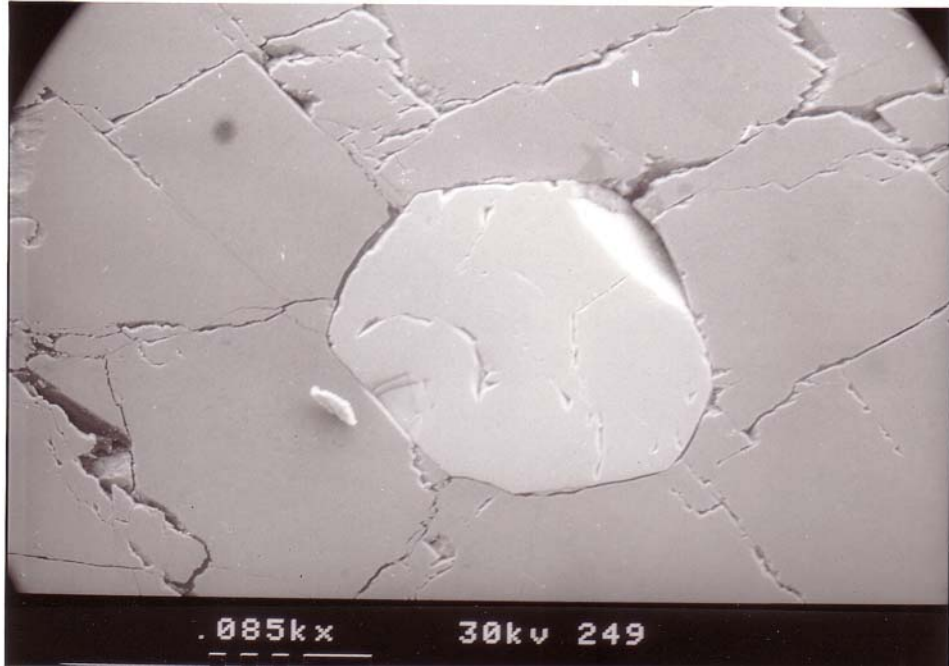


Figure 6.7: Micrograph of chalcopyrite particle in calcite matrix exposed to 3MW pulses of 1 μ s duration, at a pulse repetition frequency of 50Hz for 10s.

6.2.5 Implications for Mineral Processing

This intergranular fracture was a very interesting result in that the plasticity was concentrated around the grain boundary. This initial result demonstrated how fractures were initiated inside the material due to expansion of the heated phase. This would have the effect of weakening the material, so that less energy would be required for crushing or grinding. Any weakening of ore material can prove significant as demonstrated in Chapter 3.

This result also shows how increased liberation of the heated phase may potentially be possible. The fractures originated at the grain boundary between heated and transparent phases. As more heat was applied the fractures were largely concentrated outside the grain boundary inside the transparent phase. Comparatively few areas of plasticity were noted inside the heated particle. If this particle was subsequently loaded, it was likely that the heated particle would be wholly liberated, as the cracks would surround the entire particle. Also the likelihood is that the particle would remain intact. This could have implications for mineral processing in that liberation could be facilitated through preferential weakening of grain boundaries. This would also result in the heated phase being liberated at a coarser size, negating the need for further energy consuming grinding. It is thought that there are two possibilities of how this may occur. One possibility is as a result of the material properties of the constituent phases, with one phase being more susceptible to cracking than the other. The materials used (i.e. pyrite and calcite), have different stiffness moduli, with pyrite being the stiffest. It was thought that this lead to a situation where the stiffer heated particle caused greater damage. However, this theory was discounted when another model was constructed with the same mechanical and thermal properties throughout as shown in Figure 6.8, with the heat only applied to the central portion, but the fractures were even more pronounced. The same was attempted but using the material properties for calcite throughout, and again applying the heating rate only to the central circular region. Fewer fractures were seen as shown in Figure 6.9 than in the all-pyrite case in Figure 6.8. This could be due to the differences in thermal expansion coefficient in the calcite ($2 \times 10^{-5} \text{ }^{\circ}\text{C}^{-1}$ whereas for pyrite it is specified as $4 \times 10^{-5} \text{ }^{\circ}\text{C}^{-1}$).

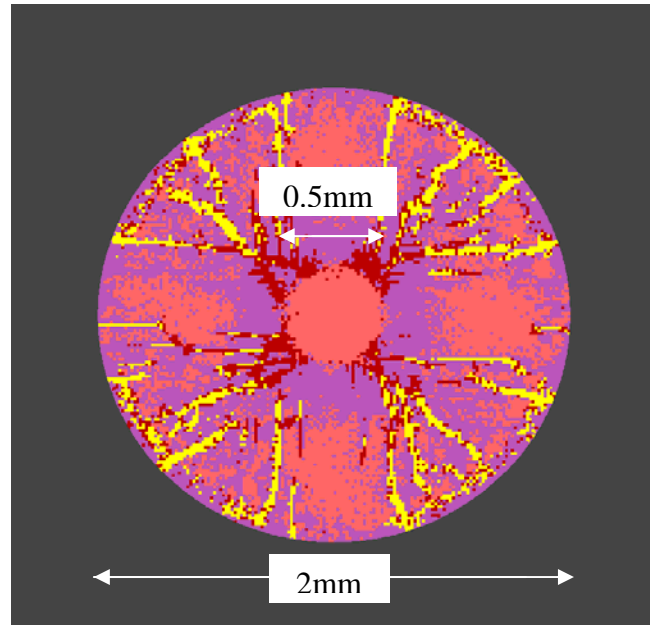


Figure 6.8: Extensive fractures in all-pyrite sample

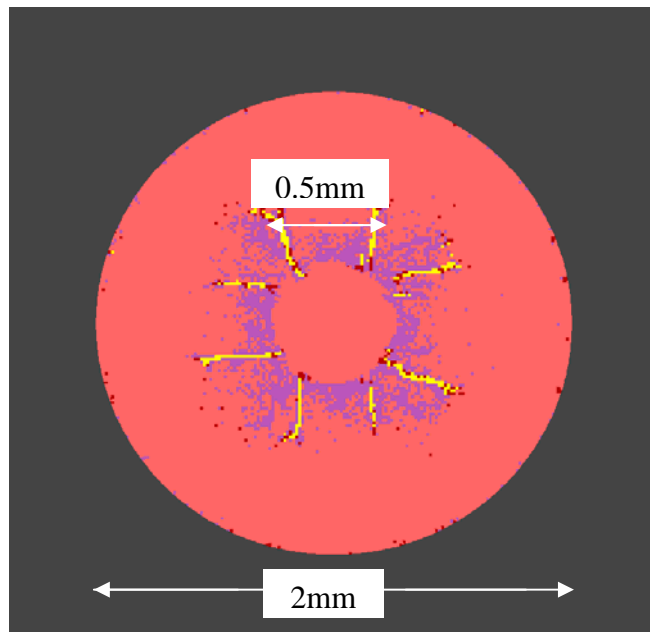


Figure 6.9: Fewer fractures in all-calcite sample due to lower stiffness

It was therefore thought that the MW-induced fracturing is mainly due to the rapid expansion of a heated phase against a transparent phase but it was clear that more investigation was necessary in order to determine the exact stress regime which gave rise to these fractures, and investigate how the stress and strain parameters varied

throughout the sample. More detailed information was required on how the stresses and strains varied across the sample. The next section details how the parameters such as the various stresses, strains, displacements and velocities vary with time as well as position in the sample.

6.3 Parameter Variation with Position and Time

6.3.1 Introduction

This section investigates in more detail the variation of stresses, strains, displacements and velocities in the single heated particle in a transparent matrix system. Precise knowledge of the variation of temperature, strains and magnitude and the direction in which the stresses were acting, as well as the displacements and velocities would yield a better understanding of the results obtained in section 6.2. It was thought that there would be a marked difference in behaviour near the grain boundary, and this study would show the exact variation of each parameter.

6.3.2 Methodology

History locations, as described in section 5.3, were specified along the vertical axis of symmetry from the centre, downwards to the boundary between the heated phase and the transparent phase, and then further points beyond. The history function logs the variation of a particular parameter with each timestep as detailed in section 5.3.

The parameters that were logged in this study were temperature, volumetric strain, volumetric strain rate, shear strain increment, shear stress and displacement. Many parameters were logged in this case in order to see the interactions between each property. The model was 160 zones in diameter, with the heated particle in the centre

having a 40 zone diameter. The centre of the heated particle is located at (80,80). The history locations are located at an interval of 2 zones until zone j=64. Then each history is logged at each zone thereafter until zone j=58 for greater resolution near the heated particle boundary. Hence history points were located at the following coordinates along the vertical centreline (where the horizontal coordinate is i=80):

80,80	(- centre of heated particle)
80,78	
80,76	
80,74	
80,72	
80,70	
80,68	
80,64	
80,63	
80,62	
80,61	(- extent of heated particle)
80,60	(- extent of transparent particle)
80,59	
80,58	(- 3 zones inside transparent particle)

A closer view of the model geometry is shown in Figure 6.10. The history locations are shown at the zones (denoted by yellow history numbers) and at the nodes (black).

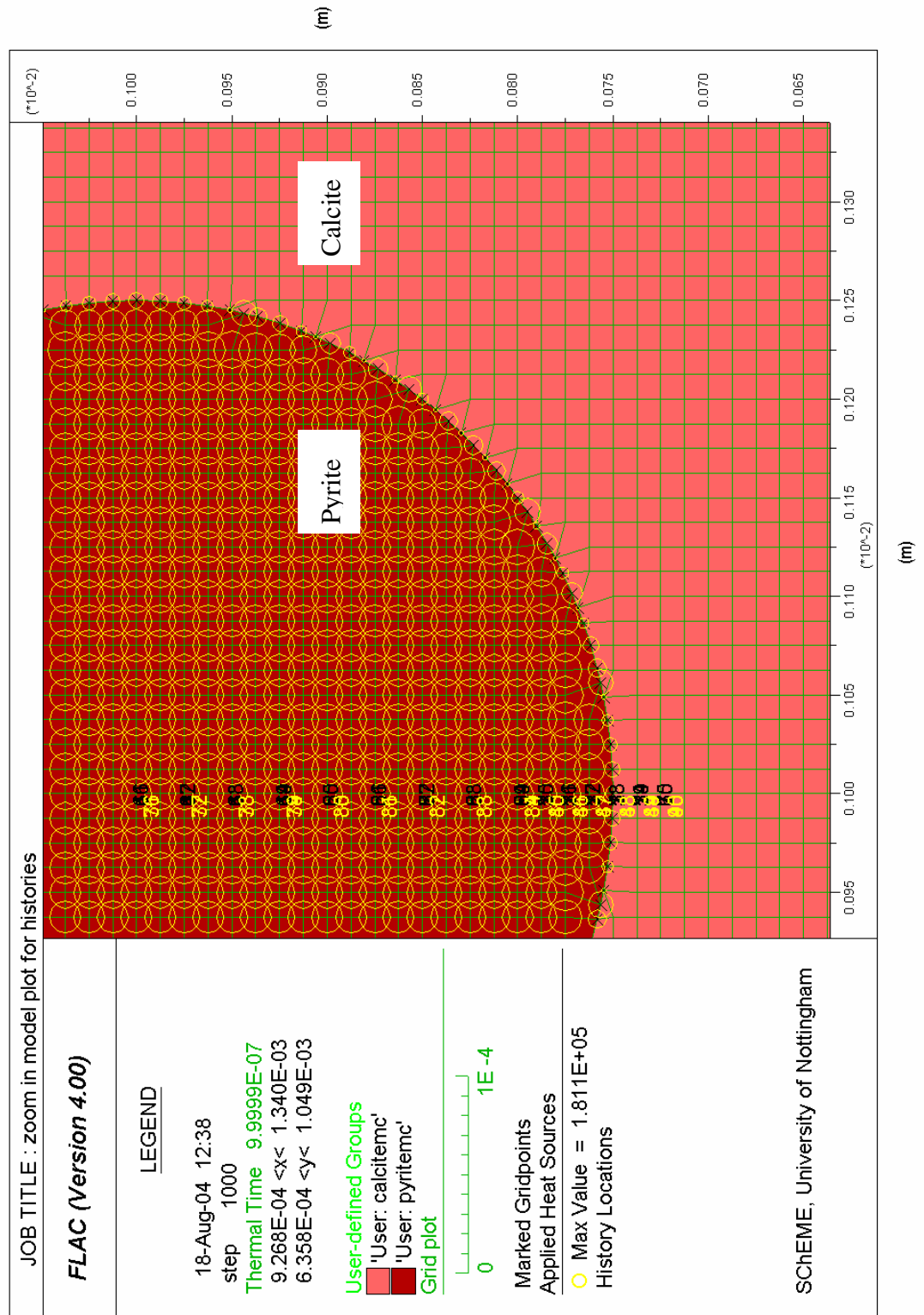


Figure 6.10: Close-up of history locations - boundary lies between 80,61 and 80,60.

Note in Figure 6.10 the scales in use. The centre of the particle lies at (0.100,0.100) but these values need to be multiplied by 1×10^{-2} for the exact value. Hence the centre of the particle lies at (0.001,0.001). A heating rate of $1 \times 10^{11} \text{ W/m}^3$ was again applied to the sample although for a shorter interval of 0.2 ms in order to examine the early stages of heating more closely. The first signs of plasticity appeared after 0.25ms in the study in previous section therefore a heating time was chosen so that no plasticity would appear which would distort the stress field and make the results more difficult to interpret. Also note in Figure 6.10 the magnitude of the power density applied to the zones near the grain boundary is changed according to where discretisation results in a deviation from the nominal zone size.

6.3.3 Results

This section contains the history of each assigned parameter as the simulation progressed. Figure 6.11 shows the variation of temperature with time for the various points within the sample. The left side of the plot details the coordinate points where the histories are logged as detailed in section 6.2.2. The origin of the coordinate grid is at the bottom left corner of the plot. The temperature increases almost linearly with timestep for most of the history points. The peak temperature in this case was 17.81°C , and therefore a temperature rise of 7.81°C . This was attained in the centre of the particle (at (80,80)), and then the maximum temperature attained then decreases as the measurement location approaches the heated particle boundary.

At the centre, conduction in to the transparent phase is minimised, and the heat lost is negligible. As distance from the centre increases, the transparent phase becomes closer, and therefore the tendency to conduct outwards (from the centre of the heated particle) is increased. The lowest temperature increase is at the furthestmost point from the heated particle centre as to be expected.

The temperature plots outside the particle boundary have different shapes from those inside the heated particle. The rate of temperature increase inside the heated particle decreases with time, as greater time is allowed for conduction into the transparent phase. Outside the heated particle, the rate of temperature increase, increases with time, as progressively there is a greater temperature difference between the inside of the heated particle and the transparent phase, leading to a greater driving force for conduction, and in turn a greater heat flux. This variation of temperature profiles will lead to greater variation in the magnitude of expansion and stress within the material.

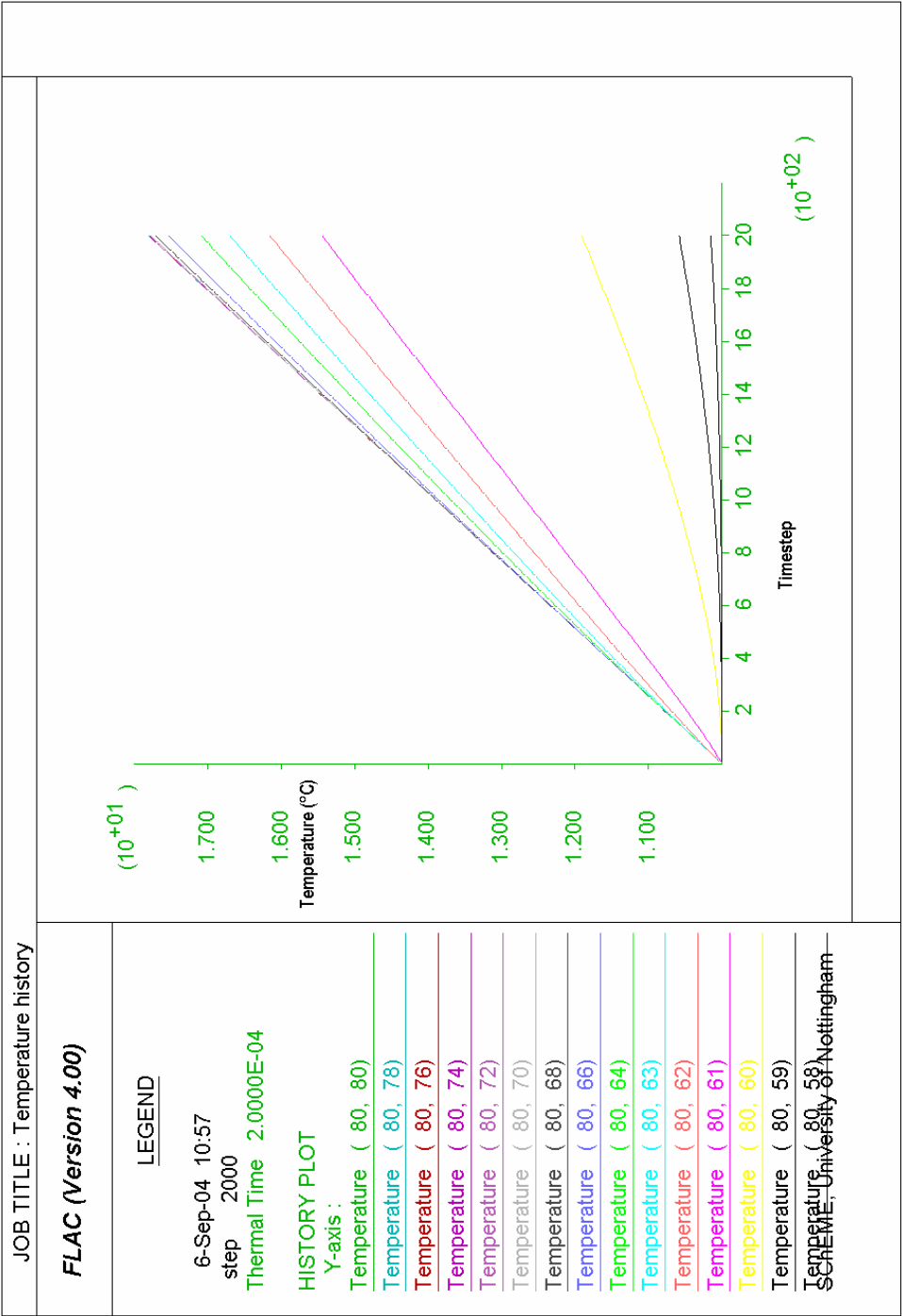


Figure 6.11: Variation of temperature with timestep for different positions in the model. Highest temperature rise occurs for centre position (80,80) and then decreases as grain boundary is approached.

The history locations were then assigned the volumetric strain parameter for recording. On initial examination the Figure seems very similar to the pattern observed in Figure 6.11. However, it can now be seen that the peak volumetric strain does not correspond to the positions of the history locations. The highest volumetric strain increase is at locations $j=76$ and $j=72$ which correspond to regions inside the heated particle. The maxima then occur at the following positions accordingly:

$j=74, j=68, j=70, j=64, j=78, j=66, j=80, j=63, j=62, j=61, j=60, j=59, j=58$

Here, the prefix j relates to the vertical zones in the model. The grain boundary occurs between $j=60$ and $j=61$. For positions near the grain boundary, i.e. $j=63, j=62, j=61, j=60, j=59, j=58$ the volumetric strains decrease in order away from the heated particle centre. Locations $j=60, j=59$ and $j=58$ lie inside the transparent phase. Inside the heated particle the regime is more complex.

This irregularity is possibly due to the effect of confinement on the material, or it could be a volumetric effect, due to the history points occupying regions where the heat transfer area is changing. It could also be due in part to the standard deviation applied to some of the strength parameters. However, it is still the case that the highest volumetric strain is inside the heated particle as expected. If fewer steps are run then it is possible to zoom in to the earlier stages as in the next plot, and here there is another variation occurring. It is as yet unclear as to the reasons for this wilder fluctuation.

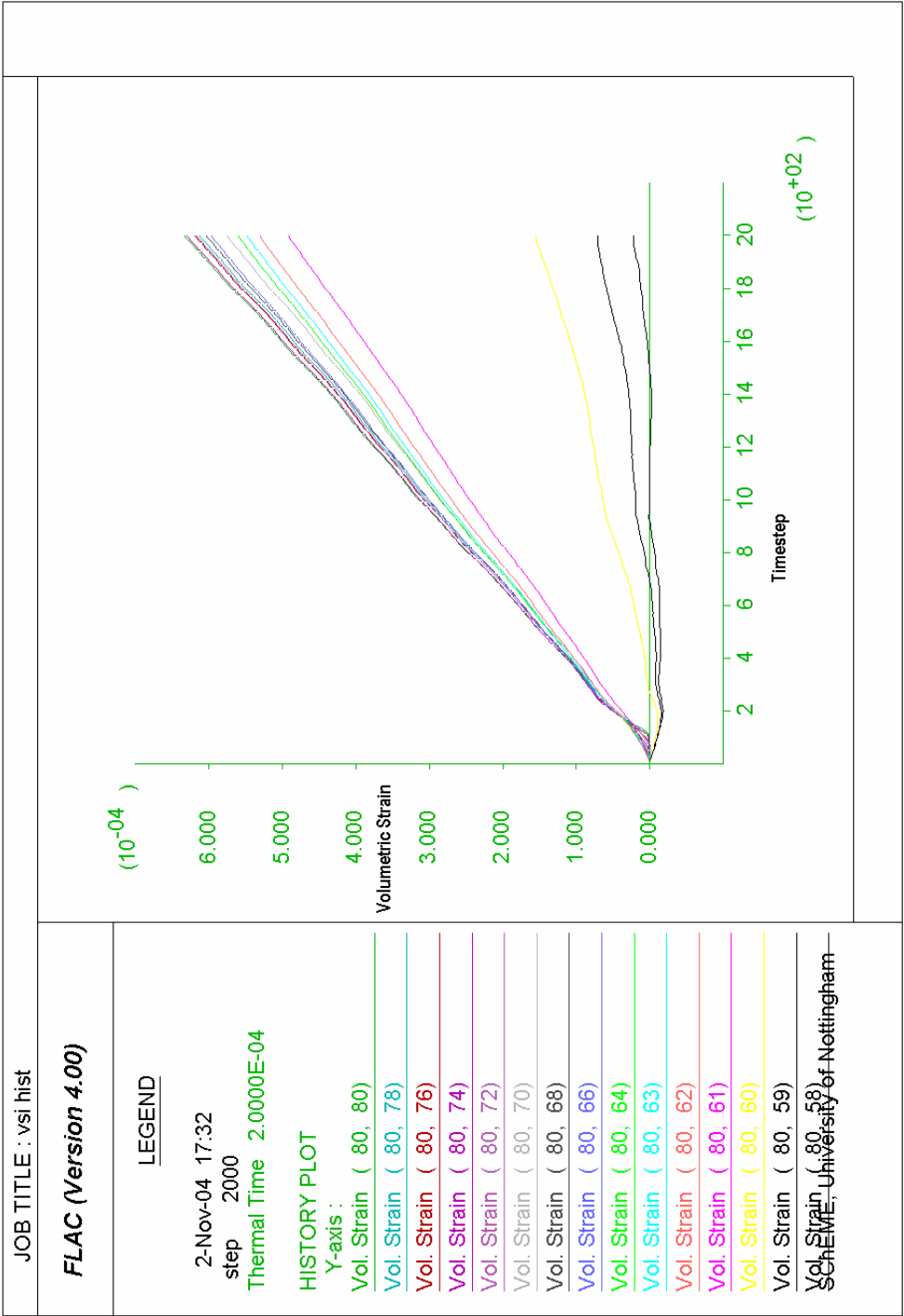


Figure 6.12: Plot showing volumetric strain increment profiles for various positions in the sample.

The next parameter to be studied was the volumetric strain rate. Figure 6.13 shows the volumetric strain histories for the locations in the sample. The peak value occurs for the central (80,80) point. Maxima occur subsequently for the other points in the complete particle. It is possible that these peaks in strain rate correspond with the times where the first fractures occur. High strain rates will lead to high stresses, but these stresses may occur in tension, compression or shear. The directionality of these stresses will determine the points in the material which are most likely to be weakened, as compression is likely to strengthen the material at that point. It is thought that the underlying mechanism is a balance between the quantity of heat input, and the rate at which it is applied. Too little total heat input will not give rise to sufficient strain. Too low a heating rate will not generate sufficient stresses as they will have time to redistribute and dissipate.

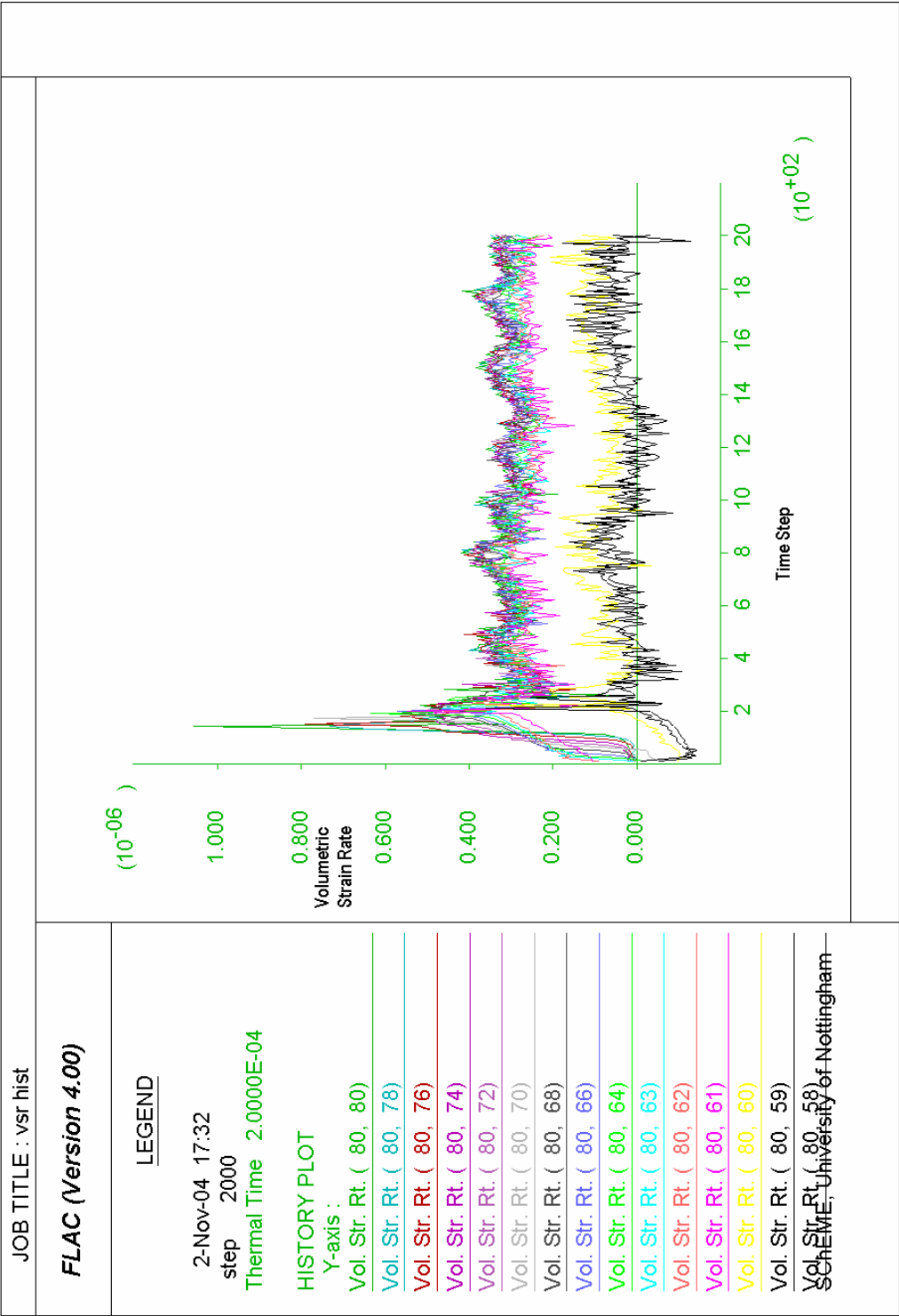


Figure 6.13: Volumetric strain rate histories.

In Figure 6.14 below it can be seen that the highest shear strain occurs in the transparent phase at locations $j=60$, $j=59$ and $j=58$. These strains are significantly higher than in the heated particle. The material is weaker in shear than in compression. This result suggests that the region immediately outside the heated particle will be subjected to localised high shear stresses resulting in fractures as observed in section 6.2.3. The heated particle itself seems to be undergoing very little shear strain as shown by the plots, with the centre position experiencing the least as expected.

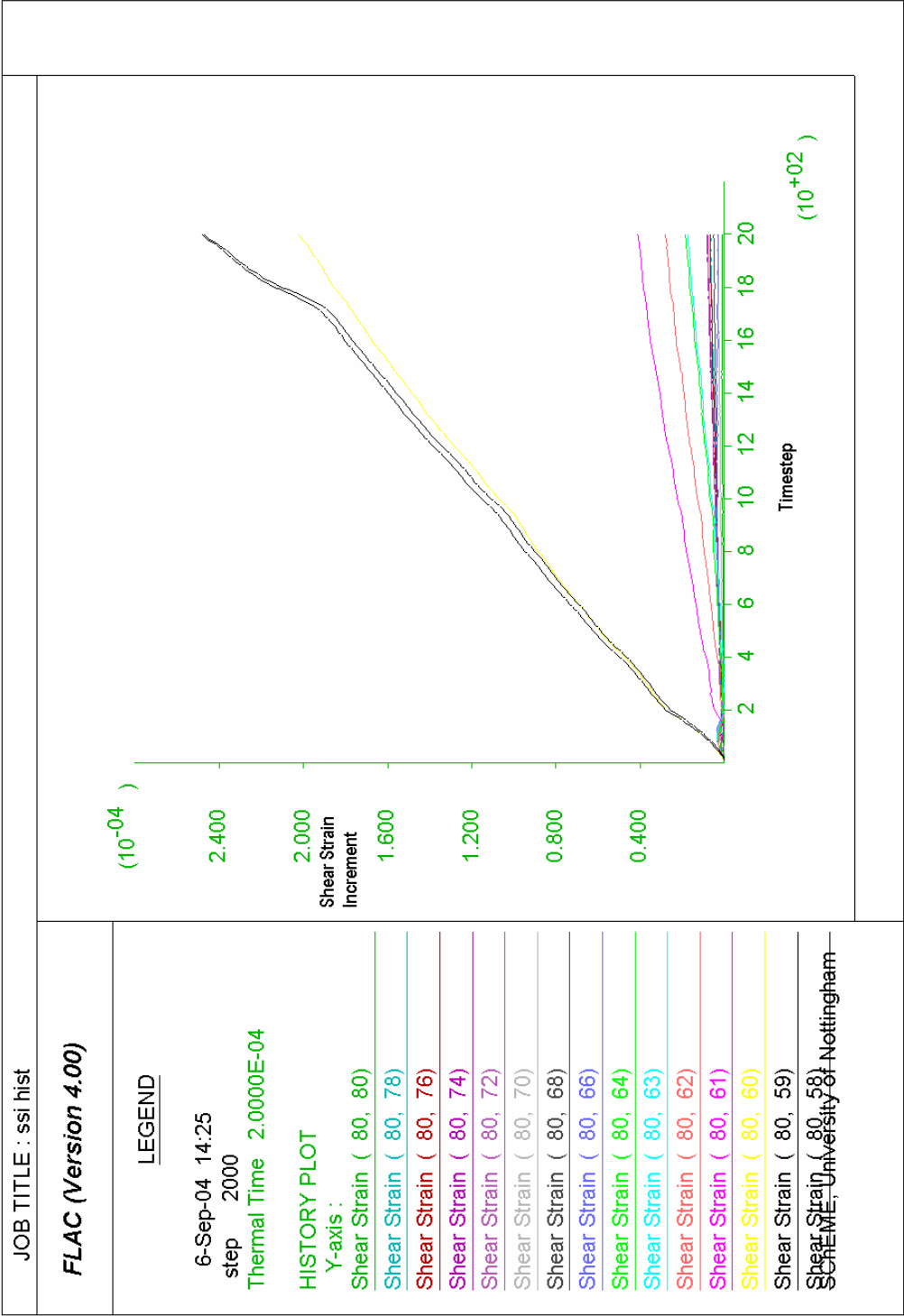


Figure 6.14: Shear strain increment histories at various positions.

Figure 6.15 is a complex plot and details the rise of shear stress in the sample as heating progresses. The shear stress is rising at all locations within the particle. The highest rise in shear stress occurs at $j=61$ (purple) and this corresponds with the outermost region of the heated particle adjacent to the grain boundary. The locations at which subsequent maxima occur does not appear to follow the same order as the history locations along the vertical and it seems the whole stress regime is very chaotic. However, there does seem to be a steadiness in terms of the rate at which the stress is increasing, but there is no correlation between position and stress. It is interesting to note that the plots for the heated particle zone adjacent to the grain boundary, $j=61$, and the transparent phase zones, $j=60$, $j=59$, and $j=58$ appear to reach plateau after 1600 steps. This corresponds with the first appearance of plasticity in the transparent phase as shown in Figure 6.16. This suggests that the stresses and strains at these points have resulted in a substantial degree of strain softening, and that no further stress increase is likely.

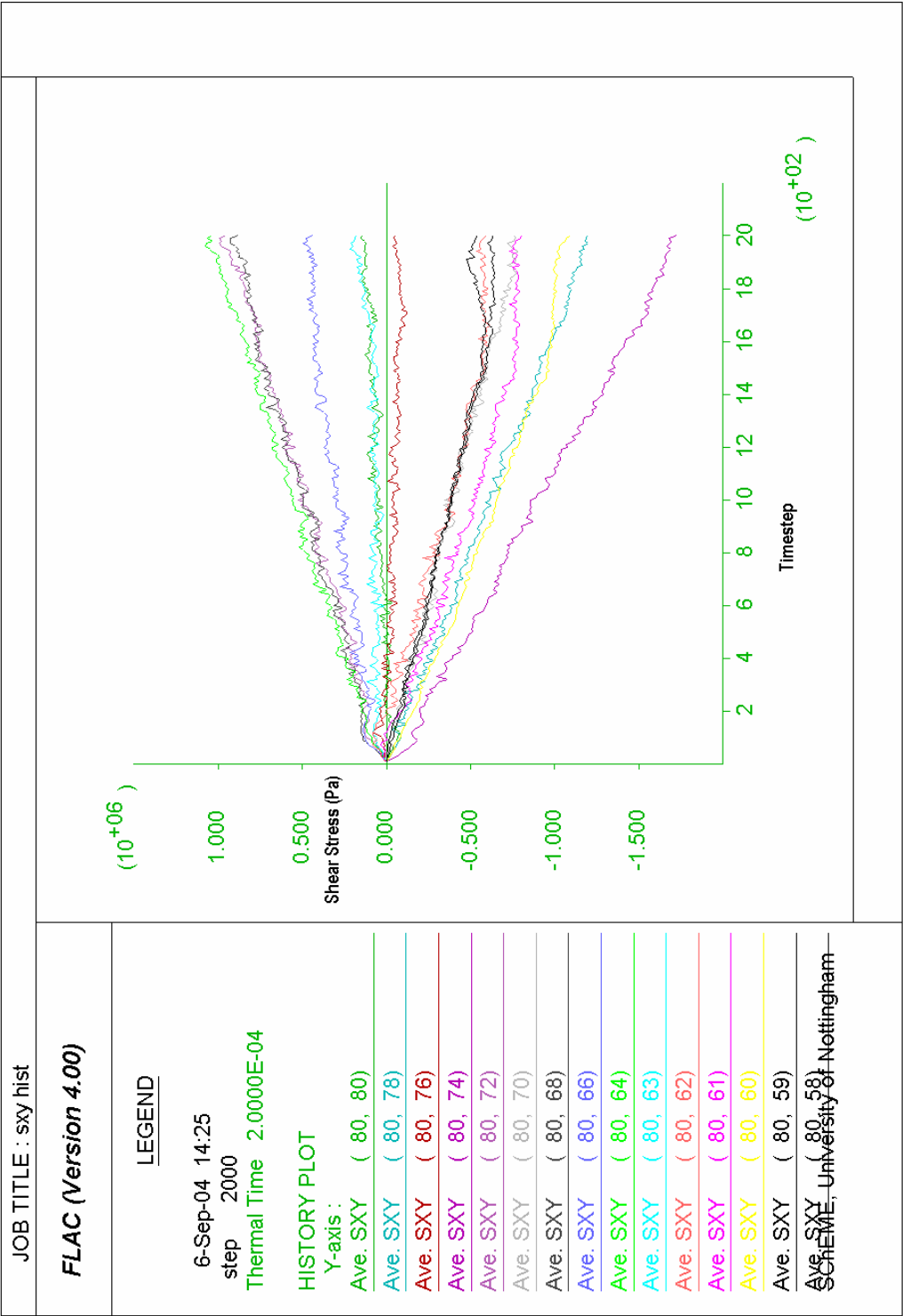


Figure 6.15: Plot showing variation of shear stress with timestep

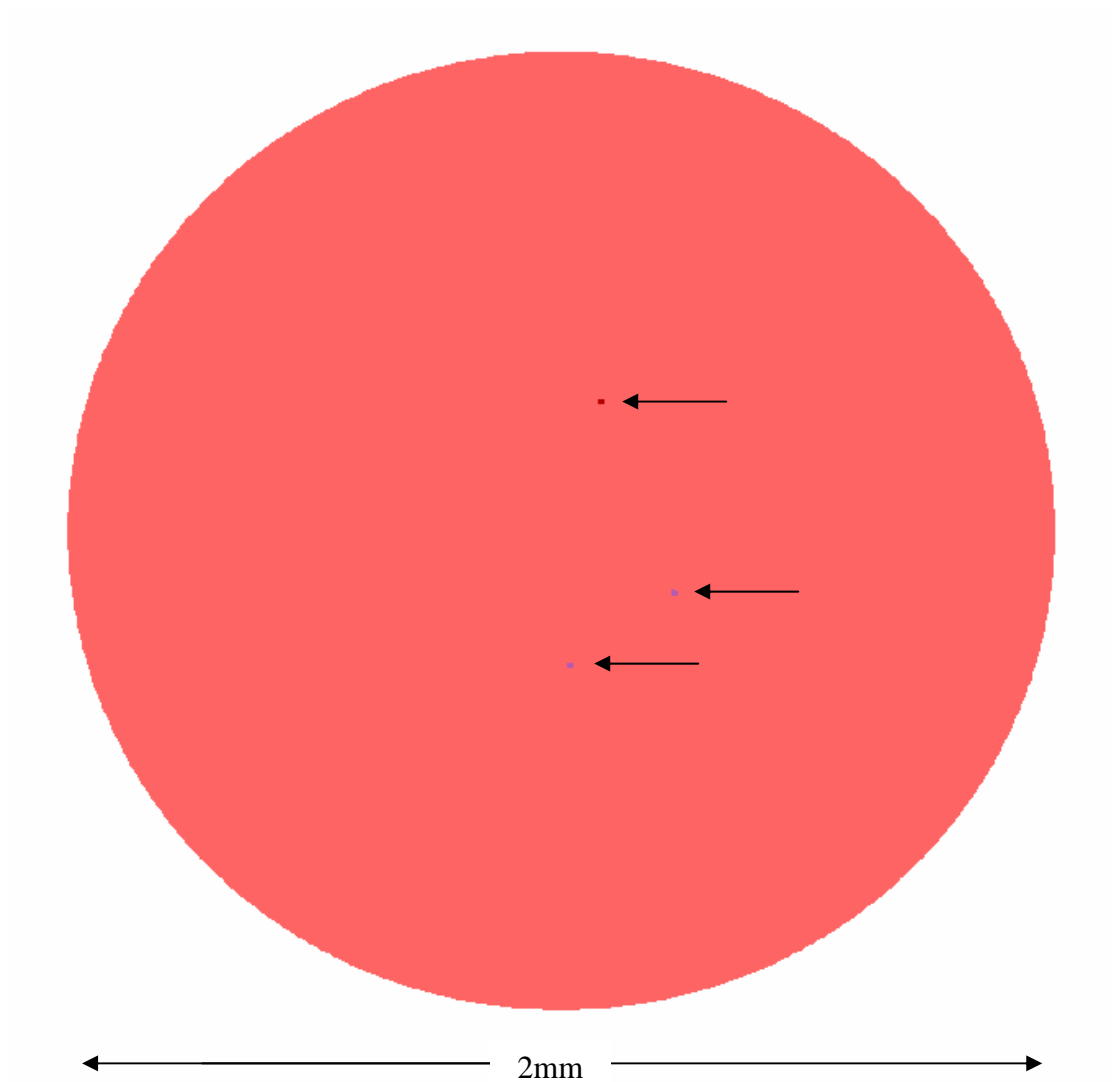


Figure 6.16: First appearance of plasticity after 1600 steps (0.16ms). Plasticity is denoted by the single zones marked with darker red colour or purple, depending on cause of plasticity. Plasticity again appears around grain boundary initially.

In Figure 6.17 there is a strong correlation with displacement inside the heated particle and location within the grain, showing that the innermost regions of the heated particle undergo less displacement than those near the particle boundary. The highest displacement occurs for the $j=61$ point – one zone inside the heated particle. This is to be expected, as it would undergo the sum of all the displacements undergone by all the innermost heated particle points.

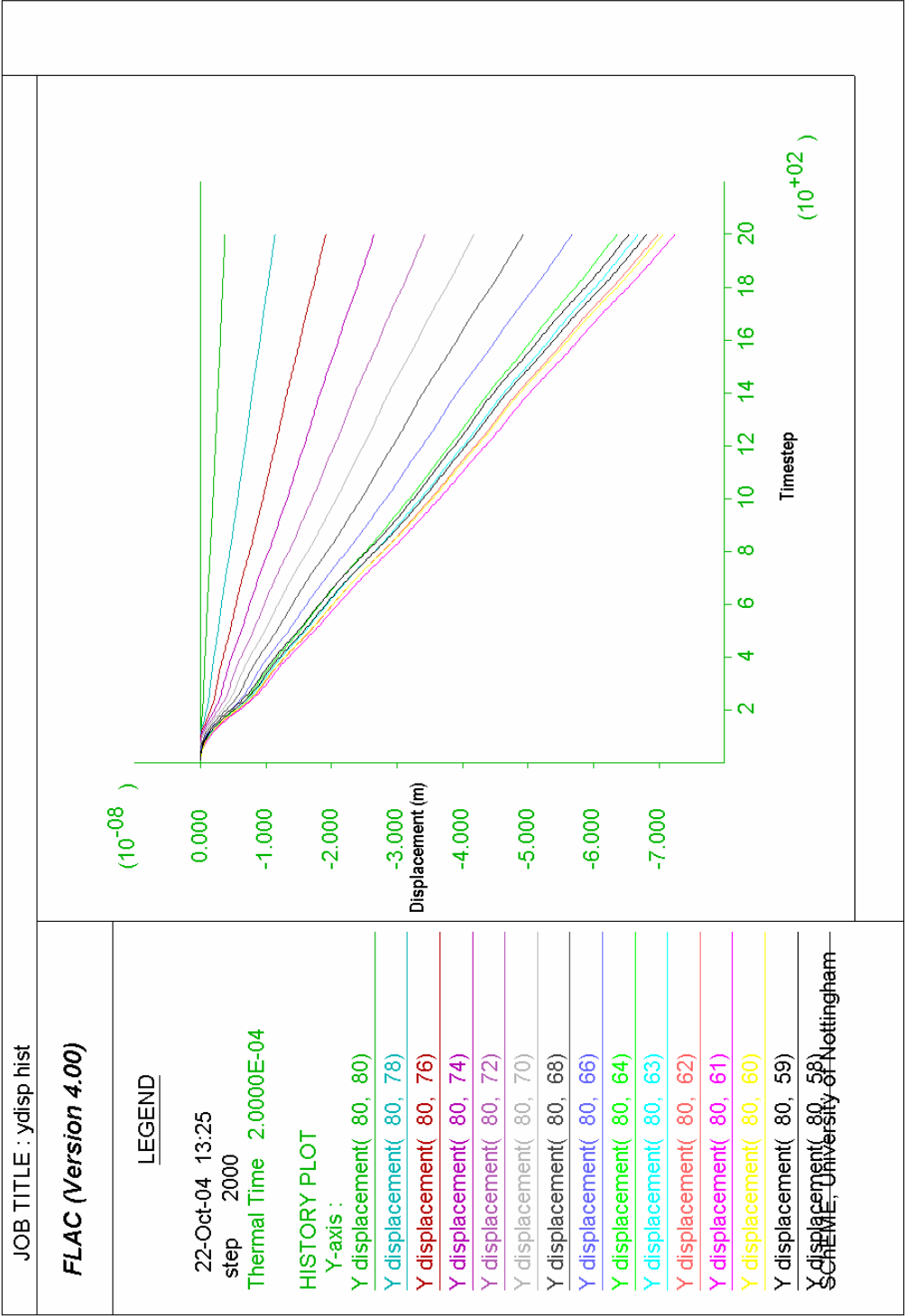


Figure 6.17: Displacement in vertical direction.

6.3.4 Discussion

The work in this section has examined the stresses and strains that arise from rapid heating of the central heated phase. Again the main conclusion that can be drawn is that the particle is most likely to fracture at the grain boundary. The highest shear strains and shear stresses occur inside the transparent phases closest to the grain boundary. This weakening is not dependent on the temperature at these locations, as Figure 6.11 shows that the temperature rise is much lower than in the heated particle. The weakening is likelier to be dependent on high rates of temperature rise with time inside the heated particle and consequently high rates of change of temperature with position in the vicinity of the grain boundary. This shows that microwave treatment may not only increase the likelihood of fracture at the grain boundary, but that the grain boundary is the location for where fracture is most likely to occur. However, this holds true for this simplified system where circular particles have been used. It is expected that deviation from circular models would result in a greater predominance of trans-granular failure as any angularity would introduce stress concentration due to imbalance in the stress distribution.

The higher probability of grain boundary fracture could result in significant process benefits. When the material is crushed, there is a higher probability that the heated particle is liberated at a coarser size, and negates the need for further energy intensive crushing. It could also mean that as the heated phase is liberated at a coarser size, then fewer fines are likely to result. These fines can potentially be lost to tailings, and the efficiency of recovery is decreased.

6.4 Closer Examination of Stress Regime

6.4.1 Introduction

This section examines the stress differences and hence the occurrence of shear stresses in the sample in order to better understand the state plots in Figures 6.3 to 6.6, 6.8, 6.9 and 6.16. High stress difference will result in high shear stresses. It was thought that if the stress difference and state plots were compared then the stress regime would become clearer. The objective was to better understand how the stress regime gave rise to these areas of tensile and shear failure.

6.4.2 Methodology

The same model was examined as in the previous sections whereby a circular 2mm transparent phase contained a 500µm heated particle. A power density of $1 \times 10^{11} \text{ W/m}^3$ was applied to the heated phase for 0.2ms. The state plot was compared the stress difference plots. The stress difference plots had various threshold values assigned. This means that contours were only plotted for areas in the particle where a stress difference of greater than a prescribed value was occurring. These values were 25MPa, 20MPa, and 15MPa. This was in order to discover at which level of stress difference the state plot began to indicate shear or tensile failure.

6.4.3 Results

The extent of the heated particle can be seen in Figure 6.18, and the initial stages of plasticity development can be seen surrounding it. This corresponds well with the plots of stress difference in Figure 6.19, which has a threshold of 25MPa assigned to the stress difference contours. The contour range is shown in the key on the left side of the plot. In the first plot, the minimum contour is 25MPa. Therefore any stress difference lower than this is omitted from the plot.

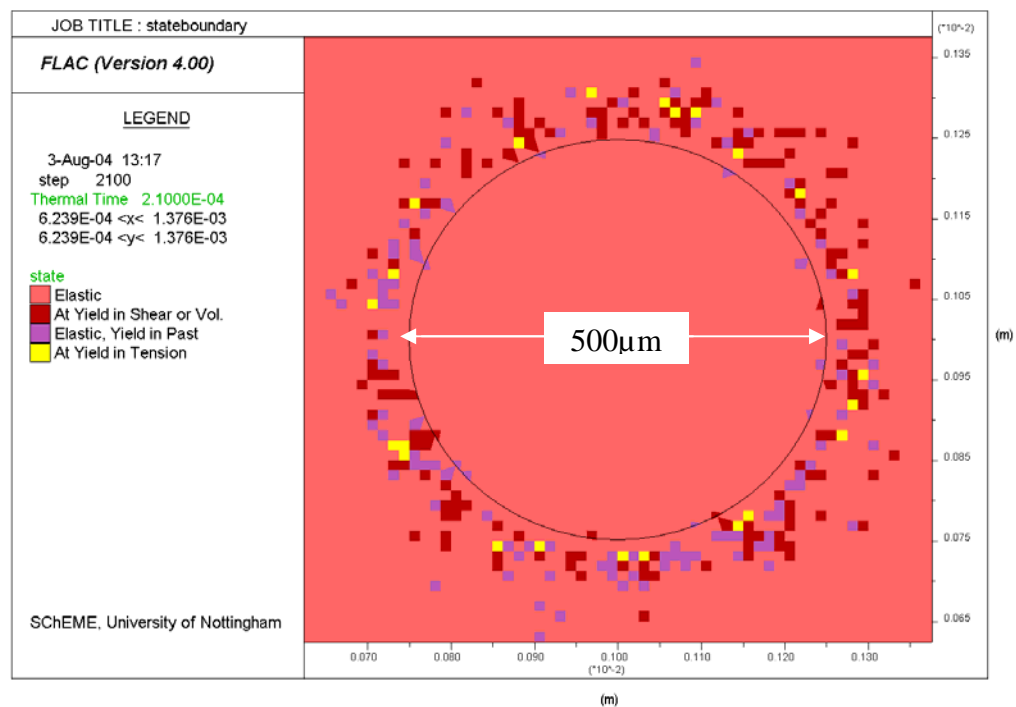


Figure 6.18: State plot detailing fractures outside heated particle boundary

It is interesting to note the change as the stress difference minimum limit is decreased. In the following plots the limit is decreased to 20MPa and 15MPa respectively. Then it should be possible to determine the approximate stress difference level that corresponds with the onset of plasticity.

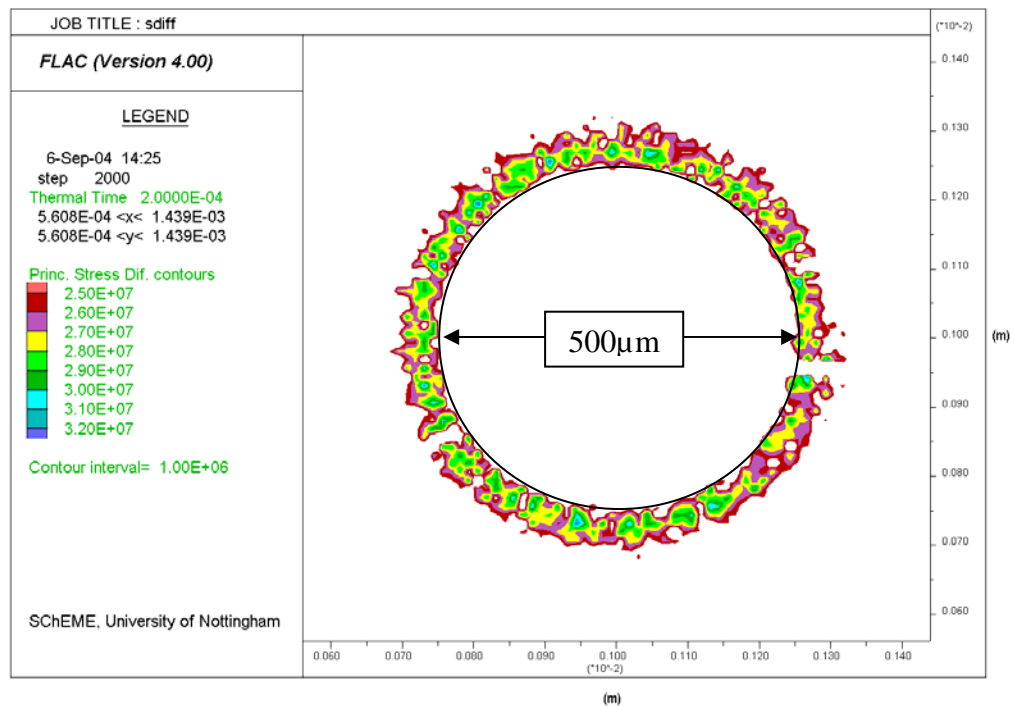


Figure 6.19: Stress Difference contours, minimum 25MPa

With the threshold set at 20MPa, it is clear that the area covered by the contours in Figure 6.20 matches closely the area covered by Figure 6.18. It is evident that above a stress difference of 20MPa, plasticity is very likely.

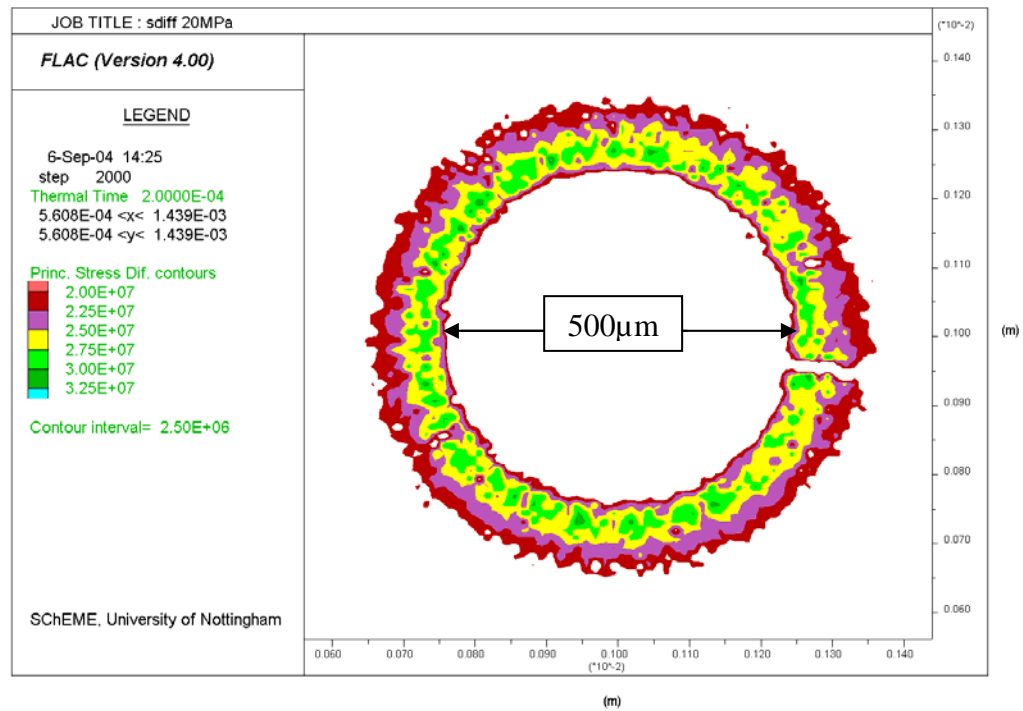


Figure 6.20: Stress Difference contours, minimum 20MPa

When the stress difference threshold is set to 15MPa, the area covered by the contours becomes much larger, and no longer corresponds to the state plot in Figure 6.18. Therefore it is unlikely that below 15MPa stress difference that plasticity is likely to occur.

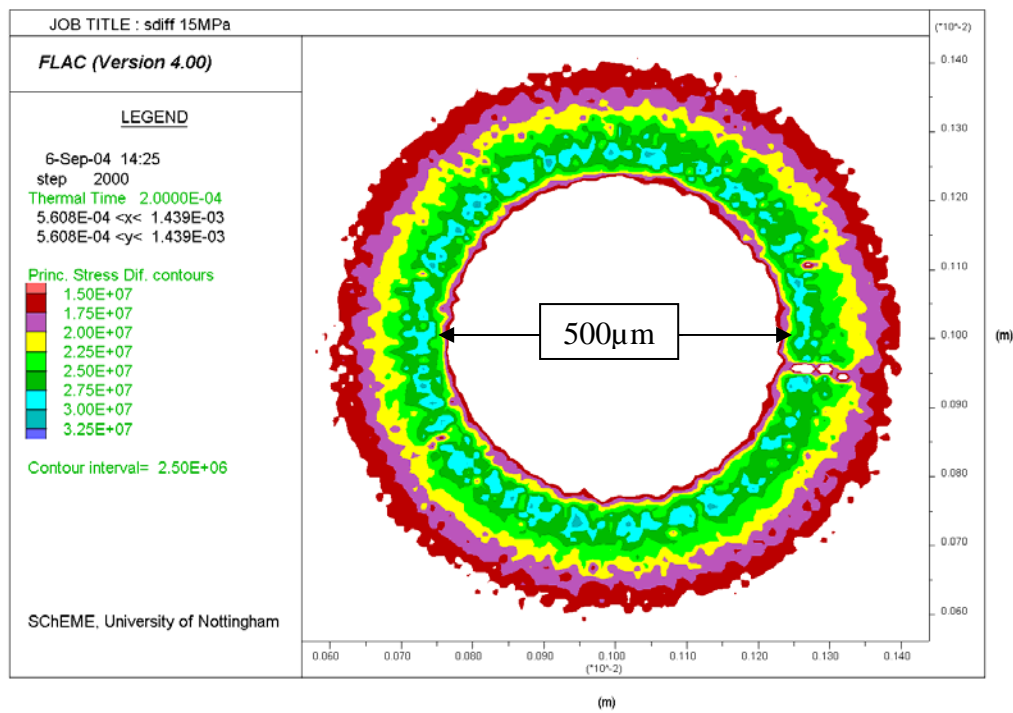


Figure 6.21: Stress Difference contours, minimum 15MPa

6.4.4 Discussion

Again the study has demonstrated that high shear stresses occur in the transparent phase adjacent to the heated particle boundary. In an idealised system, this could facilitate enhanced liberation, in that the weakening is occurring around the grain boundary, and that the responsive particle is left intact. This would decrease the likelihood of transgranular fracture, as any external compression will now liberate the locked heated particle effectively. It can be seen that shear or tensile fractures occur when shear stresses of 20-25MPa develop in the sample.

6.5 Further Parameter Variation with Position inside the Particle

6.5.1 Introduction

The following section details the plots obtained when a profile line is drawn from the centre of the heated particle to across the boundary and into the transparent phase. It is possible to assign almost any parameter such as temperature, the various stress types or strains to the profile line to indicate how the parameter varies with position.

6.5.2 Methodology

The same model conditions were used as in the previous section: a 2mm circular transparent particle containing a 500µm circular heated particle exposed to 1×10^{11} W/m³ for 0.2ms. The profile line was drawn diagonally downwards to the left from the centre of the heated particle towards the heated particle boundary and beyond. The diagonal line was necessary due to *FLAC*'s convention with positive and negative shear stresses as explained in section 5.3. Various parameters were assigned to the profile line and these included temperature, volumetric strain, shear strain, stress difference, shear stress, principal stress, and compressive stress in both horizontal and vertical directions. This was completed in order to study the interactions between parameters and study the variation with position.

6.5.3 Results

Figure 6.22 shows the variation of temperature as the profile line moves from the centre of the heated particle along diagonal profile line. The temperature remains constant at 17.8°C inside the majority of the heated particle and then begins to drop off, gradually to begin with inside and then most rapidly on the grain boundary itself. The temperature falls back to an ambient temperature of 10°C. The material thermal properties change as the grain boundary is crossed so that there is a slight kink in the curve, as the effects of changing specific heat capacity and conduction manifest themselves. This plot represents a temperature change of 7.8°C over little more than 0.1mm, and it is thought that these extremely localised temperature variations give rise to the predominance of shear stresses close to the grain boundary.

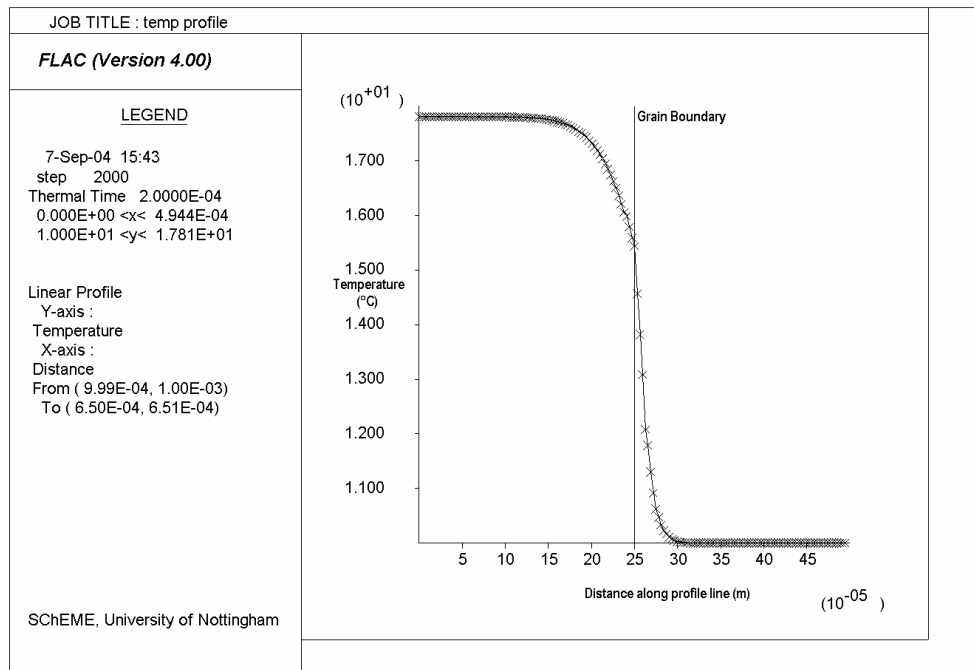


Figure 6.22: Temperature profile plot along diagonal from centre

Figure 6.23 shows the variation of volumetric strain along the profile line. As expected, the volumetric strain increment profile closely matches that of the temperature plot. It can be concluded that volumetric strain is solely dependent on the temperature in this case. The same pattern is repeated as in Figure 6.22 where the volumetric strain remains fairly constant inside the heated particle and drops off very rapidly inside the transparent phase.

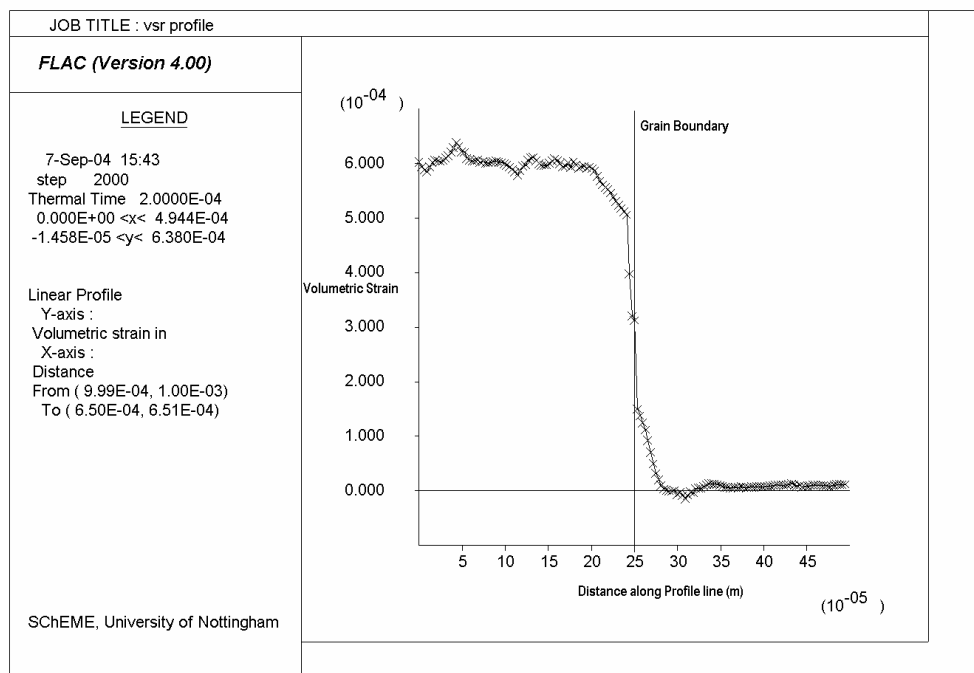


Figure 6.23: Volumetric Strain increment profile plot

In Figure 6.24 there is a very large increase in shear strain as the profile approaches the boundary. The peak shear strain of 24×10^{-5} occurs just inside the transparent phase. The strain then falls off gradually as the distance from the grain boundary increases into the transparent phase. As expected there is very little shear strain inside the heated particle. Figure 6.24 clearly illustrates why shear failure is likely on the grain boundary.

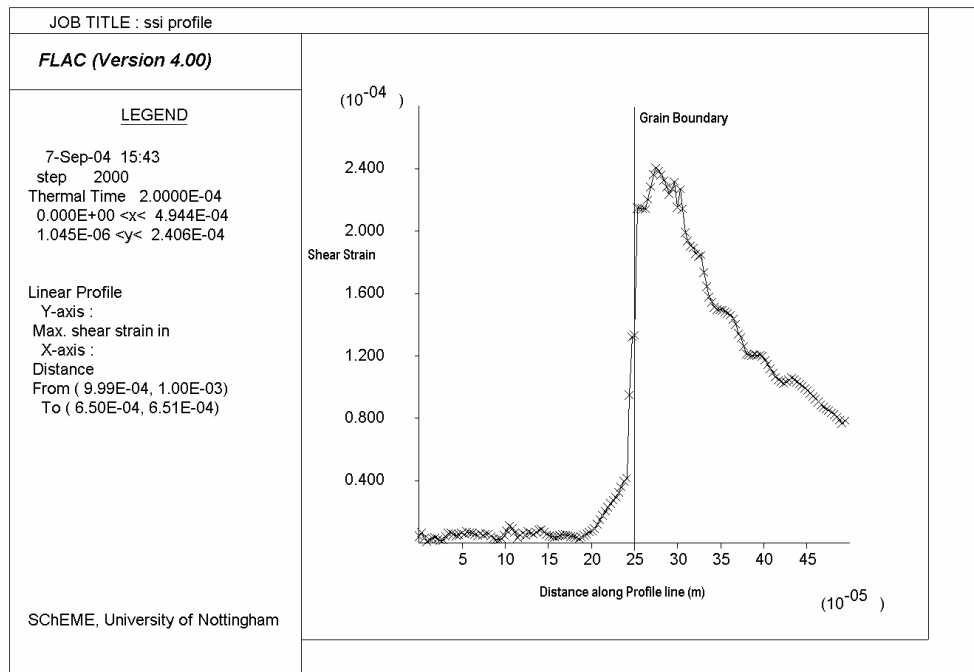


Figure 6.24: Shear Strain increment profile plot

The peak of shear strain around the grain boundary in Figure 6.24 seems to correspond with Figure 6.25 – showing the peak in the stress difference. The plot is not as regular as the shear strain increment plot but follows it closely overall. Again the peak is located outside the boundary at around 27×10^{-5} m from the centre. The peak stress difference is approximately 28MPa. These elevated stress differences would seem to indicate that there is a large degree of shear stress at that point. Convention dictates that shear stresses in the upper-right-to-lower-left direction are positive, which as previously mentioned is why the diagonal profile line was used. This has no other consequence due to the symmetry of the system.

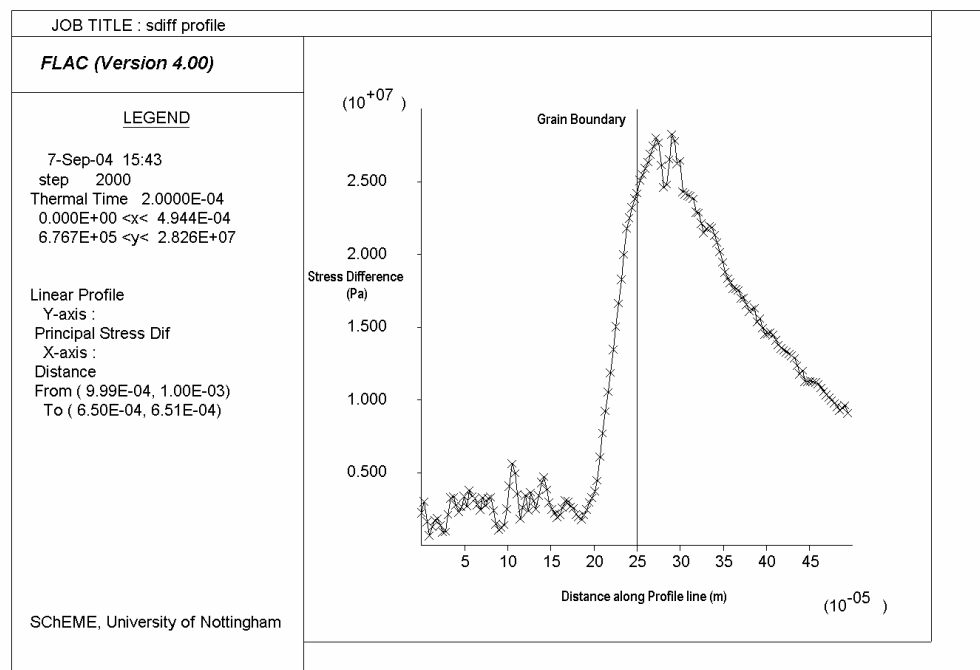


Figure 6.25: Stress difference profile plot

If the shear stress is plotted along this diagonal profile line as in Figure 6.26, again a peak is seen around $27 \times 10^{-5} \text{ m}$ along the profile line. The heated phase extends $25 \times 10^{-5} \text{ m}$ from the centre. Stresses are plotted as negative on this plot. The peak stress here is approximately 14MPa. This is half the value of the peak stress difference shown in Figure 6.25, which is to be expected as it is possible to infer that 14MPa is acting tangentially along or just outside the grain boundary and 14MPa acting in the opposite direction. This area of highest shear stress will result in the first cracks that appear in the material. Eventually as more heat is applied the shear stress will become high enough so that the entire region outside the grain boundary begins to behave plastically. This plot is symmetrical about the horizontal axis of the previous plot.

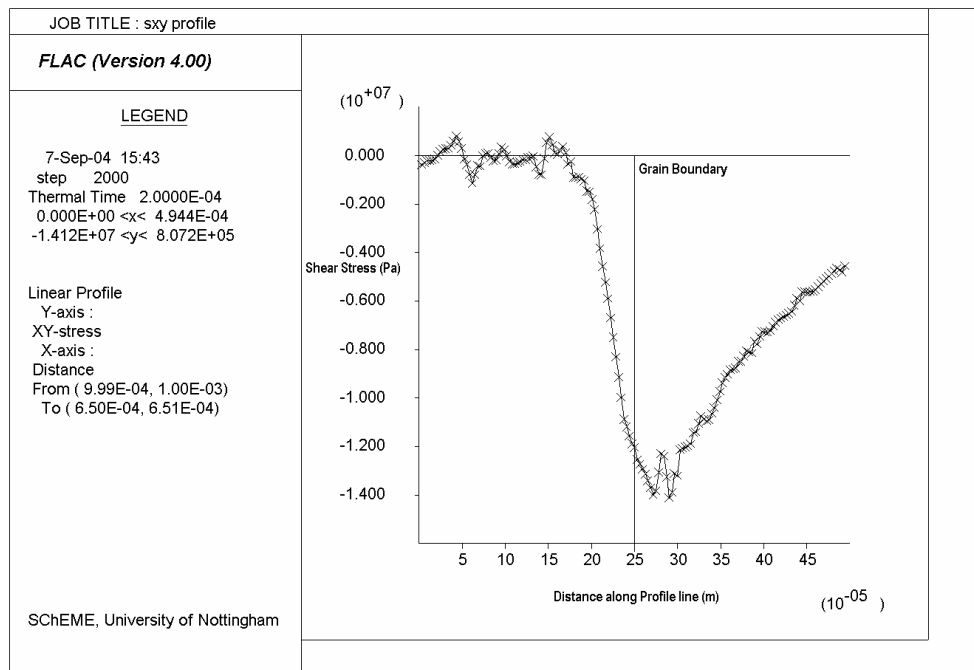


Figure 6.26: Shear Stress Profile plot

The variation of principal stresses with position is presented in Figure 6.27. The highest principal stress is in the heated particle sample at around 4×10^{-5} m along the profile line, and then tails off towards zero after passing the grain boundary. The peak principal stress here (Sig. 1) is around 30MPa. High confining pressure results in a stronger material. Therefore this plot shows that the high degree of confining pressure is unlikely to cause fracture in the heated phase.

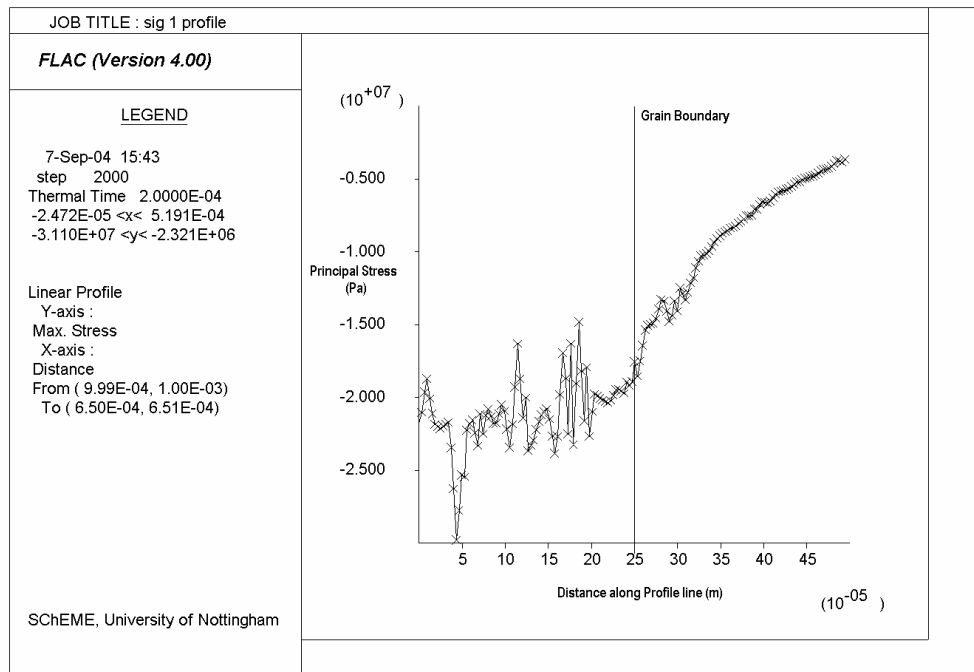


Figure 6.27: Principal stress profile. Stresses are negative due to convention.

The variation of compressive stress in the vertical direction is shown in Figure 6.28. The maximum peak stress in the vertical direction (S_{yy}) is approximately 29MPa. These compressive stress profiles are quite irregular in the heated particle. The stress field is therefore very complex inside the heated particle as all its constituent points are expanding against each other because of the volumetric heating rate. The high compressive stresses will not result in failure in this case. These stresses are believed to be acting radially inwards or outwards in the sample. They will merely result in confinement and an increase in the strength of the material at that point.

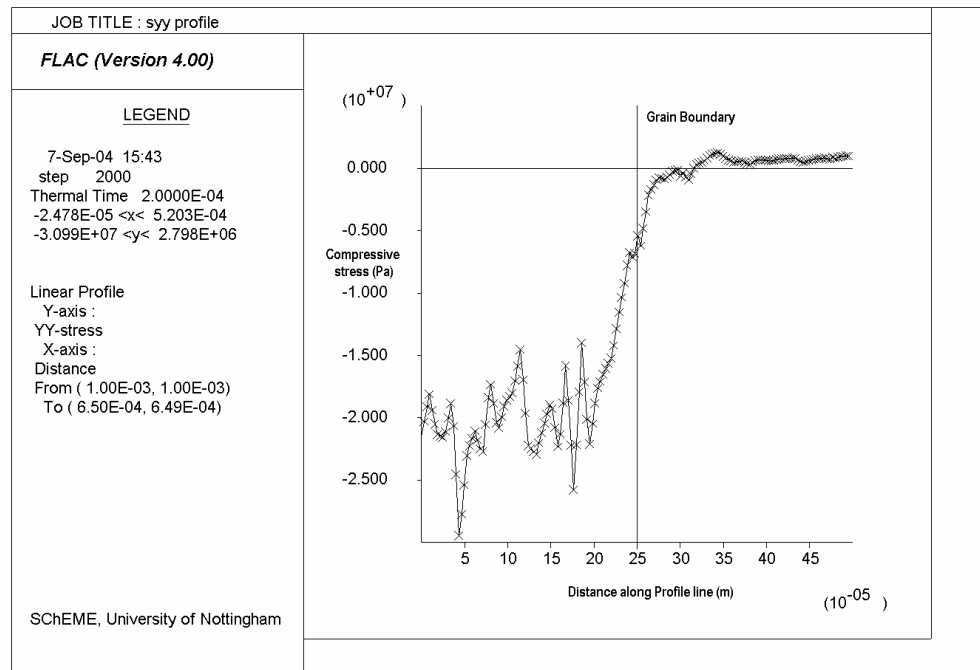


Figure 6.28: Compressive stress in the vertical direction.

Again the same pattern is shown in Figure 6.29 where the variation of the compressive stresses in the horizontal direction is shown to yield significant compression in the central heated particle and very little confinement outside the heated particle. This low degree of confinement in the transparent phase will allow the formation of shear and tensile stresses as shown previously in this section.

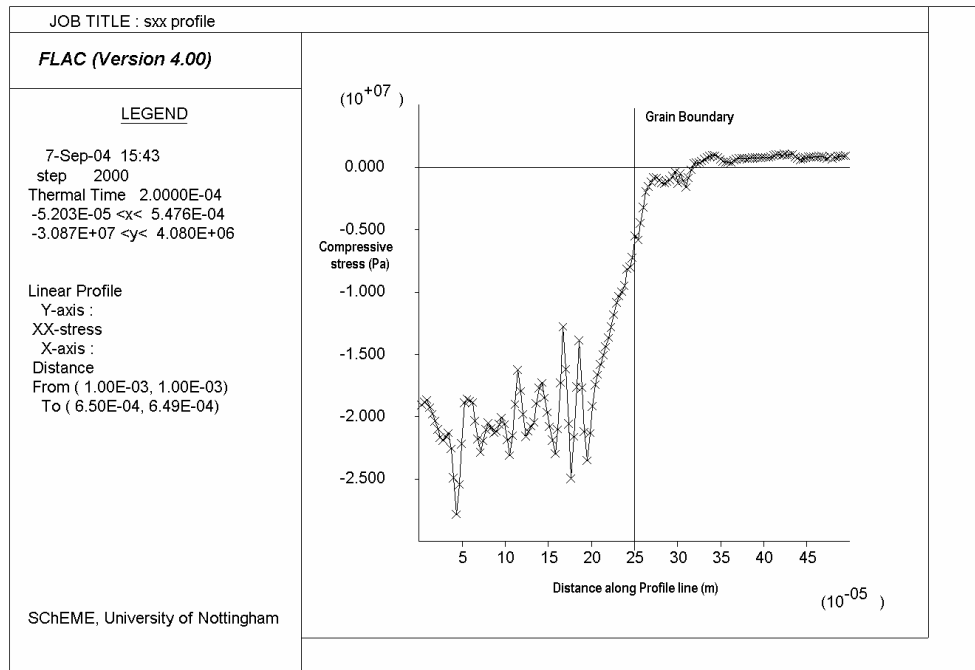


Figure 6.29: Compressive stress in the horizontal

6.5.4 Discussion

This section has again shown that the highest shear stresses are likeliest to occur in the transparent phase immediately outside the heated particle boundary. It has also been shown that the highest compressive stresses occur inside the heated particle. This would result in making the heated particle less susceptible to fracture, as it is harder for cracks to initiate and propagate. Again this work has shown that liberation can be improved by increasing the probability of intergranular fracture, whilst keeping the heated phase intact. This would effectively increase the liberation size; result in fewer fines of heated phase being generated, whilst also reducing the overall comminution energy. All this can be achieved for very small temperature increases, as long as the power density is sufficiently high and the exposure time sufficiently low in order to maintain a favourable energy balance.

6.6 Influence of Grain Size on Development of Stresses and Strains

6.6.1 Introduction

This section details a study designed to examine the effect of varying the size of the particles involved. It has been discussed in Chapter 3 that there is a decrease in efficiency of microwave-assisted breakage when smaller size fractions are treated.

6.6.2 Methodology

A 500 μm heated particle was placed in a 2mm circular transparent particle. The diameter of the heated particle was varied from 50 μm to 500 μm . The power density was varied from $1 \times 10^8 \text{ W/m}^3$ to $1 \times 10^{11} \text{ W/m}^3$. One study was conducted after applying the heating rate for 1ms, and another smaller study examined the case where heat was applied for 10ms to see if the patterns were repeated. The power densities were chosen to be representative of those that are possible using current general laboratory microwave equipment. The exposure times were chosen so that the total energy input remained realistic, and not prohibitive to possible industrial implementation.

The peak temperature attained, peak compressive stress, peak shear strain and peak shear stress in the sample were noted and are presented in the following section.

6.6.3 Results

Table 6.1 shows the peak temperature, compressive stress, shear strain and shear stress attained in the sample for each particle size and for a power density of $1 \times 10^8 \text{ W/m}^3$. It can be seen from the table that as the diameter of the heated particle rises then so do the peak temperatures attained. This consequently increases shear strain and the compressive and shear stresses. The total temperature rise in this case is very small and yet the stresses generated are very significant. There is a larger difference between the results obtained for 50 μm and 100 μm than there is between the results obtained for 450 μm and 500 μm , and this suggests that the temperature rise decreases rapidly for the smaller sizes. This would result in smaller stresses being generated for the smallest sizes.

Diameter (μm)	Temp ($^{\circ}\text{C}$)	P.D. (W/m^3)	Compressive Stress (Pa)	log Sxx	Shear Strain	log ssi	Shear Stress (Pa)	log Sxy
50	10.0111	10^8	2.80E+04	4.45	1.60E-07	-6.80	1.09E+04	4.04
100	10.0195		6.30E+04	4.80	3.30E-07	-6.48	2.10E+04	4.32
150	10.026		8.30E+04	4.92	5.00E-07	-6.30	3.40E+04	4.53
200	10.029		9.40E+04	4.97	6.40E-07	-6.19	3.80E+04	4.58
250	10.033		1.06E+05	5.03	7.50E-07	-6.12	4.70E+04	4.67
300	10.035		1.17E+05	5.07	8.00E-07	-6.10	5.10E+04	4.71
350	10.037		1.21E+05	5.08	8.40E-07	-6.08	5.50E+04	4.74
400	10.037		1.23E+05	5.09	9.30E-07	-6.03	5.80E+04	4.76
450	10.038		1.30E+05	5.11	9.40E-07	-6.03	6.30E+04	4.80
500	10.038		1.40E+05	5.15	1.00E-06	-6.00	6.70E+04	4.83

Table 6.1: Peak stresses and strains for 1millisecond at $1 \times 10^8 \text{ W/m}^3$

If the power density is increased tenfold from $1 \times 10^8 \text{ W/m}^3$ to $1 \times 10^9 \text{ W/m}^3$ then Table 6.2 is obtained. Again the pattern is repeated where as the size increases so does the peak temperature rise, and subsequently so do the magnitudes of the stresses and strains. As the power density is increased tenfold so is the total temperature rise in each case. There is also an approximate tenfold rise in the magnitude of the stresses and strains. These stresses are not likely to be large enough to cause strain softening in the model and are therefore too low to cause fractures in the particle.

Diameter (μm)	Temp ($^{\circ}\text{C}$)	P.D. (W/m^3)	Compressive stress (Pa)	log Sxx	Shear Strain	log ssi	Shear Stress (Pa)	log Sxy
50	10.14	10^9	2.90E+05	5.46	1.86E-06	-5.73	1.17E+05	5.07
100	10.195		6.00E+05	5.78	3.90E-06	-5.41	2.40E+05	5.38
150	10.26		7.50E+05	5.88	5.20E-06	-5.28	3.30E+05	5.52
200	10.3		1.04E+06	6.02	6.10E-06	-5.21	3.80E+05	5.58
250	10.33		1.11E+06	6.05	8.20E-06	-5.09	4.90E+05	5.69
300	10.35		1.22E+06	6.09	8.50E-06	-5.07	5.50E+05	5.74
350	10.36		1.19E+06	6.08	9.00E-06	-5.05	5.60E+05	5.75
400	10.37		1.31E+06	6.12	9.40E-06	-5.03	5.90E+05	5.77
450	10.38		1.32E+06	6.12	9.50E-06	-5.02	6.30E+05	5.80
500	10.38		1.40E+06	6.15	1.05E-05	-4.98	6.00E+05	5.78

Table 6.2: Peak Stresses and strains for 1 millisecond at $1 \times 10^9 \text{ W/m}^3$

If the power density is again increased fivefold from $1 \times 10^9 \text{ W/m}^3$ to $5 \times 10^9 \text{ W/m}^3$ then Table 6.3 is obtained. Again the pattern is repeated where as the size increases so does the peak temperature rise, and subsequently so do the magnitudes of the stresses and strains. The total temperature rise in each case has increased fivefold on the values shown in Table 6.2. There is also a further approximate fivefold rise in the magnitude of the stresses and strains. The shear stresses are now almost high enough at the larger sizes for significant strain softening to occur. The elevated stress will result in associated strain, and it is the strain which is the limiting component for strain softening to occur as described in Section 5.2

Diameter (μm)	Temp ($^{\circ}\text{C}$)	P.D. (W/m^3)	Compressive stress (Pa)	log Sxx	Shear Strain	log ssi	Shear Stress (Pa)	log Sxy
25	10.2	5×10^9	5.90E+05	5.77	2.60E-06	-5.59	1.08E+05	5.03
50	10.52		1.56E+06	6.19	6.70E-06	-5.17	3.80E+05	5.58
100	10.98		3.20E+06	6.51	1.62E-05	-4.79	9.70E+05	5.99
150	11.29		4.20E+06	6.62	2.60E-05	-4.59	1.50E+06	6.18
200	11.50		4.70E+06	6.67	3.30E-05	-4.48	2.20E+06	6.34
250	11.65		6.20E+06	6.79	3.50E-05	-4.46	2.30E+06	6.36
300	11.76		6.50E+06	6.81	4.00E-05	-4.40	2.60E+06	6.41
350	11.84		6.20E+06	6.79	4.60E-05	-4.34	2.80E+06	6.45
400	11.88		6.70E+06	6.83	4.70E-05	-4.33	2.90E+06	6.46
450	11.92		6.80E+06	6.83	4.80E-05	-4.32	3.10E+06	6.49
500	11.94		7.00E+06	6.85	5.20E-05	-4.28	3.20E+06	6.51

Table 6.3: Peak Stresses and strains for 1 millisecond at $5 \times 10^9 \text{ W/m}^3$

Once again the power density was increased, this time it was doubled from 5×10^9 W/m³ to 1×10^{10} W/m³. It can be seen that the maximum temperature rise has increased tenfold on those shown in table 6.2.

Diameter (μm)	Temp ($^{\circ}\text{C}$)	P.D. (W/m ³)	Compressive stress (Pa)	log Sxx	Shear Strain	log ssi	Shear Stress (Pa)	log Sxy
50	11.04	10^{10}	3.00E+06	6.48	1.40E-05	-4.85	8.50E+05	5.93
100	11.97		6.20E+06	6.79	3.10E-05	-4.51	2.10E+06	6.32
150	12.5		8.60E+06	6.93	5.20E-05	-4.28	3.30E+06	6.52
200	13.0		1.00E+07	7.00	6.70E-05	-4.17	3.90E+06	6.59
250	13.3		1.05E+07	7.02	7.00E-05	-4.15	4.60E+06	6.66
300	13.5		1.23E+07	7.09	8.10E-05	-4.09	5.20E+06	6.72
350	13.7		1.28E+07	7.11	8.80E-05	-4.06	5.50E+06	6.74
400	13.8		1.48E+07	7.17	9.40E-05	-4.03	5.70E+06	6.76
450	13.8		1.32E+07	7.12	9.60E-05	-4.02	6.00E+06	6.78
500	13.9		1.41E+07	7.15	1.02E-04	-3.99	6.20E+06	6.79

Table 6.4: Peak Stresses and strains for 1 millisecond at 1×10^{10} W/m³

Again a fivefold increase in power density was implemented to raise the power density from $1 \times 10^{10} \text{ W/m}^3$ to $5 \times 10^{10} \text{ W/m}^3$. As it was shown in section 6.4 fractures will appear when the shear stress exceeds 20-25MPa, and it is clear now that the shear stresses are high enough at sizes above 250 μm to induce significant fracturing. Hence a reduction in maximum compressive stress can be seen when the size increases from 450 μm to 500 μm , as the fracturing will result in redistribution of stresses, and a consequent reduction in the compressive stress maxima. The stresses are still not high enough to induce fracturing in the smaller sizes.

Diameter (μm)	Temp ($^{\circ}\text{C}$)	P.D. (W/m^3)	Compressive stress (Pa)	log Sxx	Shear Strain	log ssi	Shear Stress (Pa)	log Sxy
25	12	5×10^{10}	5.50E+06	6.74	2.40E-05	-4.62	1.00E+06	6.00
50	15.2		1.55E+07	7.19	7.40E-05	-4.13	4.50E+06	6.65
100	19.8		3.10E+07	7.49	1.70E-04	-3.77	1.03E+07	7.01
150	22.7		4.30E+07	7.63	2.60E-04	-3.59	1.65E+07	7.22
200	25		4.90E+07	7.69	3.20E-04	-3.49	1.85E+07	7.27
250	26.5		5.40E+07	7.73	3.80E-04	-3.42	2.20E+07	7.34
300	27.5		5.40E+07	7.73	4.70E-04	-3.33	2.30E+07	7.36
350	28.3		5.70E+07	7.76	5.10E-04	-3.29	2.40E+07	7.38
400	28.7		6.20E+07	7.79	4.70E-04	-3.33	2.30E+07	7.36
450	28.8		5.80E+07	7.76	6.40E-04	-3.19	3.00E+07	7.48

Table 6.5: Peak Stresses and strains for 1 millisecond at $5 \times 10^{10} \text{ W/m}^3$

The power density was doubled to $1 \times 10^{11} \text{ W/m}^3$, and now it can be seen that fracturing is likely in all sizes except the $50\mu\text{m}$ particle as the shear stresses have exceeded 20MPa in all the other sizes. It can be assumed that there is insufficient temperature rise in the $50\mu\text{m}$ heated particle to cause the necessary stress for fracturing. The temperature rise may be attenuated by the proportional increase in circumference which increases the proportion of heat conducted into the transparent phase. It is also possible that as the particle size and the subsequent magnitude of expansion decreases, the area over which the heated particle's surface's expansion is impinging is increasing proportionally.

Diameter (μm)	Temp ($^{\circ}\text{C}$)	P.D. (W/m^3)	Compressive stress (Pa)	log Sxx	Shear Strain	log ssi	Shear Stress (Pa)	log Sxy
50	20.3	10^{11}	2.80E+07	7.45	1.35E-04	-3.87	8.00E+06	6.90
100	29.6		5.60E+07	7.75	3.70E-04	-3.43	2.05E+07	7.31
150	36		7.80E+07	7.89	9.40E-04	-3.03	2.80E+07	7.45
200	40		9.00E+07	7.95	7.70E-04	-3.11	3.50E+07	7.54
250	43		9.90E+07	8.00	1.70E-03	-2.77	3.20E+07	7.51
300	45		1.03E+08	8.01	1.67E-03	-2.78	3.30E+07	7.52
350	47		1.08E+08	8.03	3.60E-03	-2.44	4.50E+07	7.65
400	48		1.15E+08	8.06	8.10E-03	-2.09	4.80E+07	7.68
450	48		1.07E+08	8.03	1.70E-03	-2.77	5.50E+07	7.74
500	49		1.10E+08	8.04	1.90E-03	-2.72	5.00E+07	7.70

Table 6.6: Peak Stresses and strains for 1 millisecond at $1 \times 10^{11} \text{ W/m}^3$

Finally the study was repeated but by increasing the exposure time tenfold for all power densities and grain sizes. Figure 6.30 was obtained. Essentially the same pattern is repeated but the maximum temperatures are an order of magnitude higher. Again it can be seen that there is proportionally a much lower temperature rise for the smaller sizes. The highest temperature recorded for the 500 μm heated particle here is 268°C.

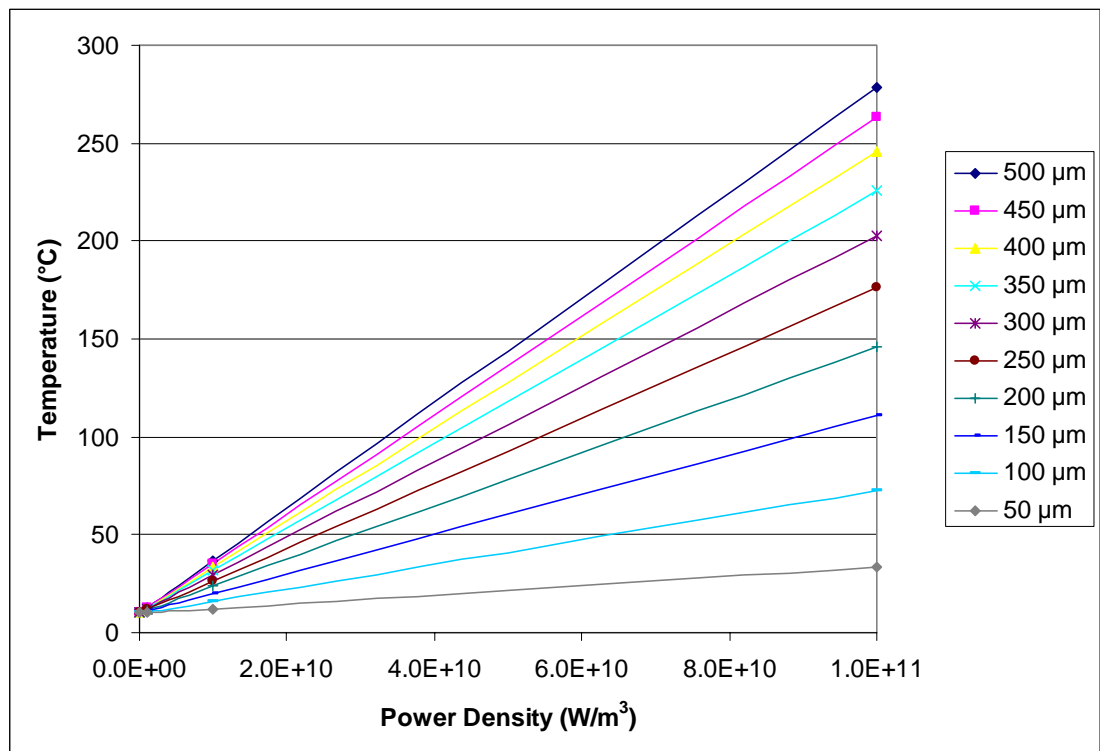


Figure 6.30: Line plot for peak temperature in the sample for varying power density and heated particle size, for 10ms exposure time.

6.6.4 Discussion

The temperature has been shown to rise linearly with power density for the 2mm transparent particle with 500 μ m heated particle. This consequently results in elevated stresses and strains. Therefore fracturing is likely to be facilitated at higher power densities. The size of heated particle has also been varied, and it has been shown that at lower sizes that fracturing is less likely. It can also be concluded that for the lower sizes, higher power densities are required in order to induce fracturing. This explains why decreased efficiencies have been observed when small particle sizes have been treated in the laboratory (Kingman et al., 2003).

However, it does not fully explain the mechanism. Possibilities include the proportionally fewer flaws that smaller particles contain. A large particle will have a significant number of flaws, which render the rock weaker than if it were completely intact. A smaller rock will have fewer flaws, and therefore this will result in fewer crack initiation and propagation sites. At very small sizes ($<2\mu$ m) it is conceivable that a rock may have no flaws at all, and will therefore behave completely elastically when loaded. Further detail on the simulation of flaws is included in chapter 5.2.

Another potential mechanism that could explain why smaller particles are less affected by microwave radiation is the proportional increase in surface area through which heat is lost at lower sizes. It could be possible to examine this effect by simulating the thermal emissivity of the samples due to radiation, conduction, and convection into air. However, no boundary conditions have been applied to the model, as this would increase the complexity, and hence the computational load to the detriment of the study.

The exposure time was increased ten-fold to see if the patterns were repeated, and these results were presented in Figure 6.30. An analytical calculation to check the findings is presented as follows.

Using equation 2.3 we can estimate the peak temperature.

$$\frac{dT}{dt} = \frac{P \cdot d.}{C_p \cdot \rho} \quad (\text{Equation 2.3})$$

If we assume an average specific heat capacity of 600 J/kg.K, and a pyrite density of 5012 kg/m³ then we obtain:

$$\frac{dT}{dt} = \frac{1 \times 10^{11}}{600 \cdot 5012} = 33253.524^\circ\text{C} / \text{s}$$

For a perfectly insulated heated particle and an exposure time of 10 milliseconds we would therefore expect a temperature rise of 332°C. This is slightly higher than the recorded value of 268°C in Figure 6.30 due to heat loss away from the heated particle centre and in to the transparent phase.

6.7 Quantification of Damage in the Sample

6.7.1 Introduction

It was proposed that a means of quantifying the degree of damage incurred by the material from thermally induced stresses should be devised. It had already been proposed that a UCS test be used to quantify the weakening. Whilst this test was directly analogous to a real laboratory test, it had proven time consuming, with each test taking up to four hours depending on the resolution required. It was suggested that a more rapid means of quantification of damage was devised, partly in order to corroborate the UCS results, and partly to enable the analysis of a far wider range of test conditions that otherwise would have proven excessively laborious.

The main objective here was to implement a representation of mineral texture, and then to vary the total particle size whilst maintaining a constant heated particle size. The aim was to again explain the decrease in efficiency which has been observed in laboratory work when smaller sizes are exposed to microwave radiation.

6.7.2 Methodology

The damage parameters were defined as being the percentage of the total number of zones in the sample that had undergone strain softening. One damage parameter was assigned to tensile strength, and one was applied to the cohesion of the material. Cohesion is defined as the internal resistance of individual grains to separate from one another and is discussed in more detail in section 5.2.

A *FISH* function was written to examine each zone in the sample once the thermal simulation had run, and to count the number of zones in the sample that had undergone

strain-softening. This *FISH* function is shown in Figure 6.31. In this particular study, the effect of varying the size of total sample was studied, whilst keeping the same size zones and therefore same heated particle size.

Heated particles were disseminated in a 10% (by area) random distribution within a circular transparent sample, and the total size of the transparent sample was varied from 10 zones to 200 zones. The size of the heated particles was kept constant at 0.5mm. The sample size therefore varied from 5mm to 100mm in diameter. In order to formulate this series of simulations, a square grid of microwave-transparent material was specified to the required sample diameter. A circle was then specified in the centre of the model. The 10% random heated particle distribution was applied to the entire sample. Then the four corners outside the circle were assigned to be null models. Only a circular microwave-transparent sample containing 10% heated particles remained. A power density of $1 \times 10^{12} \text{ W/m}^3$ was then assigned to the heated zones, for 1 millisecond.

The *FISH* function examines the cohesion and tensile strength in the zone and determines whether or not the value is less than the original specified strength of 25MPa and 15MPa for cohesion and tensile strength respectively. If the zone still retains the original strength parameters then that zone is discounted. The function then counts all the zones that has undergone strain softening and expresses it as a total number. The percentage of zones that have undergone strain-softening can then be determined by dividing by the total number of zones in the sample. A *FISH* function was also devised for this purpose by counting the number of zones that are prone to strain softening.

def damage	(- assigns the <i>FISH</i> function name)
loop i (1,izones)	(- loops horizontal zones)
loop j (1,jzones)	(- loops vertical zones)
if cohesion(i,j)< 25e6 then	(- specifies cohesion condition)
cd=cd+1	(- includes zone in count)
end_if	
if tension(i,j)< 15e6 then	(- specifies tensile strength condition)
td=td+1	(- includes zone in count)
end_if	
tot=tot+1	(- includes total zones in total zone count)
end_loop	(- ends horizontal loop)
end_loop	(- ends vertical loop)
cd1=100*cd/tot	(- calculates cohesive damage as %)
td1=100*td/tot	(-calculates tensile damage as %)
command	
print Cd1	(- displays cohesion damage parameter)
print Td1	(- displays tensile damage parameter)
end_command	
end	
damage	(- executes function)

Figure 6.31: Detail of *FISH* function devised for obtaining damage parameter.

Therefore 'Td' is defined as the number of zones which have undergone a reduction in tensile strength, and 'Cd' is defined as the number of zones which have undergone a reduction in cohesion, expressed as a percentage of the total number of zones.

At the smaller sizes of 10, 20 and 30 zones, the simulations had to be repeated 5 times in order to negate the effects of the discretisation. The applied random heated particle distribution results in a different number of particles assigned each time a model is run, and in a small model with few zones this can have a large effect with a variance of up to $\pm 40\%$. For example, with the 5mm sample, it can be seen from Figure 6.33 that only 5 heated particles were assigned to the transparent matrix. It is feasible that if a repeat simulation was run that only 3 heated particles be assigned to the model, or as many as 8 heated particles. It is unlikely but it was thought that some repeat simulations were required in order to negate these effects. However at the larger sizes there is greater probability that there will be an even distribution of heated particles assigned to the sample, and therefore repeat readings were not required.

6.7.3 Results

Both the 5mm (smallest) and 100mm (largest) sample heated particle distributions are shown in Figure 6.32 and Figure 6.33 respectively. Here there are only five 0.5mm heated particles assigned to the model as the total particle size is only 5mm across. The area occupied by the heated particles still amounts to 10% of the total area of the complete particle.

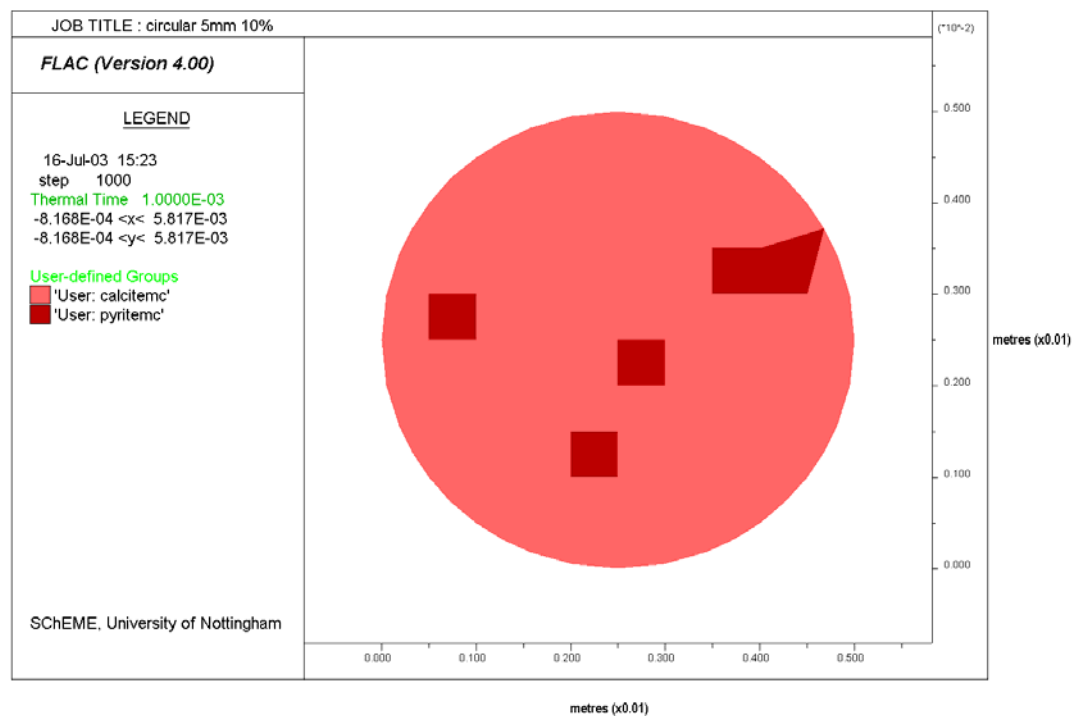


Figure 6.32: Distribution of heated particles in 5mm circular transparent particle

The 100mm particle is shown in Figure 6.33. Here the total sample size is much larger than in Figure 6.32. The heated particle size remains at 0.5mm. Therefore the heated particle distribution is much more finely disseminated throughout the transparent matrix.

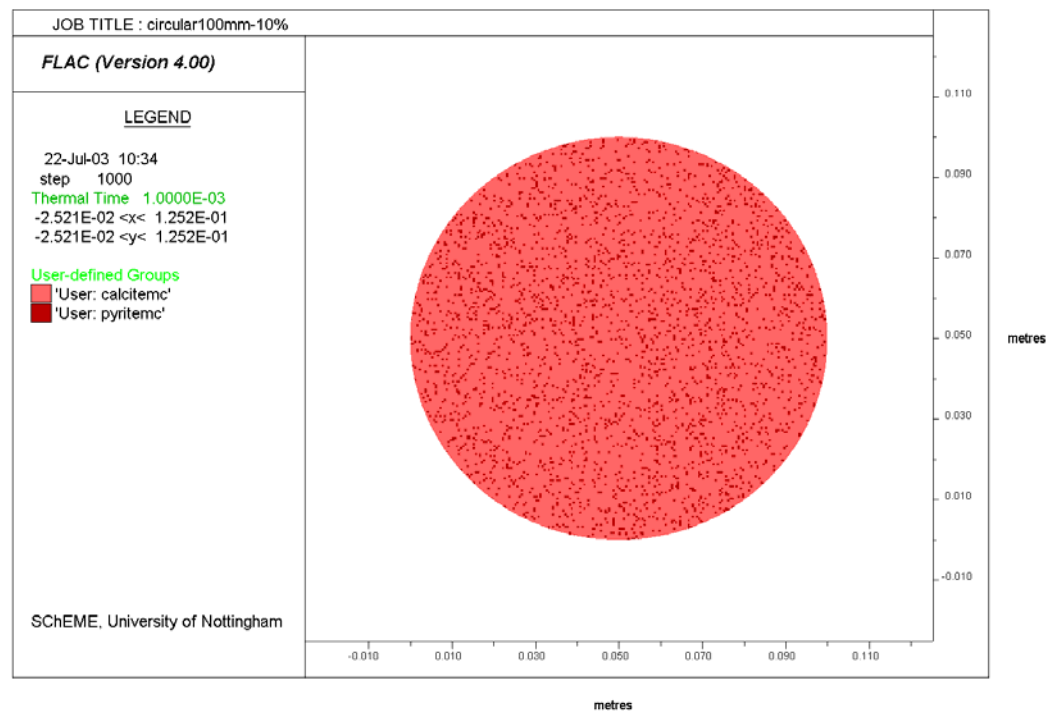


Figure 6.33: Distribution of heated particles in 100mm circular transparent particle

There now follows a series of plots obtained from this particular study, and some of the underlying mechanisms which govern the efficiency of weakening are investigated.

In Figure 6.34 we can see the tensile strength plot for the smallest 5mm sample. The key on the left indicates the values of tensile strength shown in the plot. The maximum value is 15×10^6 Pa, which is the original tensile strength for that particular zone. In some zones the strength has been reduced to a value of 2.5MPa as denoted by the dark red colour. There are areas where the tensile strength remains higher and this corresponds with the regions immediately outside the heated particle distribution, with the tensile strength having remained highest in the heated particle centres due to the compressive effect explained in section 6.5.4. Interactions between the stress fields generated by the expansion of the heated particles give rise to other areas where the tensile strength is greatly reduced such as the region at approximately (0.1, 0.2) in Figure 6.34 even when there is no heated particle in that exact location, but there are two heated particles either side.

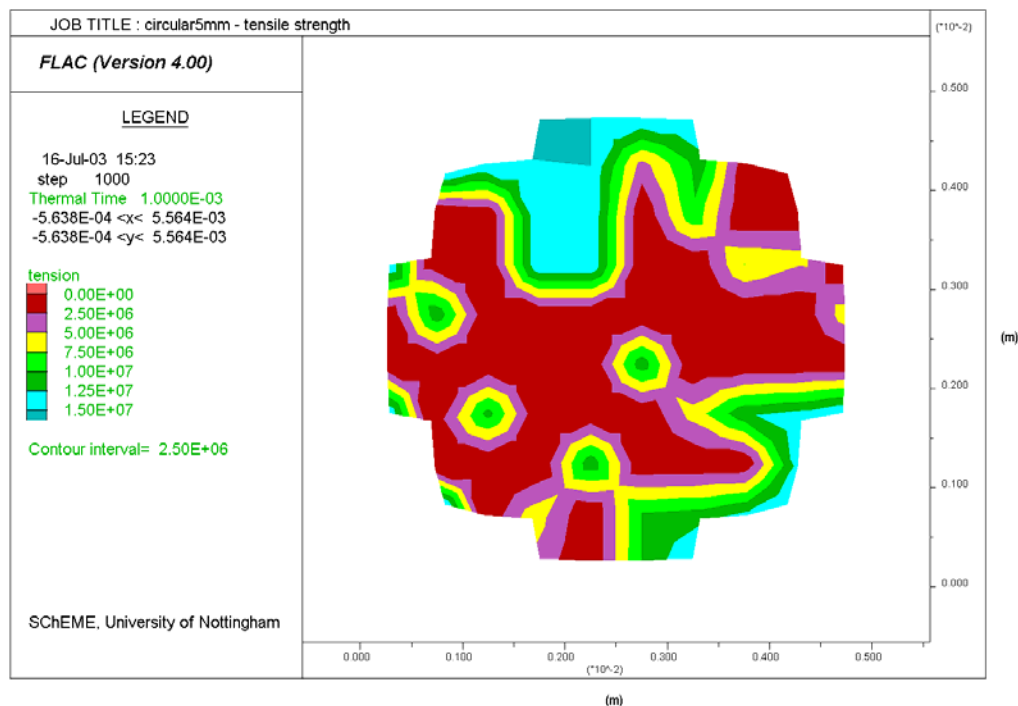


Figure 6.34: Plot showing residual tensile strength in the 5mm sample

The corresponding plot for the 100mm sample is shown in Figure 6.35. As the heated particle distribution is more finely disseminated it is more difficult to determine the precise behaviour. The distribution of heated particles leads to less irregularity in the stress field, and is less distorted by the heated particle distribution. The tensile strength remains predominantly highest in the middle of the sample (grey/blue), where confinement is greater. The highest reduction in tensile strength is experienced at the edges of the sample (red/purple). It is thought that this is because the summation of the internal expansion results in a net outwards expansion. The transparent phase is not expanding as such and is therefore being pulled apart at the edges. Due to the fineness of the distribution it is useful to closely examine the plots, and these are shown in Figure 6.36 and 6.37.

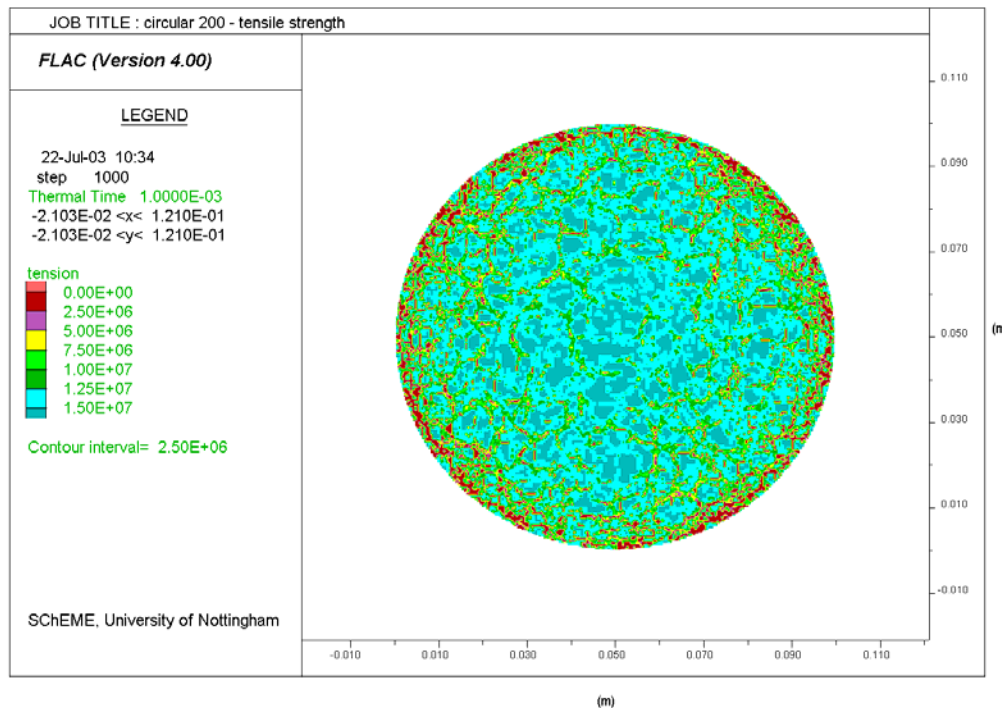


Figure 6.35: Plot showing residual tensile strength in the 100mm sample

When zoom function in *FLAC* is used to take a closer examination of the reduction in tensile strength Figure 6.37 is obtained. The corresponding heated particle distribution is included in Figure 6.38. On closer inspection of the plots it can be concluded that there is less likelihood of tensile strength reduction in the compressed heated particle centres, as previously shown in section 6.5.4, but where the heated particles occur in close proximity to each other there seems to be a large reduction in tensile strength between the heated particles. Note the arrows in Figure 6.37 and Figure 6.38.

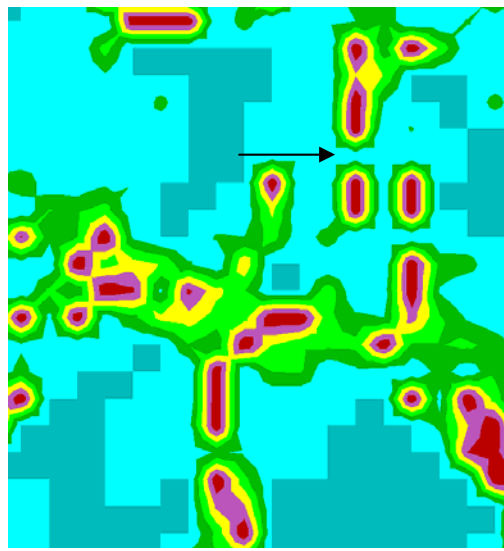


Figure 6.36: Close-up of Figure 6.36

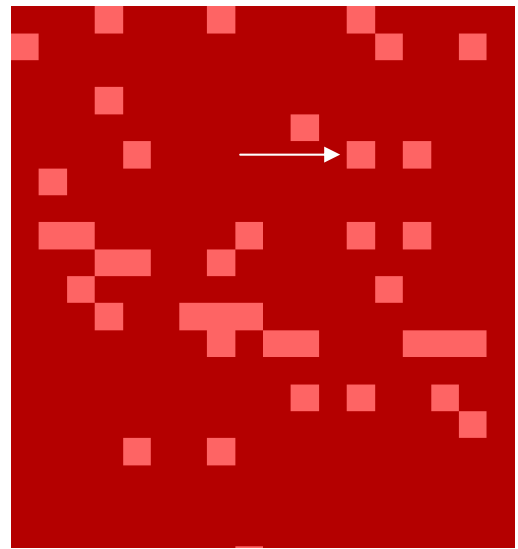


Figure 6.37: Heater distribution

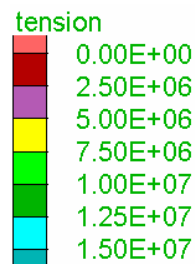


Figure 6.38: Key to tensile strength contours.

The corresponding plot for the cohesion damage in the 5mm sample is shown in Figure 6.39. The heated particle distribution has already been shown in Figure 6.32. Here the

greatest reduction in cohesion has occurred in the heated particle centres, and is greatest where there is an agglomeration of heated particles on the upper-right side of the figure. The lowest reduction in cohesion can be seen farthest away from the heated particle centres, and these regions still have the original prescribed cohesion of 25MPa (shown in blue).

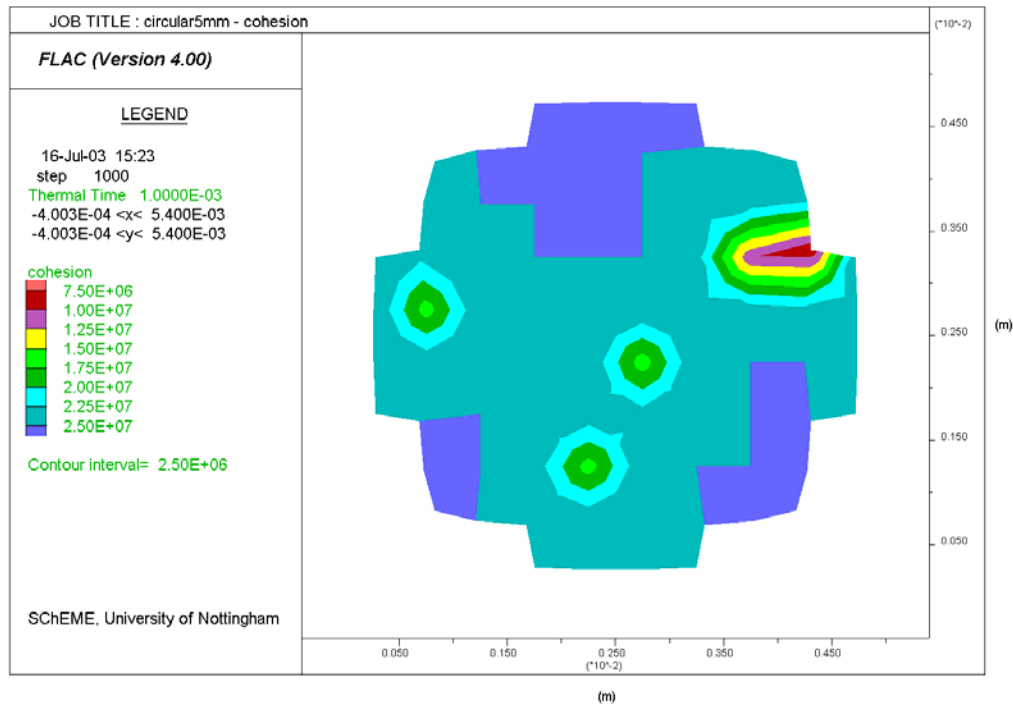


Figure 6.39: Cohesion contours in the 5mm sample, showing greatest cohesion reduction in vicinity of heated particle centres.

The results of this study are contained within Table 6.7 and Figure 6.40. Values of T_d and C_d are shown for the respective sample size. It can be seen that as sample size increases, C_d also increases, whilst T_d generally decreases. This was an interesting result and shows that further understanding of rock mechanics modelling is required to explain the almost conflicting results.

Sample diameter (mm)	Zone diameter	Number of zones with reduced cohesion	Number of zones with reduced tensile strength	Total number of zones in sample	Cd %	Td %
5	10	39	64	80	48.8	80.0
10	20	183	279	316	58.0	88.4
15	30	443	638	716	61.9	89.1
20	40	860	1153	1264	68.0	91.2
25	50	1420	1780	1976	71.9	90.1
30	60	2168	2479	2828	76.7	87.7
37	74	3487	3720	4296	81.2	86.6
40	80	4089	4249	5024	81.4	84.6
45	90	5275	5300	6376	82.7	83.1
50	100	6662	6432	7860	84.8	81.8
60	120	9776	8662	11304	86.5	76.6
80	160	17823	13558	20108	88.6	67.4
100	200	27686	17628	31428	88.1	56.1

Table 6.7: Damage Parameter results with variation in size of sample.

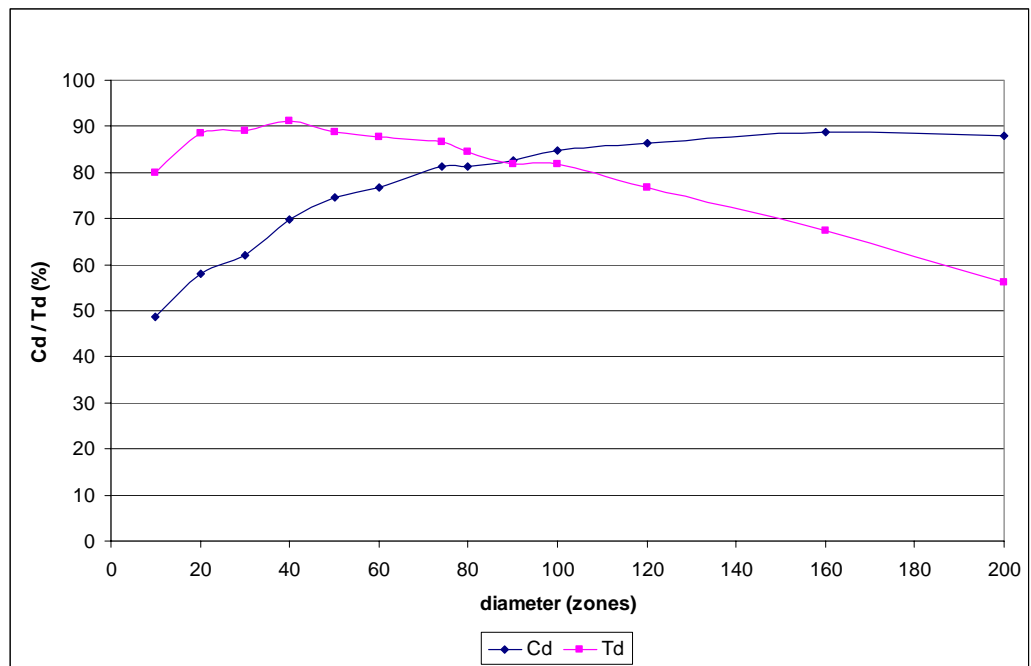


Figure 6.40: Plot of Cd, Td versus diameter

The data below relates to the 100mm sample. The ‘*damage*’ function returns the following for values of total zones, Td, and Cd.

```
>print cd  
cd = 27640  
>print td  
td = 17569  
>print tot  
tot = 31415
```

This 100mm diameter sample has a radius of 100 zones; therefore the total number of zones is expected to be:

$$\pi \cdot 100^2 = 31415 \text{ zones}$$

The total number of zones that have a reduced cohesion was reported as 27640 and the total number of zones that had reduced tensile strength was 17569. The percentage damage (Cd) was therefore 88.0% and 55.9% tensile strength damage.

6.7.4 Discussion

The results show there are possibly two underlying mechanisms. At smaller sizes, the heated particles are larger in proportion to the total sample size, resulting in a greater predominance of tensile stresses, as the corners of the square heated particles act as stress concentrators. At larger sizes, there is a much finer distribution, and consequently the stress concentrator effect is lessened. It is also interesting to note that at the 3 lowest sizes, the tensile strength reduction appears to decrease. It is fair to assume that at even smaller sample sizes that very little damage would occur as suggested by the work in section 6.6.3.

It is evident that the presence of heated particles results in a local strength reduction. The heated particles themselves remain intact whilst interactions between the heated particles' expansion can result to weakened areas in the vicinity.

The power density ($1 \times 10^{12} \text{ W/m}^3$) and exposure time (1ms) used for this study has resulted in a total energy input of $1 \times 10^9 \text{ J/m}^3$ of heated phase. Whilst this initially sounds like a large amount of energy, when linked to the actual mass of heated phase it becomes much more realistic. If 1m^3 of heated phase weighs 5012 kg, and this heated phase constitutes 10% of the total mineral content, then a further 9m^3 of transparent phase will weigh 24408 kg. This yields 10m^3 of rock weighing a total of 29420 kg. If $1 \times 10^9 \text{ J} = 277.77 \text{ kW.h}$, then this results in a comminution energy of:

$$277.77 / 29.42 = 9.44 \text{ kW.h/tonne}$$

This is a relatively low figure considering that even for the 5mm sample, 80% of the zones have undergone strain softening. This suggests that the economics of the process could potentially be viable.

6.8 Effects of Power Density and Exposure Time on Damage Parameter

6.8.1 Introduction

This section investigates the effects of power density and exposure time in more detail. A wider range of input parameters were used in order to check the feasibility of more powerful systems with shorter exposure time. The aim was also to determine the energy input above which breakage was facilitated. The breakage was quantified using the damage parameters.

6.8.2 Methodology

The power densities used ranged from $1 \times 10^8 \text{ W/m}^3$ to $1 \times 10^{12} \text{ W/m}^3$ whilst varying the exposure time from 1s down to $1\mu\text{s}$. The sample was a 100×100 zone square with 1mm zones. A 1% (by area) randomly distributed heated particle distribution was applied. After the heating was completed the damage parameter function (as shown in Figure 6.32) was run and the number of strain softened zones was counted.

6.8.3 Results

The results are detailed in Table 6.8 and Table 6.9. It can be seen that at the lower exposure times and the lower power densities that little if any damage is incurred in the sample. However once a certain combination of power density and exposure time is exceeded then the damage is incurred. It can be seen that this threshold energy input corresponds to either 0.01s at $1 \times 10^9 \text{ W/m}^3$, or 0.001s at $1 \times 10^{10} \text{ W/m}^3$, and so on. This is a total energy input of $1 \times 10^7 \text{ J/m}^3$, and must be exceeded before any damage is incurred. The pattern is very similar for both the tensile strength and the cohesion reduction data.

Exposure time (s)	Power Density (W/m ³)				
	10 ⁸	10 ⁹	10 ¹⁰	10 ¹¹	10 ¹²
0.000001	0.00	0.00	0.00	0.00	0.00
0.00001	0.00	0.00	0.00	0.00	0.40
0.0001	0.00	0.00	0.00	0.40	76.98
0.001	0.00	0.00	0.30	76.90	98.92
0.01	0.00	0.20	76.47	98.79	100.00
0.1	0.00	74.03	98.92	98.98	100.00
1	67.22	74.03	98.92	100.00	100.00

Table 6.8: Number of zones with tensile strength reduction

It can be seen also that for a constant energy input of 10⁸ J/m³ that there is a slight increase in the level of damage incurred as the exposure time is reduced from 1s to 1 μ s. The number of zones that have undergone tensile strength reduction have increased from 67.22% to 76.98%. The same applies for the cohesion reduction results where the percentage of strain softened zones increases from 77.05% to 80.45%.

Exposure time (s)	Power Density (W/m ³)				
	10 ⁸	10 ⁹	10 ¹⁰	10 ¹¹	10 ¹²
0.000001	0.00	0.00	0.00	0.00	0.00
0.00001	0.00	0.00	0.00	0.00	0.57
0.0001	0.00	0.00	0.00	0.56	80.45
0.001	0.00	0.00	0.56	80.44	99.79
0.01	0.00	0.56	80.38	99.79	100.00
0.1	0.07	80.29	99.82	100.00	100.00
1	77.05	80.29	99.82	100.00	100.00

Table 6.9: Number of zones with cohesion reduction

6.8.4 Discussion

It can be seen from both the tensile strength results in Table 6.8 and cohesion results table in Table 6.9 that there is a clear threshold energy input above which significant weakening is facilitated. If the power density is multiplied by the exposure time we obtain the total volumetric energy input (into the heated particle and not the total sample volume). Therefore for a power density of $1 \times 10^{12} \text{ W/m}^3$ and an exposure time of 1s yields a total volumetric heat input of $1 \times 10^{12} \text{ J/m}^3$. If the results are examined then it can be seen that above $1 \times 10^8 \text{ J/m}^3$ significant damage is incurred. This may be the required volumetric energy input required for effective weakening of rock, and above this value further weakening would occur. As already stated there may be an advantage in using lower exposure times. The greatest increase in efficiency is to be seen as the exposure time decreases from 1s at $1 \times 10^8 \text{ W/m}^3$ to 0.1s at $1 \times 10^9 \text{ W/m}^3$, and consequent reductions in the exposure time by a factor of ten, have proportionally lower increase in damage. The same pattern is repeated for the cohesion reduction results. There may be two reasons for this, and these are investigated in the following sections.

6.9 Investigating Effects of Decreased Time for Conduction

6.9.1 Introduction

The previous section where showed that greater damage can be generated when shorter exposure times are used, as long as the total energy input is sufficient. It was suggested that the longer exposure times give rise to a greater length of time for conduction to occur between the heated particles and the surrounding transparent phase. This would in turn lead to lower peak temperatures in the heated particle centres. It would also lead to a more diffuse temperature distribution surrounding the heated particle, which is to say that the thermal gradients would be lower. This study looks at how the thermal gradients, with respect to time, and position, vary as the power density and exposure time are varied.

6.9.2 Methodology

A series of simulations were carried out to illustrate the mechanism by which conduction is minimised at shorter exposure times. A 2mm circular calcite particle encasing a 0.5mm heated particle was simulated. The model was 160 zones in diameter, with the heated particle in the centre having a 40 zone diameter. History points were located along the vertical centreline of the sample, $i=80$, from the centre of the heated particle downwards. The locations where the temperature histories were recorded were the same as in section 6.3.2.

The heated particle/transparent phase boundary lies between 80,61 and 80,60. Power density was varied from $1 \times 10^{15} \text{ W/m}^3$ to $5 \times 10^{11} \text{ W/m}^3$ and exposure times were modified to keep the total volumetric energy input into the sample constant at $1 \times 10^9 \text{ J/(m}^3 \text{ of heated phase)}$. The resulting temperature history plots were then obtained.

6.9.3 Results

The x-axis represents the number of steps in the calculation, with each simulation having been run for 1000 steps. The thermal time step was varied each time so that varying total heating time was possible. The data is illustrated in Figures 6.41 and 6.42.

It can be seen that most history plot lines with the higher gradients lie on top of each other. The history plots from inside the heated phase all lie within a narrow range. The lines are very close to linear – showing very even heating inside the heated particle. The line which represents the boundary between the heated particle and the transparent phase has intermediate gradient, and then the three histories corresponding to the areas outside the heated particle all lie on top of each other with very little temperature increase with time. This plot shows that the sample has had very little time for conduction to occur from the heated particle to the transparent phase, and consequently the history lines inside the heated particle are practically linear, and the history lines for the transparent phase are effectively flat.

If the power density is decreased by a factor of ten to $1 \times 10^{14} \text{ W/m}^3$, and the heating interval increased by a factor of ten to $10\mu\text{s}$, then Figure 6.42 is obtained.

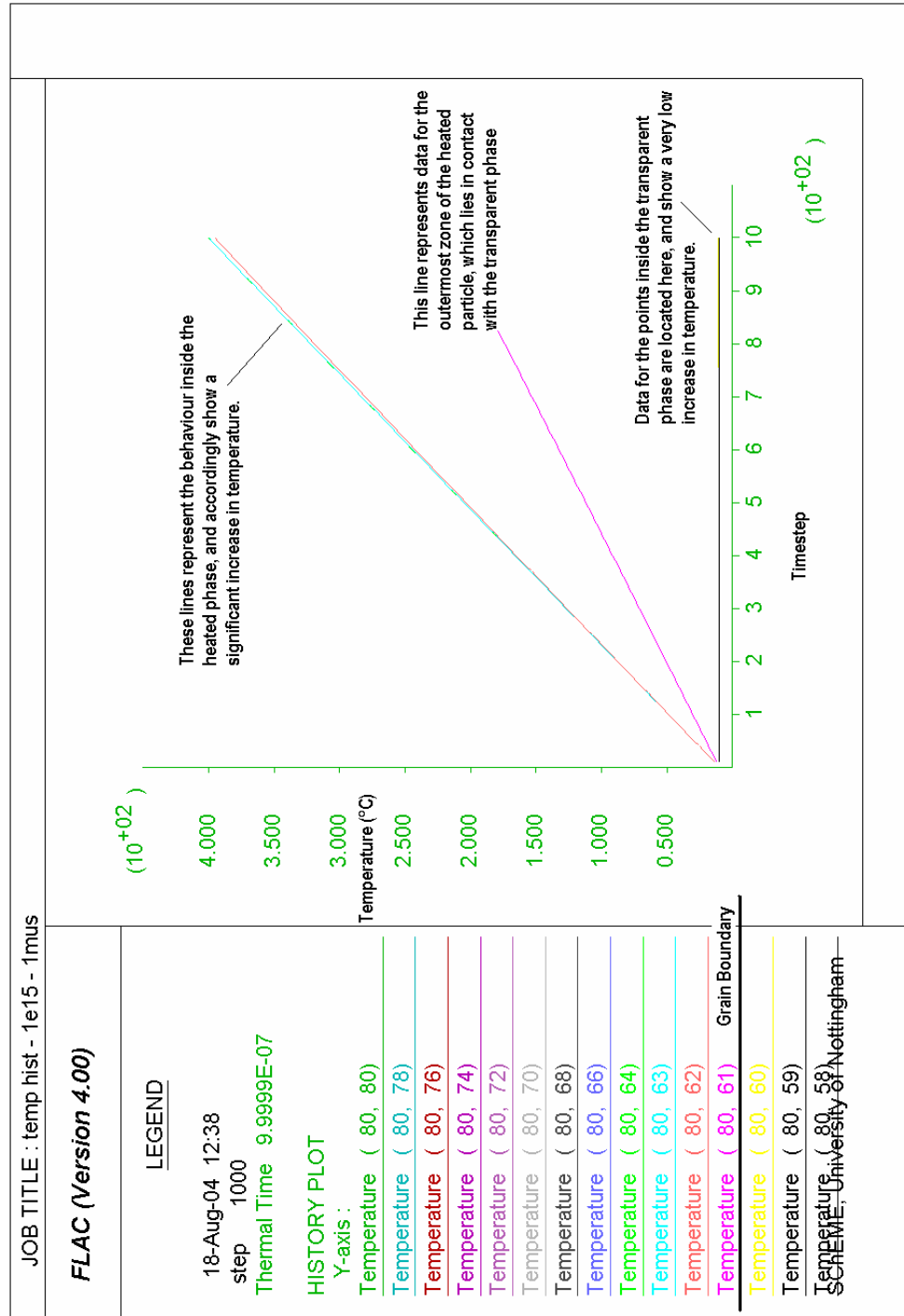


Figure 6.41: Temperature history plots for $1 \times 10^{15} \text{ W/m}^3$ for $1 \mu\text{s}$.

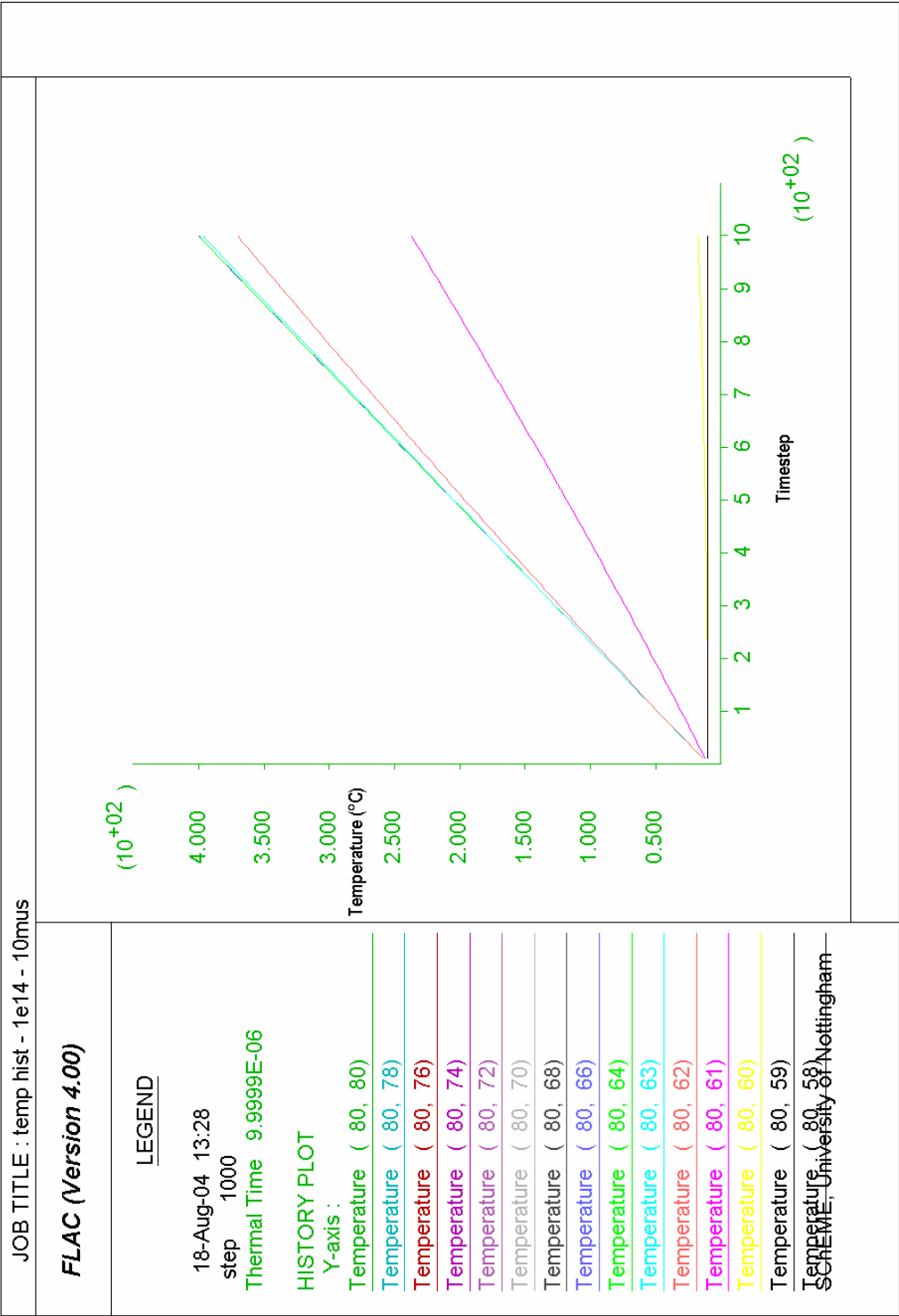


Figure 6.42: Temperature history plots for $1 \times 10^{14} \text{ W/m}^3$ for $10 \mu\text{s}$.

Note that there is now more of a deviation from the linear for the history plots inside the heated particle, with the temperature history at location close to the grain boundary (80,62) being attenuated due to its proximity to the transparent phase. The temperature history for the central (80,80) point shows signs of increasing with time, which shows that there has now been sufficient time for conduction to occur from the heated particle in to the transparent phase. The same can be said for the plot at the outermost heated particle (80,61) – which is now increasing its gradient as time increases. This also shows that the boundary is receiving increased heat.

If the power density is further decreased by a factor of ten to $1 \times 10^{13} \text{ W/m}^3$, whilst the heating time is increased by a factor of ten to $100\mu\text{s}$, Figure 6.43 is obtained. Note now there is a much wider spread within the history lines for the locations inside the heated particle, and conduction into the transparent phase is becoming significant.

The history lines for the lower three history points are all now deviating from the horizontal, showing that as time increase the points are receiving more heat from the heated particle through conduction.

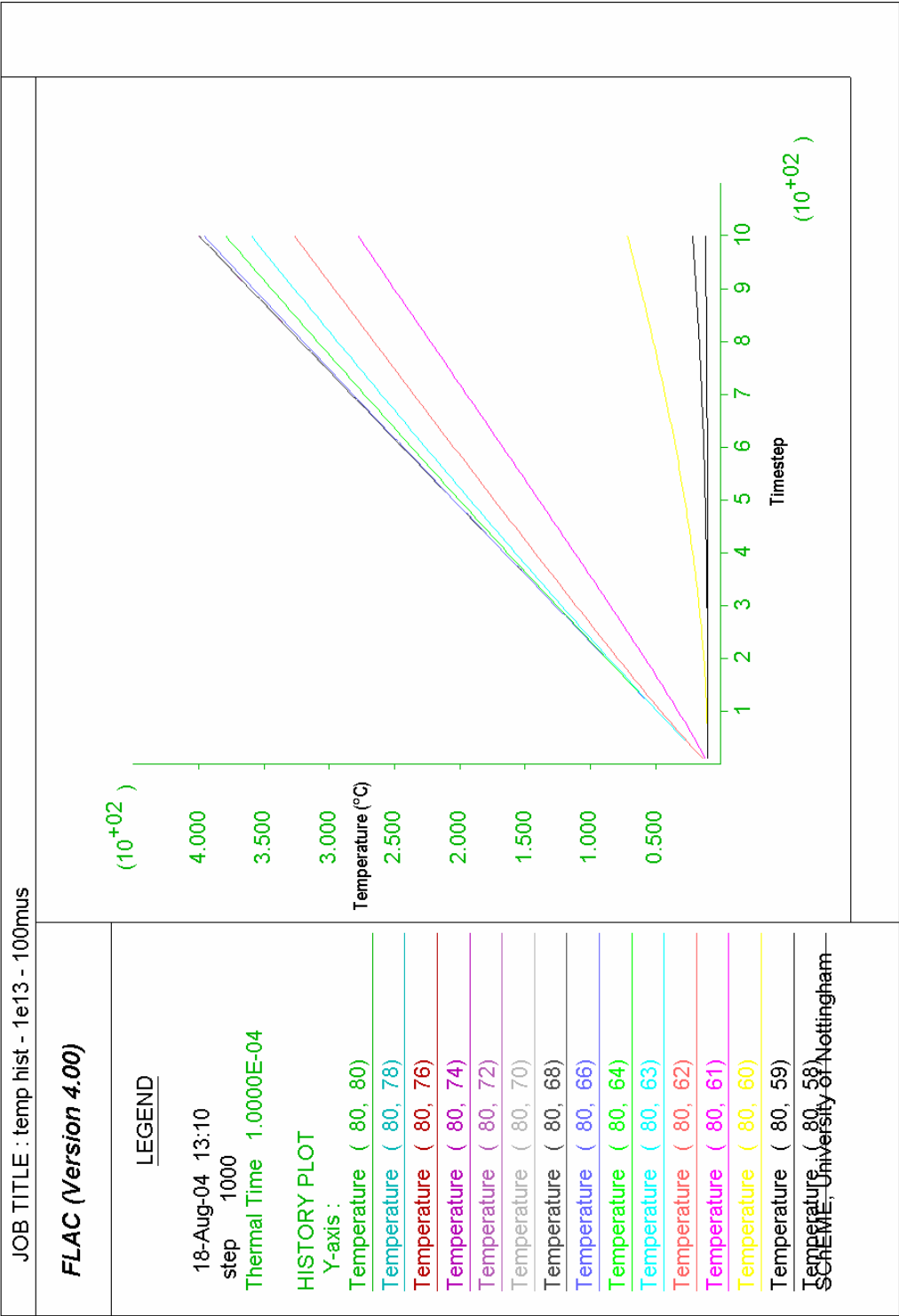


Figure 6.43: Temperature history plots for $1 \times 10^{13} \text{ W/m}^3$ for $100 \mu\text{s}$.

The power density was again reduced by a factor of ten to $1 \times 10^{12} \text{ W/m}^3$ and the exposure time consequently increased to 1ms. Again the pattern is repeated in Figure 6.44, with more deviation from the linear, and an even greater spread of temperatures in the heated particle showing substantial thermal gradients with position inside the heated particle due to conduction outwards into the transparent phase.

For the last plot in this section, Figure 6.45, the power density was halved to $5 \times 10^{11} \text{ W/m}^3$ and the heating time doubled to 2ms. It was not possible to further increase the heating time as the necessary thermal time step would cause instability in the model. Had a larger model been used, (of the order of centimetres) then longer heating times and lower power densities could possibly have been used.

Again an increased spread of temperatures in the centre of the heated particle can be seen, and the history lines are converging with the lines from the histories from the transparent phase. The transparent phase was now experiencing temperatures of 100°C and above. It is worth noting that the peak temperature in the heated particle has dropped from approximately 400°C in Figure 6.41 to approximately 375°C in Figure 6.46.

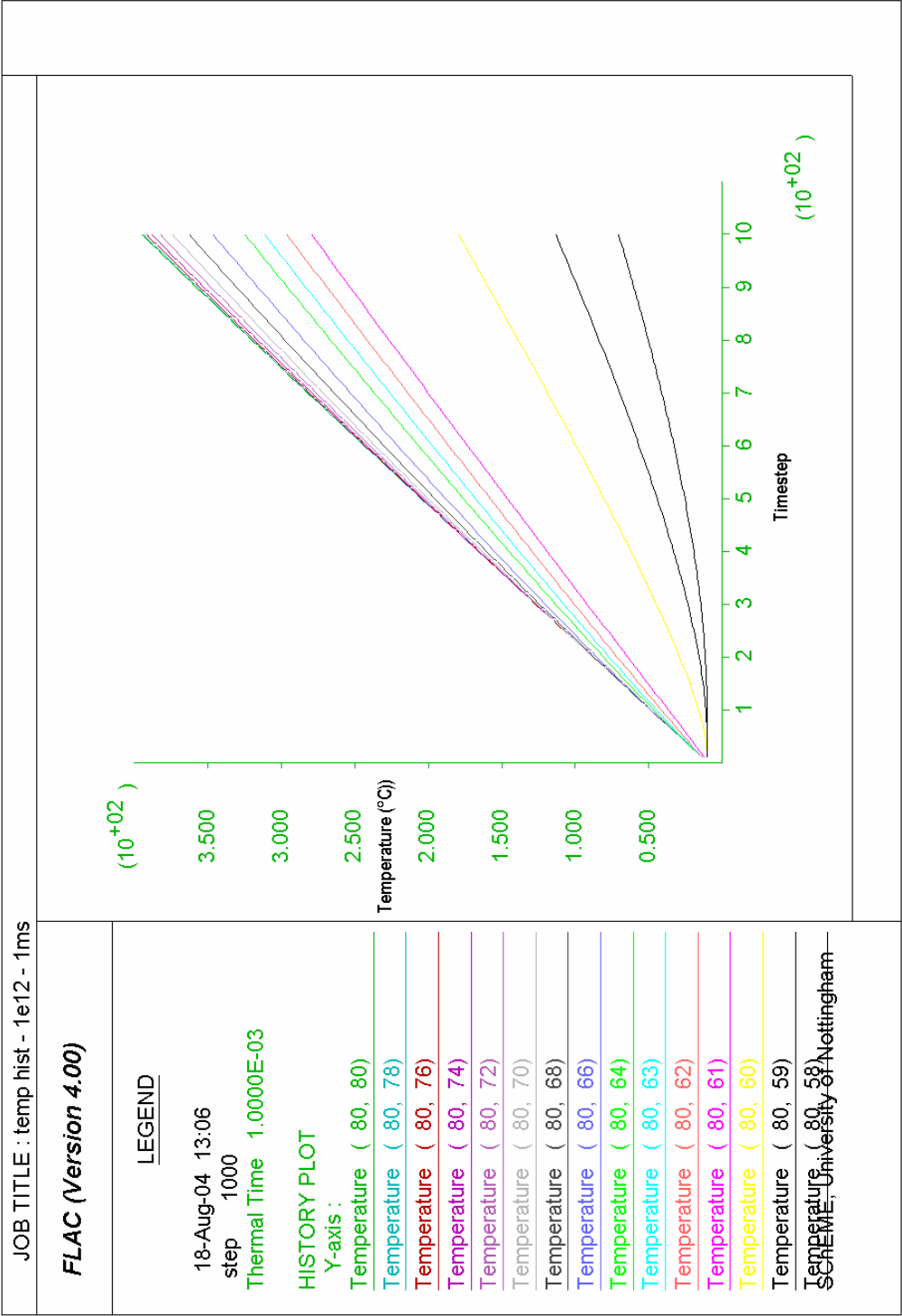


Figure 6.44: Temperature history plots for $1 \times 10^{12} \text{ W/m}^3$ for 1ms.

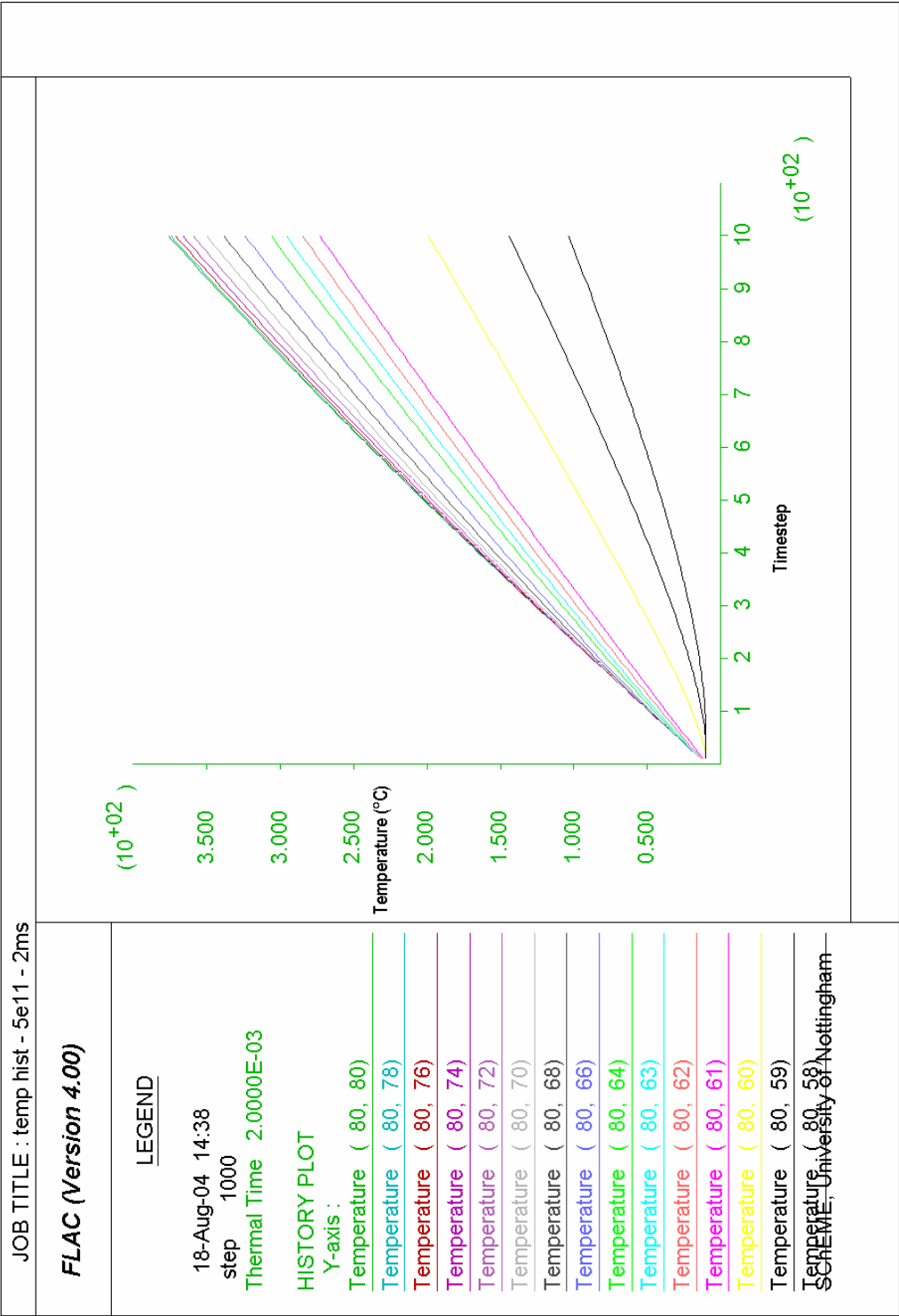


Figure 6.45: Temperature history plots for $5 \times 10^{11} \text{ W/m}^3$ for 2ms.

6.9.4 Discussion

This section has examined the effects of decreasing the power density and increasing exposure time to show how the thermal gradients change. It can be seen that at very high power densities and low exposure times the heat transfer into the transparent phase is minimised. Therefore the temperature is maintained higher inside the heated phase, and the thermal gradients are maximised. It has already been shown in section 6.3.3 that the highest thermal gradients give rise to the highest shear stresses in the sample. Therefore it can be concluded that higher power densities and lower exposure times will yield the optimum weakening conditions.

6.10 Investigation of Increased Magnitude of Particle Boundary Acceleration

6.10.1 Introduction

It was thought that another possible reason for the results seen in section 6.8 is that as the exposure time decreases, the velocity, and therefore the acceleration of the heated particle boundary increases. Force is defined as the rate of change of momentum. A brief series of calculations illustrates this fundamental mechanism. For a given volumetric heat input, the total temperature rise should remain roughly the same, if the effects of conduction into the transparent phase are ignored unlike the work in section 6.9 previously. Thus the total expansion should be equivalent in both cases. For the shorter expansion times, this expansion will be occurring in a shorter time interval. The average velocity of the heated particle boundary can be said to equal the displacement divided by the time interval.

6.10.2 Methodology

At the lower time intervals, the associated acceleration will be much higher, as illustrated by the following table of theoretical results assuming 50µm expansion occurring over the prescribed exposure time interval. A 50µm expansion would be expected when a 5mm particle with a thermal expansion coefficient of $4 \times 10^{-5} \text{ }^{\circ}\text{C}^{-1}$ has its temperature raised by 250°C or when a 50mm particle experiences a temperature rise of 25°C, and so on.

Here the expansion has been assumed to be 50µm, and then the exposure time within which the expansion is occurring has been decreased from 1 second to 1 µs. The resulting velocities and accelerations have been presented in Table 6.10.

6.10.3 Results and Discussion

Table 6.10 shows the velocities and accelerations that can be expected from the conditions specified. Note how as the heating time interval decreases by a factor of ten the acceleration increases by a factor of a hundred, and so forth. Hence very small heating intervals will give rise to very large accelerations. These large accelerations will give rise to very large forces, and in turn high stresses. When exposure time is of the order of microseconds, the accelerations involved are significant. As the forces generated are proportional to the acceleration, the forces can be expected to be extremely large. Therefore, assuming the microwave energy can be deposited into the material rapidly enough; the shorter exposure times will be likelier to yield significant weakening of the material.

time	velocity	acceleration
s	m/s	m/s ²
1	0.00005	0.00005
0.1	0.0005	0.005
0.01	0.005	0.5
0.001	0.05	50
0.0001	0.5	5000
0.00001	5	500000
0.000001	50	50000000

Table 6.10: Theoretical Particle Boundary Velocities and Accelerations

6.11 Effect of Varying Exposure Time on Damage Incurred

6.11.1 Introduction

Section 6.10 illustrated why shorter exposure times are likely to result in higher stresses generated within the sample. This section attempts to quantify the effect of these elevated stresses on the level of damage that can be expected using the damage parameters T_d and C_d . Again a representation of texture was incorporated into the model.

6.11.2 Methodology

For the modelling in this study, the heating intervals were chosen between $1\mu\text{s}$ and 10seconds. Exposure times above 0.1s were deemed to be ‘long exposure’ times, and below were deemed ‘short exposure’. The power densities applied to the material ranged between $1 \times 10^9 \text{ W/m}^3$ and $2 \times 10^{15} \text{ W/m}^3$. Those power densities $4 \times 10^{10} \text{ W/m}^3$ and below were deemed ‘low power’ and those above were deemed ‘high power’.

The study examined a 1% random heated particle distribution in UCS samples of aspect ratio 2:1, experiencing varying exposure time and the rate at which energy is delivered into the sample. One sample was treated at $1 \times 10^9 \text{ W/m}^3$ for up to 0.5 seconds and another treated at $1 \times 10^{15} \text{ W/m}^3$ for up to $0.5 \mu\text{s}$. This was to compare relatively low power densities and longer exposure times, with higher power densities and shorter exposure times. The simulation was stopped at intervals, and the number of strain-softened zones was counted in order to give a sense of the rate at which the damage was incurred.

6.11.3 Results

A gradual increase in the degree of cohesion and tensile strength damage can be seen for both microwave application types from the offset in Figure 6.48. However it can be seen that the degree of damage is higher in the high power short exposure type application than in the low power long exposure type application. This is slightly unexpected given that the total energy input in to the sample is the same in both application types. These results show that the rate of heat application is a driving mechanism of fracture, as well as the total heat put into the sample. If this is the case then the high heating rates possible with higher power microwaves with short exposure times should generate a greater degree of damage initially, and any subsequent heat input will have less effect in terms of the rate at which damage is incurred.

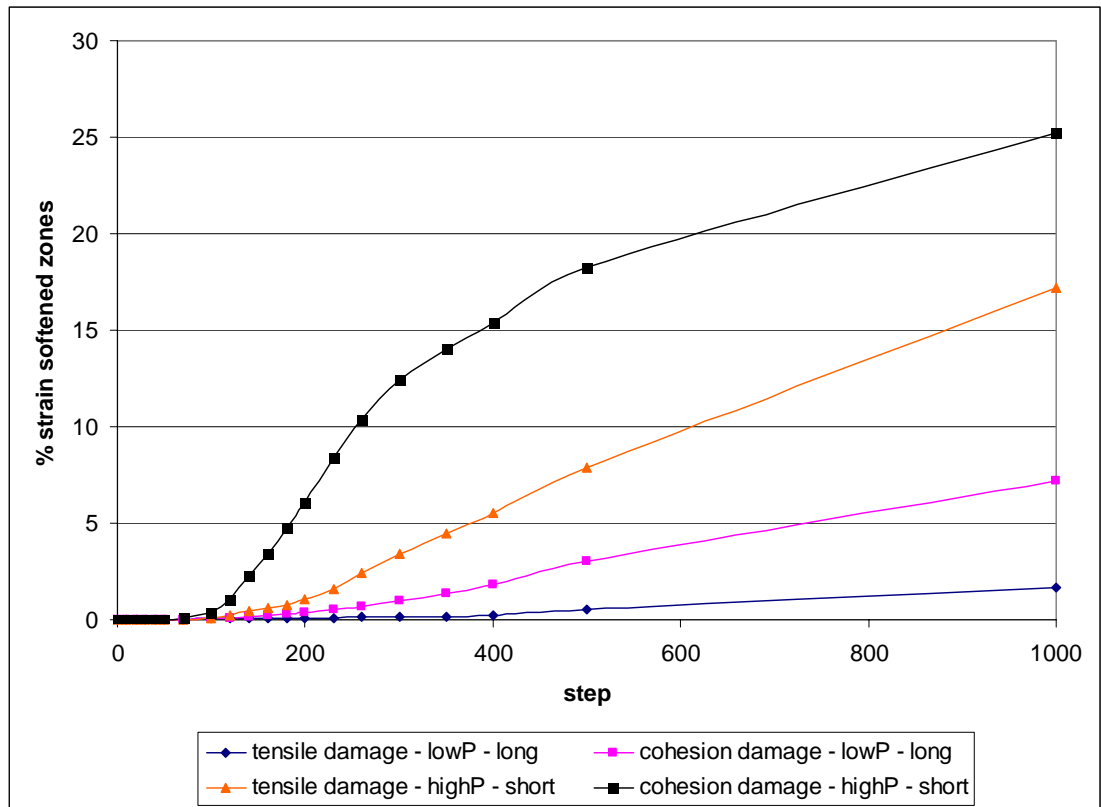


Figure 6.46: Plot showing variation of Td and Cd with timestep for 1×10^9 (W/m³) and 1×10^{15} (W/m³) for $1\mu\text{s}$

6.11.4 Discussion

This section has shown that higher degrees of damage can be incurred with application of microwaves at high power density and short exposure times. Therefore for a given energy input, the weakening is maximised when the power density is maximised, and the exposure time is minimised.

6.12 Comparison of Damage Parameter with UCS results

6.12.1 Introduction

It was seen in Section 6.11 that a much higher level of damage was incurred by the sample exposed to the short exposure, high power density application. It would be expected that this sample would yield and fail at a much lower stress than the lower power density and longer exposure time case, as it has far more zones where the strength has been reduced. It was proposed that the two samples that were treated in the previous section were then subjected to a Uniaxial Compressive Strength (UCS) test in order to compare the strength with the damage parameter values.

6.12.2 Methodology

The experimental UCS method is contained in Chapter 3. The samples were treated as in Section 6.11. The thermal stresses were then removed and the sample loaded between two simulated steel platens at a constant displacement rate. The stresses and strains then logged as the simulation progressed so that the stress-strain behaviour could be plotted. In addition to the samples from the previous section, which had been treated at $1 \times 10^{15} \text{ W/m}^3$ and $1 \times 10^9 \text{ W/m}^3$ for $1\mu\text{s}$ and 1s respectively, an untreated sample was subjected to the UCS tests, as well as two other samples treated for $0.5\mu\text{s}$ and 0.5s at the prescribed power density.

6.12.3 Results

It can be seen in the results below that there is a slight discrepancy in strengths (i.e. the untreated has a higher strength than the high power 500 μ s). This variation is due to the different configurations of random heated particle distribution for each model. For example, a clump of heated particles assigned near the corners of the sample may result in facilitated shear plane formation at that point consequently reducing the strength of the sample. However there is marked decrease in strength once the sample has been exposed to $1 \times 10^{15} \text{ W/m}^3$ for 1 μ s.

Untreated = 128.4MPa	Untreated = 128.4MPa
$1 \times 10^9 \text{ W/m}^3$, 500ms = 128.9MPa	$1 \times 10^{15} \text{ W/m}^3$, 500ns = 128.9MPa
$1 \times 10^9 \text{ W/m}^3$, 1000ms = 128.3MPa	$1 \times 10^{15} \text{ W/m}^3$, 1000ns = 117.2MPa

Table 6.11: UCS values for various model configurations

Figure 6.47 shows the stress-strain plot obtained from *FLAC* for the untreated 40mm diameter 1% heated particle UCS sample. The plot represents the baseline data, or the control for the study. This sample has not had any heat applied, and subsequently has no thermal damage incurred. This plot shows a peak stress of 128.4 MPa, and then very rapid failure, with very little initial residual strength. This plot is typical for a brittle material with very few flaws. A material like flint would exhibit this behaviour. It has very few flaws, and fractures extremely rapidly in an explosive way when loaded.

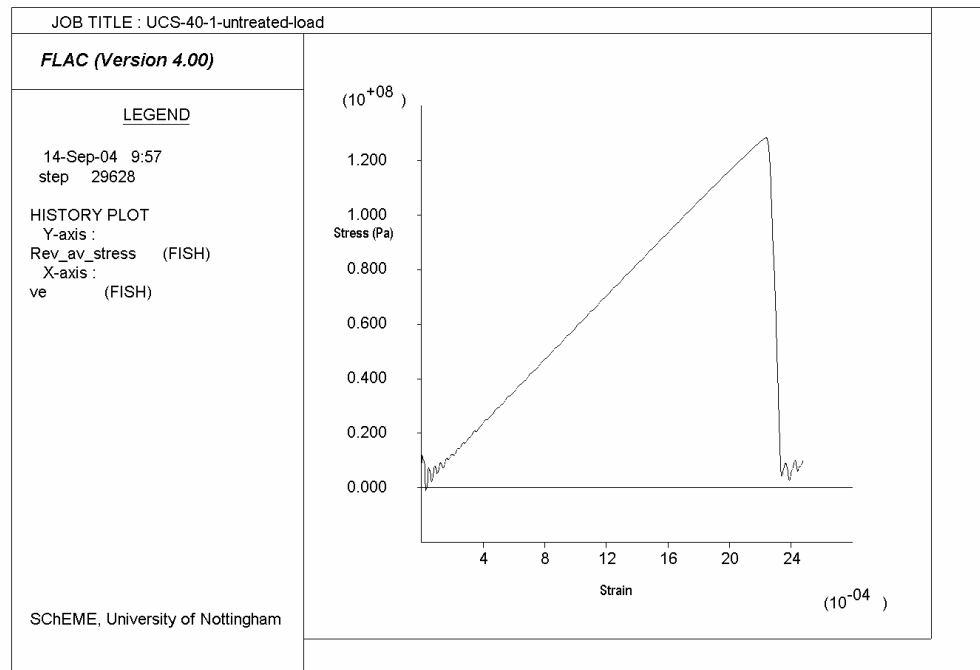


Figure 6.47: Stress vs strain plot for untreated 40mm diameter sample with 1% heated particles

Figure 6.48 shows the data from the simulated UCS test for the ‘lower power density – long exposure’ simulation at $1 \times 10^9 \text{ W/m}^3$ for 1s. The peak stress attained is almost identical to that obtained from the ‘control’ test. It was determined numerically to be 128.3MPa. This shows that in this case, the application of microwave heating has had little effect, except possibly for reducing the rate of failure. The sample has taken more steps to reach its residual strength, and this behaviour is attributable to a softer material.

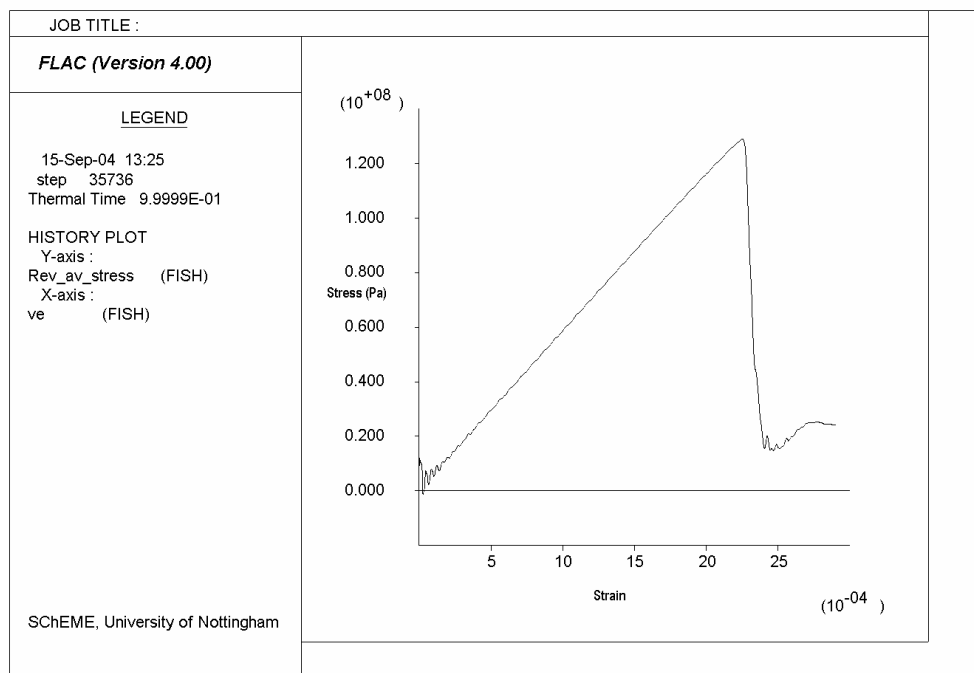


Figure 6.48: UCS test on the $1 \times 10^9 \text{ W/m}^3$ sample for 1s.

Figure 6.49 shows the UCS test data for the ‘high power short exposure time’ case where $1 \times 10^{15} \text{ W/m}^3$ were applied for 1 μ s. The plot shows that the peak strength has reduced slightly to 117.2MPa. Also the rate at which the material reaches its residual strength is also reducing. This is typical for a thermally damaged material.

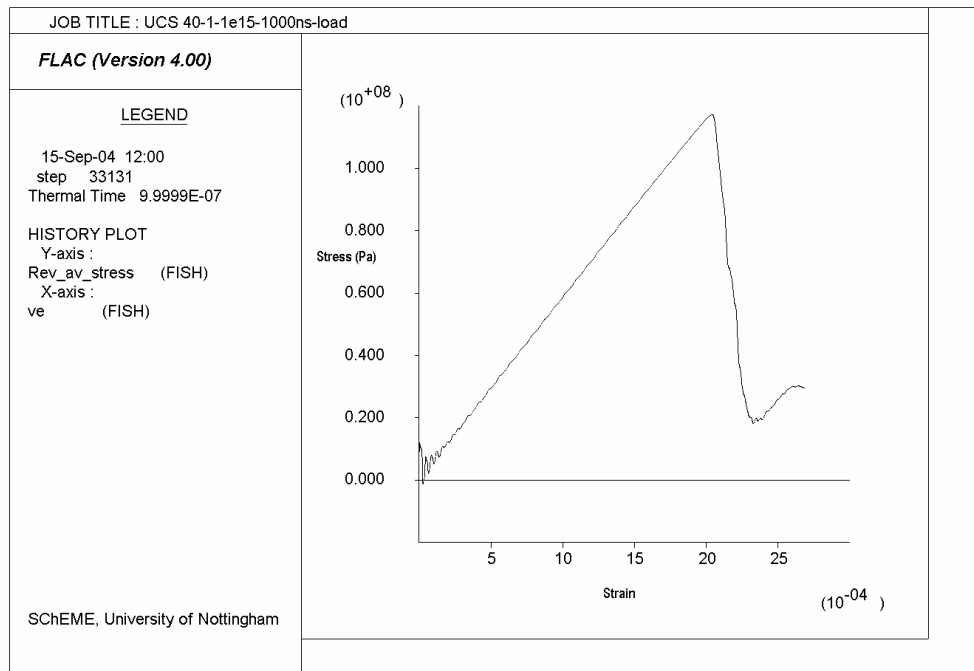


Figure 6.49: Stress vs strain plot of the UCS test on the $1 \times 10^{15} \text{ W/m}^3$ sample for $1\mu\text{s}$.

6.12.4 Discussion

When comparing the UCS data with the damage parameter data it is interesting to note how the levels of tensile strength reduction and cohesion reduction affect the UCS. After $1\mu\text{s}$ at $1 \times 10^{15} \text{ W/m}^3$, 3248 zones have undergone cohesion reduction as a result of the thermal expansion. This is quite a high proportion considering the model is only 12880 zones, and therefore constitutes over 25% of the total as shown in Figure 6.46. Further correlation between UCS and damage parameters is developed in the next section.

6.13 Correlation between UCS and Damage Parameters

6.13.1 Introduction

This section details a study to examine the effects of thermal damage on the sample with increasing time, and the effects on the damage parameters, and the UCS. The aim was to examine what correlation, if any, there was between the damage parameters and the UCS values. It was only possible to examine the percentage reduction in each case in order to plot both sets of data on equivalent scales.

6.13.2 Methodology

The ‘high power short exposure’ applied condition was studied in this case, with a power density of $1 \times 10^{15} \text{ W/m}^3$ applied for $1 \mu\text{s}$. The mechanical properties assigned to this model differed slightly from those used in the previous section in that no standard deviation was applied to the strength parameters. In section 6.12 previously, the strength of the $1 \times 10^{15} \text{ W/m}^3 - 1 \mu\text{s}$ sample was 117.2 MPa. All the mechanical properties were assigned standard deviations of 10%. This was fully explained in section 5.2. Here, without the random strength distribution, the resulting UCS of the $1 \times 10^{15} \text{ W/m}^3 - 1 \mu\text{s}$ sample was slightly higher at 125.6 MPa. Each timestep was equal to 1 nanosecond, and the model was run for a total of 10000 steps in order to give a heating time of $1 \mu\text{s}$. The model was again stopped at various intervals, and the number of zones with cohesion and tensile strength reduction were determined.

6.13.3 Results

The following tables detail the tensile strength and cohesion reduction undergone by the high power short exposure case. Note how the degree of damage increases as the time increases. The majority of the damage appears to occur between 100 and 500ns.

Timestep (ns)	Cd	reduction	%	% reduction
0	0	12880	100.00	0.00
100	29	12851	99.77	0.23
500	2531	10349	80.35	19.65
1000	3261	9619	74.68	25.32
2000	3696	9184	71.30	28.70
3000	3862	9018	70.02	29.98
5000	4170	8710	67.62	32.38
10000	4932	7948	61.71	38.29

Table 6.12: Calculation of reduction in cohesion damage for the high power short exposure case

Timestep (ns)	Td	reduction	%	% reduction
0	0	12880	100.00	0.00
100	7	12873	99.95	0.05
500	722	12158	94.39	5.61
1000	2288	10592	82.24	17.76
2000	4424	8456	65.65	34.35
3000	5472	7408	57.52	42.48
5000	6257	6623	51.42	48.58
10000	7158	5722	44.43	55.57

Table 6.13: Calculation of reduction in tensile strength damage for high power short exposure case

Table 6.14 details the equivalent UCS data for some of the model conditions detailed in tables 6.12 and 6.13 previously. Here the greatest reduction in strength occurs after the sample has been exposed to $1 \times 10^{15} \text{ W/m}^3$ for a duration between 1000 and 2000ns (1 and 2 μs). The strength reductions are extremely significant, and would result in greatly reduced comminution energy.

Timestep (ns)	UCS (MPa)	%	% reduction
0	144.11	100.00	0.00
100	143.40	99.51	0.49
500	140.46	97.47	2.53
1000	125.61	87.17	12.83
2000	82.12	56.99	43.01
3000	78.99	54.81	45.19
5000	71.33	49.50	50.50
10000	63.87	44.32	55.68

Table 6.14: Equivalent UCS reduction for high power short exposure case

The following tables detail the tensile strength and cohesion reduction undergone by the lower power long exposure case. Again note how the degree of damage increases as the time increases. The majority of the damage appears to occur between 100 and 500ns.

Timestep (ns)	Cd	reduction	%	% reduction
0	0	12880	100.00	0.00
100	12	12868	99.91	0.09
200	54	12826	99.58	0.42
300	119	12761	99.08	0.92
500	386	12494	97.00	3.00
750	677	12203	94.74	5.26
1000	964	11916	92.52	7.48
1500	1539	11341	88.05	11.95
2000	1949	10931	84.87	15.13
3000	2584	10296	79.94	20.06
10000	7615	5265	40.88	59.12

Table 6.15: Calculation of reduction in tensile strength damage for low power long exposure case

Timestep (ns)	Td total	Td	reduction	%	% reduction
0	0	0	12880	100.00	0.00
100	2	2	12878	99.98	0.02
200	7	5	12875	99.96	0.04
300	17	10	12870	99.92	0.08
500	67	50	12830	99.61	0.39
750	238	171	12709	98.67	1.33
1000	506	268	12612	97.92	2.08
1500	1174	668	12212	94.81	5.19
2000	2240	1066	11814	91.72	8.28
3000	3703	1463	11417	88.64	11.36
10000	6523	2820	10060	78.11	21.89

Table 6.16: Calculation of reduction in cohesion damage for low power long exposure case

The corresponding UCS data for the above simulation is detailed in Table 6.17 below.

Timestep (ns)	UCS (MPa)	%	% reduction
0	144.11	100.00	0.00
100	143.64	99.68	0.32
500	143.59	99.64	0.36
1000	143.95	99.89	0.11
2000	142.21	98.68	1.32
3000	141.44	98.15	1.85
5000	138.15	95.87	4.13
10000	128.16	88.94	11.06

Table 6.17: Equivalent UCS reduction for high power short exposure case

In Figure 6.50, the percentage reduction in UCS is plotted for the high power short exposure case and the low power short exposure case, as well as the equivalent data for percentage of zones which have undergone strength reduction. Note that in general the reduction in strength in terms of UCS and damage parameters is higher in the high power short exposure case. Also, it seems that in the high power short exposure case the majority of the damage appears to have been incurred by 2000 steps. Any further increase in input energy here yields minimal further reductions in strength. For the low power long exposure case the damage appears to be incurred in a more cumulative fashion, increasing almost linearly with time.

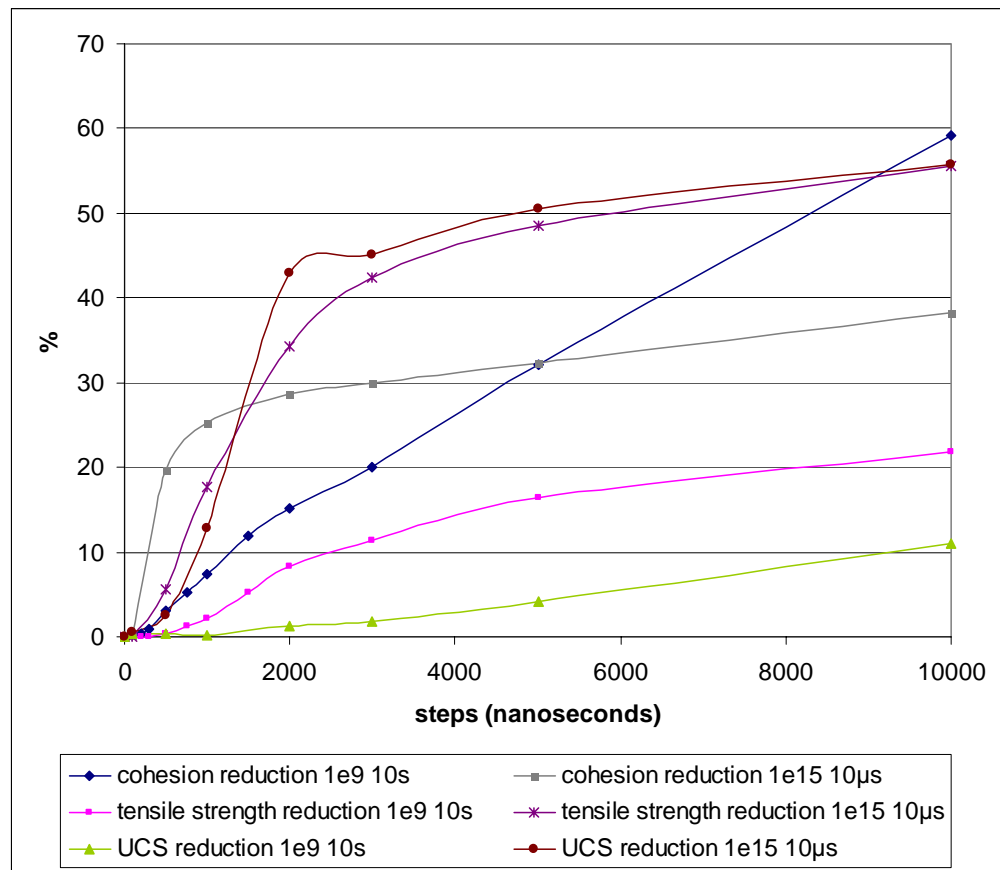


Figure 6.50: Comparison of % reduction in UCS, and total number of strain softened zones.

It was clear from the above data that the low power long exposure and the high power short exposure cases affected the cohesion and tensile strength reduction in different ways. Therefore the following figures show the temperature plots and the corresponding fracture plot for each microwave application case. Figure 6.51 shows the temperature contours for the low power long exposure case. The peak temperature attained here is 175°C. However the temperature contours show a diffuse distribution of thermal energy throughout the sample.

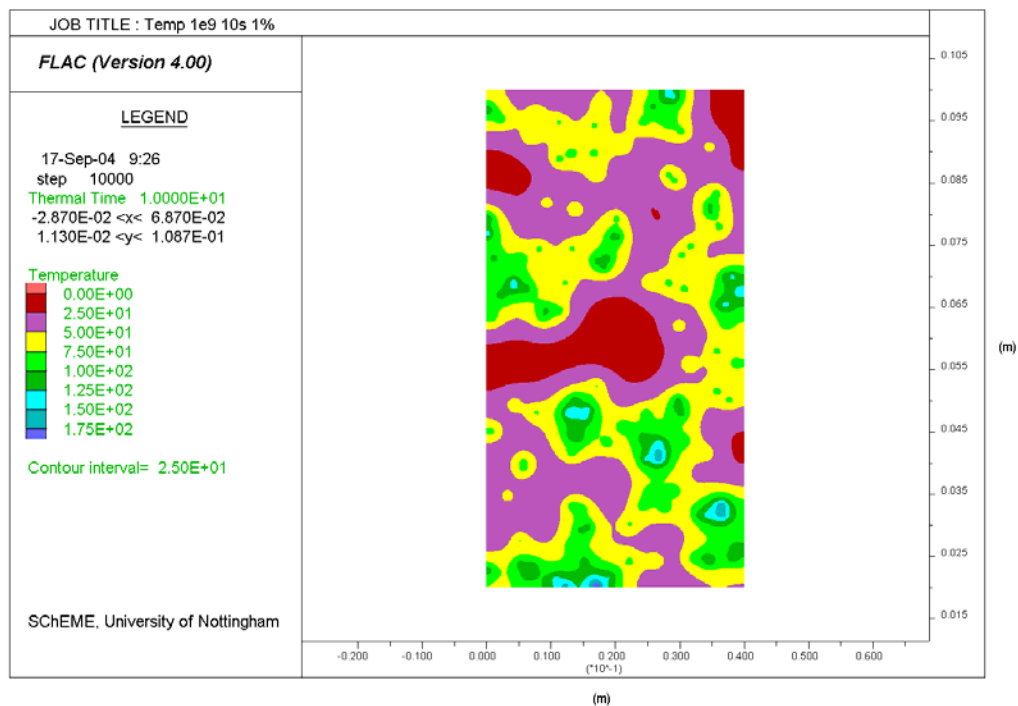


Figure 6.51: Temperature contours for the low power long exposure after 10s heating at $1 \times 10^9 \text{ W/m}^3$

Figure 6.52 shows the fractures in the sample in the form of areas that have failed in tension, in shear or have yielded in the past. There are large regions at yield in shear, or have yielded in the past shown by the dark red and purple colours. There are comparatively few tensile cracks (shown in yellow). Most of the tensile cracks run into or out of the areas with the most heated particle centres. The regions at yield in shear also surround these regions.

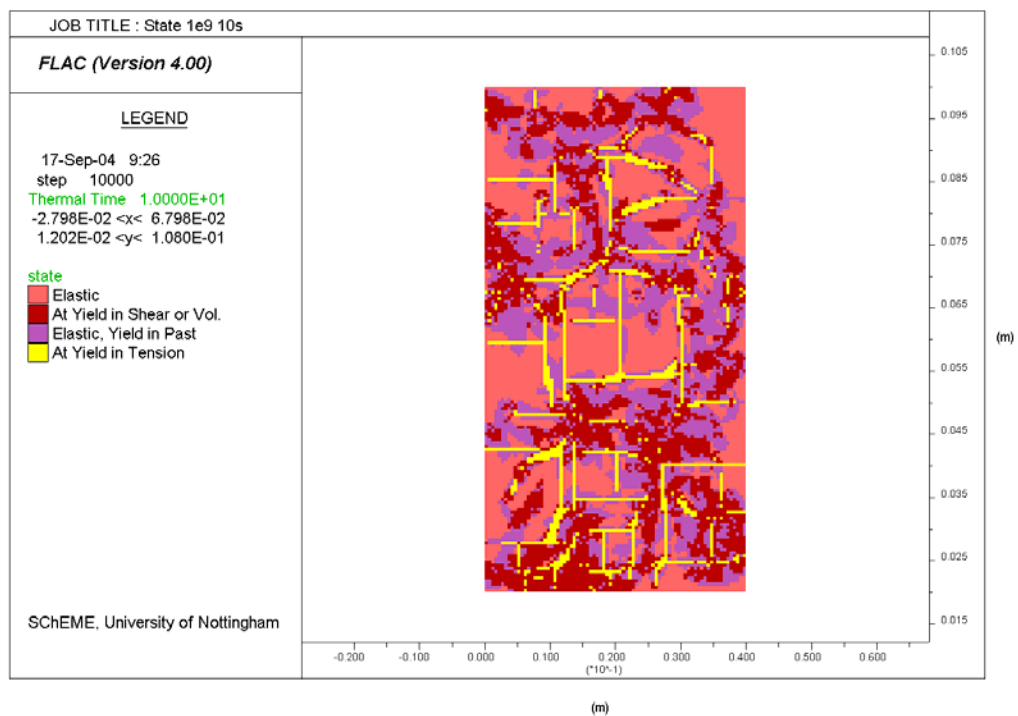


Figure 6.52: State plot for the low power long exposure after 10s heating at 1×10^9 W/m^3

If the high power short exposure case is examined in the same way then it can be seen that the temperature gradients are very well defined and localised. This has resulted in a maximum temperature of 2000°C as presented in Figure 6.53. Compare this with the 175°C obtained in the low power long exposure case. The same total energy input was applied in both cases; therefore the reduced time for conduction out of the heated particle centres into the transparent phase has resulted in greater heat retention in the high power short exposure case. This explains why the high power short exposure sample appears to have incurred much greater damage. Not only is the time in which the expansion is occurring shorter, which in itself causes greater stresses as shown in Section 6.10, but also the decreased time for conduction results in even higher temperature gradients resulting in an even greater expansion of the heated phases as shown in Section 6.9.

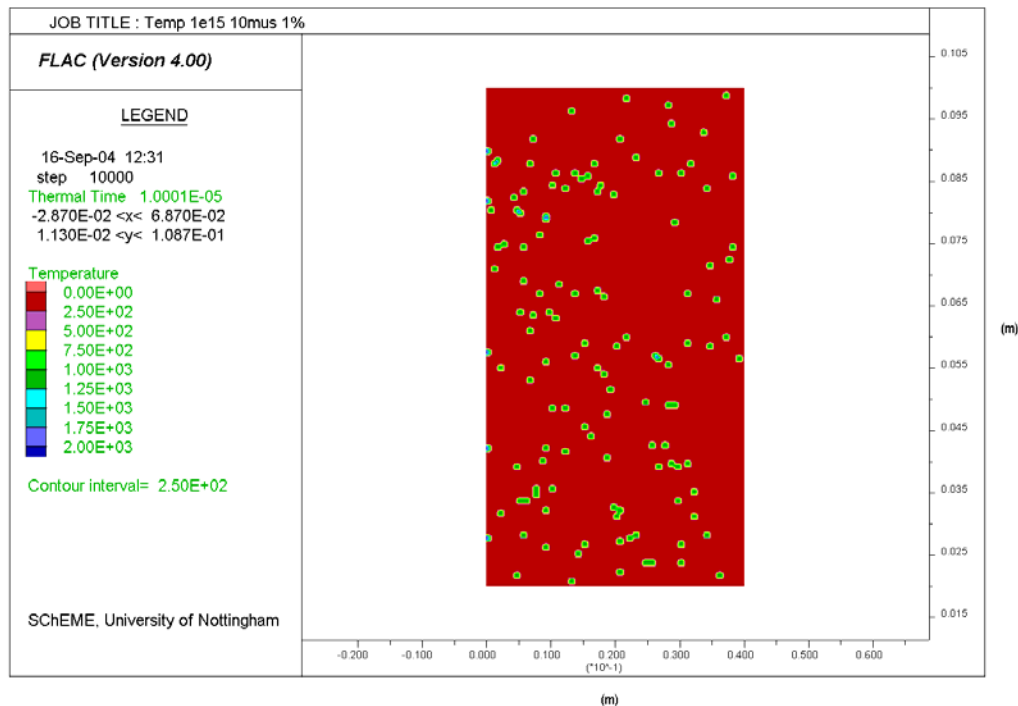


Figure 6.53: Temperature contours after 10µs heating at $1 \times 10^{15} \text{ W/m}^3$.

If the fracture plot is shown for the high power short exposure case the result is again very different from the low power long exposure wave case, with a predominance of tensile fractures in the sample. Again these fractures appear to emanate from the areas of highest heated particle concentration.

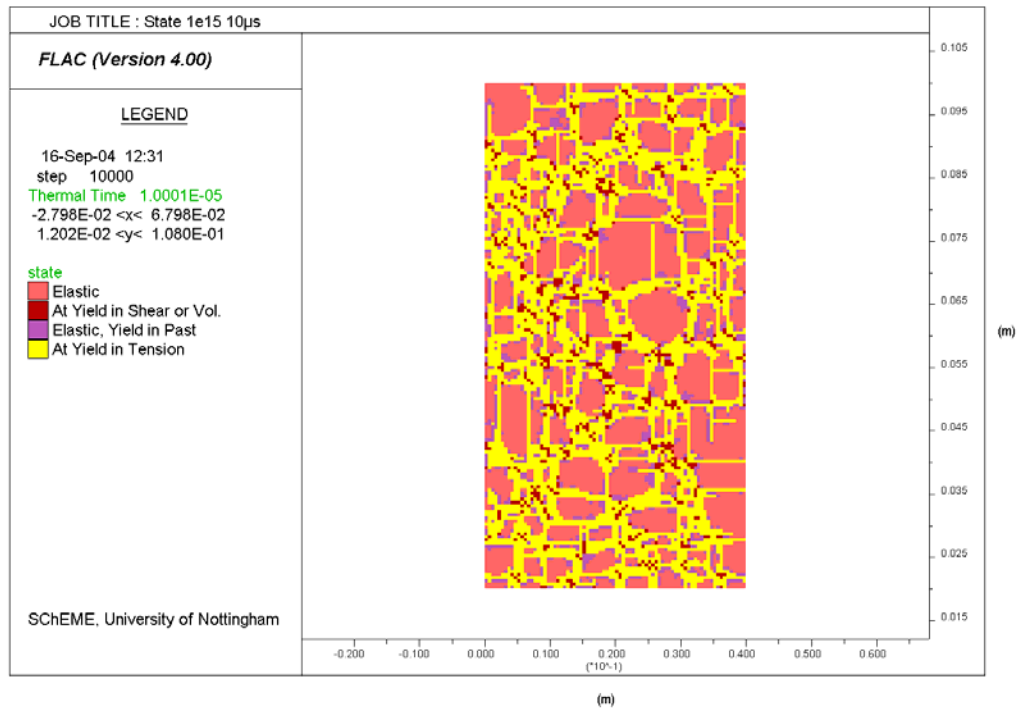


Figure 6.54: State plot for the high power short exposure case. There many tensile cracks, and very few areas of shear or past yield.

6.13.4 Discussion

There appears to be very little meaningful correlation between the UCS data and the damage parameter data. However the general trends are similar in that rapid reduction of the strength in the zones has resulted in a rapid reduction of UCS. The UCS data for the high power short exposure sample appears to follow the tensile strength reduction plot relatively closely. However it is unlikely that it is possible to derive direct

correlation between the damage parameters and the UCS. It is interesting to note how the cohesion reduction for the simulations finishes with a higher degree of damage than the high power short exposure case, whilst still resulting in a much lower UCS. It is also evident that in the high power short exposure case, the tensile strength reduction eventually ends up higher than the cohesion damage, whilst the opposite is true for the low power long exposure case. The cohesion reduction is higher than the tensile strength reduction initially for the high power short exposure case case, whilst the opposite is true for the low power long exposure case. The cohesion damage remains higher for the duration of the heating for the low power long exposure case. This may indicate that as the heating rate is higher in the high power short exposure case, it may result in a greater degree of initial tensile strength reduction. This may indicate a different mode of weakening in each situation. The rapidity of the heating in the high power short exposure case will mean that the material has less time to redistribute thermal stresses, and as a consequence higher stresses and stress differences will be more likely to occur locally. The fracture plots in Figure 6.52 and 6.54 show very different behaviours and may correspond with the values for the tensile strength reduction shown in Figure 6.50. There was a significant reduction in tensile strength for the high power short exposure case, and consequently there was a significant reduction in the UCS. For the low power long exposure case, the tensile strength reduction was not as significant, and the UCS reduction was minimal. The fracture plot for the high power short exposure shows a predominance of tensile strength reduction. This has resulted in a much lower UCS. It may therefore be that the shorter exposure times coupled with high power results in a greater predominance of tensile strength reduction, which in turn is more effective at reducing the strength of the sample.

6.14 Influence of Microwave Energy Input on Strength Reduction

6.14.1 Introduction

The modelling was undertaken to determine the effects of changes in power density and exposure time on the weakening of the theoretical sample during microwave heating. Damage parameter studies have indicated that higher rates of energy input result in significantly higher degrees of weakening. This UCS test will yield a more useful quantification of the weakening that will be useful in preparing possible future process benefits, as this measure can be correlated with breakage characterisation indexes such as fracture toughness and the breakage parameters A and b as discussed in Chapter 3.

6.14.2 Methodology

In the low power long exposure simulations, six ‘low’ power densities were simulated to vary between 1×10^9 and $4 \times 10^{10} \text{ W/m}^3$ for heating times varying between 0.1 and 10 seconds.

The high power short exposure simulations were undertaken for short durations of less than 0.1 seconds. For these simulations the power density was varied from 1×10^{13} to $2 \times 10^{15} \text{ W/m}^3$. The heating durations were varied between 0.1 microseconds to 10 microseconds.

Each sample was then subjected to the UCS test. The peak stress was logged and tabulated, and these values were plotted against time for each power density.

6.14.3 Results of Low Power Longer Exposure Simulations

The results of the low power long exposure simulation have been tabulated as a matrix of unconfined compressive strength values for individual power densities and exposure times (Table 6.18 and Figure 6.55).

It can be seen from this table that, above a certain power density, as exposure time is increased, greater damage is incurred in the sample. As would be expected, if the power density is increased, a given stress reduction can be achieved after a shorter exposure time. However, another effect for a decrease in exposure time (and a consequent increase in power density) is that even greater damage is incurred by the sample. Therefore, for a given amount of energy, greater damage is incurred when the power density is high and the exposure time is low. This is best illustrated in Figure 6.55.

Heating time (seconds)	0	0.1	0.5	1	2	3	5	10
$1 \times 10^9 \text{ W/m}^3$	144.11	143.64	143.59	143.95	142.21	141.44	138.15	128.16
$2 \times 10^9 \text{ W/m}^3$	144.11	144.08	143.51	141.61	128.55	120.35	108.49	93.80
$3 \times 10^9 \text{ W/m}^3$	144.11	-	-	126.37	-	-	85.77	70.27
$5 \times 10^9 \text{ W/m}^3$	144.11	143.60	116.10	82.85	77.70	73.09	63.36	42.19
$7 \times 10^9 \text{ W/m}^3$	144.11	-	-	-	-	-	47.10	-
$1 \times 10^{10} \text{ W/m}^3$	144.11	141.66	76.52	58.97	54.06	46.53	30.90	17.19
$2 \times 10^{10} \text{ W/m}^3$	144.11	-	-	49.69	-	-	-	-
$4 \times 10^{10} \text{ W/m}^3$	144.11	87.88	48.47	28.99	17.74	17.33	16.38	16.28

Table 6.18: Low power longer exposure uniaxial compressive strength test matrix of results (MPa)

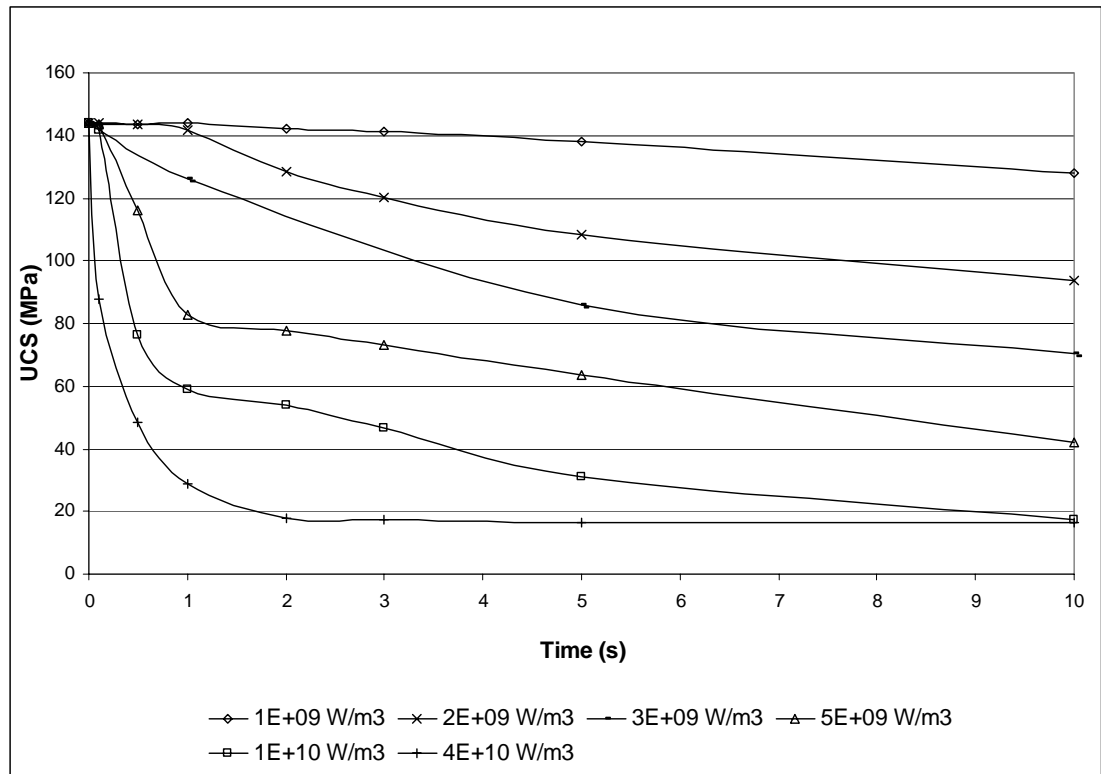


Figure 6.55: Variation of UCS with low power long exposure

An example of this is the contrast between the cases at $4 \times 10^{10} \text{ W/m}^3$ and $2 \times 10^9 \text{ W/m}^3$. In the case at $2 \times 10^9 \text{ W/m}^3$, after 10 seconds the strength has been reduced to 93.8 MPa from 144.1 MPa. If the same amount of energy is applied to the sample but at $4 \times 10^{10} \text{ W/m}^3$, but over 0.5s (i.e. $2 \times 10^{10} \text{ J/m}^3$) then the strength is reduced by 66% to 48.5 MPa. This difference in the reduction in strength for the same energy input can be attributed to the amount of time that is available for the heat to conduct from the absorbent phase into the surrounding matrix. If the power density is higher and the heating interval is lower, then there is less time for conduction out of the absorbent phase; the temperature remains higher in the absorbent grain, and the resulting elevated thermal expansion occurs over a shorter time interval. This should increase the stresses even further due to a thermal shock mechanism. For a given energy per unit volume, the greatest reduction in strength is achieved with the highest power density.

This observation is thought to be due to the decreased time for conduction to occur from the heated particle centres to the transparent phase as the heating is applied. Less time for conduction will result in a higher heated particle temperature being maintained. These higher maintained temperatures will result in higher degrees of thermal expansion. Also, as the temperature is higher in the heated particle, a greater thermal gradient will be maintained over the grain boundary. This has been shown in section 6.8 to result in higher shear stresses at the grain boundary, and this will yield to a more rapid reduction of the constituent elements cohesion and tensile strength at that point. This increased level of damage will in turn yield a softer, less fracture tough material, and this will in turn yield lower values of uniaxial compressive strength.

These trends were illustrated in the laboratory by (Kingman et al., 2004) where point load tests were conducted on samples treated at 5, 10 and 15kW power levels, and 0.1, 0.5 and 1 second exposure time in an automatically tuned single-mode cavity. A greater reduction in strength was achieved at higher power levels and exposure times. This data was presented in Section 3.11.3.

The magnitude of the strength reduction is very similar in the modelling data presented in Figure 6.55 above and the laboratory data presented in Figure 3.8. It is thought that at 15kW the single mode cavity is capable of sustaining a power density of at least $2 \times 10^8 \text{ W/m}^3$ (Bradshaw, 2004). Therefore the power densities simulated are within an order of magnitude of those predicted.

6.14.4 High Power Short Exposure Simulations

The results of the high power short exposure simulation have also been tabulated as a matrix of unconfined compressive strength values for individual power densities and exposure times (Table 6.19 and Figure 6.56).

Pulsewidth (μs)	0	0.1	0.5	1	2	3	5	10
$1 \times 10^{13} \text{ W/m}^3$	144.11	144.11	144.11	144.11	144.11	144.11	144.11	144.12
$1 \times 10^{14} \text{ W/m}^3$	144.11	144.11	144.11	144.11	144.11	142.25	138.43	122.92
$2 \times 10^{14} \text{ W/m}^3$	144.11	144.11	144.11	144.11	141.01	134.66	115.31	102.16
$5 \times 10^{14} \text{ W/m}^3$	144.11	143.52	143.52	140.58	118.82	98.29	93.94	78.73
$1 \times 10^{15} \text{ W/m}^3$	144.11	143.40	140.46	125.61	82.12	78.99	71.33	63.87
$2 \times 10^{15} \text{ W/m}^3$	144.11	143.48	125.70	81.57	64.57	63.24	58.88	52.33

Table 6.19: High power short exposure uniaxial compressive strength matrix of results (MPa)

The trend is repeated for the high power short exposure simulations, so that a greater reduction in strength is observed as the power density increases. However, the high power short exposure simulations were over a slightly larger range of power densities. This suggests that the reduction in strength diminishes as the power density is increased. This is to say that doubling a lower power density and longer exposure time would yield a greater reduction in strength than doubling a higher power density with shorter exposure time. It follows that there should be a power density above which, any further increase becomes inefficient, as the subsequent reduction in strength becomes too small to justify the extra energy requirement.

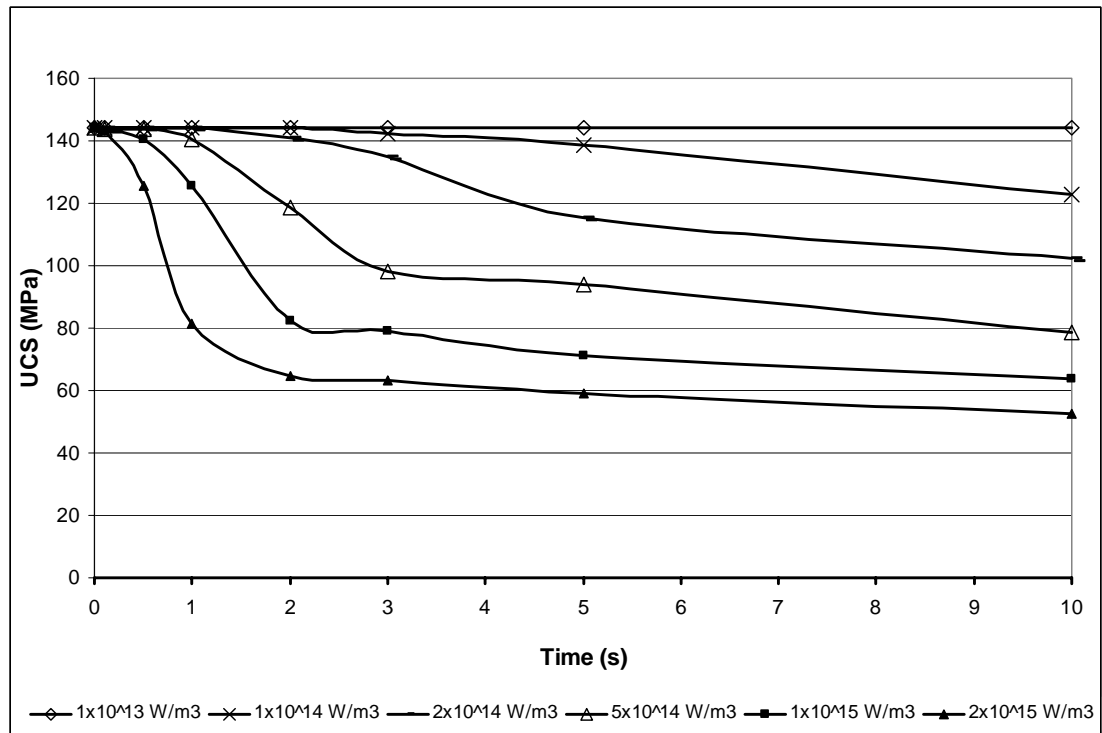


Figure 6.56: Variation of UCS with high power short exposure.

6.14.5 Constant Energy Results

The results of both the high power short exposure and low power long exposure type simulations were collected and expressed in a format which expresses the reduction in strength for each energy input. This energy input can then be applied to mineral processing energy balances in order to determine the economic viability of such an installation. The product of the power density and exposure time yields a total energy input per unit volume. Hence the horizontal axis shows constant energy input per unit volume for each vertical asymptote. Only the values up to $5 \times 10^9 \text{ J/m}^3$ are shown in figure 6.57. The curves progress in the horizontal direction in the time domain, so that each curve represents a total energy input of $1 \times 10^{10} \text{ J/m}^3$. In order to achieve this, the different power densities applied had to be of a particular duration so that the total energy input per unit volume was constant for each case. It can be seen from Figure 6.57 that a greater reduction in strength is achieved as the power density increases. Again it can be

seen that as the heating interval decreases and the power density increases, it is possible to achieve a greater reduction in strength. For example, it is possible to reduce the strength of the material by more than 13% if a power density of $5 \times 10^9 \text{ W/m}^3$ is applied for 0.4 seconds, and this corresponds to a total energy input of $2 \times 10^9 \text{ J/m}^3$. However if a power density of $1 \times 10^{12} \text{ W/m}^3$ is applied for 1ms, then the same reduction in strength can be achieved for half the total energy input, in this case $1 \times 10^9 \text{ J/m}^3$. Similarly, approximately 2.5% strength reduction can be achieved with $5 \times 10^8 \text{ J/m}^3$ when a power density of $1 \times 10^{15} \text{ W/m}^3$ is applied for $0.5\mu\text{s}$, whilst in order to achieve the same degree of strength reduction with a power density of $1 \times 10^9 \text{ W/m}^3$ would require 4s of treatment resulting in a total energy input of $4 \times 10^9 \text{ W/m}^3$ – an eight-fold increase in energy consumption for the same strength reduction.

It can be seen that there is a much greater difference in the strength reduction between the cases at $1 \times 10^9 \text{ W/m}^3$ and $1 \times 10^{10} \text{ W/m}^3$ (one order of magnitude difference) than there is between the cases at $1 \times 10^{12} \text{ W/m}^3$ and $1 \times 10^{15} \text{ W/m}^3$ (three orders of magnitude difference).

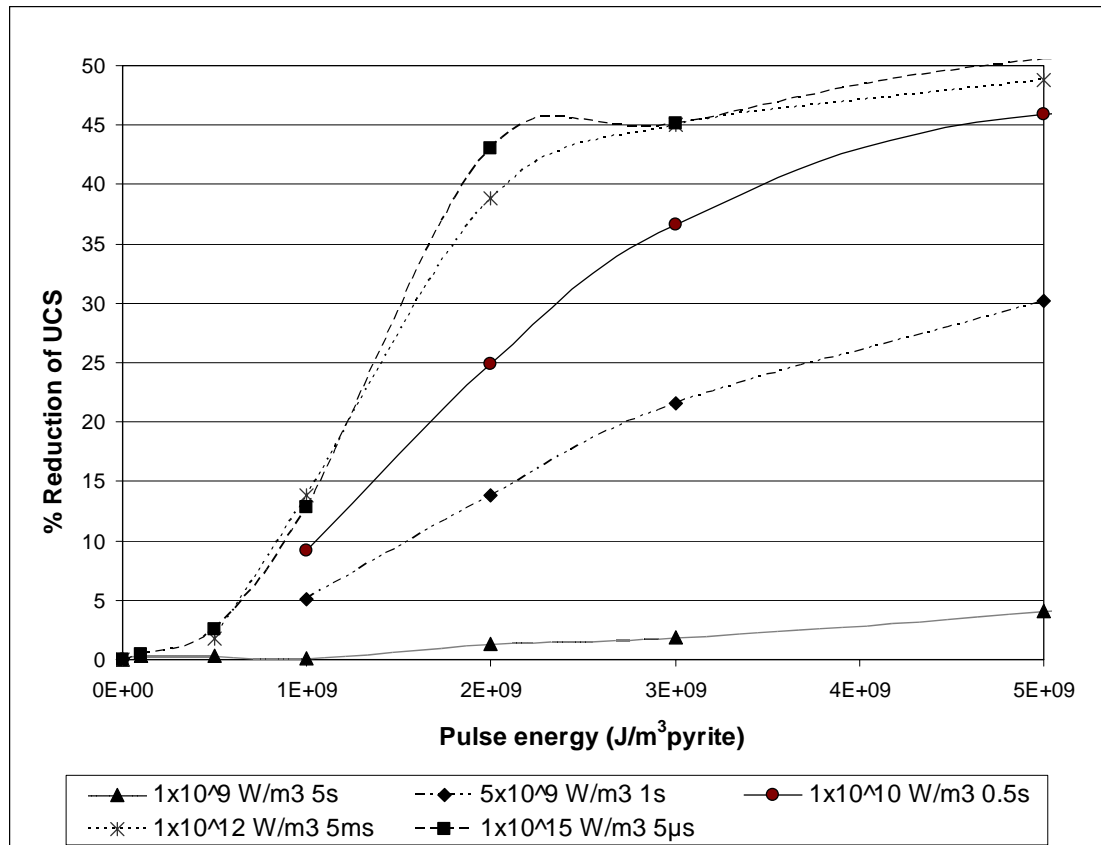


Figure 6.57: Summary of reduction in UCS with constant energy inputs.

6.14.6 Discussion

This section has again illustrated the increases in the efficiency of weakening when higher power densities and shorter exposure times are used. Also this suggests that for a given mineralogy there exists a power density above which any further increase yields insufficient reductions in strength to warrant the technological advances required to deliver such an energy intensive delivery. The degree of weakening required will depend on the process, with some applications requiring greater strength reduction than others. It is possible to conclude that each application will require specific microwave delivery type depending on the process requirements.

6.15 Effects of Varying Texture on Strength

6.15.1 Introduction

This section investigates the effects on UCS and damage parameter when the proportion of heaters was varied in order to yield better understanding of how texture affects the degree of weakening. One study was conducted with a constant power density of $1 \times 10^{15} \text{ W/m}^3$. The other took into account the change in volume of heaters that occurred when more heaters were introduced into the sample, and the power density was reduced accordingly.

6.15.2 Methodology

The first study applied the same power density throughout the study. The percentage heated particle concentration was increased from 1% to 100%. This effectively meant that more heat was absorbed by the sample, and therefore more cracks were to be expected. The percentage heated particle quantities used in the sample were 0%, 1%, 50% and 100%. The sample was exposed to $1 \times 10^{15} \text{ W/m}^3$ for $1\mu\text{s}$. Each sample which had varying proportions of heated particles was then subjected to the UCS test.

Another study was conducted to determine the effect on the number of strain-softened zones when the same net heat was applied to the total sample each time, whilst again varying the heated particle concentration from 1% to 100%. If a real ore sample has a greater degree of absorbers then it may be the case that the maximum power density in the sample may be reduced as the presence of greater volumes of high loss materials increases. Therefore this study investigated the degree of strain softening resulting from the same total heat input, whilst varying the % of absorbers. In the 10% sample, the power density has been reduced by a factor of 10. In the 50% sample, the power

density was reduced by a factor of 50, and similarly the 100% sample was exposed to $1 \times 10^{13} \text{ W/m}^3$ – a hundred fold reduction in power density with a hundred-fold increase in the proportion of heaters.

6.15.3 Results and Discussion

The results for the constant power density study can be seen in Figure 6.58. The plot shows the data for the treated and untreated curves. It is interesting to note how much the percentage of heated particles affects the UCS in the untreated sample. The pure transparent sample is strongest, and the introduction of heated particles into the system reduces the overall strength from 145 MPa to 125 MPa. Application of high power short exposure heating further reduces the strength by 5 MPa in this instance. The untreated strength of the 50% heated particle sample is 115 MPa. This shows that the introduction of heated particles dramatically weakens the untreated samples. This may be due to the higher stiffness of heated particles in this case allowing higher stresses (and consequently increased strain softening) to be generated when the load is applied. However, the increase in strength for the pure heated phase case indicates that the mixture of transparent phase and heated particles results in a weaker sample.

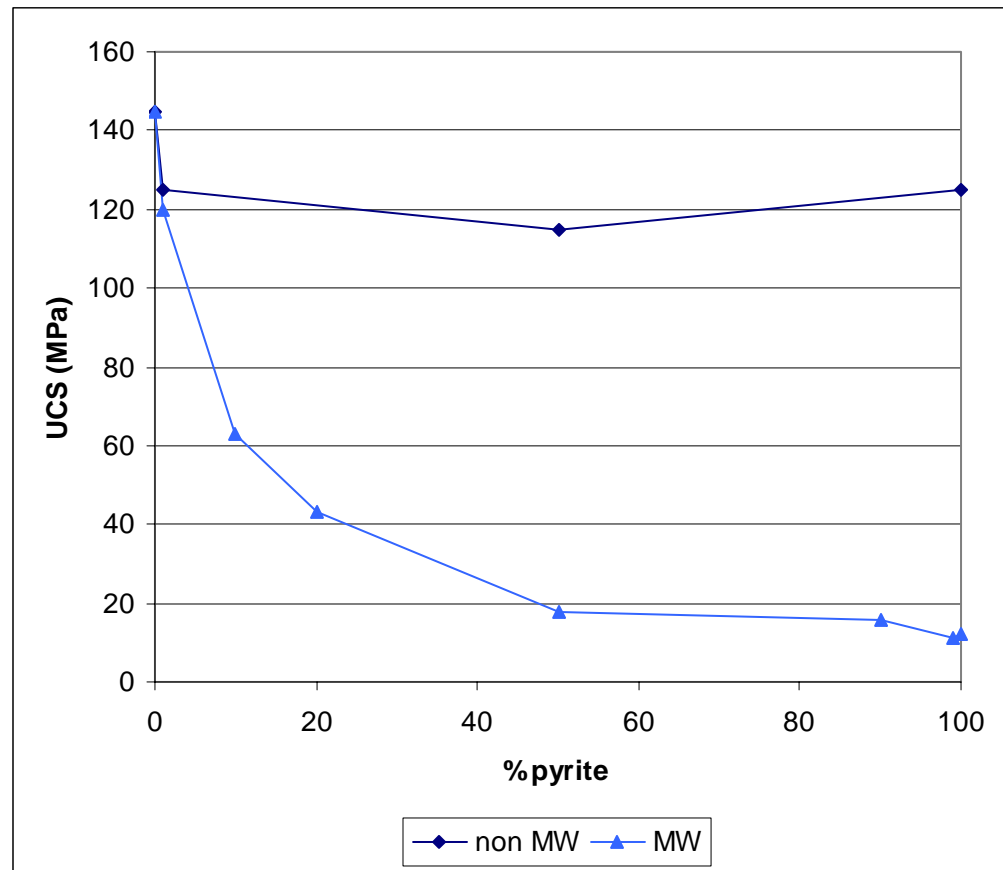


Figure 6.58: Plot detailing strength reduction with varying composition

The fact that the UCS decreases with increasing heated particle content is to be expected, as the higher concentrations result in a higher net heat input into the total sample, which in turn should lead to greater thermal stresses.

Table 6.20 shows the results from the constant energy input experiment. More results are required to draw full conclusions, but it is possible to infer that above certain concentrations, the power density is too low to generate the sufficient rate of temperature increase required to exceed the strength of the material. However, there may be an optimum concentration of heated particle that facilitates weakening, due to the number of crack initiation sites available when a certain percentage of heated particle is exceeded. As was discussed earlier, the untreated transparent/heated particle mixture is weaker than the untreated pure transparent phase, and the untreated pure heated phase.

% Heated particle	Power Density (W/m ³)	% zones w/cohesion reduction	% zones w/tensile strength reduction
1	1×10^{15}	25.1	35.4
10	1×10^{14}	41.2	37.3
50	2×10^{13}	0	17.1
100	1×10^{13}	0	16.7

Table 6.20: Results from the variation of percentage of heaters with constant energy input

6.16 Conclusions

- For a single spherical heated particle the highest stresses will occur just outside the particle boundary. These stresses are predominantly shear stresses that arise from the containment that the transparent phases impose on the heated phase when it is expanding. This can lead to enhanced liberation. This can occur when fractures are concentrated around the grain boundary leading to more exposed valuable heated mineral for physico-chemical treatments. It can also occur by effectively releasing the valuable heated mineral completely intact. This effectively facilitates liberation at a coarser size. This negates the need for further energy intensive grinding to separate the valuable heated phase from the transparent phase.
- When the heated phases are disseminated throughout a transparent matrix, areas of elevated stress occur around the heated phases when a heat input is applied. When the sample is loaded, these concentrations of heated phases are instrumental in crack initiation and propagation. This results in a much weaker sample that will require less comminution energy to reach the liberation size.
- At lower sizes, greater microwave energy input is required to heat the particles sufficiently so that an appreciable magnitude of expansion is achieved due to the increase in surface heat losses arising from increased area/volume ratio.
- It is apparent that the stresses generated increase as power density increases. This in turn leads to greater damage within the sample characterised by a lower UCS and greater number of zones with cohesion and tensile strength reduction. The higher power densities yield greater temperature rises, and hence a greater magnitude of thermal expansion.

- Greater reductions in strength are observed for a given energy input if the exposure time is decreased. This is implemented by the decreased time for the expansion to occur, which in itself yields higher stresses. Also the decreased time for conduction effectively maintains a higher temperature and therefore a higher degree of expansion within the material.
- It is suggested that a diminishing rate of reduction of strength exists as power density is increased. This is to say that there may be a power density above which no further reduction in strength is possible. This is shown by the large differences in the reductions in strength obtained when a sample is exposed to $1 \times 10^9 \text{ W/m}^3$ and $1 \times 10^{10} \text{ W/m}^3$ and the relatively small differences observed between the behaviour at $1 \times 10^{12} \text{ W/m}^3$ and $1 \times 10^{15} \text{ W/m}^3$ as shown in Figure 6.60. This suggests that the optimum power density may be of the order of $1 \times 10^{11} \text{ W/m}^3$ or $1 \times 10^{12} \text{ W/m}^3$ with an exposure time of between 0.01 and 1ms.
- Based on the above conclusion, it is possible to determine optimum pulse energy based on the reduction in strength, and its impact on breakage energy required in mineral processing plant, for example using the correlation between the UCS values and the JKMRC breakage parameters A and b .

Chapter 7

7.1 Conclusion

Due to the energy intensive nature of mineral processing, and the inherent inefficiencies in the crushing and grinding stages of comminution, even a marginal improvement in operational efficiency can lead to substantial energy savings and reduced environmental impact. These drivers have meant that a significant body of research has been carried out over the last few decades in an effort to improve efficiency. One technique that offers promise of achieving a step change improvement in what is the use of microwave pre-treatment. As shown in Chapter 3 it has suggested as a means of improving the efficiency of mineral comminution processes by inducing disorder at grain boundaries as a result of differential heating and expansion. Many positive process benefits, including reduced comminution energy required and enhanced liberation of valuable mineral, have been noted.

Unfortunately, until recently, these have been achieved at microwave energy inputs which are not economic as a consequence of the exact mechanisms of weakening being poorly understood. Previous work has varied the amount of microwave energy deposited into the minerals by varying the exposure time. What this numerical modelling study has achieved is to confirm that the variation of power density has much more effect on the degree of weakening and subsequent increase in liberation.

Recent work by Kingman et al. (2003) confirmed this theory by achieving strength reductions of over 70% with energy inputs of less than 1kW.h/t when a 15kW single-mode cavity was used to treat a copper carbonatite ore. By increasing the magnetron power from 5kW to 15kW a marked increase in strength reduction was observed.

This microwave cavity is capable of power densities many orders of magnitude higher than those used in previous studies and it was thought that this facilitated the dramatic weakening.

When high power densities and short exposure times are simulated using numerical modelling it is clear that weakening is facilitated at lower total energy inputs for two reasons. One reason, which was detailed in section 6.9, is that the time for conduction from the heated phase into the transparent phase is minimised, hence thermal gradients are maximised between the heated and transparent phases. These elevated temperature gradients across the grain boundary result in much higher shear stresses, and consequently these stresses exceed the strength of the material causing fracture

The other reason for high power density and shorter exposure times facilitating weakening, which was detailed in section 6.10, is that as heating times decreases, the magnitude of the acceleration of the heated particle surface increases. If conduction from the heated phase into the transparent phase is ignored, then a particular total energy input will yield the same magnitude of total expansion regardless of exposure time. However as the exposure time decreases, the time in which the expansion occurs is also decreasing, and hence the distance the surface of the heated particle is travelling is being covered more rapidly. Consequently the particle surface's velocity and acceleration increases and the force that the particle is exerting over the surrounding transparent phase will also increase resulting in a greater likelihood that the strength of the material at that point will be exceeded.

These findings explain why most previous studies on the microwave treatment of ores have failed to yield strength reduction at economic energy inputs as the power densities that were used were too low to induce the required rate of expansion for exceeding the strength of the material. Consequently most of the energy used in these studies ends up being wasted by heat conducting into the transparent phase. Therefore the variation of exposure time does not fully examine the effects of microwave radiation on ores as it merely exacerbates the heat ‘lost’ in to the transparent phases.

If it were therefore possible to accurately vary power density when exposing minerals to microwave radiation in the laboratory then it would be expected that far better experimental results would be obtained when higher power densities were used. The economics of industrial implementation of the research would be improved by minimising exposure time, as it is clear that it is not the total magnitude of temperature rise that is most important for facilitated weakening but the magnitude of the rate of temperature rise. If it is possible to selectively raise the temperature of a grain by even 1°C in a sufficiently short period, then it is feasible that the rate of temperature increase is sufficient to induce fracture due to the associated shear stresses that occur near the heated particle boundary.

It is these shear stresses that are thought to be responsible for another observation from the laboratory results in that liberation can be significantly enhanced by microwave treatment. The models suggest that the degree of liberation is potentially maximised whereby the spherical heated particle can be wholly liberated from the transparent phase due to the characteristics of the system geometry resulting in the

highest shear stresses occurring outside the heated particle boundary. The degree of liberation will of course decrease as the shape of the heated particle deviates from the spherical, as any angularity will result in a localisation of stress and strain-softening will ensue.

The attraction of this research for the mineral processing industry is that comminution energy can be greatly reduced. As already detailed in section 5.4.3.2, given a comminution energy of 3kW.h/t a 70% reduction in strength from 144MPa as in the case of the untreated 1% heated particle to 40MPa would result in the breakage parameter product of $A \times b$ increasing from 84 to 890. The t_{10} would increase from 54 to 66% passing 10% of the original sample size.

This increase in the amount of fines produced would negate the need for a large proportion of the energy required to grind to these fine sizes. The grinding of fines is the most energy intensive portion of the comminution process therefore any reduction of the amount of this energy intensive grinding stage will yield significant reductions in total energy consumption.

From the study it is possible to suggest the ideal operating criteria for future microwave equipment for the examined systems. It can be seen that very little reduction in strength is achieved when the power density is set to $1 \times 10^9 \text{ W/m}^3$ and the material heated for 5 seconds. Yet significant weakening is possible when the power density is increased tenfold to $1 \times 10^{10} \text{ W/m}^3$ and the subsequent exposure time decreased to 0.5s. Even greater strength reductions are obtained when the power density is again increased by 2 orders of magnitude to $1 \times 10^{12} \text{ W/m}^3$ and the

exposure time similarly reduced by 2 orders of magnitude to 5ms. However, only a slight improvement is gained when the power density is increased to $1 \times 10^{15} \text{ W/m}^3$ and the exposure time decreased to $5\mu\text{s}$.

It is clear that for the highest power density simulated here of $1 \times 10^{15} \text{ W/m}^3$, very little further decrease in strength is observed after $2\mu\text{s}$. Therefore it would be unwise to double the total energy input by increasing the heating time to $4\mu\text{s}$ in order to gain a further 5% reduction in strength. If the maximum amount of weakening is required then it would be achieved at the most economic energy input with a power density of $1 \times 10^{15} \text{ W/m}^3$ sustained for $2\mu\text{s}$. However, significant weakening still occurs when a power density of $1 \times 10^{10} \text{ W/m}^3$ is sustained for 0.1s. It may be the case that a 45% reduction in strength is not desirable, and that a 10% or 15% reduction is sufficient, and a power density of between $1 \times 10^{10} \text{ W/m}^3$ and $1 \times 10^{12} \text{ W/m}^3$ would suffice.

Regardless of power density it is clear that a total energy input of above $1 \times 10^9 \text{ J}$ per m^3 of heaters is required to facilitate weakening. It may be easier to implement this energy input at power densities of the order of 10^{10} W/m^3 than at the higher power densities of $1 \times 10^{15} \text{ W/m}^3$. Cavity design becomes a major factor at this stage of industrial implementation as it depends on whether the extremely high power densities can be generated without the need for excessively power-intensive equipment.

7.2 Further Work

The main limitations of this study have been those of computing power and material properties data. More complex modelling requires greater memory requirements and faster processing speeds in order to complete the simulation. Finer grids are required for the detailed analysis of material parameters when grain sizes are of the order of microns. Memory requirements rise exponentially as the fineness of the grid increases. Increased fineness of grid will also allow for the expression of the variation of the shape of the grains as long as the finite difference grid is sufficiently fine that grains can be made up of multiple zones. An alternative approach is to use distinct element analysis coupled with finite element, which allows for the simulation of grains as discrete bodies that are bound together by certain conditions. Modelling in 3 dimensions would also increase the realism but computational requirements would increase immensely.

Any future work is likely to be undertaken on more powerful computers in line with what becomes available commercially. However, it is thought that a step change in processing power is required in order to fully express the mineralogy, texture, thermal and mechanical properties of a real ore. Grid computing could be a viable means of increasing the processing power in this case. However it is likely that *FLAC* would be unsuitable for this purpose.

In order for the technology to be applied to industrial processes, potentially viable ores must first be identified. However, it is apparent that there is a shortage of reliable material properties data in the literature. If the modelling capability becomes such that acceptable degrees of realism can easily be expressed in the model, then

detailed thermal, mechanical and dielectric properties for each constituent phase must be determined in order to assess the amenability of each ore for microwave treatment. The data on the material properties has been limited in terms of the number of species for which data is available, and the accuracy of those measured properties over the likely temperature range experienced. The measurement of dielectric properties is a field of research in its own right, and further advances are required in order to gain realistic estimates of the likely power density that is likely when a mineral is exposed to microwave radiation. Advances in electromagnetic modelling of microwave cavities will yield better estimations of the likely power density throughout the sample, taking into account factors such as cavity dimensions and geometry, frequency of radiation, sample geometry and its dielectric properties.

In terms of the thermo-mechanical modelling, a greater number of species are required for analysis in order to represent the complex mineralogies of certain economic mineral deposits. Therefore their thermal and mechanical properties are required to be known in detail. This would effectively be another research area in itself in order to determine how these properties vary over the expected range of temperatures and confining pressures.

In terms of finite difference continuum modelling the strain softening parameters require refinement to some extent. It is conceivable that better approximations of the strain softening properties can be obtained by the back-fitting of data obtained from the post failure behaviour of samples in an UCS test for example. However this raises the issue of whether the strain softening properties of the material may differ greatly post-treatment and may not be representative.

More specifically in terms of this study, a wider variety of shapes could be examined to examine how deviation from the spherical affects the degree of liberation. Liberation could be measured by incorporation of an exposure model such as those suggested by Hsieh et al. (1995).

- Andres, U., Timoshkin I., Jirestig J., Stallknecht H., T.H., (2001) "Liberation of valuable inclusions in ores and slags by electrical pulses" *Powder Technology*, Vol.114, Issues 1-3, pp40-50
- Austin, L.G., Klimpel, R.R., Luckie, P.T., (1984) "Process Engineering of Size Reduction" *Ball Milling SME*, New York. ISBN 0-89520-421-5.
- Baláž, P., Sekula, F., Jakabský, Š., Kammel, R. (1995) "Application of attrition grinding in alkaline leaching of tetrahedrite" *Minerals Engineering* Vol.11, pp1299-1309
- Bass, J. D., (1995) "Elasticity of Minerals, Glasses, and Melts" In: Handbook of Physical Constants, (T. J. Ahrens, ed.) *American Geophysical Union*, Washington, DC, pp45-63.
- Bearman, R.A., (1999) "The use of the point load test for the rapid estimation of Mode I fracture toughness" *Int. J. Rock Mech. Min. Sci.* Vol.36 (2), pp257-263.
- Bearman, R.A., Briggs, C.A., Kojovic, T., (1997) "The application of rock mechanics parameters to the prediction of comminution behaviour" *Minerals Engineering* Vol.10 (3), pp255-264.
- Bieniawski, Z.T., (1975) "The point load test in engineering practice" *Engineering Geology* Vol.9, pp1-11.
- Blackburn, S., (1983) "The effect of Heat Treatment on the Magnetic Properties of Wolframite" PhD Thesis, University for Birmingham.
- Bond, F.C. (1946), *Crushing Tests by Pressure and Impact*, *Trans SME/AIME* Vol.169, pp58-66
- Bottcher, C.J.F., and Bordewijk, P., (1978) "Theory of Electric Polarisation" Vol.2, Elsevier Science Publishing Co. Ltd. Amsterdam

Brady, B.H.G., Brown, E.T., (1993) "Rock Mechanics for Underground Mining"

Chapman & Hall p89

Broch, E., and Franklin, J.A., (1972) "The point load strength test" *Int.*

J. Rock Mechanics. Mining Sci. Vol.9 pp669-697

Broch, E.S., (1971) Point Load Testing of Rocks. London, Imperial College of

Science and Technology.

Cargill, J.S., and Shakoor A., (1990) "Evaluation of empirical methods for measuring

the uniaxial compressive strength" *Int. J. Rock Mechanics Min. Sci* Vol.27

pp495-503

Chatterjee, I., Misra, M., (1991) "Electromagnetic and thermal modelling of

microwave drying of fine coal" *Minerals and Metallurgical Processing*

pp110-114

Chau, K.T. and Wong, R.H.C., (1985) "Uniaxial compressive strength and point load

strength" *Bull Int Assoc Eng Geol* Vol.31 pp183-188 (Technical Note)

Chen, T.T., Dutrizac, J.E., Haque, K.E., Wyslouzil, W. and Kashyap, S., (1984) "The

relative transparency of minerals to microwave radiation" *Canadian*

Metallurgical Quarterly, Vol.23, No.3, pp349-351

Church, R.H. et al, (1993) *USBOM Report of Investigations* 9194.

Coetzee M.J., Hart R.D., Varona P.M. and Cundall P.A., (1993) "*FLAC Basics*",

Itasca Consulting Group Inc.

Cohen H.E. (1983) "Energy Usage in Mineral Processing" *Trans. Inst. Min. Metall.*,

Vol.92, pp160-163

Cumbane, A.J. (2003) "Microwave treatment of minerals and ores" Ph.D. Thesis

University of Nottingham

- D'Andrea, D.V., Fischer, R.L., Fogelson, D.E., (1965) "Prediction of compressive strength from other rock properties" *US Bureau of Mines Report of Investigations* 6702,
- Deer, W.A., Howie, R.A., Zussman, J. 1962; "Rock Forming Minerals", Vol.5, pp128-180
- Diernat, F., and Duffaut, P. (1966) "Essais sur echantillons de forme irregulaire" *Proc. 1st Congr. Int. Soc. Rock Mechanics*, Lisbon
- Dorfmann, A., Rothenburg, L., Bruno, M.S., (1997) "Micromechanical modelling of sand production and arching effects around a cavity", *Int. J. of Rock Mechanics & Mining Sci.*, Vol.34, No.3/4, p.363, paper no 68
- Drost J.J., and Mahan, W.M., (1973) "Effects of thermal treatment upon grindability of a non-magnetic ore, *USBM R17797*
- Duffaut, P. (1968). "Effect d'échelle dans l'écrasement de blocs de forme irreguliere." *Revue de L'Industrie Minerale*
- Duffaut, P., and Maury, V. (1970) "Etudes photoelastiques sur l'essai Protodyakonov" *2nd Congr. Int. Soc. Rock Mechanics*, Belgrade.
- Duncan T., (1981) "Advanced Physics: Materials and Mechanics". 2nd Edition, Pub. *John Murray*, London
- Duncan, J. M., P. Byrne, K. S. Wong and P. Mabry. (1980) "Strength Stress-Strain and Bulk Modulus Parameters for Finite Element Analyses of Stresses and Movements in Soil Masses," University of California, Berkeley, College of Engineering, Report No. UCB/GT/80-01
- El Bied, A., Sulem, J., Martineau, F., (2002) "Microstructure of shear zones in Fontainebleau sandstone" *Int. J. Rock Mech. & Min. Sci.* Vol.39 pp917-932

- Fang, Z., Harrison, J.P., (2002) "Development of a local degradation approach to the modelling of brittle fracture in heterogeneous rocks" *Int J Rock Mechanics & Mining Sciences* Vol.39 pp443-457
- Fletcher, R. (1995) "Investigation into microwave heating of uranium dioxide"
Electrical Engineering, University of Nottingham
- Florek, I., Lovás, M., Múrová, I., (1996) "The effect of microwave irradiation on magnetic properties of grained iron containing minerals" In. Proc. 31st *Int. Microwave Power Symposium* , Boston, USA
- Florek, I., Lovás, M., Múrová, I., (1996) "Influence of microwave radiation on the leaching of tetrahedrite" *Mineralia Slovaca*, Vol.28, pp450-454.
- Florek, I., Lovás, M., Murová, I., (1996) "Intensification of magnetic separation of chalcopyrite ore by microwave radiation" in Proc. VI. *Int. Conf. on Microwave and Frequency Heating*, Fermo, Italy
- Ford, J.D. and Pei, D.C.T., (1967) *Journal of Microwave Power* 2, pp61-64.
- Forster, I.R., (1983) "The Influence of core sample geometry on the axial point-load test" *Int J Rock Mech Min Sci*; Vol.20;pp291-295
- Garratt M.H. (1997) "Computer Modelling as a Tool for Strata Control and Reinforcement Design", *Symposium on Developments in Ground Control*,
University of Nottingham
- Gaudin, A.M. and Hukki, R.T., (1946 "Principles of comminution – size and surface Distribution", *Trans. Am. Inst. Min (metall) Engr*, , Vol.169, pp67-87
- Geller, L.B. & Tervo,R.O., (1975) "Grinding of Preheated Rocks"
Trans. IMM (SecC) Vol.84, no25

- Grasso, P., Xu, S., Mahtab. A., (1992) "Problems and promises of index testing of rocks". *In: Tillerson, Wawersik, editors. Rock Mechanics.* Balkema, Rotterdam, ISBN 9054100451, pp879-888
- Gross, J. (1938) "Crushing and Grinding" *US Bureau of Mines Bulletin* 402, pp1-48
- Gunsallus, K.L., and Kulhawy, F.H. (1984) "A comparative evaluation of rock strength Measures". *Int J Rock Mech Min Sci* Vol.21, pp233-248
- Hajiabdolmajida, V., Kaisera, P.K., Martin, C.D., (2002) "Modelling brittle failure of rock" *Int J Rock Mech Min Sci* Vol.39, pp731-741
- Hallbauer DK, Wagner H, Cook N.G.W., (1973) "Some observations concerning the Microscopic and mechanical behaviour of quartzite specimens in situ, triaxial compression tests" *Int J Rock Mech Min Sci & Geomech Abstr*, 10:713±26.
- Haque, K.E., (1987) "Microwave irradiation pre-treatment of refractory gold Concentrate" *International Symposium on Gold Metallurgy*, Winnipeg, Canada
- Haque, K.E., (1999) "Microwave Energy for mineral treatment processes - a brief review" *International Journal of Mineral Processing* Vol.57, pp1-24
- Hariharan, K., and Venkatchalam, S., (1977) "Influence of Thermal Treatment upon Grindability of Quartz" *Mining Magazine* Vol. p105
- Harrison, P.C. (1995) "A Fundamental Study of the effects of 2.45GHz Microwave Radiation on the Properties of Minerals" M.Phil. Thesis, University of Birmingham
- Harrison, P.C. (1998) "A Fundamental Study of the heating effects of 2.45GHz microwave radiation on the Properties of Minerals" Ph.D. Thesis, University of Birmingham
- Harrison, P.C., and Rowson, N.A., (1996) "The effect of heat treatment on the grindability of coals" 2nd *European Conference for young researchers*

- Hassani, F.P., Scoble, M.J., Whittaker, B.N., (1980) "Application of point-load index test to strength determination of rock and proposals for new size-correction chart" *In: Proceedings of the 21st US Symposium on Rock Mechanics*, Rolla, pp543-564
- Hearmon, R.F.S., (1979) "The elastic constants of crystals and other anisotropic materials", in *Landolt-Bornstein Tables*, III/11, pp1-244, edited by K.H. Hellwege and A.M. Hellwege, *Springer Verlag*, Berlin
- Herbst, J.A., and Fuerstenau, D.W., "The zero order production of fines in comminution and its implications in simulation". *Trans. SME/AIME* Vol.241, pp531-549
- Hoek E. and Brown E.T. (1980) "Underground Excavations in Rock", published by *Institution of Mining and Metallurgy*, London.
- Hoek E. and Brown E.T. (1997) "Practical Estimates of Rock Mass Strength", *International Journal of Rock Mechanics, Mining Sciences and Geomechanics Abstracts*, Vol.34, No. 8, pp1165-1186.
- Holman B.W. (1926) *Trans. IMM*. Vol.26, pp219-225
- Holman, B.W., 1927 - Heat Treatment as an Agent in Rock Breaking. *Trans IMM*
- International Society of Rock Mechanics Commission on Standardization of Laboratory Field Tests (ISRM commission, 1979)
- ISRM Suggested Methods, (1978) Suggested Method for the quantitative description of discontinuities in rock masses. *Int J Rock Mech Min Sci*; Vol.15, pp319-68
- Jacobs, S., Kelland, D.R., Levinson, L.M., Maxwell, E. (1982) "Magnetic separation and thermo-magneto-chemical properties of coal liquefaction mineral participates" *Fuel* 61:4

- Jacobs, I.S., (1982) "Tracking Pyrite Sulfur in the microwave desulfurization of coal"
Journal of Applied Physics Vol.53 (2), pp2730-2732
- Jaeger, J.C., and Cook, N.G.W., (1979) "Fundamentals of Rock Mechanics" *Methuen and Co.* London.
- Ji, S., Wang, Q., Xia, B., (2002) "Handbook of Seismic Properties of Minerals, Rocks and Ores" *Polytechnic International Press* Canada
- Jinga, L., Hudson, J.A., CivilZone review paper (2002) "Numerical methods in rock mechanics", *Int. J. Rock Mechanics Mining Sci.* Vol.39 pp409-427
- Kahraman, S., (2001) *Int J Rock Mechanics & mining Sciences* Vol.38, pp981-994
- Kanellopoulos, A., and Ball, A., (1975) "The Fracture and Thermal Weakening of Quartzite in Relation to Comminution" *J.S.A.I.M.M* Vol.76 p42
- Kelland, D.R., (1988) *IEEE Transactions on Magnetics.* Vol.24, no6, pp2434-2436
- King, R.P. (2001) "Modeling & Simulation of Mineral Processing Systems" BH
- Kingman, S.W., (1998) "The effect of microwave radiation upon the comminution and beneficiation of mineral" Ph.D. thesis, University of Birmingham.
- Kingman, S.W., Corfield, G.M. & Rowson, N.A., (1999) "Effects of microwave radiation upon the Mineralogy and Magnetic Processing of a Massive Norwegian Ilmenite Ore" *Magnetic and Mineral Separation* Vol.9, pp131-148
- Kingman, S.W., Jackson, K., Cumbane, A.J., Bradshaw, S.W., Greenwood, R. & Rowson, N.A. (2004) "Recent developments in microwave-assisted comminution" *International Journal of Mineral Processing*, Vol.74, pp71-83
- Kingman, S.W., Vorster, W., Rowson, N.A., (2000) "The influence of mineralogy on microwave assisted grinding" *Miner. Eng.* Vol.13 (3), pp313-327.
- Knacke, Kubachewski and Hesselmann, (1991). "Thermochemical Properties of Inorganic Compounds – Publishers Springer-Verlag

- Koukkala, V.T., and Vuoristo, T. (2003) "Hopkinson Pressure Bar Experiment"
<http://www.ccm.udel.edu/reports-pubs/spring 02-reviews/.2003>
- Kranz RL. (1979) "Crack growth and development during creep in Westerly granite"
Int J Rock Mech Min Sci & Geomech Abstr 16:23±36.
- Lanigan P.G., (1989) *Proc. First Aus. Symp. On Microwave Power Applications*.
 pp160-176.
- Lyttle, J., et al. (1992) "Influence of preheating on grindability of coal"
International Journal of Mineral Processing Vol.36, pp107-112
- Marland, S., Merchant, A., and Rowson, N.A., (2001) "Dielectric Properties of Coal".
Fuel Vol.80 (13), pp1839-1849
- McGill, S.L., et al. (1988) "The Effects of Power Level on the Microwave Heating of
 Selected Chemicals and Minerals" *Materials Research Society Proceedings*
 Vol.124, pp247-252
- Meredith, R., (1998) "Engineer's Handbook of Industrial Microwave Heating" *IEEE*,
Peter Peregrinus Ltd
- Metaxas, A.C., & Meredith, R.J. (1983) "Industrial Microwave Heating"
Peter Peregrinus Ltd
- Napier, JAL, Peirce, SS. 1995 "Simulation of extensive fracture formation and
 interaction in brittle materials". In: *Rossmann H-P, Proceedings of the Second
 International Conference on Mechanics of Jointed and Faulted Rock*, pp63–74.
- Napier-Munn, T.J., Morell, S., Morrison, R.D., Kojovic, T., (1996) "Mineral
 comminution circuits. Their operation and optimisation" *JKMRC Monograph
 Series in Mining and Mineral Processing* 2. JKMRC, Queensland, Australia,
 pp81-83.

- Nelson, S.O., and Kraszewski, A.W., (1990) *Drying Technology* Vol.8, no5
pp1123-1142
- Osepchuck, J.M., (1984) “A History of Microwave Heating Applications” *IEEE Transactions of Microwave Theory and Techniques*
- Parker, S.P. (1993) McGraw-Hill Encyclopaedia of Physics (2nd edition). McGraw-Hill Inc. New York
- Peng, SS. (1976) “A photoelastic coating technique for rock fracture analysis” *Int J Rock Mech Min Sci Geomech Abstr* Vol.13, pp173-176.
- Pocock, J., Veasey, T.J., Tavares, L. M., and King, R. P. (1998) “The effect of heating and quenching on grinding characteristics of quartzite”, *Powder Technology*, Volume 95, Issue 2, pp137-142
- Read, J.R.L., Thornten, P.N., Regan, W.M., (1980) “A rational approach to the point load test. In: *Proceedings Aust-N.Z. Geomechanics*, vol2 p35-9
- Reddish, D.J., Stace, L.R., Vanichkobchinda, P. and Whittles, D.N., “Numerical simulation of the dynamic impact breakage testing of rock”, *NUMOG IX*
- Rhodes, M., 1998. “Introduction to Particle Technology” *Wiley*, Chichester, UK.
- Roberts B.H. (1994) “A Study of small Scale Coal Mining with particular Reference to the Longwall System and its Means of Support”, PhD Thesis, University of Nottingham.
- Rowson, N.A., and Rice, N.M. (1990) Technical Note: Desulphurisation of Coal using Low Power Microwave Energy. *Minerals Engineering* Vol.3, pp 363-368
- Salsman, J.B., Williamson, R.L., Tolley, W.K., Rice, D.A., 1996 “Short Pulse Microwave Treatment of Disseminated Sulphide Ores” *Miner. Eng.* Vol.9 (1), pp43-54.
- Schonert, K. (1972) “Role of fracture physics in understanding comminution

- phenomena” *Trans. SME/AIME* 252: 21-26
- Seaton, C.E. *Trans. ISIJ*. Vol.23, pp490-496.
- Simmons, G., and Birch, F., (1963) “Elastic Constants of Pyrite”, *Journal of Applied Physics* Vol.34, pp2736-2738
- Standish, N. and Yu, A.B., (1990) “A study of particle size distributions”, *Powder Technology* Vol.62:2 pp101-118
- Starfield A.M. and Cundall P.A. (1988) “Towards a Methodology for Rock Mechanics Modelling”, *International Journal of Rock Mechanics, Mining Science and Geomechanics Abstracts*, Vol.25, No.3 pp99-106.
- Sutton, W. H. (1993) “Key Issues in Microwave Process Technology” *Ceramic Transactions*, Vol. 36, pp3-18 “Theory and Application in Materials Processing” II. D. E. Clark, W. R. Tinga, and J. R. Laia, eds. Westerville, Ohio: American Ceramic Society.
- Tapponier P, Brace WF. (1976) “Development of stress-induced microcracks in Westerly Granite”. *Int J Rock Mech Min Sci & Geomech Abstr* vol13:103±12.
- Thostenson, E.T., Chou, T.-W., (1999) “Microwave Processing: Fundamentals and Applications”, *Composites: Part A* 30, pp1055-1071
- Valery, W. (1997) “A model for dynamic and steady-state simulation of Autogenous and SAG mills”. PhD Thesis, University of Queensland (JKMRC)
- Veasey, T.J. and Fitzgibbon, K.E., (1990) “Thermally Assisted Liberation - A Review” *Minerals Engineering*, Vol.3, pp181-185
- Viswanathan, M. (1990) “Investigations on the Effect of Microwave Pre-Treatment on Comminution” *International Coal Preparation Congress*: pp151-155
- Von Hippel. A. (1954) “Dielectric Materials and Applications”, *Technology Press*,

John Wiley and Sons, NY.

Walkiewicz, J.W., Clark, A.E., McGill, S.L., (1991) "Microwave Assisted Grinding",

IEEE Transactions on Industry Applications, Vol.27, no.2

Walkiewicz, J.W., Kazonich, G., McGill, S.L., (1988) Microwave Heating

Characteristics of Selected Minerals and Compounds. *Mineral and*

Metallurgical Processing Vol.5 (1), pp39-42

Wang, Y., Forrsberg, E., (2000) "Microwave assisted comminution and liberation of minerals" In: Ozbayoglu, G., et al. (Ed.), *Mineral Processing on the Verge of the 21st Century*. Balkema, Rotterdam, pp3 –9. ISBN 905809 1724.

Warner, H.K., et al. (1989) *Proc. First. Aus. Symp. On Microwave Power Applications*. pp179-188.

Whittles, D.N., Kingman, S.W., Reddish, D.J., (2002) Application of numerical modelling for prediction of the influence of power density on microwave-assisted breakage, *Int J Miner Process* Vol.68 pp71-91

Whittles, D.N., Ph.D. Thesis - The application of rock mass classification principles to coal mine design (1999). xiv, 318

Whyatt J.K. and Julien M. (1988) "A Fundamental Question: The Role of Numerical Methods in Rock Mechanics Design" *Key Questions in Rock Mechanics*, Edited by Cundall, Published by A.A. Balkema, pp311-315.

Wills, B.A., (1997) *Mineral Processing Technology*, sixth edition, Butterworth Heinemann

Wong, T.F., and Brace, W. F., (1979) "Thermal expansion of rocks: some measurements at high pressure" *Tectonophysics*, Vol.57, Issues 2-4, pp95-117

Woodcock J.T. (1989) "Possibilities for using microwave energy in the extraction of gold" *Proc. First. Aus. Symp. On Microwave Power Applications* pp139-152.

- Wong, T.F., Yang, X.W., Baud, P., (2000) “Micromechanics of compressive failure and special evolution of anisotropic damage in Darley Dale sandstone” *Int. J. of Rock Mech. and Min. Sci.* Vol.37 pp143-160
- Yates, A., (1919) “Effect of Heating and Quenching Cornish Tin Ores Before Crushing” *Trans I.M.M.* Vol.28 p41
- Zavitsanos, P.D., Bleiker, K.W., and Golden, J.A. (1979) “Coal Desulphurisation using alkali metal or alkali earth compounds and electromagnetic energy” *US patent No 4152120.*

List of Appendices

Appendix I	Publication
Appendix II	Complete detailed model code for heating simulation and loading simulation

APPENDIX 1 NOT COPIED
ON INSTRUCTION FROM
UNIVERSITY

Appendix II

Complete detailed model code

<pre> config thermal ; in mm, specify sample diameter def diam diam = 40 end ; in mm, specify zone diameter def zonemm zonemm = 0.5 end ; specify sample width in zones def horcoor horcoor = diam/zonemm end ; specify sample height def totalheight totalheight = 3*horcoor end ; specify width plus one def xplone xplone = horcoor + 1 end ; specify height plus one def heightplone heightplone = totalheight + 1 end </pre>	<p>Sets thermal mode</p> <p>‘def’ is shorthand for ‘define’</p> <p>Sets sample diameter as 40mm</p> <p>Defines each zone to be 0.5mm</p> <p>Sets diameter in terms of zones</p> <p>Sample is 2:1, and steel platens are half the diameter tall. Therefore total sample height is 3 x diameter</p> <p>Some boundary conditions require zonal specification and others nodal. This modification allows for specification of nodal and zonal diameter</p>
---	--

<pre> grid horcoor,totalheight ; specify platen coordinates ; specify bottom platen top side def pbcoor pbcoor = (horcoor * 0.5) - 1 end ; specify top platen bottom side def ptcoor ptcoor = totalheight - pbcoor end ; specify bottom platen top side plus one def pbplone pbplone = pbcoor + 1 end ; specify bottom platen top side minus one def pbminone pbminone = pbcoor - 1 end ; specify top platen bottom side minus one def ptminone ptminone = ptcoor - 1 end ; specify top platen bottom side plus one def ptplone ptplone = ptcoor + 1 </pre>	<p>Specifies total grid area in terms of zones</p> <p>Specifies top zonal coordinate of lower platen</p> <p>Specifies bottom zonal coordinate of upper platen</p> <p>Similar specification of nodal dimensions</p> <p>Specifies top extent of lower interface</p> <p>Similarly for bottom extent of upper interface</p> <p>Similarly for upper extent of upper interface</p>
---	--

<pre> end ; real spacial dimensions def XRIGHT XRIGHT = diam * 0.001 end def YTOP YTOP = XRIGHT * 3 end def platbot PLATBOT = XRIGHT * 0.5 end def platop PLATOP = YTOP - PLATBOT end gen 0.0,0.0 0.0,PLATBOT XRIGHT,PLATBOT XRIGHT,0.0 i 1 xplone j 1 pbcoor gen 0.0,PLATBOT 0.0,PLATOP XRIGHT,PLATOP XRIGHT,PLATBOT & i 1 xplone j pbplone ptcoor gen 0.0,PLATOP 0.0,YTOP XRIGHT,YTOP XRIGHT,PLATOP & i 1 xplone j ptplone heightplone * strain softening model model ss </pre>	<p>Specifies true spatial horizontal coordinates</p> <p>Specifies true spatial vertical coordinates</p> <p>Specifies true spatial lower platen coordinates</p> <p>Specifies true spatial lower platen coordinates</p> <p>Generates lower platen area</p> <p>Maps grid onto lower platen</p> <p>Generates sample UCS sample area</p> <p>Maps grid onto UCS sample area</p> <p>Generates upper platen area</p> <p>Maps grid onto upper platen</p> <p>Specifies model type as strain softening</p>
---	---

<p>* properties for strain softening</p> <p>* peak strength propeties</p> <p>prop fric 54 tens 15e6 coh 25e6 i=1,horcoor</p> <p>j=pbplone,ptminone</p> <p>* strain softening properties</p> <p>* ttab = tensile strength softening table</p> <p>* ctab = cohesion softening table</p> <p>prop ttab=1 ctab=2 i=1,horcoor</p> <p>j=pbplone,ptminone</p> <p>table 1 0,15e6 .001,0.1e6</p> <p>table 2 0,25e6 .01,2.5e6</p> <p>group 'User: calcitemc' region horcoor horcoor</p> <p>prop dens=2712 bulk=7.3299993E10</p> <p>shear=3.1999998E10 group 'User: calcitemc'</p> <p>prop coh=25E6 fric=54.0 dil=0.0 ten=15E6</p> <p>group 'User: calcitemc'</p> <p>MOD null I=1,horcoor J=1,pbminone</p> <p>MOD null I=1,horcoor J=ptcoor,totalheight</p> <p>* randomly generates pyrite distribution</p> <p>def percent</p> <p>percent = 0.01*(horcoor * (totalheight - horcoor))</p> <p>end</p>	<p>Specifies friction, tensile strength, cohesion peak values</p> <p>Specifies tensile strength softening</p> <p>Specifies cohesion softening</p> <p>Applies behaviour over sample area</p> <p>Specifies tensile strength reduction with 0.1% strain</p> <p>Specifies cohesion reduction with 1% strain</p> <p>Specifies sample area to have calcite material properties: density, bulk + shear modulus, cohesion, friction, tensile strength</p> <p>Sets lower interface regions as null</p> <p>Sets lower interface regions as null</p> <p>Defines percentage of pyrite to be applied to the model as 1%</p>
---	--

<pre> DEF RandomPyr LOOP M (1,percent) COOX = (URAND*horcoor) COOY = (URAND*(totalheight-horcoor)) + (horcoor * 0.5) COMMAND group 'User: pyritemc' I=COOX J=COOY prop density=5000.0 bulk= 1.427e11 shear=1.257e11 group 'User: pyritemc' prop coh=25E6 fric=54.0 dil=0.0 ten=15E6 group 'User: pyritemc' END_COMMAND END_LOOP END RandomPyr * applies interior heating source def source loop i (1,horcoor) loop j (pbplone,ptminone) if density(i,j) = 5000.0 then command interior source 1e15 i=i j=j end_command end_if end_loop </pre>	<p>Defines the function to apply random distribution of pyrite to the model as in Section 5.2.12.3</p> <p>Specifies pyrite material properties: density, bulk + shear modulus, cohesion, friction, dilation, tensile strength</p> <p>Executes random pyrite distribution</p> <p>Defines function to apply ‘power density’ to sample</p> <p>As explained in section 5.2.12.6</p>
---	---

<pre> end_loop end source save 40-500mu-1e15.sav ; thermal portion initial temperature 10.0 i 1 xplone j pbplone ptminone model th_isotropic i 1 xplone j pbplone ptminone def trop ; loop each grid node loop i (1,horcoor) loop j (pbplone,ptminone) ; for calcite if density(i,j)<3000 then thexp(i,j)=2E-5 end_if if density(i,j)<3000 then conductivity(i,j)=((temp(i,j)+273)*(-0.0053)) + 4.02 end_if if density(i,j)<3000 and if (temp(i,j)+273)>550 then spec_heat(i,j)=(0.2967*(temp(i,j)+273)) + 937.14 </pre>	<p>Saves current complete model state</p> <p>Specifies initial model temperature</p> <p>Specifies thermal isotropy</p> <p>Defines heating function – following constituent parts are detailed in sections 5.2.11.1 to 5.2.11.3</p>
--	--

```

end_if

end_if

if density(i,j)<3000 and

if (temp(i,j)+273)<550 then

spec_heat(i,j)= (1.1001*(temp(i,j)+273)) +

505.58

end_if

end_if

if temp(i,j)>485 then

conductivity(i,j)=0.1

end_if

; for pyrite

if density(i,j)>4000 then

thexp(i,j)=4E-5

end_if

if density(i,j)>4000 then

conductivity(i,j)=((temp(i,j)+273)*(-0.07545))

+ 37.9

end_if

if density(i,j)>4000 and

if (temp(i,j)+273)<450 then

spec_heat(i,j)=(0.4882*(temp(i,j)+273))+374.13

end_if

end_if

if density(i,j)>4000 and

```

<pre> if (temp(i,j)+273)>450 then spec_heat(i,j)=(0.1482*(temp(i,j)+273))+533.75 end_if end_if if temp(i,j)>220 then conductivity(i,j)=0.1 end_if end_loop end_loop command step 100 end_command end set thdt=0.0000000010 trop def damage loop i (1,izones) loop j (1,jzones) if model(i,j) # 1 then if cohesion(i,j)< 2.5e7 then cd=cd+1 end_if if tension(i,j)< 1.5e7 then td=td+1 </pre>	<p>Sets model to run for 100 steps</p> <p>Sets thermal time step as 1 nanosecond</p> <p>Executes heating function</p> <p>Specifies damage parameter function, as detailed in section 6.7.2</p>
--	--

<pre> end_if tot=tot+1 end_if end_loop end_loop command print cd print td print tot end_command end damage save 40-500mz-1e15-100ns.sav step 400 damage save 40-500mz-1e15-500ns.sav step 500 damage save 40-500mz-1e15-1000ns.sav step 1000 damage save 40-500mz-1e15-2000ns.sav step 1000 </pre>	<p>Saves model state</p> <p>Runs model for further 400 steps</p> <p>Runs damage function to examine how much damage those 400 thermal steps have generated</p> <p>Again saves model state</p> <p>Process repeated for number of heating simulation intervals</p>
--	--

<p>damage</p> <p>save 40-500mz-1e15-3000ns.sav</p> <p>step 2000</p> <p>damage</p> <p>save 40-500mz-1e15-5000ns.sav</p> <p>step 5000</p> <p>damage</p> <p>save 40-500mz-1e15-10000ns.sav</p> <p>restore 40-1-1e15-1000ms.sav</p> <p>MOD EL I=1,horcoor J=1,pbminone</p> <p>PROP DENS=7500 BULK=21E10</p> <p>SHEAR=8.1E10 I=1,horcoor J=1,pbminone</p> <p>MOD EL I=1,horcoor J=ptplone,totalheight</p> <p>PROP DENS=7500 BULK=21E10</p> <p>SHEAR=8.1E10 I=1,horcoor</p> <p>J=ptplone,totalheight</p> <p>INT 1 ASIDE FROM 1,pbcoor TO</p> <p>xplone,pbcoor BSIDE FROM 1,pbplone &</p> <p>TO xplone,pbplone</p> <p>INT 1 KN 2E12 KS 5E12 FRIC 32</p> <p>INT 2 ASIDE FROM 1,ptcoor TO</p> <p>xplone,ptcoor BSIDE FROM 1,ptplone &</p> <p>to xplone,ptplone</p>	<p>Specifies lower steel platen as elastic, with density, bulk + shear modulus</p> <p>Specifies upper steel platen as elastic, with density, bulk + shear modulus</p> <p>Specifies lower interface lower side coordinates and lower interface upper side</p> <p>Specifies stiffness parameters for interface</p> <p>Specifies upper interface lower side coordinates and upper interface upper side</p>
---	---

<p>INT 2 KN 2E12 KS 5E12 FRIC 32</p> <p>set thermal =off</p> <p>*set optimum damping method for ucs test</p> <p>set st_damp comb</p> <p>* remove thermal stresses</p> <p>ini sxx=0 i 1 xplone j 1 totalheight</p> <p>ini sxy=0 i 1 xplone j 1 totalheight</p> <p>ini syy=0 i 1 xplone j 1 totalheight</p> <p>ini szz=0 i 1 xplone j 1 totalheight</p> <p>ini ydis=0 i 1 xplone j 1 totalheight</p> <p>ini xdis=0 i 1 xplone j 1 totalheight</p> <p>ini xvel=0 i 1 xplone j 1 totalheight</p> <p>ini yvel=0 i 1 xplone j 1 totalheight</p> <p>* apply constant displacement rate to bottom</p> <p>* and to top boundary (units are m/step)</p> <p>apply yvel=-5e-9 j=totalheight</p> <p>apply yvel=5e-9 j=1</p> <p>* fish function to record sample strain</p> <p>* and stress during ucs simulation</p> <p>def load</p> <p>; loading for 40000 steps</p> <p>loop st(1,8000)</p> <p>command</p>	<p>Specifies stiffness parameters for interface</p> <p>Sets damping conditions for UCS test</p> <p>Removal of all thermal stress types after heating simulation from entire model</p> <p>Applies downwards velocity to upper platen</p> <p>Applies upwards velocity to lower platen</p> <p>Sets loading simulation to run for 8000 steps</p>
--	--

end_command	
top_load=0	Sets initial loading conditions
bot_load=0	
loop ts(1,igp-1)	
top_stress=top_stress+syy(ts,totalheight)	Defines area over which to average stress for top platen
bot_stress=bot_stress+syy(ts,1)	Defines area over which to average stress for bottom platen
end_loop	
top_stress=top_stress/xplone	
bot_stress=bot_stress/xplone	
av_stress=(top_stress+bot_stress)/2	Defines stress parameter to be logged for UCS curves
ve=(ydisp(40,1)-ydisp(40,240))/(y(40,240)-y(40,1))	Defines strain parameter to be logged for UCS curves
command	
print bot_stress	
history av_stress	Specifies history to be logged for stress
history ve	Specifies history to be logged for strain
step 5	Specifies logging every 5 loading steps
end_command	
end_loop	
end	
load	Executes loading function
save 40-1-1e15-1000ms-load.sav	Saves completed model state